LBNL-46763

ERNEST ORLANDO LAWRENCE
BERKELEY NATIONAL LABORATORY

Photoisomerization and Photodissociation Dynamics of Reactive Free Radicals

Ryan T. Bise

Chemical Sciences Division

August 2000

Ph.D. Thesis

LBNL-46763

Photoisomerization and Photodissociation Dynamics of Reactive Free Radicals

Ryan Tyler Bise
Ph.D. Thesis

Department of Chemistry
University of California, Berkeley

and

Chemical Sciences Division
Ernest Orlando Lawrence Berkeley National Laboratory
University of California
Berkeley, CA 94720

August 2000

This work was supported by the Director, Office of Science, Office of Basic Energy Sciences, Chemical Sciences Division, of the U.S. Department of Energy under Contract No. DE-AC03-76SF00098.

Photoisomerization and Photodissociation Dynamics of Reactive Free Radicals

by

Ryan Tyler Bise

B.S. (University of California at Los Angeles) 1995

A dissertation submitted in partial satisfaction of the

requirements for the degree of

Doctor of Philosopy
in

Chemistry

in the

GRADUATE DIVISION

of the

UNIVERSITY OF CALIFORNIA, BERKELEY

Committee in charge:

Professor Daniel M. Neumark, Chair
Professor Richard J. Saykally
Professor Robert W. Dibble

Fall 2000

Photoisomerization and Photodissociation Dynamics of Reactive Free Radicals

by

Ryan Tyler Bise

Abstract

Photoisomerization and Photodissociation Dynamics of Reactive Free Radicals

by

Ryan Tyler Bise

Doctor of Philosophy in Chemistry

University of California, Berkeley

Professor Daniel M. Neumark, Chair

The photofragmentation pathways of chemically reactive free radicals have been examined using the technique of fast beam photofragment translational spectroscopy. Measurements of the photodissociation cross-sections, product branching ratios, product state energy distributions, and angular distributions provide insight into the excited state potential energy surfaces and nonadiabatic processes involved in the dissociation mechanisms.

Photodissociation spectroscopy and dynamics of the predissociative $\tilde{A}^2A_1$ and $\tilde{B}^2A_2$ states of CH_3S have been investigated. At all photon energies, $CH_3 + S(^3P_j)$, was the main reaction channel. The translational energy distributions reveal resolved structure corresponding to vibrational excitation of the CH_3 umbrella mode and the $S(^3P_j)$ fine-structure distribution from which the nature of the coupled repulsive surfaces is inferred. Dissociation rates are deduced from the photofragment angular distributions, which depend intimately on the degree of vibrational excitation in the C-S stretch.

Nitrogen combustion radicals, NCN, CNN and HNCN have also been studied. For all three radicals, the elimination of molecular nitrogen is the primary reaction channel. Excitation to linear excited triplet and singlet electronic states of the NCN radical generates resolved vibrational structure of the N_2 photofragment. The relatively low fragment rotational excitation suggests dissociation via a symmetric C_{2v} transition state. Resolved vibrational structure of the N_2 photofragment is also observed in the photodissociation of the HNCN radical. The fragment vibrational and rotational distributions broaden with increased excitation energy. Simple dissociation models suggest that the HNCN radical isomerizes to a cyclic intermediate (c-HCNN) which then dissociates via a tight cyclic transition state. In contrast to the radicals mentioned above, resolved vibrational structure was not observed for the CNN radical due to extensive fragment rotational excitation, suggesting that intermediate bent states are strongly coupled along the dissociation pathway.

The measurements performed in this Thesis have additionally refined the heats of formation and bond dissociation energies of these radicals and have unambiguously confirmed and added to the known electronic spectroscopy.

Table of Contents

Acknowledgements

Anyone who has had more than a five-minute conversation with me immediately recognizes that I must have had an awful lot of help and support to complete a doctoral degree at Berkeley and I accordingly recognize the numerous people who have made this possible.

I am particularly grateful to my research advisor Professor Daniel Neumark. Throughout my graduate research, Dan has challenged and encouraged me, providing a wealth of information and ideas as well as affording me the freedom to explore my own ideas. Dan has also generously offered his opinions and advice regarding various career paths. I wish him the best of luck in his future research endeavors and as the newly appointed director of the Chemical Sciences Division of Lawrence Berkeley Laboratories.

Dr. David Osborn and the now infamous Dr. David H. Mordaunt deserve mention for showing me the beauty and elegance of the fast radical beam machine and of photodissociation in general. I additionally had the pleasure of working with Dr. Hyeon "S." Choi for four of my five years in graduate school. I eventually came to learn that Hyeon was almost always right, although I rarely recognized this at the time or gave him credit for it. Vampiress, Alexandra Hoops, perfectly willing to sit in the dark for hours has proven to be valuable addition to the FRBM team, learning to coax the ions and lasers into cooperating. Dr. Jason Gascooke has recently arrived from down under, bringing with him an impressive host of experimental and computing skills which have already made substantial impact towards the project. I look forward to seeing the

exciting results to be obtained by both Alex and Jason upon implementation of the new imaging detector.

I have also been fortunate to have been surrounded by the other talented graduate students and postdocs of the Neumark group. Dr. Martin Zanni brought an excitement and intensity to research that was truly inspiring. Dr. Travis Taylor was an instrumental part of the NCN studies, performing the necessary photoelectron studies. Travis' creativity and exploratory nature both in and out of the lab made him an interestiing person to be around. Dr. Cangshan Xu is my hero. I am also indebted to Dr. Thomas Lenzer for showing me things about lasers I didn't even know were possible and to Dr. Knut Asmis for encouraging my caffeine addition during our nearly daily visits to Strada for a daily dose of cappacino and spectroscopy. I also would like to thank Dr. Zhuan Liu for taking the HNCN photoelectron spectrum.

Michael Furlanetto has been a fantastic colleague, roommate and friend over the past five years. I have thoroughly benefited from our discussions of experimental techniques, possible research projects, the wisdom of our advisor, basketball, women, sex, drugs and rock and roll. Our numerous excursions for basketball, beer or camping made graduate school much more enjoyable. I have no doubt that he will successfully traverse the slippery BrHI neutral potential energy surface. I also want to thank Michael's parents for the Lexus, a powerful and luxurious automobile. If you have the means, I highly recommend it.

I am obliged to Jason Robinson, Alison Davis, Harry Gomez, and Nick Pivonka for allowing me to "borrow" laser and ion beam equipment which have become permanent fixtures of the FRBM setup. I will miss the early morning coffee BS sessions

with Nick and Jason, although I am certain that a whole lot more work will be accomplished. A fellow Alcatraz swimmer, Nick, should be comforted in knowing that no jail can hold him. Harry Gomez has learned that the ions don't make themselves and has patiently dealt with my slow and painful progress towards understanding Microsoft and a host of other computer applications.

My undergraduate research advisor, Professor Miguel A. Garcia-Garibay requires special mention for introducing me to experimental research and showing me that high quality physical chemistry can indeed be done without lasers. The crude synthetic skills learned in his laboratory gave me enough confidence to attempt to synthesize the highly reactive C_3O_2 and H_2CNN molecules.

In addition to my colleagues, I have been surrounded by supportive friends and family during my graduate studies. Of particular note is Aaron Axton who provided numerous weekend outings which usually centered around eating, drinking, basketball and swimming although rarely in that order. Axton and "the heads" were genuinely supportive and encouraging throughout my studies and provided a nice change of environment from the dungeon. For the past two years, I have been fortunate to have my younger brother, Michael, living in Berkeley. The few surfing trips, foiled Alcatraz swim, Sunday family dinners and other activities with Michael *et al.* have made my last few years here by far the most enjoyable.

Chapter 1. Introduction

Free radicals, defined as molecules possessing one or more unpaired electrons, are highly reactive transient species that play an important role in a variety of environments such as combustion, interstellar chemistry, atmospheric processes, and plasmas. Relevant to the work presented in this Thesis, the NCN, CNN and HNCN radicals have all been proposed as important intermediates in the reactions of C-atoms and CH with molecular nitrogen,

$$C + N_2 \rightarrow CN + N$$

$$CH + N_2 \rightarrow HCN + N$$

providing low-energy pathways for the cleavage of molecular nitrogen, the initiating steps in the formation of prompt NO.[1-3] To determine the relative importance of reactions such as the ones listed above in combustion or atmospheric cycles, accurate values for the enthalpies of reaction, $\Delta_{rxn}H_0$ and barrier heights along the reactive potential energy surfaces are required. Despite their chemical importance, characterization of the reactive potential energy surfaces of free radicals has been limited due to the difficulty in preparing intense sources of radicals with high purity.[4] Our laboratory has developed a general method for overcoming this problem by generating pure neutral radical beams via the photodetachment of mass-selected anions. Photodissociation studies are then performed on the free radical of interest. A description of this technique, Fast Radical Beam Photofragment Translational Spectrocopy, is shown below, Eq 1, for a model polyatomic radical, A.

$$A^- + h\nu_{detach} \rightarrow A + h\nu_{dissociation} \rightarrow B + C \qquad (1)$$

where A^-, the negative ion precursor is photodetached near threshold by $h\nu_{detach}$ generating a beam of cold neutral radicals, A. These neutral A radicals are subsequently photodissociated by $h\nu_{dissociation}$ generating atomic or molecular fragments B and C which are detected by a "universal" detector. Above, 'free radicals' were defined as molecules possessing unpaired electron. However this term is loosely applied to a number of transient singlet species such as NH($a^1\Delta$), NCN($\tilde{a}^1\Delta_g$) and O_3($\tilde{X}^1A_1$). In this experiment, any molecule which effectively binds an electron can be studied.

Photodissociation Methods

Photodissociation of an isolated gas-phase molecule is one of the simplest chemical reactions using the energy of a photon to initiate unimolecular decomposition. Detailed measurements of the photodissociation cross-sections, rates of reaction, nascent photofragment branching ratios, bond dissociation energies and the photofragment internal energy and angular distributions combined with high-level *ab initio* potential energy surfaces and dynamics calculations allow chemists to assess which electronic surfaces and nuclear motions are involved in the fragmentation process.[5,6] Free-radicals are generally less bound than closed-shell molecules. While closed shell molecules frequently dissociate into two radical fragments, dissociation of a neutral radical frequently gives rise to a radical and a stable closed-shell molecule. As a result, free radicals typically have numerous low-lying electronic states and product states, and therefore provide model systems to investigate the couplings and interactions of excited states in bond dissociation.

A number of state-of-the-art experimental techniques have been employed to elucidate the forces involved in the dissociation mechanism. The general focus of these

methods has been to determine how the excess energy above the dissociation asymptote is distributed between the relative translational motion and the vibrational and rotational states of the nascent fragments. The energy balance for the overall energy partitioning for the photodissociation of radical A to photofragments B and C is given in Eq. 2,

$$h\nu - D_0 = E_T + E_B^{vib/rot} + E_C^{vib/rot} \qquad (2)$$

where hν is the photon energy and D_0 is the dissociation energy of A respectively, E_T is the relative translational energy, and $E_B^{vib/rot}$ and $E_C^{vib/rot}$ are the vibrational and rotational energies for the B and C fragments respectively.

As stated by Butler and Neumark in a recent review,[7] modern detection techniques are a "compromise between generality, sensitivity and resolution." Sensitive high resolution spectroscopic probes such as laser-induced fluorescence (LIF) or resonance-enhanced multi-photon ionization (REMPI) yield specific vibrational and rotational quantum state distributions for a single photofragment as well as detailed descriptions of the alignment and orientation of recoiling photofragments. However, these spectroscopic techniques offer little information regarding the translational energy or internal energy partitioning of the other nascent photofragment. Coupling LIF or REMPI with Doppler spectroscopy yields translational energy distribution from which the internal energy distribution of the counter fragment can be inferred. However, the resolution of the resulting translational energy distributions displays, at best, vibrational structure.[8,9] These methods are particularly suited to atomic or diatomic photofragments whose electronic spectroscopy is well-described. Extending these detection schemes to larger polyatomic photofragments is technically challenging due to the increased density of states and less extensive spectral information.

An alternative scheme measures the translational energy distribution, which reflects the combined internal energy distributions of the two photofragments. A general method for measuring the translational energy distribution was pioneered by Wilson and coworkers[10] (1969) and refined by Lee and coworkers .[11,12] In this technique, photofragment translational spectroscopy, the velocity distribution of a single photofragment is determined by measuring the time required for nascent fragment to travel from the photolysis laser to the detector. This particular technique employs a "universal" detector, allowing all possible photofragments in any quantum to be detected, and hence can be applied to nearly any system. However, techniques such as these are limited to vibrational resolution. More recent time-of-flight methods have been developed, most notably that of H-atom time-of-flight developed by Ashfold and coworkers[13] which affords rotationally resolved translational energy distributions. However, as evidenced form the name of the technique, it is specific to the detection of H-atoms.

Recently, ion imaging techniques,[8,14] (1995) have provide an alternative method for measuring the photofragment translational energy distribution. In these experiments a photofragment is ionized via resonance-enhanced multi-photon ionization (REMPI), extracted onto multi-channel plate detector which is then imaged by a CCD camera. The image obtained describes the velocity distribution of the photofragments, yielding the energy and angular distributions. This technique is essentially background free and the recent higher resolution method of velocity-map imaging[15] affords vibrationally resolved translational energy distributions. However, the technique is inherently fragment and state-specific. As a result, most ion imaging experiments probe atomic photofragments

due to the low density of states. Notable exceptions are recent experiments on CH_3I (Refs. 16) and HNCO (Refs. 17-20), which respectively probed the CH_3 and CO fragments.

Radical Photodissociation

Numerous photodissociation experiments have been performed on chemically stable radicals such as O_2, O_3, ClO_2, NO, and NO_2. The generation of more reactive radicals requires highly energetic environments such as photolysis, pyrolysis, gas-dischages, and chemical flow-reactors. These radical sources are frequently indiscriminate, producing a variety of radicals, cations and anions, making it extremely difficult to produce a clean source of radicals in well-defined energy states. In spite of the non-selective nature of these radical sources, the selectivity and sensitive nature of spectroscopic techniques has allowed bound vibrational and electronic states to be characterized for a number of radicals.[21-24] Photodissociation experiments require both intense and pure sources of radicals, which has limited experiments of this nature to only a handful of radicals, a number of which have been reviewed by Whitehead in 1996.[4] More recently, Davis and coworkers[25] and Suits and coworkers[26] have used laser photolysis sources to study the photodissociation dynamics of the H_2CN and the C_2H_3 radicals respectively. The "flash-pyrolysis" source developed by Chen and coworkers[27] has been particularly successful in generating clean sources of hydrocarbon radicals such as C_3H_3,[28] C_3H_5,[29] and C_2H_5.[30] It is not clear yet whether this source is generally applicable to other types of radicals.

Fast Beam Photofragment Translational Spectrometer

A general scheme has been developed in our laboratory to generate a clean source of neutral radicals via the photodetachment of negative ion precursors. In this experiment, we take advantage of the fact that open-shell radicals typically have positive electron affinities and therefore form stable negative ions. Since we start with anions, these charged species can be accelerated to high lab velocity and separated using mass spectroscopy. The apparatus, the Fast Radical Beam Photofragment Machine (FRBM), originally constructed by Cyr, Continetti, Metz, and Neumark,[31] has been described in rigorous detail previously.[32] This technique employs a sensitive "universal" detector which can yield vibrationally resolved translational energy distributions and can in principle be applied to any radical with a postive electron affinity. A general description of the apparatus and detection principles will be given here. The FRBM apparatus is shown in Figure 1.

Ions are prepared by supersonically expanding a gas mixture containing roughly 5-10% of ion precursors seeded in an inert carrier gas through a pulsed molecular beam valve at 60 Hz into a pulsed electric discharge.[33] The molecular beam is also crossed by an ~ 1 keV electron beam upon exiting the discharge. The ions generated continue to undergo supersonic expansion and are cooled both vibrationally and rotationally with typical vibrational and rotational temperatures of 100 K and 50 K respectively. The ion beam is skimmed and accelerated to high laboratory beam energies (5-9 keV.) The anions are separated using a Bakker time-of-flight mass spectrometer [34,35] with a mass resoluton of $m/\Delta m$ ~ 100. The anion of interest is selectively photodetached by a tunable excimer-pumped dye laser, generating a mass-selected beam of neutral radicals. The

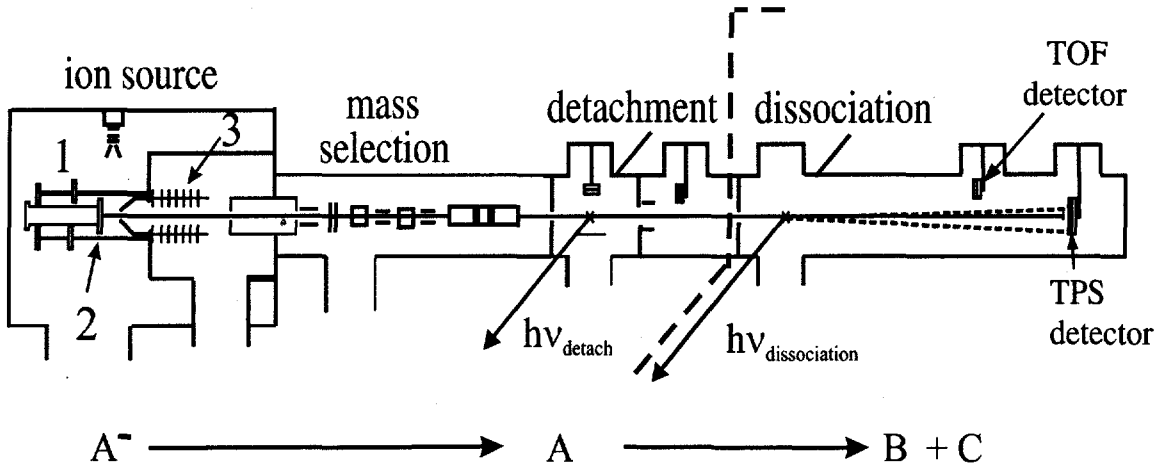

Figure 1. Fast radical beam translational spectrometer. In the ion source region, the pulsed valve (1), electric dischage plates (2) and acceleration plates (3) are indicated. The mass-selection, detachment and dissociation regions and indicated along with the detachment and dissociation lasers. The radical production and photodissociation regions are separated with a dashed line. The time-of-flight (TOF) and time-and-position sensing (TPS) detectors are shown.

photodetachment energy is usually tuned close to the electron affinity so that the neutrals are produced in the ground vibrational and electronic state. Anions which are not photodetached are deflected out of the flight path by electrostatic plates. The neutral radicals are subsequently intersected by a second excimer-pumped dye laser with frequency-doubling capabilities. A fraction of neutrals absorb laser light and dissociate, yielding photofragments which are detected directly without an ionization step by either the TOF or TPS (time-and-position sensing) micro-channel plate detector assemblies. The TOF detector is retractable and is pulled out of the beam path when using the TPS detector. A beam block is located at the center of each detector to prevent undissociated neutrals from impacting the detector. The observed signal is therefore from photofragments exclusively.

Two general types of experiments are performed. First the spectroscopy of the dissociative electronic states is determined by measuring the total flux of photofragments arriving at the TOF detector, located 0.68 m from the dissociation laser as a function of the photon energy. The resulting photofragment yield (PFY) spectra is complementary to absorption and fluorescence measurements.

Once the spectroscopy of the dissociative states has been examined, the photodissociation laser is set to particular frequencies of interest and the dissociation dyanamics are examined by detecting *in coincidence* both photofragments from the dissociation of a single neutral radical using a time-and-position sensing (TPS) detector similar to that developed by de Bruijn and Los.[36] The TPS detector records the positions of the fragments as well as the difference in time-of-arrival of the photofragments. This information is then used to determine the masses of the fragments, their relative translational energy, E_T, and the scattering angle θ between the relative velocity vector and the electric vector, $\vec{E}$, of the polarized dissociation laser. The kinematic equations used in this transformation are given below with the corresponding vector quantities shown in Figure 2.

$$\frac{m_B}{m_C} = \frac{r_B}{r_C} \cdot \left(1 - \frac{v_0 \tau}{L}\right) \qquad (1.3),$$

$$E_T = E_0 \cdot \frac{m_B m_C}{(m_A)^2} \cdot \left[\frac{(v_0\tau)^2 + R_{XY}{}^2}{L^2}\right] \cdot \left[1 + 2 \cdot \frac{m_B - m_C}{m_A} \cdot \frac{v_0 \tau}{L}\right] \qquad (1.4),$$

$$\theta = \arctan \frac{R_{XY}}{v_0 \tau} \quad (\vec{E} \text{ parallel to the beam axis}), \qquad (1.5).$$

Here, r_B and r_C are the distances of each photofragment on the detector face to the center of the radical beam. $R = r_B + r_C$ is the distance between the two photofragments and τ is the difference in time of arrival of the two photofragments. The photofragment masses are given by m_B and m_C. E_0 and v_0 are the parent beam energies and beam velocities respectively and L is the distance from the dissociation laser to the detector face.The flight distance, L, is normally kept at 1 m, but can be extended to 2 m to look at lower recoil energies. The photofragment mass resolution is $m/\Delta m \approx 10$ while the translational energy resolutions is ~ $\Delta E_T/E_T = 2.0\%$

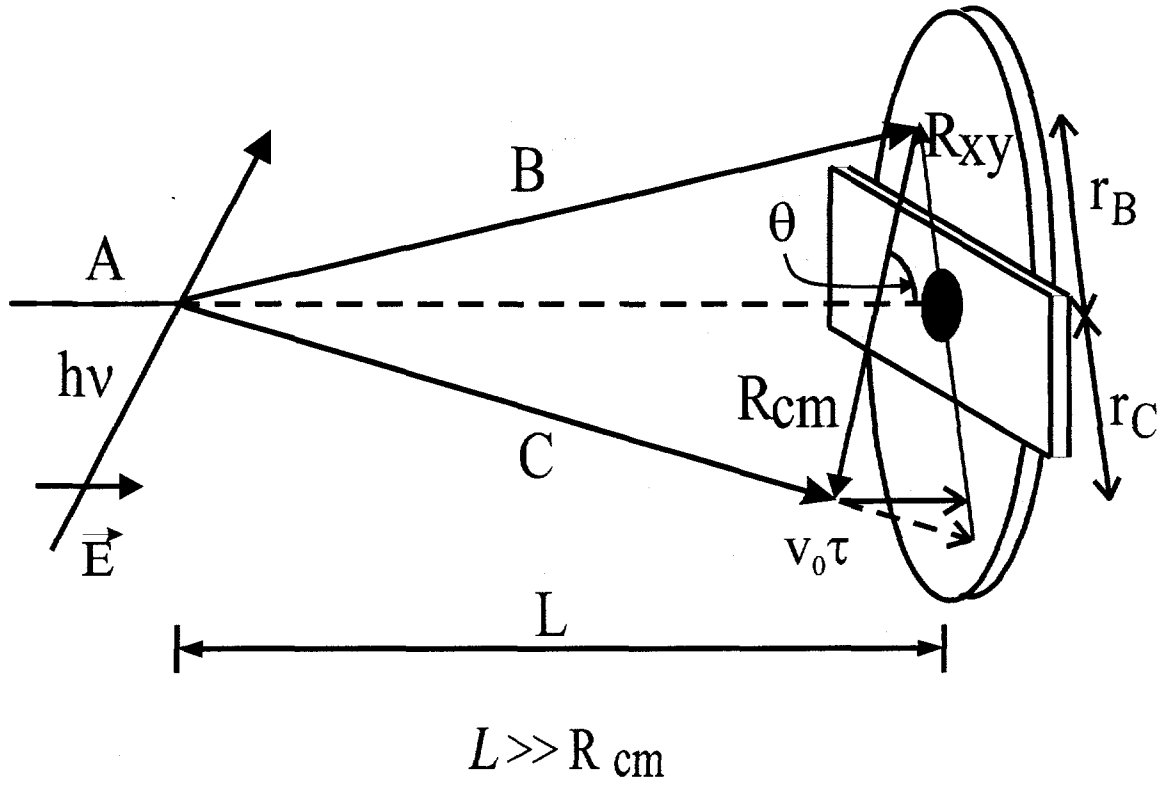

Figure 2. Schematic of the kinematics for coincidence detection of photofragments using the Fast beam photofragment translational spectrometer for a model *A* radical with photofragments *B* and *C*. The vector quantities are described in the text.

Due to the geometry of the TPS detector, which is 40 mm in diameter with an 8 mm beam block located at the center, the collection efficiency of photofragments depends on their values of θ and E_T. The beam block, in addition to blocking undissociated radicals, prevents fragments of low translational energy or with values of θ close to 0° or 180° from reaching the detector, while high-energy recoil fragments with values of θ close to 90° miss the detector. The raw translational energy distributions are therefore normalized by the calculated detector acceptance function, $D(E_T, \theta)$, which has been described in detail by Continetti *et al.*[37] The geometry of the detector also limits the photofragment mass ratio to ~ 4:1. For larger mass ratios the recoil distance of light fragment would extend beyond the detector while the heavy fragment would not clear the beam block, making our technique insensitive to light atom dissociation channels such as H-atom loss, hence the quotations associated with the "universal" detector.

While the use of photodetachment of negative ion precursors allows mass-selection, the neutral beam densities are typically 10^3-10^4 molecules/cm^3 compared to $5 \cdot 10^{12}$ molecules/cm^3 for typical neutral beam experiments.[38] Photodissociation experiments with such low number densities are possible since the fast beam technique allows the detector to collect nearly all of the dissociation volume with a high detection efficiency (> 50% for neutrals with more than 1 keV of translational energy).[39] The universal nature of the detector allows multiple product channels to be examined simultaneously while the high energy resolution (typically 20 meV) yields vibrationally resolved translational energy distributions. Due to the low-lying electronic states and product states associated with radicals and the high detection efficiency of this technique, the tunable ultra-violet output from a frequency doubled excimer-pumped dye laser (3 to

6 eV, 10-100 mJ/cm^2) is sufficient for dissociation studies and hence enables one to assess the influence of the total photon energy, excited electronic state, or vibrational motion upon the product branching ratios and product state distributions providing further insight into the essential features of the potential energy surface. Furthermore, the inherent multiplexed nature of the Fast Radical Beam Technique allows multiple product states and recoil angles to be examined simultaneously making an investigation of the dissociation dynamics at multiple dissociation wavelengths experimentally tractable. This is in marked contrast to photodissociation experiments of closed-shell molecules, which are generally limited to only few photolysis energies.

Advantages of photodetachment

The photodetachment of a fast mass-selected negative-ion beam is a general method for producing cold well-defined beam of neutral radicals. However, for studies in which there are multiple bound structural isomers, mass-selection may not be enough. One solution to this problem is by starting with precursors similar to the structure of the desired radical, e.g. H_2NCN was the chosen precursor for the NCN and HNCN radicals while H_2CNN was used in the production of CNN. Additionally, structural isomers typically have different electron affinities and therefore, the photodetachment energy can be tuned to discriminate between isomeric structures.

In addition to isomer discrimination, the photodetachment energy can be tuned to selectively populate metastable states of the neutral radical which are inaccessible by standard optical spectroscopy. This ability was first demonstrated in this group in 1998 for the CCO radical,[40] and subsequently for the isoelectronic NCN free radical.[41] The

selection rules for photodetachment require that the neutral state configuration is accessible via removal of one electron from the negative ion. Removal of the outermost π-orbital of $NCN^-(\tilde{X}^2\Pi_g)$ yields the $\tilde{X}^3\Sigma_g^-$, $\tilde{a}^1\Delta_g$ and $\tilde{b}^1\Sigma_g^+$ neutral states of NCN (see Figure 3.) with binding energies of 2.484 eV, 3.494 eV, and 4.113 eV respectively.[42] Due to spin selection rules, the $\tilde{a}^1\Delta_g$, $\tilde{b}^1\Sigma_g^+$ or higher-energy singlet states cannot be

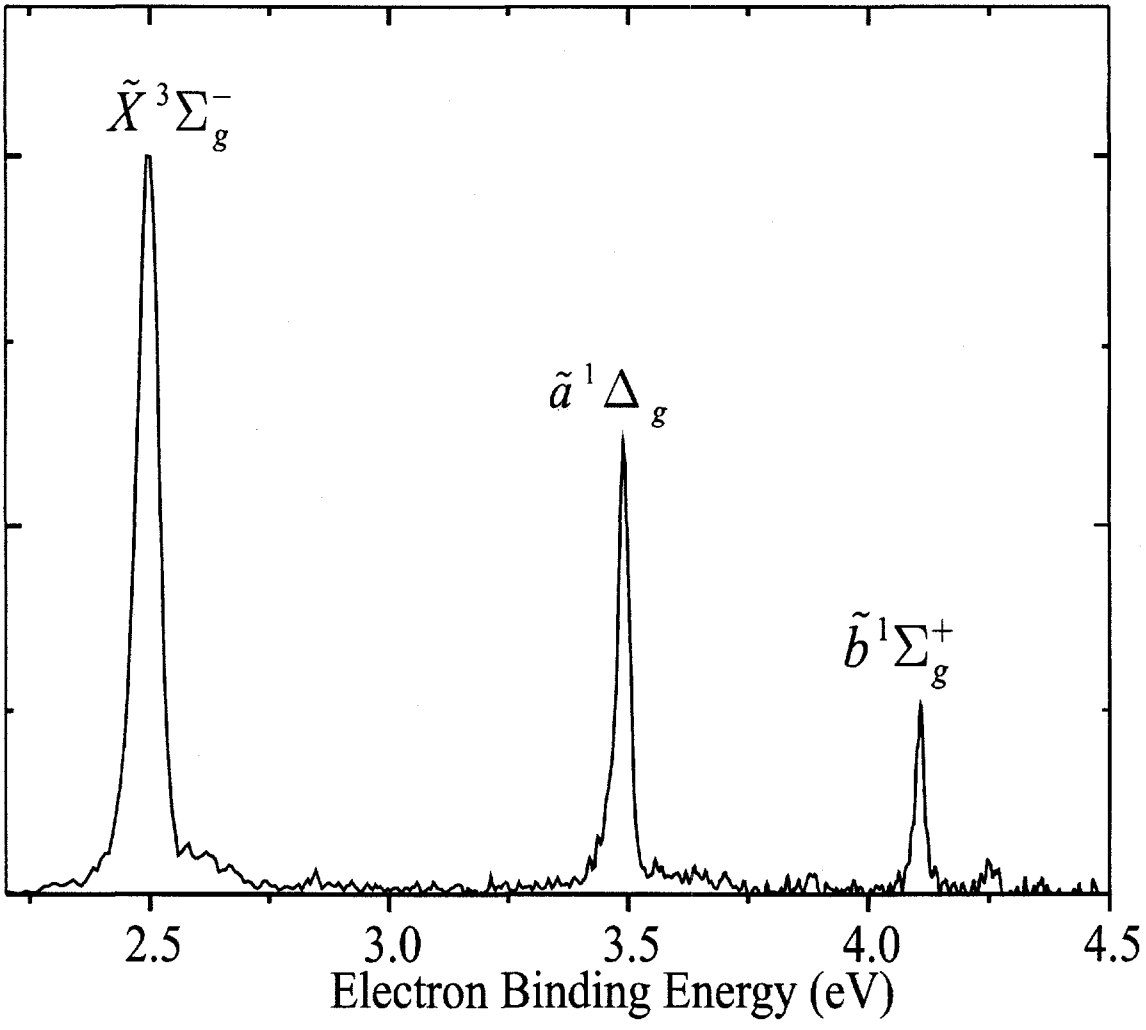

Figure 3. Photoelectron spectrum of NCN^- by Taylor *et al.*[42] The electronic states and symmetries of the neutral radical are indicated.

accessed from the ground $\tilde{X}^3\Sigma_g^-$ state via optical excitation. A photodetachment energy between 2.5-3.4 eV generates NCN radicals in the $\tilde{X}^3\Sigma_g^-$ state exclusively. By increasing the photon energy to 4.03 eV, both the $\tilde{a}^1\Delta_g$ and $\tilde{X}^3\Sigma_g^-$ state are populated with a relative ratio of approximately 2:1. The metastable $\tilde{a}^1\Delta_g$ state can then be optically excited to higher-energy singlet states allowing one to explore the dissociation dynamics of the singlet manifold. This technique is rotationally cold due to the initial supersonic expansion and allows tunable control over the metastable state population. In principle, this method can be applied to any metastable state, electronic or vibrational, whose lifetime is longer than the time required to travel between the photodetachment and photodissociation interaction regions. (~ 5 μs).

The mass-selectivity, universal detection scheme, and the tunability of the photdetachment and photodissociation lasers provided by the Fast Radical Beam Translational Spectrometer permit unambiguous and detailed investigation of the reactive potential energy surfaces of free radicals. In this Thesis, the results of photodissociation studies of the CH_3S, NCN, CNN and HNCN free radicals are reported. In addition to extending the known electronic spectroscopy and substantially improving the values for the heats of formation, this work has provided an in depth examination of the nonadiabatic dissociation pathways of these radicals. A particularly surprising and interesting result of the work presented here is the importance of bent and cyclic intermediates and transition states in the dissociation of the NCN, CNN and HNCN free radicals. While cyclic minimum energy structures for these molecules have been

determined theoretically[43-45] and proposed as important structures in combustion processes, this work provides the first experimental observations of such states.

References

1 C. P. Fenimore, in *Procedings of the Thirteenth Symposium (International) on Combustion* (The Combustion Institute, Pittsburgh, PA, 1971), pp. 373.

2 J. A. Miller and C. T. Bowman, Prog. Energy Combust. Sci. **15,** 287 (1989).

3 A. J. Dean, R. K. Hanson, and C. T. Bowman, in *Proceedings of the Twenty-third Symposium (International) on Combustion* (The Combusiton Institute, Pittsburg, PA, 1990), pp. 259.

4 J. C. Whitehead, Rep. Prog. Phys. **59,** 993 (1996).

5 J. R. Huber and R. Schinke, J. Phys. Chem. **97,** 3463 (1993).

6 A. J. Alexander and R. N. Zare, Accts. Chem. Res. **33,** 199 (2000).

7 L. J. Butler and D. M. Neumark, J. Phys. Chem. **100,** 12801 (1996).

8 P. L. Houston, J. Phys. Chem. **100,** 12757 (1996).

9 P. L. Houston, Laser Focus World **28,** 23 (1992).

10 G. E. Busch, R. T. Mahoney, R. I. Morse, and K. R. Wilson, J. Chem. Phys **51,** 449 (1969).

11 A. M. Wodtke, Ph. D. Thesis, University of California, Berkeley, 1986.

12 A. M. Wodtke and Y. T. Lee, in *Molecular Photodissociation Dynamics*, edited by M. N. R. Ashfold and J. E. Baggot (Royal Chemical Society, London, 1986), pp. 29.

13 M. N. R. Ashfold, I. R. Lambert, D. H. Mordaunt, G. P. Morley, and C. M. Western, J. Phys. Chem. **96,** 2938 (1992).

14 P. L. Houston, Accts. Chem. Res. **28,** 453 (1995).

15 A. Eppink and D. H. Parker, Rev. Sci. Instrum. **68,** 3477 (1997).

16 A. Eppink and D. H. Parker, J. Chem. Phys **110,** 832 (1999).

Chapter 2. Photodissociation Spectroscopy and Dynamics of the Methylthio Radical (CH_3S)[†]

The photodissociation spectroscopy and dynamics of the CH_3S and CD_3S radicals have been investigated using fast radical beam photofragment spectroscopy of the $\tilde{A}\ ^2A_1 \leftarrow \tilde{X}\ ^2E$ electronic band ($T_0 \cong 26{,}400\ cm^{-1}$) and an unstructured band near 45,600 cm^{-1}. Our detection scheme is most sensitive to C-S bond fission channels. At all photon energies, only one major product channel, $CH_3(\tilde{X}\ ^2A_2'') + S(^3P_j)$, was observed. Photofragment yield spectra for the $\tilde{A}\ ^2A_1 \leftarrow \tilde{X}\ ^2E$ electronic band show resolved vibrational progressions extended well beyond those seen in laser-induced fluorescence studies of this band. Photofragment translational energy distributions yield the $S(^3P_j)$ fine-structure distribution for each vibrational level of the CH_3 product. Photofragment angular distributions were found to be highly anisotropic ($\beta = -0.2$ to -1.0 ± 0.1) with increasing anisotropy at higher photon energies. The results yield a refined heat of formation for CH_3S (1.346 ± 0.018 eV) as well as the mechanism by which the $\tilde{A}\ ^2A_1$ state is predissociated. Results at 45,600 cm^{-1} imply that dissociation occurs on the repulsive $\tilde{B}\ ^2A_2$ state.

I. Introduction

Photodissociation of polyatomic molecules provides a rich probe of excited state potential energy surfaces and their interactions. Measurements of photofragment yield spectra, translational energy distributions, product branching ratios, and fine-structure

---

[†] Originally published in J. Chem. Phys. **110**, 805 (1999).

distributions, probe the detailed coupling of excited electronic states with the dissociation continuum.[1-3] While there have been many photodissociation studies of stable closed-shell molecules over the past 15 years, corresponding studies of open-shell radicals have been limited. Our laboratory has demonstrated the ability to generate a well-characterized source of radicals via photodetachment of negative ions, allowing us to perform photodissociation experiments on reactive open-shell species. In this article, we present the ultraviolet photodissociation spectroscopy and dynamics of the methylthio radical (CH_3S).

The methylthio radical has been proposed as an important intermediate in atmospheric oxidation of naturally occuring sulfur species such as dimethyl sulfide (CH_3SCH_3), dimethyl disulfide (CH_3SSCH_3) and methyl mercaptan (CH_3SH).[4] There have been numerous spectroscopic studies of the methylthio radical since the first spectroscopic observation of a diffuse abosorption band centered at 45770 cm^{-1} in 1969 by Callear and Dickson.[5] Anion photoelectron and photodetachment spectroscopy,[6-8] microwave[9] and infrared spectroscopy,[10] and electronic emission[11] studies have provided information regarding the geometry, spin-orbit splitting and vibrational frequencies of the $\tilde{X}\,^2E$ ground state.

The excited $\tilde{A}\,^2A_1$ state has also been characterized in detail through laser-induced fluorescence (LIF) experiments on the $\tilde{A}\,^2A_1 \leftarrow \tilde{X}\,^2E$ transition.[12-16] Vibrationally-resolved measurements show progressions in the in the totally symmetric C-S stretch (ν_3) and CH_3 umbrella mode (ν_2) modes.[12,13,15-18] The weak 6_0^1 Jahn-Teller active transition involving the methyl rocking mode has also been observed.[15,17] Rotationally resolved

LIF experiments by Miller and coworkers[14] show that the C-S bond distancce increases by 0.3 Å and the HCS bond angle decreases by ≈ 4° in the $\tilde{A}$ state, thus explaining the observed vibrational progressions. Radiative lifetime measurements show a significant decrease for $\tilde{A}$ state vibrational levels ≥800 cm^{-1} above the origin.[12,13,15,18] This effect, a likely signature of predissociation, limits LIF measurements to the region between 26,200-28,000 cm^{-1}, in contrast to low-resolution ultraviolet absorption measurements that show the $\tilde{A} \leftarrow \tilde{X}$ band extends to 31,000 cm^{-1}.[19]

The methylthio radical has also been the subject of theoretical interest, motivated in part by the interactions between Jahn-Teller and spin-orbit effects in the degenerate $\tilde{X}\,^2E$ ground state.[20] Several *ab initio* calculations have been performed to determine the energetics and geometry of the methylthio radical in its ground and excited electronic states.[8,21-23] Figure 1 shows the potential energy surfaces for the CH_3S radical along the C-S bond based upon the ab initio calculations of both Cui *et al.*[24] and Hsu *et al.*[22] The $\tilde{A}\ ^2A_1$ surface, which correlates asymptotically to excited state products CH_3 + $S(^1D)$, is crossed by three repulsive surfaces, the $^4A_2$, ^4E, and $^2A_2$ states. These correlate to ground state products CH_3 + $S(^3P_{2,1,0})$ and induce predissociation in the $\tilde{A}$ state. Recent *ab initio* studies by Cui and Morokuma[24] have focused on the predissociation of the $\tilde{A} \leftarrow \tilde{X}$ transitions for CH_3S, as well as the related species CH_3O, CF_3O, and CF_3S, calculating the minimum seams of crossing and spin-orbit coupling elements between the $\tilde{A}\ ^2A_1$ and the repulsive ^4E and $^4A_2$ states. While most of the experimental and theoretical work has focused on the $\tilde{A} \leftarrow \tilde{X}$ band, the photolysis of CH_3S has also been studied at higher

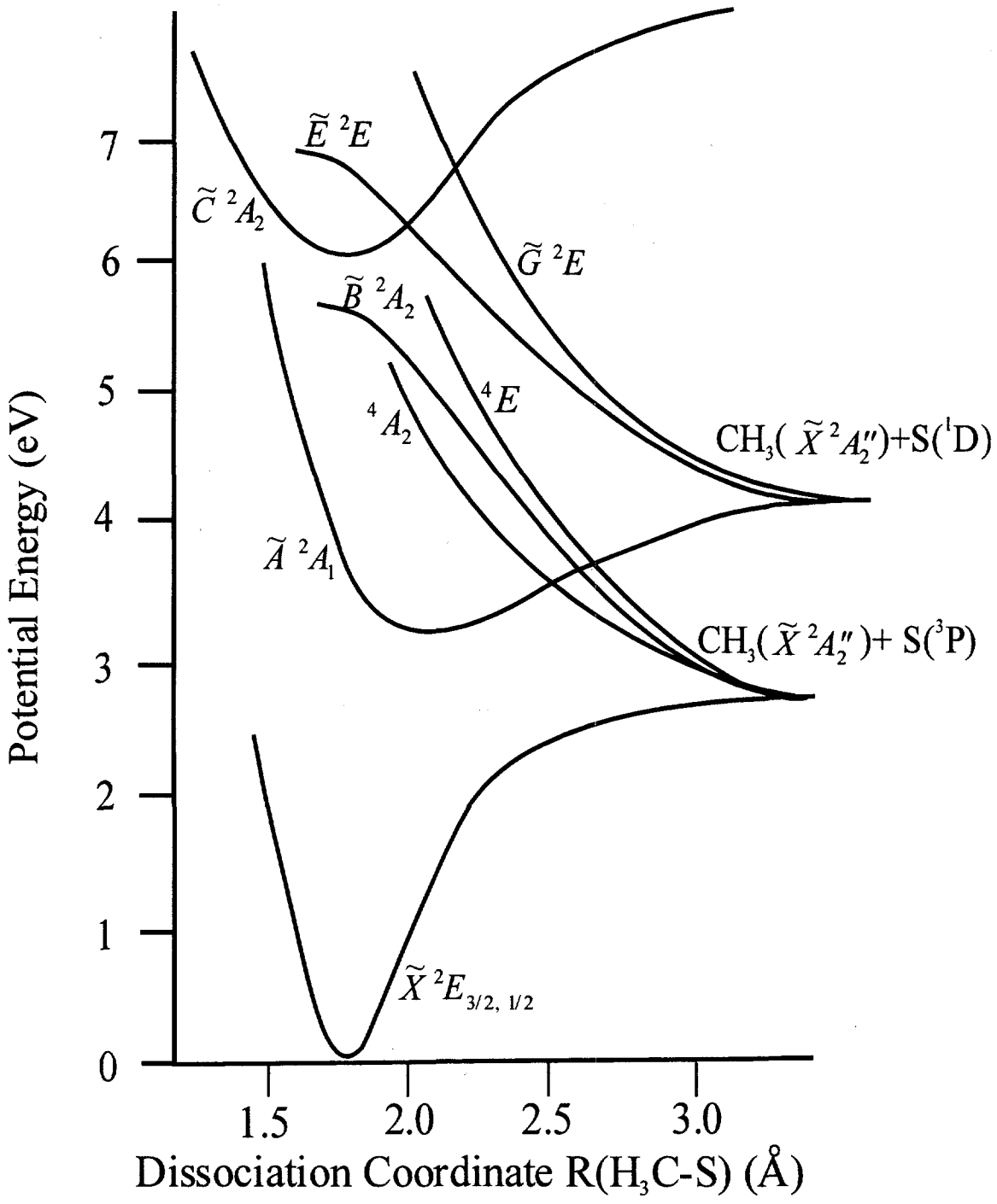

Figure 1. Schematic C_{3v} potential energy surfaces for CH_3S along the C-S reaction coordinate based on calculations by Hsu et al.[22] and Cui et al.[24].

photon energies. Hsu *et al.*[22] have examined the $S(^3P_{2,1,0}; {}^1D)$ production from 193 nm photodissociation of CH_3S using a 2+1 resonance-enhanced multi-photon ionization technique, determining the $S(^3P)/S(^1D)$ ratio to be 0.15/0.85 and the fine-structure distribution for the $S(^3P_{2,1,0})$ levels to be nearly statistical. Wilson *et al.*[25] have studied the photodissociation of CH_3SH using H-atom time-of-flight photodissociation spectroscropy, observing $CH_3S(\tilde{X}\,^2E) + H(^1S)$ as the major photodissociation products. Their results suggest that at 46,230 cm^{-1}, the CH_3S photofragment absorbs a second photon and dissociates to $H + CH_2S(\tilde{A}\,^1A_2)$.

In the present study, a mass selected beam of CH_3S radicals is generated from laser photodetachment of CH_3S^- ions. A second laser is then used to probe the dissociative excited states of the methylthio radical, CH_3S. We report the first observation of several predissociative vibronic transitions of the $\tilde{A}\,^2A_1 \leftarrow \tilde{X}\,^2E$ electronic band and also observe dissociation from an unstructured band at 45,600 cm^{-1} that corresponds to the band originally observed by Callear and Dickson.[5] The primary photodissociation products were found to be $CH_3(\tilde{X}\,^2A_2'') + S(^3P_j)$ for all photodissociation energies, however the detection scheme employed in these experiments is relatively insensitive to hydrogen loss channels. Photofragment translational energy and angular distributions reveal resolved vibrational product state distributions of the CH_3 fragment as well as fine-structure distributions for the $S(^3P_j)$ fragment. The experimental results and data analysis are presented in sections III and IV. Based on our results, we discuss the involvement of the $^4A_2$ and ^4E states in the predissociation of

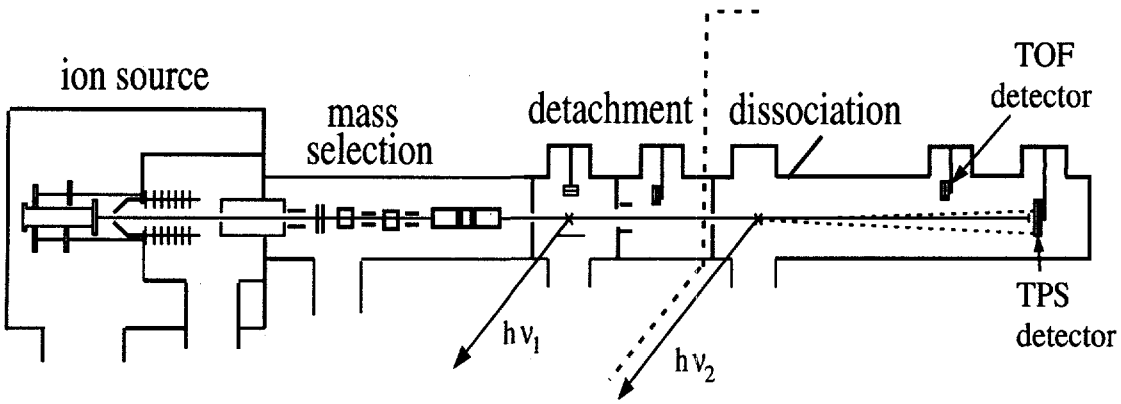

Figure 2. Fast radical beam translational spectrometer. The dotted line separates the radical production section on the left from the actual photodissociation experiment on the right.

the $\tilde{A}$ state and propose that photodissociation at 219.3 nm occurs along the more highly excited $\tilde{B}\ ^2A_2$ surface.

II. Experiment

The fast beam photofragment translational spectrometer, Figure 2, has been described in detail elsewhere;[26-28] only a brief description will follow. In this experiment, a clean source of neutral radicals is generated by mass-selective laser photodetachment of a beam of negative ions. The neutral radicals are then photodissociated by a second laser.

$$CH_3S^- \xrightarrow{h\upsilon_1} CH_3S + e^- \xrightarrow{h\upsilon_2} CH_3 + S \qquad (1)$$

Methylthio anions are generated from a pulsed supersonic expansion of 800 mTorr of dimethyl disulfide (CH_3SSCH_3) seeded in 3 atm of Ar. For d_3-methylthio anions, d_6-dimethyl sulfide (CD_3SCD_3) is used as the precursor. The molecular beam immediately passes through a pulsed electric discharge. This generates negative ions,

which are cooled both rotationally and vibrationally.[29] The ions are accelerated to a laboratory beam energy that can be varied from 6000 to 9000 eV and are mass selected using the Bakker time-of-flight (TOF) method,[30,31] resulting in ion packets with very low energy spread. An excimer-pumped pulsed dye laser then intersects the ion beam at the appropriate time so as to selectively photodetach the methylthio anions. Undetached anions are deflected from the beam by a pulsed electric field. Based upon electron affinities determined in previous photodetachment measurements,[6-8] a photodetachment energy of 1.93 eV was chosen to produce vibrationally and rotationally cold CH_3S radicals in the $^2E_{3/2}$ and $^2E_{1/2}$ states. The photodetachment energy was lowered to 1.88 eV when it was desired to produce CH_3S radicals in the $^2E_{3/2}$ state exclusively. For the production of d_3-methylthio radicals, photon energies of 1.92 eV and 1.87 eV were used.[8]

In the dissociation region, a second excimer-pumped pulsed dye laser intersects the beam of methylthio radicals. The fragments from photodissociation of the radical are detected directly by one of two microchannel plate detector assemblies. An aluminum blocking strip is positioned at the center of each detector to prohibit any undissociated radicals from impacting the detector, so the signal is entirely from recoiling photofragments. In the present experiments, the fundamental output of the dye laser with a bandwidth of 0.3 cm^{-1} was used between 27 000-29 800 cm^{-1}. The dye laser was frequency-doubled to produce photon energies between 29 500-32 300 cm^{-1} and 45 045-46730 cm^{-1} with bandwidths of 0.4 cm^{-1} and 0.5 cm^{-1} respectively.

Two types of experiments are performed. First, the spectroscopy of the dissociative electronic states is examined by measuring the total flux of photofragments arriving at the TOF detector, located 0.68 m from the dissociation laser, as a function of

laser photon energy. The resulting photofragment yield (PFY) spectra is complementary to absorption and fluorescence measurements.

Once the spectroscopy of the dissociative states has been examined, the dissociation dynamics are probed using a coincidence detection scheme. Both photofragments from a single parent radical are detected in coincidence using a time-and-position sensitive detector based on the design of de Brujin and Los.[32] Our implementation of this detection scheme has been described in detail elsewhere.[26,27] The detector records the positions and difference in arrival time of the two photofragments from a single dissociation event. This information is then used to determine the masses of the fragments, their relative translational energy E_T, and the scattering angle θ between the relative velocity vector and the electric vector of the polarized dissociation laser (perpendicular to the ion beam axis):

$$\frac{m_1}{m_2} = \frac{r_1}{r_2}\left(1 - \frac{v_0\tau}{L}\right) \qquad (2)$$

$$E_T = E_0 \cdot \frac{m_1 m_2}{M^2} \cdot \frac{\left\{(v_0\tau)^2 + R^2\right\}}{L^2} \cdot \left(1 + 2\frac{m_1 - m_2}{M}\frac{v_0\tau}{L}\right) \qquad (3)$$

$$\theta = \arctan\left(\frac{v_0\tau}{R}\right) \qquad (4)$$

Here, r_1 and r_2 are the distances of each photofragment on the detector face to the center of the radical beam. $R = r_1 + r_2$ is the distance between the two photofragments and τ is the difference in arrival time of the fragments. M, m_1, and m_2 are the masses of the parent radical and photofragments respectively. E_0 and v_0 are the radical beam energy and velocity respectively and L is the distance from the dissociation laser to the detector face.

A flight distance of 2(1) meters was used for photoexcitation energies less (greater) than 30 000 cm^{-1}. The photofragment mass resolution is $m/\Delta m \approx 10$ while the translational energy resolution for these experiments is $\Delta E_T/E_T$ = 3.0 % and 2.2 % for data recorded at 1 and 2 m flight lengths respectively. This coincidence detection scheme is only possible when the mass ratio of the two photofragments $m_1/m_2 \leq 4$, making coincident detection of light atom dissociation channels involving H or D impossible.

III. Results

A. Photofragment Yield Spectra, $\tilde{A}\ ^2A_1 \leftarrow \tilde{X}\ ^2E$ band

Figure 3 shows the PFY signal for the $\tilde{A}\ ^2A_1 \leftarrow \tilde{X}\ ^2E_{3/2,1/2}$ band system of CH_3S. The spectrum is highly structured with the first distinct peak occurring at 27 324 cm^{-1}. The transition frequencies and vibrational assignments are listed in Table I. The PFY spectra clearly extend to considerably higher energy than the LIF measurements, which were limited to transitions below 28 010 cm^{-1}, illustrating the competition between predissociation and fluorescence in the $\tilde{A}\ ^2A_1$ state. The observed vibrational progressions can be assigned in a relatively straightforward manner using the previously determined vibrational frequencies and anharmonicities from LIF measurements.[15-17] All progressions show a spacing of approximately 390 cm^{-1}, characteristic of excitation in the ν_3 C-S stretching mode. Two of these progressions are separated by approximately 260 cm^{-1}, the spin-orbit splitting of CH_3S in the $\tilde{X}\ ^2E$ state, and are assigned to 3_0^n progression from the $^2E_{3/2}$ and $^2E_{1/2}$ states. Transitions from the $^2E_{3/2}$ level are approximately twice as intense as transitions from the $^2E_{1/2}$, due to the larger cross-section for photodetachment of CH_3S^- to the (lower) $^2E_{3/2}$ state at 1.93 eV. A third

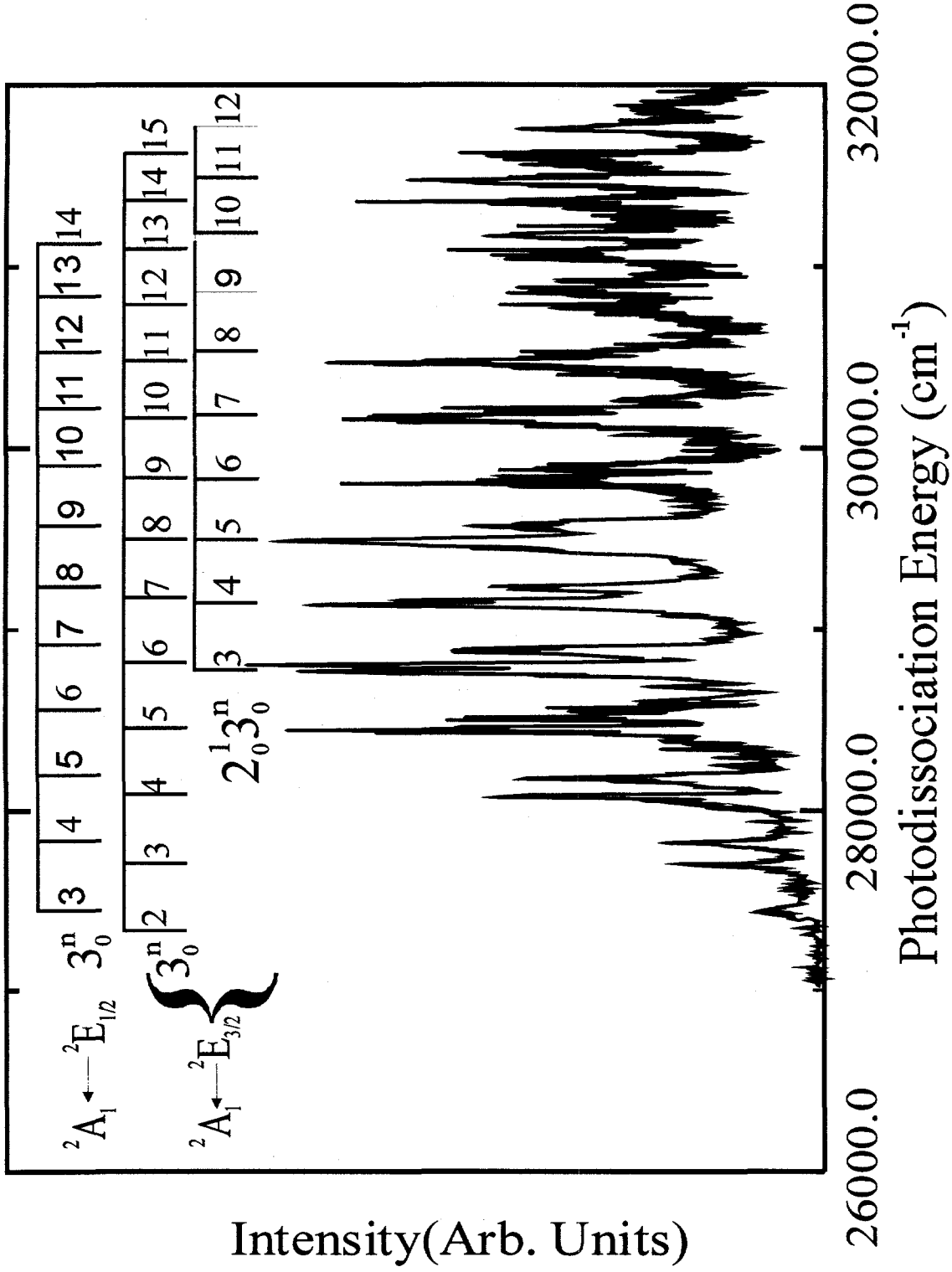

Figure 3. Photofragment yield spectrum for the $\tilde{A} \leftarrow \tilde{X}$ band of CH_3S

Table I. Observed transitions, lifetimes, and assignments for the CH_3S $\tilde{A}\ ^2A_1 \leftarrow \tilde{X}\ ^2E$ Photofragment Yield Spectrum

Transition energy (cm^{-1})			
$\tilde{A}\ ^2A_1 \leftarrow \tilde{X}\ ^2E_{3/2}$	$\tilde{A}\ ^2A_1 \leftarrow \tilde{X}\ ^2E_{1/2}$	Assignment	Lifetime (ns)
27321.3[a], 27323.2	27062.2[a]	3_0^2	250±20[a]
27707.1, 27708.2	27447.5	3_0^3	72± 30[a]
28082.3	27824.1	3_0^4	0.025±.025
28450.7	28186.2	3_0^5	0.010±.007
28780.5		$2_0^1 3_0^3$	0.025±.025
28810.3	28536.3	3_0^6	0.004±.002
29144.3		$2_0^1 3_0^4$	0.008±.005
29176.5	28998.7	3_0^7	0.002±.002
29498.7	29241.1	3_0^8, $2_0^1 3_0^5$	
29817.4	29580.7	3_0^9, $2_0^1 3_0^6$	
30162.4	29889.6	3_0^{10}, $2_0^1 3_0^7$	
30479.8	30221.1	3_0^{11}	0.002±.002
30523.5	30265.7	$2_0^1 3_0^8$	
30787.7	30527.8	3_0^{12}	
30626.6		$2_0^1 3_0^9$	
31088.0		3_0^{13}	
31171.9	30910.3	$2_0^1 3_0^{10}$	
31375.6		3_0^{14}	
31479.8		$2_0^1 3_0^{11}$	
31641.5		3_0^{15}	
31762.6		$2_0^1 3_0^{12}$	

[a] Transitions and lifetimes observed in Ref. 15.

progression begins at 28 780 cm^{-1}, approximately 1080 cm^{-1} above the 3_0^3 ($^2E_{3/2}$) transition. Based on the excited state ν_2 umbrella mode frequency of 1096 cm^{-1},[15] this band is assigned to the $2_0^1 3_0^n$ ($^2E_{3/2}$) progression with $n \geq 3$. A number of $2_0^1 3_0^n$ ($^2E_{1/2}$) transitions are resolved and are indicated in Table I.

Rotational resolution of the vibrational features of the PFY spectra was not attempted due to spectral congestion resulting from multiple K stacks and a low rotational constant $B' = 0.345$ cm^{-1}. The peaks of the PFY spectra are approximately 20 cm^{-1} FWHM with a tail extending to lower photon energy. The vibrational bands, scanned with laser step size of 2.5 cm^{-1} and bandwidth of 0.3 cm^{-1}, do not show significant broadening with increased excitation energy. The rotational temperatures of the vibrational peaks have been determined by fitting the peaks to a rotational contour using the rotational constants for the vibrationless level of the $\tilde{A}$ state determined by Miller and coworkers.[14] These contours yield rotational temperatures between 40-50 K.

A PFY spectrum has also been obtained for the $\tilde{A} \leftarrow \tilde{X}$ band of CD_3S, shown in Figure 4. The structure in CD_3S PFY spectrum is not as well resolved as in the corresponding CH_3S spectra because the ion beam intensity was approximately half that for CH_3S^-. Four major progressions are observed with a spacing of approximately 370 cm^{-1} and significant anharmonicity. By applying the vibrational frequencies and anharmonicities from previous LIF measurements,[16] these progressions can be assigned to 3_0^n and $2_0^1 3_0^n$ bands from the $E_{3/2}$ and $E_{1/2}$ states with a spin-orbit splitting of about 250 cm^{-1}. The transition frequencies and vibrational assignments are listed in Table II.

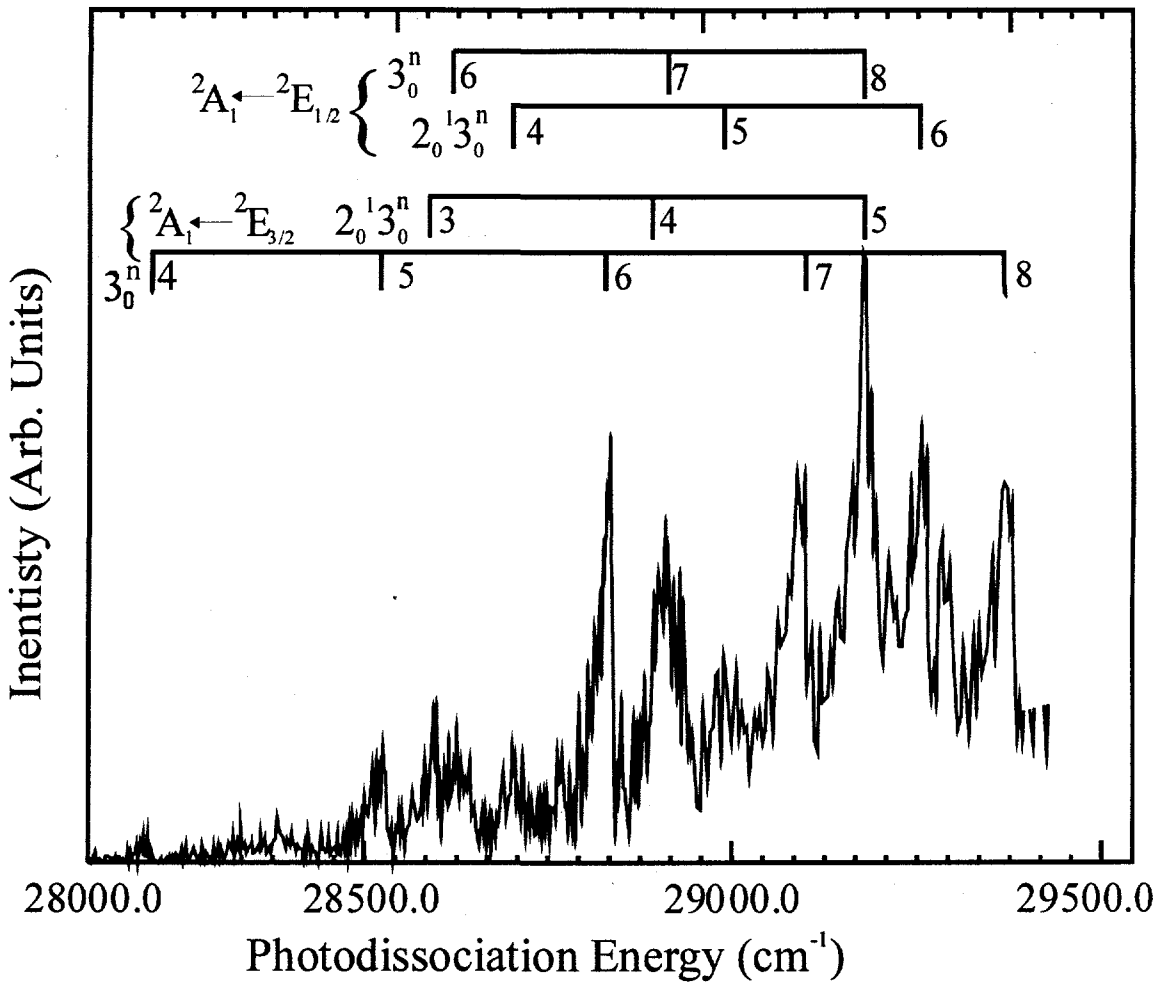

Figure 4. Photofragment yield spectrum for the $\tilde{A} \leftarrow \tilde{X}$ band of CD_3S.

Table II. Observed transitions, and assignments for the CD_3S $\tilde{A}\ ^2A_1 \leftarrow \tilde{X}\ ^2E$ Photofragment Yield Spectrum.

Transition energy (cm^{-1})		
$\tilde{A}\ ^2A_1 \leftarrow \tilde{X}\ ^2E_{3/2}$	$\tilde{A}\ ^2A_1 \leftarrow \tilde{X}\ ^2E_{1/2}$	Assignment
28089		3_0^4
28470		3_0^5
28564		$2_0^1 3_0^3$
28849	28601	3_0^6
28940	28693	$2_0^1 3_0^4$
29156	28967	3_0^7
29262	29036	$2_0^1 3_0^5$
29492	29036	3_0^8
	29357	$2_0^1 3_0^6$

B. Translational energy distributions, $\tilde{A}\ ^2A_1 \leftarrow \tilde{X}\ ^2E$ band

The possible reaction pathways for the methylthio radical for excitation energies in the $\tilde{A} \leftarrow \tilde{X}$ band are

$$CH_3S\ (\tilde{X}\ ^2E) \xrightarrow{h\upsilon} CH_3S\ (\tilde{A}\ ^2A_1) \rightarrow$$

$$CH_3\ (\tilde{X}\ ^2A_2'') + S\ (^3P_{2,1,0}) \qquad \Delta_{rxn}H_0 = 3.045 \pm 0.015\ eV \qquad (I)$$

$$CH_2S(\tilde{X}\ ^1A_1) + H(^2S) \qquad \Delta_{rxn}H_0 = 2.06 \pm 0.08\ eV \qquad (II)$$

These reaction enthaplies were calculated using the JANAF thermochemical tables[33] and $\Delta_f H_0\ (CH_3S) = 1.346 \pm 0.018$ eV, determined in this work (see below). Our coincident

detection scheme is insensitive to the H-atom dissociation channels as has been discussed by Osborn *et al.*,[28] making channel I the only detectable photodissociation pathway.

The two-dimensional coupled translational energy distribution, $P(E_T, \theta)$, obtained from equations 3 and 4 can be separated into the angle-independent translational energy distribution $P(E_T)$ and the energy-dependent anisotropy parameter $\beta(E_T)$ which describes the angular distribution of the fragments[34]

$$P(E_T,\theta) = P(E_T)[1+ \beta(E_T)P_2(\cos\theta)]. \qquad (5)$$

The anisotropy parameter β can range from +2 to −1, corresponding to $\cos^2\theta$ and $\sin^2\theta$ angular distributions respectively.

Figure 5 shows the translational energy distributions, $P(E_T)$, for a number of vibrational transitions associated with the $\tilde{A}\ ^2A_1 \leftarrow \tilde{X}\ ^2E$ band of CH_3S. The mass ratio, m_1:m_2 = 15:32, determined via Eq. 2, confirms CH_3 + S as the product channel. The structure observed in the $P(E_T)$ distributions can be attributed to the $S(^3P_{2,1,0})$ levels and the umbrella motion of the CH_3 fragment, as indicated in Figure 5 for the 3_0^7 transition with two combs representing $S(^3P_j)$ fine-structure states for the ν_2 =0 and ν_2 =1 vibrational states of the CH_3 fragment. The detailed assignment of this structure is described in Section IV. The dashed vertical lines at each excitation energy in Figure 5 indicate E_T^{max}, the maximum translational energy available, as determined below in Section IV.

The $P(E_T)$ distributions for 3_0^n excitations for n = 3-6 are dominated by single narrow peaks with a sharp cutoff at E_T^{max}, displaying little or no vibrational and/or spin-orbit excitation. The 3_0^7 $P(E_T)$ distribution shows a mild increase in the internal

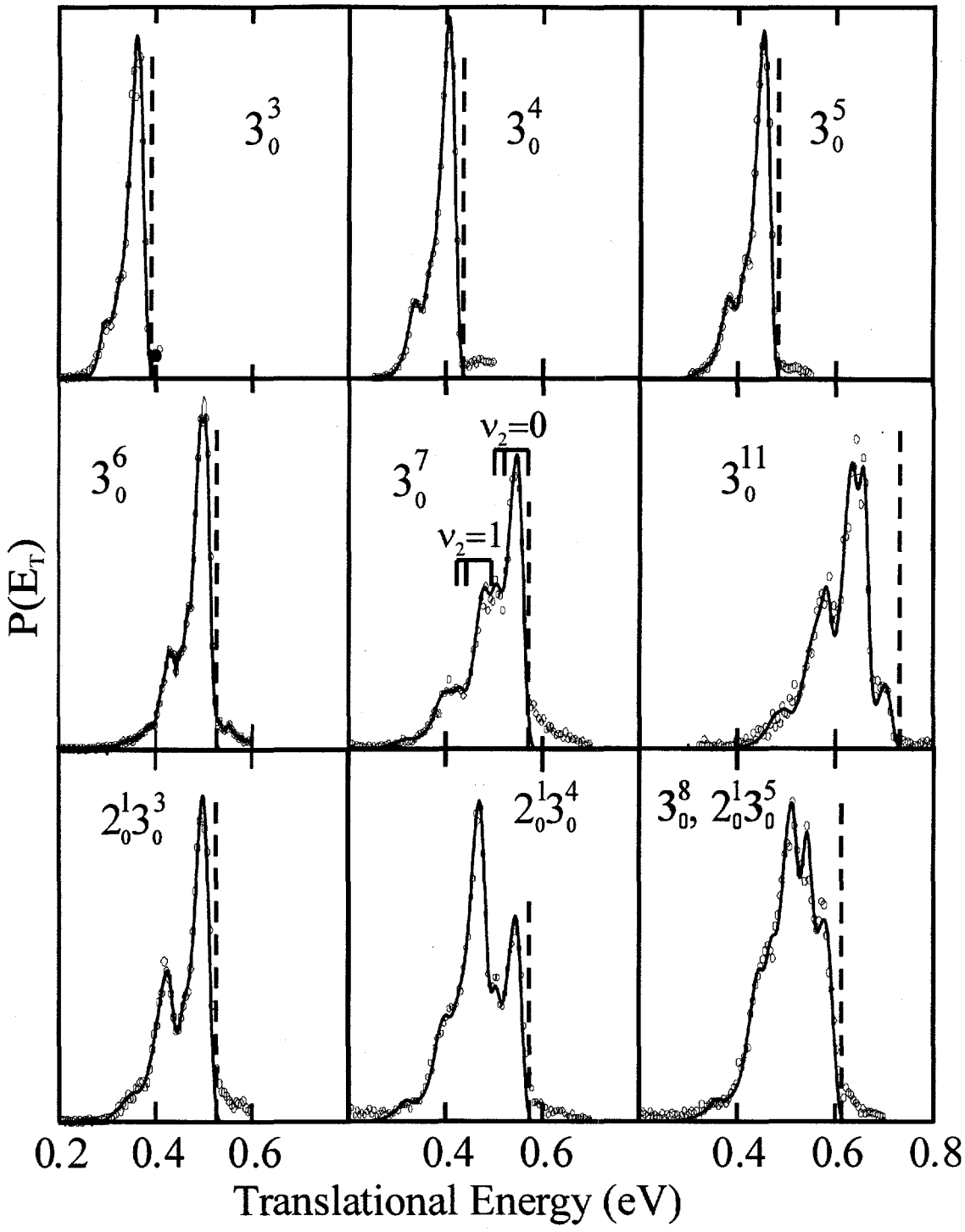

Figure 5. $P(E_T)$ distributions for $\tilde{A} \leftarrow \tilde{X}$ vibrational transitions of CH_3S. The experimental data is indicated by the open circles. The fit (——) and E_T^{max} values (-----) are shown for each $P(E_T)$ distribution. The combs shown for the 3_0^7 transition represent the fine-structure states of the $S(^3P_j)$ fragment that correspond to the ν_2=0 and ν_2=1 vibrational states of the CH_3 fragment.

excitation of the photofragments, and the 3_0^{11} $P(E_T)$ distribution demonstrates a significant increase in photofragment excitation, with a maximum in the $P(E_T)$ distribution at a translational energy 70 meV less than the maximum translational energy.

The $P(E_T)$ distributions for the $2_0^1 3_0^n$ transitions are quite different. The photon energies used to acquire the $P(E_T)$ distributions for the $2_0^1 3_0^n$ transitions differ from the 3_0^{n+3} transitions by only 25 and 22 cm^{-1}, for n =3 and 4 respectively, but the combination band transitions produce significantly more internal excitation in the photofragments. The $P(E_T)$ distribution from the overlapping $2_0^1 3_0^5$ and 3_0^8 bands is not well resolved, as one might expect for a combination of two different product state distributions. Due to the overlapping combination band and C-S stretch progressions between 29 400-30 100 cm^{-1} as well as low signal levels, no attempt was made to measure the dissociation dynamics of the 3_0^{n+3} or $2_0^1 3_0^n$ bands for n = 6 and 7.

The photofragment angular distributions are highly anisotropic with values of β ranging between –0.2 to –1.0, with a decrease in β as the C-S stretch quantum number is increased, see Figure 9. The negative β values are consistent with a perpendicular $A \leftarrow E$ transition dipole moment.

The smaller ion beam intensities for CD_3S resulted in reduced signal collection rates, and $P(E_T)$ distributions were obtained at only two photon energies, 29150 and

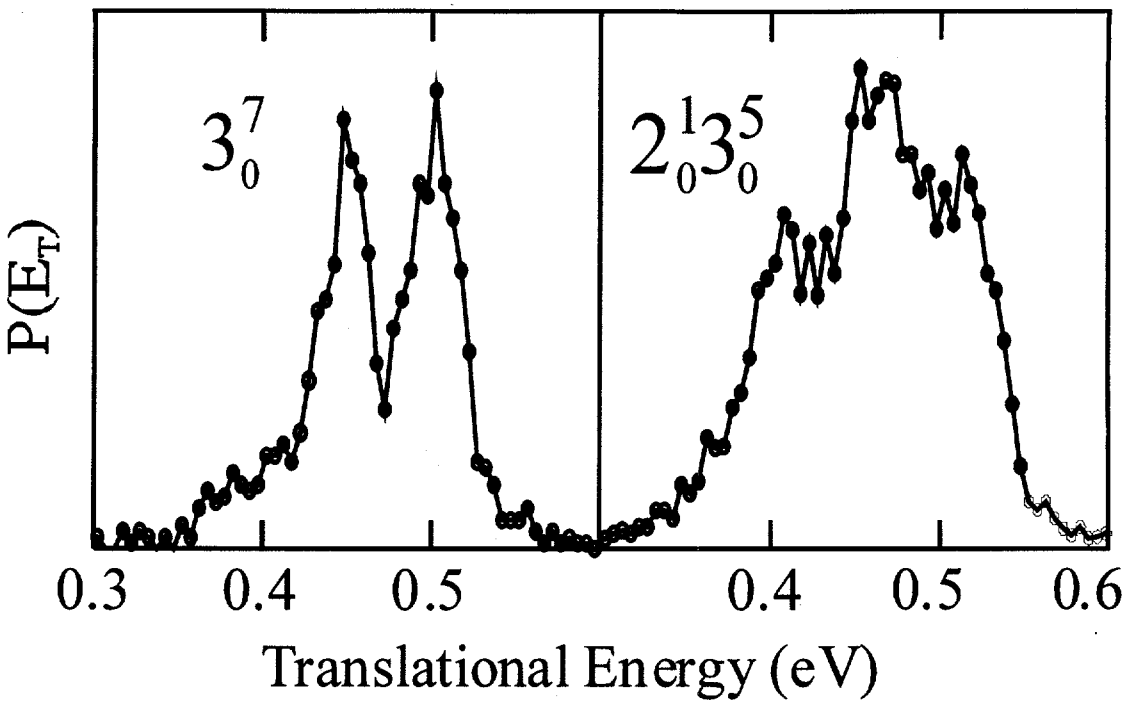

Figure 6. $P(E_T)$ distributions for the 3_0^7 and $2_0^1 3_0^5$ transitions for CD_3S.

29260 cm^{-1}, Figure 6. These transitions produce photofragments with a mass ratio of 18:32, consistent with CD_3 + S products. Photoexcitation at 29260 cm^{-1}, which overlaps the $2_0^1 3_0^5$ ($E_{3/2}$) and 3_0^8 ($E_{1/2}$) transitions, leads to substantially more internal excitation of the photofragments than the nearby 3_0^7 ($E_{3/2}$) transition at 29150 cm^{-1}. The photofragment angular distributions are described by β=–0.3 and –0.1 for the 3_0^7 and $2_0^1 3_0^5$ bands respectively.

C. Higher Excitation Energies

A PFY spectra has also been obtained for CH_3S between 45,000-46,500 cm^{-1}, Figure 7, corresponding to the UV absorption band observed originally by Callear and Dickson [5] and in more recent experiments.[19,35] Our experiment confirms that CH_3S is the carrier of this band. The peaks at 45,620 and 45,350 cm^{-1} do not correspond to vibronic

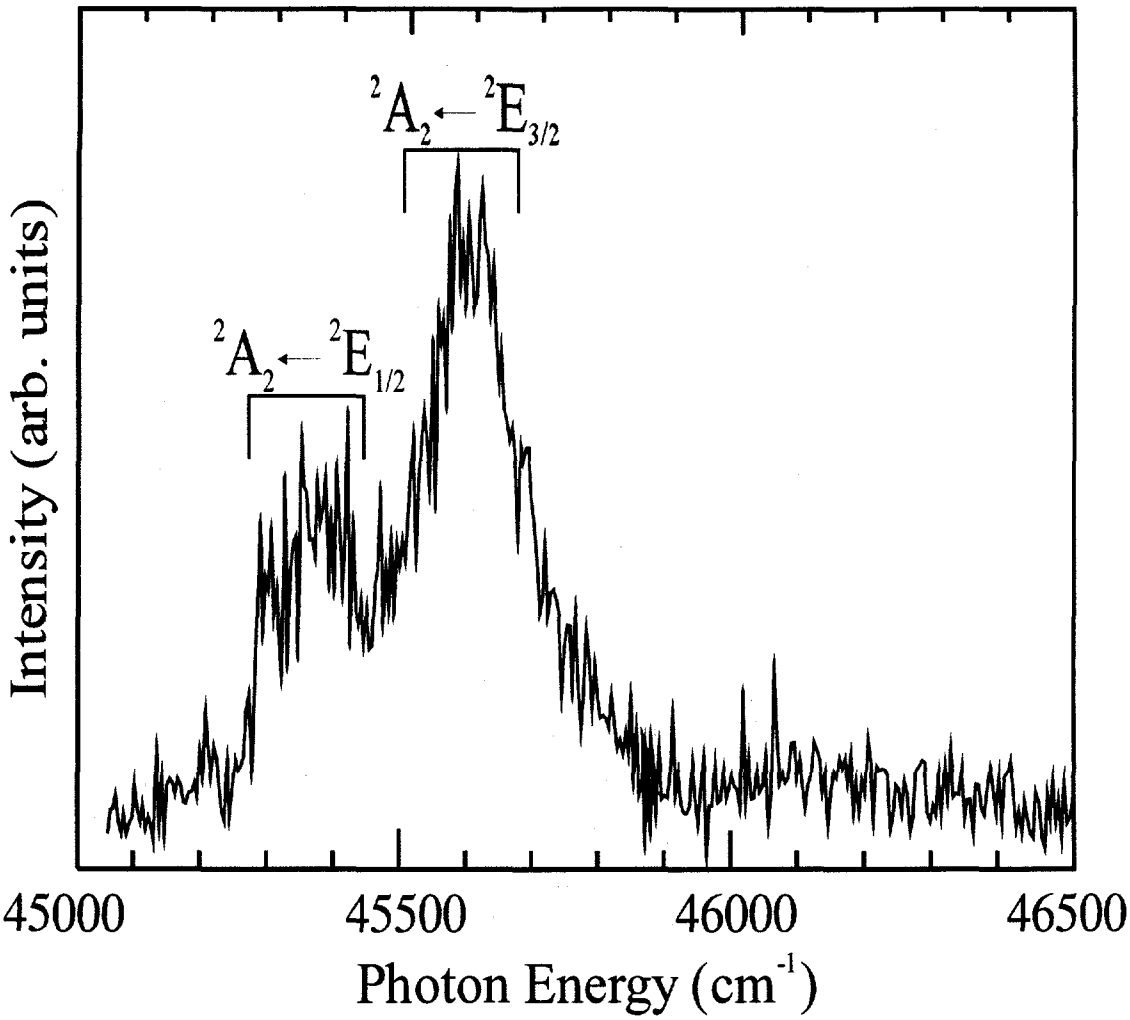

Figure 7. Photofragment yield spectrum for CH_3S from 45,000-46500 cm^{-1}. The peaks at 45,620 and 45,350 cm^{-1} are assigned to transitions arising from the $\tilde{X}$ $E_{3/2}$ and $\tilde{X}$ $E_{1/2}$ states respectively.

structure, but to transitions from the $^2E_{3/2}$ and $^2E_{1/2}$ states respectively. The relative intensity of the peaks is governed by the larger detachment cross-section to the $^2E_{3/2}$ state at 1.93 eV.[8] The peak at 45,350 cm^{-1} disappears when the detachment energy is lowered to 1.87 eV.

The photofragment mass ratio for excitation at 45,620 cm^{-1} was found to be 15:32, consistent with CH_3 + S products. The $P(E_T)$ distribution, Figure 8, peaks at

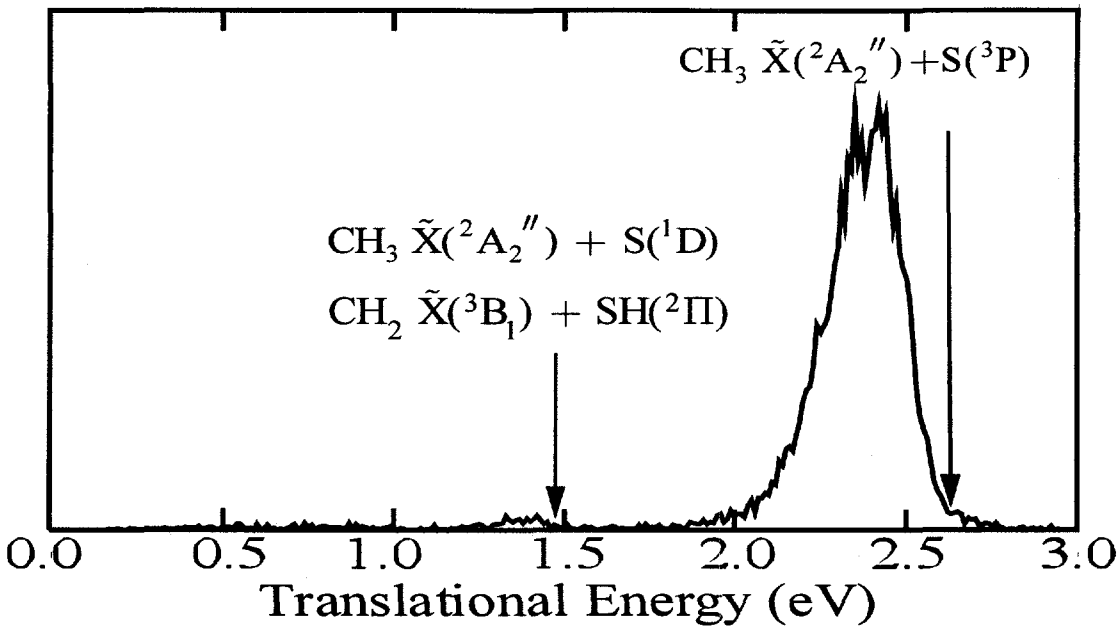

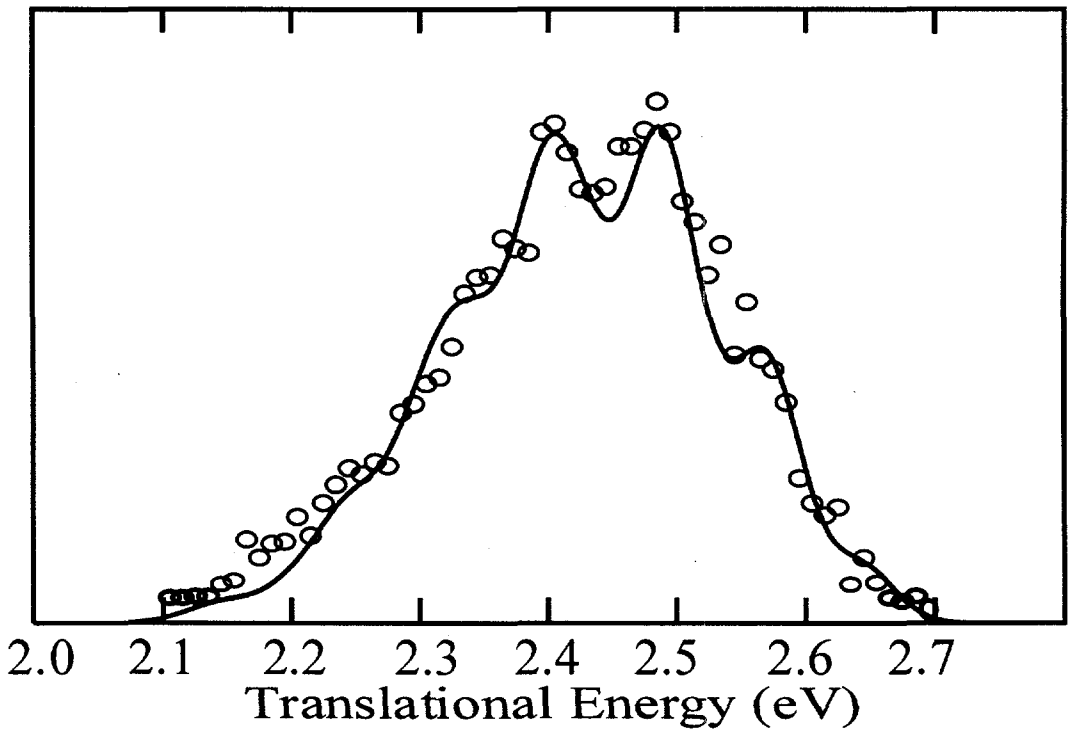

Figure 8a. $P(E_T)$ distribution from excitation at 45,620 cm^{-1}. The maximum translational energies for the $CH_3 + S(^3P)$, $CH_3 + S(^1D)$, and $CH_2 + SH(^2\Pi)$ are marked with arrows.

8b. $P(E_T)$ between 2.0 and 2.8 eV. The experimental data is displayed as open circles while the results of an impulsive dissociation model is shown with the solid (——) line.

2.40 eV, near the maximum allowable translational energy of 2.6 eV for product channel I. This distribution is structured, but much less so than the $P(E_T)$ distributions for the $\tilde{A} \leftarrow \tilde{X}$ transitions. The small feature at E_T=1.5 eV comprises ≈ 2% of the photodissociation products and is most likely from dissociation channels III or IV:

$$CH_3(\tilde{X}\,(^2A_2'')) + S(^1D) \qquad \Delta H_{rxn,0} = 4.190 \pm 0.015 \qquad \text{(III)}$$

$$CH_2(\tilde{X}\,(^3B_1'')) + SH(^2\Pi) \qquad \Delta H_{rxn,0} = 4.14 \pm 0.05 \qquad \text{(IV)}$$

The photofragment angular distribution is highly anisotropic with β= -0.98 ± 0.10.

Attempts to determine the relative branching ratios of the H-atom versus S-atom channels at 45,620 cm^{-1} through the use of a non-coincident time-of-flight technique[28] were unsuccessful. Our ability to detect the H-atom dissociation products $H(^1S)$ + $CH_2S(\tilde{A}\,^1A_2)$ observed by Wilson *et al.* at 216.3 nm (Ref.25) is extremely limited by our detector geometry. The H-atom detection efficiency is ≤ 1% and only a small fraction (<10 %) of $CH_2S(\tilde{A}\,^1A_1)$ fragments are expected to contain sufficient kinetic energy to clear the 3 mm beam block used to prevent undissociated neutrals from impacting the detector.

IV. Analysis

A. CH_3S Photofragment Yield Spectra, $\tilde{A}\,^2A_1 \leftarrow \tilde{X}\,^2E$ band

Our photofragment yield experiments are the first to present resolved vibrational transitions of $\tilde{A} \leftarrow \tilde{X}$ band with more than three quanta in the ν_3 mode, showing an extended 3_0^n progression containing up to 15 quanta and a $2_0^1 3_0^n$ combination band

progression. These progressions are consistent with the large change in the C-S bond length upon exciation to the $\tilde{A}$ state (1.767 Å to 2.057 Å).[14] Our observed frequencies for the 3_0^2 and $3_0{}^3$ $E_{3/2}$ transitions for CH_3S agree to within ± 2 cm^{-1} with those observed in previous LIF studies.[15,17] The 3_0^n progressions, n = 2-15, can be fit effectively using with the frequency, $\omega_3' = 409.2 \pm 0.2$ cm^{-1}, and anharmonicity, $x_{33}' = 3.9 \pm 0.1$ cm^{-1}, from Chiang *et al.*[15] The combination band progression, $2_0^1 3_0^n$, can be fit by including an additional term $x_{23}' = 6.6 \pm 0.1$ cm^{-1}, from Chiang et al.[15] to describe the interaction of the ν_2 and ν_3 mode.

Previous fluorescence lifetime measurements reveal a sharp decrease in the lifetime of the excited state for the 3_0^2 transition (250 ± 20 ns) relative to the 0_0^0 transition (1130 ± 70 ns), suggesting the former to be the onset of predissociation.[12,15,18] The PFY spectra obtained in this study indeed shows the 3_0^2 transition to be the first dissociative transition. The most energetic peaks observed via LIF are the 3_0^3 and $2_0^1 3_0^1$ transitions, with lifetimes of 72 ± 30 ns and 85 ± 15 ns respectively. While we do observe the 3_0^3 transition, we are not able to detect the $2_0^1 3_0^1$ transition at 28 016 cm^{-1} even though the reported lifetime of 85±15 ns suggests rapid predissociation. Although extensive efforts were made to observe both the $2_0^1 3_0^1$ and $2_0^1 3_0^2$ bands, the combination bands $2_0^1 3_0^n$ were not clearly observed until $n \geq 3$.

B. CD_3S Photofragment Yield Spectra

The CD_3S photofragment yield spectrum is also comprised of 3_0^n and $2_0^1 3_0^n$ progressions. The 3_0^n transitions from the current PFY spectra and LIF transitions found by Suzuki *et al.*[16] can be fit using $\omega_3' = 402.5 \pm 1.0$ cm^{-1} and $x_{33}' = 4.15 \pm 0.2$ cm^{-1}. The combination bands can be fit by including a cross anharmonicity x_{23}' of 4.0 ± 0.5 cm^{-1}.

Radiative lifetime meaurements of Suzuki *et al.* suggest the onset of predissociation occurs at the 3_0^3 transition. We have been unable to locate the 3_0^3 transition in our PFY experiments and do not observe significant dissociation signal until the 3_0^4 transition. Our inability to detect the 3_0^3 transition probably results from a combination of poor Franck-Condon factors and small ion beam intensities.

C. Translational Energy Distributions, $\tilde{A}\ ^2A_1 \leftarrow \tilde{X}\ ^2E$ band

The $P(E_T)$ distributions in Figure 5 demonstrate how the excess energy above the dissociation threshold is distributed between the photofragments. The energy balance for CH_3S photodissociation is described by

$$h\nu + E_{SO}(CH_3S) + E_{int}(CH_3S) =$$

$$D_0(CH_3\text{-}S) + E_T + E_V(CH_3) + E_R(CH_3) + E_{SO}(S\ ^3P_j) \qquad (6)$$

where $h\nu$ is the photon energy, $E_{SO}(CH_3S) = 0$ and 260 cm^{-1} for $^2E_{3/2}$ and $^2E_{1/2}$ states respectively of the parent radical and E_{int} characterizes the average rotational energy of the parent. E_T is the measured center-of-mass translational energy, E_V and E_R are the CH_3 product vibrational and rotational energies, $E_{SO}(S\ ^3P_j)$ is the spin-orbit state of the sulfur atom, and $D_0(CH_3\text{-}S)$ is the C-S bond dissociation energy. $E_{int}(CH_3S)$ for a temperature of 50 K is 33 cm^{-1}.

$D_0(CH_3\text{-}S)$ can be extracted from these distributions if we can determine E_T^{max}, the value of the translational energy corresponding to production of photofragments with zero internal energy. This is marked by a vertical dashed line for each photon energy. Although E_T^{max} is not always obvious from a $P(E_T)$ distribution, it can be readily ascertained from the distributions in Figure 5 because of the steep falloff in intensity toward high E_T. Note that the $P(E_T)$ distributions for the 3_0^6 and 3_0^7 transitions show broad tails which extend to higher translational energies than E_T^{max}. This "signal" arises when the dissociation cross-section is large enough that photofragments from different dissociation events impact the detector. While our data analysis allows us to eliminate most false coincidences, a small contribution remains when large photofragment fluxes as present.

$D_0(CH_3\text{-}S)$ is obtained independently at each photon energy; the resulting values are then averaged together to yield a value of 3.045 ± 0.015 eV. Our value of D_0 along with the known heats of formation of CH_3 and S determines $\Delta_f H_0(CH_3S) = 1.346 \pm 0.018$ eV,[33] in good agreement with the value 1.363 ± 0.023 reported by Nicovich *et al.* [36] determined from reaction kinetic measurements and with theoretical values 1.346, and 1.37 eV. [23,37] Our current value disagrees with the values of 1.54 ± 0.086, 1.53 ± 0.065, and 1.48 ± 0.065 obtained by Nourbakhsh *et al.* from molecular beam photofragmentation studies of CH_3SH,[38] CH_3SSCH_3,[39] and CH_3SCH_3,[40] respectively. The discrepancy of this value with other recent literature values has been previously discussed by Ruscic and Berkowitz[41] and by Nicovich *et al.*[36]

The CH_3 product umbrella mode (ν_2) vibrational distribution and the $S(^3P_j)$ fine-structure distribution can also be determined from the $P(E_T)$ distributions. Since both photofragments are detected in coincidence, this is a correlated distribution in the sense that we obtain the $S(^3P_j)$ distribution for each CH_3 vibrational level. These distributions have been obtained by using a similar procedure to that employed by Osborn *et al.* [42] for CH_3O dissociation with additional terms included to account for the resolved fine-structure states of the sulfur atom. The data is fit to a series of rotational distribution functions separated by the fine-structure energy levels of the sulfur atom and the term energies for the CH_3 ν_2 umbrella mode.[43, 44] The distribution functions $f_{j,n}(E_T)$, where j labels the sulfur atom fine-structure level and n labels the number of quanta in CH_3 ν_2 mode, are Boltzmann distributions described by a rotational temperature T (characteristic of the CH_3 fragment) and convoluted with a gaussian experimental energy resolution δ, FWHM=20 meV.

The total distribution is given by

$$F(E_T) = \sum_{j=0}^{2} \sum_{n=0}^{n'} \alpha_{j,n} f_{j,n}\left[E_T - \left(h\upsilon - n\omega_2 - SO_j - D_0\right), T, \delta\right] \qquad (7)$$

where ω_2 is the fundamental frequency of the ν_2 mode (606 cm^{-1}, 75 meV) [43,44], $\alpha_{j,n}$ represents the coefficient associated with each individual distribution function and SO_j is the internal energy associated with the $S(^3P_{2,1,0})$ spin-orbit levels, which have energies of 0, 49 and 71 meV[33] respectively. The rotational temperature T was manually adjusted for each peak to produce the best fit. The results of the best nonlinear least squared fits are shown as solid lines in Figure 5. Table III contains the vibrational and spin-orbit distribution for each data set. The rotational temperature of the CH_3 fragment varied

Table III. **Product Branching Ratio for $CH_3S \rightarrow CH_3(\nu_2=n) + S(^3P_j)$**

Transition	hν (cm^{-1})	$\nu_2=0$			$\nu_2=1$			$\nu_2=2$			Fine-Structure Ratio
		$^3P_2$	$^3P_1$	$^3P_0$	$^3P_2$	$^3P_1$	$^3P_0$	$^3P_2$	$^3P_1$	$^3P_0$	$^3P_2$:$^3P_1$:$^3P_0$
3_0^3	27,705	87	5	4	3	1	---	---	---	---	90:6:5
3_0^4	28,082	82	6	6	6	---	---	---	---	---	88:6:6
3_0^5	28,450	79	6	5	10	1	---	---	---	---	89:7:5
3_0^6	28,810	76	6	4	11	2	1	---	---	---	87:8:5
3_0^7	29,160	53	15	4	13	5	5	4	---	1	70:20:10
3_0^{11}	30,479	7	27	31	4	12	10	4	3	2	15:42:43
$2_0^1 3_0^3$	28,780	61	5	1	29	---	2	2	---	---	90:5:5
$2_0^1 3_0^4$	29,134	29	11	3	39	7	4	5	1	1	73:19:8

between 170 to 220 K for all correlated product distributions except for the $CH_3 + S(^3P_1)$ distributions for which the CH_3 fragment rotational temperatures varied from 50 to100 K.

The fundamental frequency of the CH_3 umbrella mode, ν_2, is $\approx$ 75 meV which is very close to the energy splitting between the $S(^3P_2)$ and $S(^3P_0)$ levels $\approx$ 71 meV. This leads to product states, $CH_3(\nu_2=0) + S(^3P_2)$ and $CH_3(\nu_2=1) + S(^3P_0)$ which are nearly degenerate within the experimental resolution of 20 meV and cannot be distinguished by the fit. This near degeneracy is removed as the number of quanta in the strongly negatively anharmonic CH_3 umbrella mode is increased. For product state energies separated by more than 15 meV, the fits were sensitive to changes in the spin-orbit and vibrational state distributions of more than 5%. The uncertainty in the product state distributions for products $CH_3(\nu_2=0) + S(^3P_2)$ and $CH_3(\nu_2=1) + S(^3P_0)$ could not be determined.

The $P(E_T)$ distributions from 3_0^n ($n\leq6$) transitions are remarkably similar with at least 86% of the CH_3 produced in the $\nu_2=0$ state. These transitions also exhibit a strong preference for the $S(^3P_2)$ level with an average $S(^3P_{2:1:0})$ distribution of 88:7:5 compared to a statistical distribution of 5:3:1. However, these trends change for n>6. The 3_0^7 transition has a spin-orbit distribution of approximately 73:18:7, showing an increase in the higher energy $^3P_1$ and $^3P_0$ levels. This transition also shows increased vibrational excitation with a vibrational distribution ν_2=0:1:2 of 72:23:5. The 3_0^{11} transition is dramatically different from the other 3_0^n transitions in Figure 5 showing a spin-orbit distribution of $S(^3P_{2:1:0})$ of 15:42:43 and a vibrational distribution ν_2=0:1:2 of 65:26:9.

Excitation of the $2_0^1 3_0^n$ combination band transitions produces $P(E_T)$ distributions with a substantial increase in the excitation of the CH_3 product umbrella mode, e.g. $CH_3(\nu_2 = 1)$ is the dominant channel from excitation of the $2_0^1 3_0^4$ transition. Since the dissociation products, $CH_3(\nu_2=0) + S(^3P_0)$ and $CH_3(\nu_2=1) + S(^3P_2)$, cannot be distinguished by the fit, it was assumed that the spin-orbit distributions for the $2_0^1 3_0^n$ transitions were the same as for the nearly isoenergetic 3_0^{n+3} transitions. The spin-orbit distributions were then adjusted slightly to see if a better fit could be produced.

D. Excited State Lifetimes

Due to spectral congestion of rotational levels in our experiment, we were unable to obtain rotationally resolve the transitions of the $\tilde{A} \leftarrow \tilde{X}$ band and therefore could not determine the excited state lifetime from linewidth measurements. We have therefore attempted to extract the excited state lifetimes from the anisotropic photofragment angular distributions and a defined excited state rotational distribution in a manner similar to that performed by Black *et al.* [45] in their study of ICN photodissociation. The anisotropy parameter β can be described classically as

$$\beta = 2 \cdot P_2(\cos\chi) \cdot g(\omega, \tau) \qquad (8)$$

where P_2 is the second Legendre polynomial, χ is the orientation of the transition dipole moment with respect to the molecular axis ($\chi = 90°$ for a perpendicular transition) and $g(\omega,\tau)$ describes the effect of molecular rotation on the photofragment angular distribution with a given dissociation lifetime τ.[46-48] The angular velocity of the separating fragments is given by ω.

For a diatomic molecule,

$$g(\omega,\tau)=\frac{1+(\omega\tau)^2}{1+4(\omega\tau)^2} \tag{9}$$

Eq. 12 describes the dependence of angular velocity upon the rotational quantum number J,

$$\omega(J)=\frac{BcJ(J+1)}{2\pi} \tag{10}$$

where B is the rotational constant of the $\tilde{A}$ state, and c is the speed of light. The anisotropy parameter as a function of lifetime, $\beta(\tau)$, is then given by,

$$\beta(\tau)=2\cdot P_2(\cos\chi)\sum_J c_J\cdot\left(\frac{1+\omega(J)\cdot\tau^2}{1+4\omega(J)\cdot\tau^2}\right) \tag{11}$$

where c_J is the fractional population for each rotational quantum number, J. The experimental value of β can then be associated with a lifetime.

Eq. 9 applies to diatomic molecules and to symmetric top rotational levels with K=0. In our experiment, the excitation energies correspond to $K'=0 \leftarrow K''=1$ transitions; the upper state $(J',K'=0)$ levels can then be considered as pseudo-diatomic rotational levels, so that Eq. 9 is appropriate. We note that these are the most prominent transitions between K levels; most of the CH_3S $\tilde{X}\,^2E$ population is in rotational levels with $K''=1$, and for *a-e* type vibronic transitions, $\Delta K=-1$ transitions are most intense.[49-51]

A cursory inspection of Equations 8-11 reveals that the upper state rotational distribution is required in this analysis. Although individual rotational lines are not resolved, it is assumed that the excited state contains discrete rotational levels and that the excitation laser with a bandwidth of ≈ 0.3 cm^{-1} selects a narrow distribution of rotational levels. The excited state rotational distribution is determined by first fitting the

contour of each vibronic transition using the known rotational parameters of the $\tilde{X}$ and $\tilde{A}$ states [9,14], a laser resolution of 0.3 cm^{-1} and then considering which part of the rotational manifold is excited for each $P(E_T)$ measurement. The β parameter dependence upon C-S stretch excitation is plotted in Figure 9 for both 3_0^n and $2_0^1 3_0^n$ transitions with the

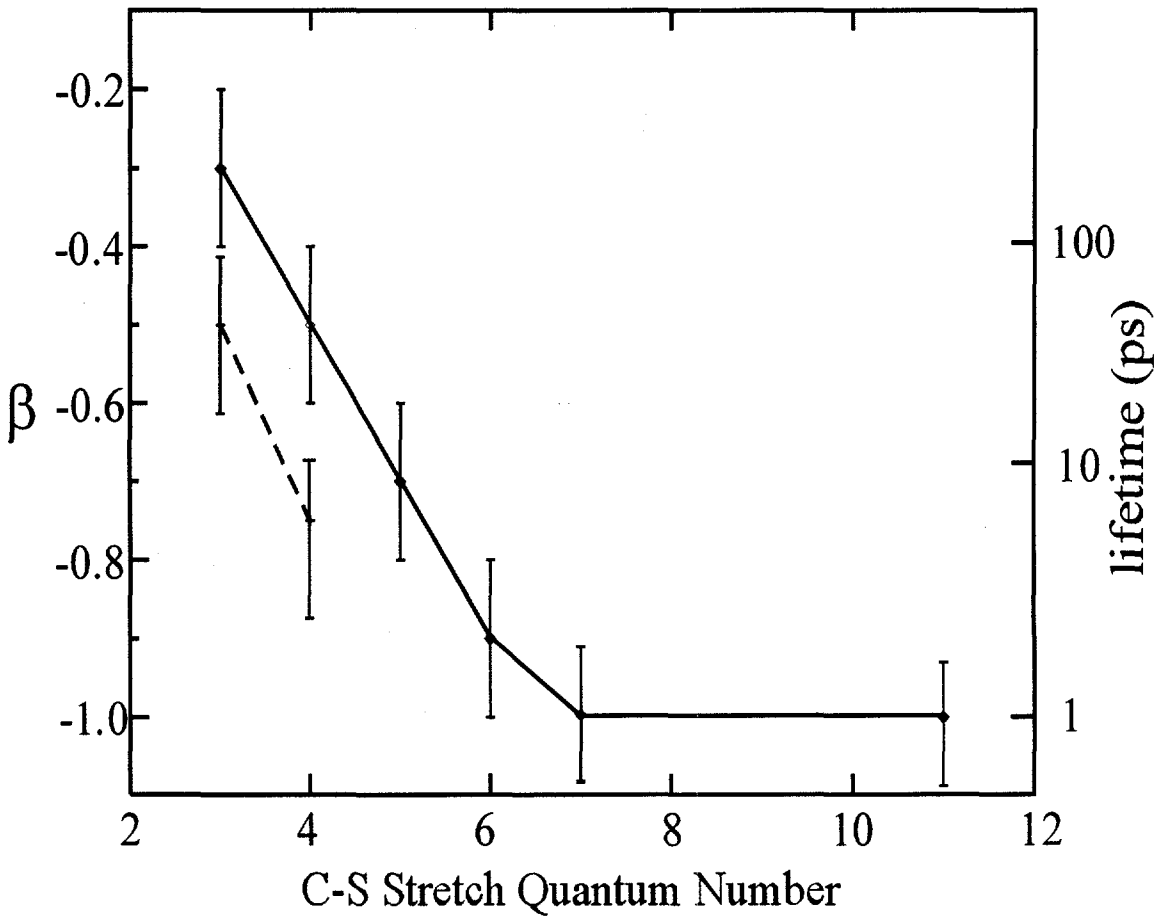

Figure 9. Dependence of the anisotropy parameter, β, as a function of C-S stretch quantum number for the 3_0^n progression (——) and the $2_0^1 3_0^n$ progression (----). Error bars of ± 0.1, for the uncertainty in the experimental value of β are shown

corresponding lifetimes and uncertainties listed in Table I, clearly illustrating the rapid decrease in β and in lifetime with increasing C-S stretch excitation. The uncertainty in the lifetime increases substantially as the photofragment anisotropy approaches its limiting classical value of –0.25 making the lifetimes for nearly isotropic distributions such as the 3_0^3 and 3_0^4 transitions less reliable. While the extracted lifetime values are only approximate, they agree surprisingly well with the lifetime values of the $\tilde{A} \leftarrow \tilde{X}$ band of the CF_3S radical reported by Powers *et al.*[52] A more detailed comparison of the CH_3S and CF_3S radicals and their excited state lifetimes will be provided in section V.

V. Discussion

A. Translational Energy Distributions, $\tilde{A}\ ^2A_1 \leftarrow \tilde{X}\ ^2E$

1. Vibrational State Distributions

The product state distributions from photodissociation provide detailed information about the electronic surfaces which mediate dissociation. In this and the following section, we discuss how the product vibrational and fine-structure distributions provide insight into the role of the three repulsive surfaces in the predissociation of the $\tilde{A}$ state.

The $P(E_T)$ distributions for the $\tilde{A} \leftarrow \tilde{X}\ 3_0^n$ ($n \leq 6$) transitions show negligible excitation of the umbrella mode in CH_3 fragment with a slight increase in $\langle E_{vib} \rangle$ as n increases from 3 to 6. $\langle E_{vib} \rangle$ rises noticeably for the 3_0^7 transition even more so for 3_0^{11} transition, suggesting that a fundamental change in the dissociation dynamics occurs

over this energy range. Cui and Morokuma[24] have performed detailed *ab initio* calculations for the predissociative surfaces of the methoxy family (CH_3O, CH_3S, CF_3O and CF_3S). In particular, these authors have analyzed how fast the H-C-O bond angle opens in CH_3O as the C-O bond breaks on both the $^4A_2$ and ^4E surfaces. They find that the H-C-O bond angle opens more quickly as the C-O bond distance increases on the ^4E surface than on the $^4A_2$ surface. The resulting higher curvature along the minimum energy path on the ^4E surface promotes increased vibrational excitation of the CH_3 photofragment at higher photon energies as observed by Osborn *et al.*[53] Assuming that the same trend holds for CH_3S, the increased CH_3 product vibrational excitation observed for the 3_0^7 and 3_0^{11} transitions is consistent with involvement of the ^4E surface in the dissociation. No calculations of this type were performed for the $^2A_2$ state, so one cannot assess the role of this state based on the vibrational distributions alone.

The $2_0^1 3_0^3$ and $2_0^1 3_0^4$ transitions result in more vibrational excitation of the CH_3 photofragment as compared to the 3_0^n bands, with initial excitation of the CH_3S parent umbrella mode leading to population of the umbrella mode in the CH_3 fragment. While this result is not entirely surprising, the $2_0^1 3_0^4$ results in significantly more vibrational excitation of the CH_3 fragment than the $2_0^1 3_0^3$ transition, with the vibrational distribution peaking at v_2= 1. This suggests that the upper level of the $2_0^1 3_0^4$ transition is also predissociated by the ^4E surface. Note that the $2_0^1 3_0^4$ transition is at nearly the same energy as the 3_0^7 transition, the first member of the 3_0^n progression in which the ^4E state appears to play a role.

2. Fine-Structure Distributions

The experimentally observed sulfur atom $S(^3P_j)$ fine-structure distributions yield further insight into the dissociative electronic states. In this section we compare the predicted fine-structure distributions for an adiabatic dissociation model for the repulsive $^4A_2$, $^2A_2$, and ^4E states to the experimentally observed fine-structure distributions. For simplicity, CH_3S will be regarded as a pseudodiatomic. The $\tilde{A}\,^2A_1$ state has angular momentum values $\Lambda=0$, $\Sigma=1/2$, and $\Omega= 1/2$ where Λ, Σ, and Ω refer to the electronic, spin, and total angular momentum along the C-S axis respectively. The $\tilde{A}\,^2A_1$ state can couple to the repulsive $^4A_2$, $^2A_2$, and ^4E states via a spin-orbit interaction. Because of the spin-orbit coupling selection rules, $\Delta\Omega = 0, \Delta\Sigma = -\Delta\Lambda = \pm 1$, or $\Delta\Sigma = \Delta\Lambda = 0$,[54] we need only consider the $\Omega=1/2$ states $^4A_{2(\Omega=1/2)}$, $^2A_{2(\Omega=1/2)}$, $^4E_{(\Omega=1/2)}$ states in our dissociation model.

In the relativistic adiabatic limit, the nuclei evolve slowly on relativistic adiabatic potentials all the way to the asymptotic products.[27,54] Adiabatic curves with the same value of Ω will undergo avoided crossings, so a one-to-one mapping between the molecular electronic states and the aymptotic fine-structure states can be performed. In the dissociation limit, Ω is defined as the projection of the total electronic angular momentum vector (spin + orbital) of the separated atoms along the internuclear axis. Following the calculations of Cui and Morokuma,[24] we have constructed an adiabatic correlation diagram, Figure 10, for the $\Omega = 1/2$ levels of CH_3S. This diagram shows that the $^4A_{2(\Omega=1/2)}$ state correlates with the $^3P_2$ products, the $^2A_{2(\Omega=1/2)}$ state correlates with $^3P_1$ products, and the $^4E_{1/2}$ states correlate with both $^3P_1$ and $^3P_0$ products.

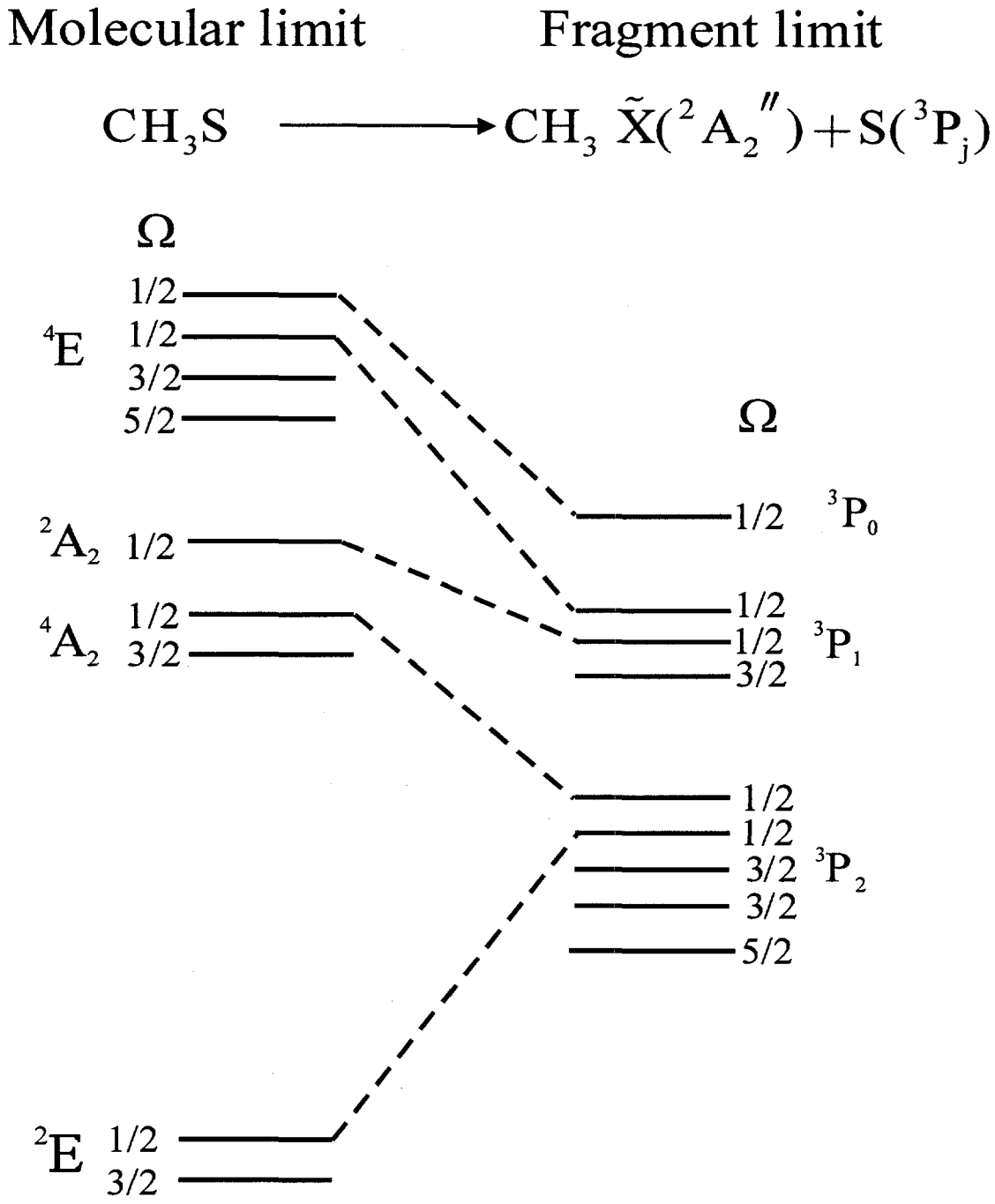

Figure 10. Adiabatic correlation diagram for CH_3S to products CH_3 + $S(^3P_j)$ for the Ω=1/2 levels based upon calculations of Cui et al.[24]

Comparison of Table III. with Figure 10 shows that for energies below the 3_0^7 and $2_0^1 3_0^4$ transitions (i.e. photon energies ≤ 29,000 cm^{-1} for transitions originating from the $^2E_{3/2}$ state), the average distribution of 88:6:6 agrees relatively well with adiabatic dissociation on the $^4A_2$ state, which should yield $^3P_2$ products exclusively. At higher energy, the spin-orbit distribution changes abruptly and exhibits an increased fraction of the $^3P_1$ and $^3P_0$ states, with these states dominating the $P(E_T)$ distribution for the 3_0^{11} transition, $S(^3P_{2:1:0}) = 14:39:46$. The spin-orbit distribution for the 3_0^7 transition of 70:20:10 suggests that while dissociation on the $^4A_2$ surface dominates, some dissociation also occurs on both the $^2A_2$ and ^4E states. For the 3_0^{11} transition, the dominance of the $^3P_1$ and $^3P_0$ products and the nearly equal $^3P_1$: $^3P_0$ ratio indicate that the dissociation mainly occurs on the ^4E state. Due to the extensive overlap of combination bands with the 3_0^8-3_0^{10} transitions, we have been unable to examine how the spin-orbit distributions change between the 3_0^7 and 3_0^{11} transitions.

The interpretation of the vibrational and spin-orbit distributions in terms of which repulsive states contribute to the dissociation are fairly consistent, the main difference being that the the spin-orbit results offers more direct evidence that the $^2A_2$ state plays a role in dissociation following excitation of the 3_0^7 transition. However, the increasing role of the ^4E state at energies above 29,000 cm^{-1} (3.6 eV) is supported by both sets of measurements.

This is consistent with the strength of the spin-orbit coupling between the $\tilde{A}\,^2A_1$ state and the three repulsive states. Cui and Morokuma[24] have calculated the spin-orbit

(SO) coupling matrix elements between the $\tilde{A}\,^2A_1$ surface and the repulsive $^4A_2$ and ^4E surfaces for CH_3S, finding $H^{SO}(^4A_2, ^2A_1)$ and $H^{SO}(^4E, ^2A_1)$ to be 75 and 152 cm^{-1} respectively with minimum seams of crossing located at 3.51 and 3.61 eV above the ground state for the $^4A_2$ and ^4E surfaces respectively. The SO matrix element $H^{SO}(^2A_2, ^2A_1)$ was not calculated for CH_3S. However, based on the analogous calculations for CH_3O, we expect $H^{SO}(^2A_2, ^2A_1)$ to be approximately 20% less than $H^{SO}(^4A_2, ^2A_1)$. These trends in H^{SO} arise because the dominant electronic configurations for the $\tilde{A}\,^2A_1$ state and the $^2A_2$ and $^4A_2$ states differ by two spin-orbitals while the ^4E state differs by one spin-orbital.[22,24] In any case, the stronger coupling to the ^4E state state suggests that it should dominate the dissociation once the crossing seam is energetically accessible, and the calculated energy minimum of the crossing seam lies very close to the experimental value at which both the vibrational and spin-orbit distributions change.

B. Excited State Lifetimes and Mode Specificity

Our excited state lifetime measurements as well as previous LIF radiative lifetime measurements[15] show that the predissociation of CH_3S is mode specific, with the ν_3 mode more strongly coupled to the dissociation coordinate than the ν_2 mode. The excited state lifetime decreases from 72 ± 30 ns for the 3_0^3 transition down to 2 ± 2 ps for the 3_0^7 transition over an energy range of approximately 180 meV. The lifetime of the $2_0^1 3_0^n$ transitions is longer than the nearly isoenergetic 3_0^{n+3} transitions and shorter than the 3_0^n transitions indicating that the umbrella mode is not completely decoupled from the dissociation coordinate, but is more weakly coupled than the C-S stretch.

Similar effects have been reported for the $\tilde{A}\ ^2A_1 \leftarrow \tilde{X}\ ^2E$ electronic band of CF_3S based on fluorescence depletion spectroscopy (FDS) linewidth measurements.[55] The $\tilde{A}$ state of CF_3S demonstrates a sharp reduction in lifetime with increased C-S stretch excitation. The lifetime decreases from 38 ns for the first predissociative transition, 3_0^4 located 1211 cm^{-1} above the origin, down to 1.1 ps for the 3_0^8 transition, over an energy range of approximately 150 meV. The lifetimes of the $2_0^1 3_0^n$ combination band transitions of CF_3S display mode-specific behavior analogous to that observed in CH_3S. The $2_0^1 3_0^2$ transition (0_0^0+1354 cm^{-1}) possesses a lifetime of 333 ns, considerably longer than the 3_0^4 transition and shorter than the 2.95 μs lifetime for the 3_0^2 transition (0_0^0 + 615 cm^{-1}). The lifetimes of these combination band transitions decrease rapidly with increased ν_3 excitation, decreasing down to 0.9 ps for the $2_0^1 3_0^8$ transition (0_0^0+3082 cm^{-1}).

C. Higher Excitation Energies

Photodissociation of the CH_3S radical following excitation excitation at higher energy is significantly different from that observed for the $\tilde{A} \leftarrow \tilde{X}$ band. The structureless photofragment yield peak, Figure 7, observed near 45,600 cm^{-1} has a FWHM of 270 ± 30 cm^{-1}. While this peak is broader than those observed in the predissociative levels of the $\tilde{A}$ state, it is not as broad as one might expect for a completely repulsive surface. The "narrowness" of his feature indicates that the electronic state is either bound or relatively flat in the Franck-Condon region. Calculations on the doublet states of CH_3S performed by Hsu *et al.*[14] show that the

$\widetilde{B}\ ^2A_2$ state is indeed flat in the Franck-Condon region, Figure 1, due to an avoided crossing between the $\widetilde{C}\ ^2A_2$ and $\widetilde{B}\ ^2A_2$ states.[22]

The $P(E_T)$ distribution obtained from excitation at 45,600 cm^{-1}, Figure 8b, is considerably broader (500 meV) and less structured than the $P(E_T)$ distributions obtained from excitation in the $\widetilde{A} \leftarrow \widetilde{X}$ band. The fine-structure distribution could not be resolved in the $P(E_T)$ distribution. However, since the dissociation has ≈ 2.6 eV available for translation, we have assumed that the fine-structure distribution from this $^2A_2$ state can be described within the diabatic limit resulting in a statistical fine-structure distribution of 5:3:1.[56] Assuming the excited state to be repulsive, we have attempted to model the product state vibrational distribution using the sudden approximation.

In the sudden limit, the dissociation is sufficiently rapid so that there is minimal coupling between the translational and vibrational degrees of freedom.[1,57] The CH_3 umbrella mode vibrational distribution is obtained by a Franck-Condon projection of the CH_3 group of the excited state methylthio radical onto the CH_3 photofragment. We assume the geometry of the excited state in the Franck-Condon region to be the same as the ground state geometry, i.e. a vertical transition. The ground state ∠HCS of 107.8°, derived from ∠HCH = 111° from the calculations of Janousek *et al.*,[8].is projected onto the planar CH_3 fragment, corresponding to ∠HCS = 90°. Figure 8b shows the results of this calculation convoluted with a statistical fine-structure distribution, an instrument resolution of 40 meV, and a CH_3 Boltzmann rotational distribution with a temperature of 350 K. This model provides a reasonable fit to the experimental data with a vibrational distribution peaking at ν_2=2 and showing excitation up to ν_2=5.

The photofragment anisotropy, $\beta = -0.98$, is consistent with a perpendicular electronic transition indicating that the excited state is of either $^2A_1$ or $^2A_2$ symmetry. The $P(E_T)$ distribution, Figure 8a, shows ground state products, $CH_3 + S(^3P)$ to be the dominant dissociation channel ($\geq 98\%$). The $\tilde{B}\ ^2A_2$ state correlates adiabatically to these ground state products. Our results are in contrast to previous photodissociation experiments[22] at 193 nm (51,800 cm^{-1}) in which $S(^1D) + CH_3$ was found to be the primary product channel with $S(^1D):S(^3P) = 85:15$. It appears that photodissociation at this energy occurs on a different electronic surface than at 45,600 cm^{-1}. *Ab initio* calculations performed by Hsu *et al.*[14] imply that excitation at 193 nm accesses the bound $\tilde{C}\ ^2A_2$ state which is predissociated by a repulsive ^2E state that correlates to $S(^1D) + CH_3$ products. The combination of our PFY spectrum, the CH_3 vibrational distribution, and the observation of ground state products indicates that dissociation at 45,600 cm^{-1} occurs on the $\tilde{B}\ ^2A_2$ state.

VI. Conclusions

In this study, we have investigated the photodissociation of CH_3S via the $\tilde{A} \leftarrow \tilde{X}$ and $\tilde{B} \leftarrow \tilde{X}$ bands. For the $\tilde{A} \leftarrow \tilde{X}$ band, we have obtained a structured PFY spectrum containing extended 3_0^n and $2_0^1 3_0^n$ progressions and have determined the onset of predissociation to occur for the 3_0^2 transition.

Measured photofragment anisotropies, β=-0.2 to -1.0 ± 0.1, have been obtained, consistent with the expected perpendicular transition dipole moment. The measured

anisotropies have been used to estimate the excited state lifetimes, which decrease rapidly with increased excitation of the ν_3 mode.

Translational energy $P(E_T)$ distributions have been obtained with sufficient resolution to observe the CH_3 fragment vibrational and $S(^3P_j)$ fine-structure distributions. The fine-structure distributions and vibrational distributions allow us to assess the relative importance of the $^4A_2$, $^2A_2$, and ^4E repulsive electronic surfaces in the predissociation of the $\tilde{A}\ ^2A_1$ state at various photon energies. At photon energies < 29,000 cm^{-1}, the vibrational and fine-structure distributions suggest that the dissociation takes place on the $^4A_2$ surface, while the increased vibrational excitation and change in fine-structure distributions at higher energies point to dissociation on the the ^4E surface. The $2_0^1 3_0^3$ and $2_0^1 3_0^4$ transitions lead to a larger fractional population of the CH_3 fragment umbrella mode than the nearly isoenergetic 3_0^{n+3} transitions, suggesting that the umbrella mode does not couple to the dissociation coordinate as well as the C-S stretch.

Photodissociation of CH_3S at 45,600 cm^{-1} shows $CH_3 + S(^3P_{2,1,0})$ to be the dominant product channel, with most of the available energy being partitioned into translation. We have modeled this dissociation using the sudden approximation to describe the vibrational distribution and the diabatic limit to describe the fine-structure distribution. The product channel, photofragment anisotropy, β= -0.98, and photofragment yield spectra suggest that the excited state is the $\tilde{B}\ ^2A_2$ state.

Acknowledgements

This research is supported by the Director, Office of Energy Research, Office of Basic Energy Sciences, Chemical Sciences Division, of the U.S. Department of Energy

under Contract No. DE-AC03-76F00098. We would like to thank Dr. Qiang Cui for providing ground and excited state geometries, frequencies, and normal coordinates.

References

[1] R. Schinke, *Photodissociation Dynamics*, 1 ed. (Cambridge University Press, Cambridge, 1993).

[2] L. J. Butler and D. M. Neumark, J. Phys. Chem. **100,** 12801 (1996).

[3] P. L. Houston, J. Phys. Chem. **100,** 12757 (1996).

[4] R. J. Charlson, J. E. Lovelock, M. O. Andreae, and S. G. Warren, Nature **326,** 655 (1987).

[5] A. B. Callear, J. Connor, and D. R. Dickson, Nature **221,** 1238 (1969).

[6] P. C. Engelking, G. B. Ellison, and W. C. Lineberger, J. Chem. Phys. **69,** 1826 (1978).

[7] S. Moran and G. B. Ellison, J. Phys. Chem. **92,** 1794 (1988).

[8] B. K. Janousek and J. I. Brauman, J. Chem. Phys. **72,** 694 (1980).

[9] Y. Endo, S. Saito, and E. Hirota, J. Chem. Phys. **85,** 1770 (1986).

[10] Y. P. Lee, Proc. SPIE **1858,** 44 (1993).

[11] K. Ohbayashi, H. Akimoto, and I. Tanaka, Chem. Phys. Lett. **52,** 47 (1977).

[12] G. Black and L. E. Jusinski, J. Chem. Soc., Faraday Trans. 2 **82,** 2143 (1986).

[13] G. Black and L. E. Jusinski, J. Chem. Phys. **85,** 5379 (1986).

[14] Y.-C. Hsu, X. Liu, and T. A. Miller, J. Chem. Phys. **90,** 6852 (1989).

[15] S.-Y. Chiang and Y. P. Lee, J. Chem. Phys. **95,** 66 (1991).

[16] M. Suzuki, G. Inoue, and H. Akimoto, J. Chem. Phys. **81,** 5405 (1984).

[17] P. Misra, Z. Xinming, and H. L. Bryant, Jr., Pure Appl. Opt. **4,** 587 (1995).

[18] Y.-Y. Lee, S.-Y. Chiang, and Y.-P. Lee, J. Chem. Phys. **93,** 4487 (1990).

[19] A. Kumar, P. K. Chowdhury, K. V. S. Rama Rao, and J. P. Mittal, Chem. Phys. Lett. **198,** 406 (1992).

[20] G. D. Bent, J. Chem. Phys. **92,** 1547 (1990).

[21] R. Fournier and A. E. DePristo, J. Chem. Phys. **96,** 1183 (1992).

[22] C. W. Hsu, C. L. Liao, Z. X. Ma, P. J. H. Tjossem, and C. Y. Ng, J. Chem. Phys. **97,** 6283 (1992).

[23] A. C. Curtiss, R. H. Nobes, J. A. Pople, and L. Radom, J. Chem. Phys. **97,** 6766 (1992).

[24] Q. Cui and K. Morokuma, Chem. Phys. Lett. **263,** 54 (1996).

[25] S. H. S. Wilson, M. N. R. Ashfold, and R. N. Dixon, J. Chem. Phys. **101,** 7538 (1994).

[26] R. E. Continetti, D. R. Cyr, R. B. Metz, and D. M. Neumark, Chem. Phys. Lett. **182,** 406 (1991).

[27] D. J. Leahy, D. L. Osborn, D. R. Cyr, and D. M. Neumark, J. Chem. Phys. **103,** 2495 (1995).

[28] D. L. Osborn, H. Choi, D. H. Mordaunt, R. T. Bise, D. M. Neumark, and C. M. Rohlfing, J. Chem. Phys. **106,** 3049 (1997).

[29] D. L. Osborn, D. J. Leahy, D. R. Cyr, and D. M. Neumark, J. Chem. Phys. **104,** 5026 (1996).

[30] J. M. B. Bakker, J. Phys. E **6,** 785 (1973).

[31] J. M. B. Bakker, J. Phys. E **7,** 364 (1974).

[32] D. P. de Bruijn and J. Los, Rev. Sci. Instrum. **53,** 1020 (1982).

[33] *JANAF Thermochemical Tables*, J. Phys. Chem. Ref. Data **14** (Supplement No. 1) (1985).

[34] R. N. Zare, Molecular Photochemistry **4,** 1 (1972).

[35] C. Anastasi, M. Broomfield, O. J. Nielsen, and P. Pagsberg, Chem. Phys. Lett. **182,** 643 (1991).

[36] J. M. Nicovich, K. D. Kreutter, C. A. van Dijk, and P. H. Wine, J. Phys. Chem. **96,** 1992 (1992).

[37] S. Lias, J. E. Bartmess, J. F. Liebman, J. L. Holmes, R. D. Levin, and W. G. Mallard, J. Phys. Chem. Ref. Data **17,** 1988 (1988).

[38] S. Nourbakhsh, K. Norwood, H. M. Yin, C. L. Liao, and C. Y. Ng, J. Chem. Phys. **95,** 946 (1991).

[39] S. Nourbakhsh, C.-L. Liao, C.Y. Ng, J. Chem. Phys. **92,** 6587 (1990).

[40] S. Nourbakhsh, K. Norwood, H. M. Yin, C.-L. Liao, and C. Y. Ng, J. Chem. Phys. **95,** 5014 (1991).

[41] B. Russic and J. Berkowitz, J. Chem. Phys. **97,** 1818 (1992).

[42] D. L. Osborn, D. J. Leahy, and D. M. Neumark, J. Phys. Chem. A **101,** 6583 (1997).

[43] H. W. Herman and S. R. Leone, J. Chem. Phys. **76,** 4759 (1982).

[44] C. H. Yamada, E; Kawaguchi, K., J. Chem. Phys. **75,** 5256 (1981).

[45] J. F. Black, J. R. Waldeck, and R. N. Zare, J. Chem. Phys. **92,** 3519 (1990).

[46] C. Jonah, J. Chem. Phys. **55,** 1915 (1971).

[47] S. Yang and R. Bersohn, J. Chem. Phys. **61,** 4400 (1974).

[48] R. Bersohn and S. H. Lin, Adv. Chem. Phys. **67,** 67 (1969).

[49] M.-C. W. Yang, J.M.; Miller, T.A., J. Mol. Spec. **186** (1997).

[50] D. E. Powers, M. B. Pushkarsky, and T. A. Miller, J. Chem. Phys. **106,** 6863 (1997).

[51] X. Lui, C. P. Damo, T. D. Lin, S. C. Foster, and P. Misra, J. Phys. Chem. **93,** 2266 (1989).

[52] D. E. Powers, M.B. Pucharsky, M.-C. Yang, T.A. Miller, J. Phys. Chem. A **101,** 9846 (1997).

[53] D. L. Osborn, D. J. Leahy, E. M. Ross, and D. M. Neumark, Chem. Phys. Lett. **235,** 484 (1995).

[54] H. Lefebvre-Brion and R. W. Field, *Perturbations in the spectra of diatomic molecules* (1986).

[55] D. E. Powers, ; Pucharsky,M; Miller, T.A., Chem. Phys. Lett. **247,** 548 (1995).

[56] S. J. Singer, K. F. Freed, and Y. B. Band, J. Chem. Phys. **79,** 6060 (1983).

[57] R. D. Levine and R. B. Bernstein, *Molecular Reaction Dynamics and Chemical Reactivity* (Oxford University Press, New York, 1987).

Chapter 3. Photodissociation dynamics of the singlet and triplet states of the NCN radical[†]

The spectroscopy and photodissociation dynamics of the NCN radical have been investigated by fast beam photofragment translational spectroscopy. The $\tilde{B}\,^3\Sigma_u^- \leftarrow \tilde{X}\,^3\Sigma_g^-$, $\tilde{c}^1\Pi_u \leftarrow \tilde{a}^1\Delta_g$, and $\tilde{d}^1\Delta_u \leftarrow \tilde{a}^1\Delta_g$ transitions were examined. The major dissociation products for the $\tilde{B}^3\Sigma_u^-$ and $\tilde{c}^1\Pi_u$ states are $N_2(X^1\Sigma_g^+)$ + C(^{3}P), while the $\tilde{d}^1\Delta_u$ state dissociates to N_2 ($X^1\Sigma_g^+$) + C(^{1}D). The dissociation channel, N(^{4}S) + CN($X^2\Sigma^+$) is observed for the $\tilde{B}^3\Sigma_u^-$ state at photon energies greater than 4.9 eV, where it comprises $\approx 25 \pm 10\%$ of the total signal. At all photon energies, the photofragment translational energy distributions show a resolved progression corresponding to the vibrational excitation of the N_2 photofragment. The rotational distributions of the molecular fragments suggest that the dissociation pathway for the N_2 loss channel involves a bent transition state while the N + CN photofragments are produced via a linear dissociation mechanism. The $P(E_T)$ distributions provide bond dissociation energies of 2.54 ± 0.030 and 4.56 ± 0.040 eV for the N_2 and CN loss channels, respectively, yielding $\Delta_f H_0(NCN) = 4.83 \pm 0.030$eV.

I. Introduction

Photodissociation of small polyatomic molecules provides a rich probe of the potential energy surfaces involved in bond rupture. Detailed measurements such as photofragment yield spectra, translational energy distributions, and product branching

[†] Originally published in J. Chem. Phys. **111**, 4923 (1999).

ratios allow for a careful examination of the dissociation mechanism.[1] While there have been numerous photodissociation studies of stable closed-shell molecules, far fewer studies of open-shell radicals have been performed. Our laboratory has demonstrated the ability to generate a well-characterized source of radicals via photodetachment of negative ions, allowing us to perform photodissociation experiments on reactive open-shell species. Here, we report the photodissociation dynamics for triplet and singlet electronic states of the NCN radical.

The NCN free radical has been proposed as an important combustion intermediate since its emission was observed in hydrocarbon flames by Jennings and Linnett.[2] It has been suggested by Smith *et al.* [3] that the NCN radical plays a significant role in the combustion of nitramine propellant molecules, given the large extent of C-N bonding in these molecules. Additionally, ultraviolet emission studies of the Comet Brorosen-Metcalf suggest that NCN is present in comets and is a source of CN radicals.[4]

The NCN radical has attracted a great deal of attention from both spectroscopists and theorists who have been particularly concerned with its bonding and geometry. The ground and relevant excited states for this study are shown in Figure 1 with the corresponding dominant electronic configurations given below:

$\ldots(3\sigma_u)^2(1\pi_u)^4(1\pi_g)^2 \qquad \widetilde{X}\,^3\Sigma_g^-,\ \widetilde{a}^1\Delta_g, \widetilde{b}^1\Sigma_g^+$

$\ldots(3\sigma_u)^1(1\pi_u)^4(1\pi_g)^3 \qquad \widetilde{A}^3\Pi_u, \widetilde{c}^1\Pi_u$

$\ldots(3\sigma_u)^2(1\pi_u)^3(1\pi_g)^3 \qquad \widetilde{B}\,^3\Sigma_u^-,\ \widetilde{d}^1\Delta_u$

According to Walsh's rules,[5] all of these electronic states are predicted to be linear.

Rotationally resolved ultraviolet absorption spectra were measured by Travis and Herzberg[6] for the $\tilde{A}^3\Pi_u \leftarrow \tilde{X}\ ^3\Sigma_g$ band and by Kroto[7,8] for the $\tilde{c}^1\Pi_u \leftarrow \tilde{a}^1\Delta_g$ band, confirming that these states are linear. Kroto observed a number of higher lying transitions attributed to the $\tilde{B}\ ^3\Sigma_u^- \leftarrow \tilde{X}\ ^3\Sigma_g^-$ and $\tilde{d}^1\Delta_u \leftarrow \tilde{a}^1\Delta_g$ bands.[9] Milligan, Jacox, and Bass observed this $\tilde{B}\ ^3\Sigma_u^- \leftarrow \tilde{X}\ ^3\Sigma_g^-$ band as well as a number of infrared absorptions in matrix isolation studies.[10,11]

In the matrix work, depletion of the NCN radical was observed at wavelengths shorter than 280 nm (4.42 eV); on the basis of secondary reaction products within the matrix, the authors proposed that NCN dissociates to $N_2(X^1\Sigma_g^+)$ + C(^{3}P) in this wavelength range, which overlaps the $\tilde{B}\ ^3\Sigma_u^- \leftarrow \tilde{X}\ ^3\Sigma_g^-$ band. Smith *et al.*[3] measured the radiative lifetime for the vibrationless level and a number of vibronic bands of the $\tilde{A}^3\Pi_u$ state, determining the radiative lifetime of the vibrationless level to be 183 ns. The radiative lifetimes show very little variation with increased vibrational excitation, implying that this state does not dissociate.

More recently, McNaughton and coworkers[12] measured a high resolution Fourier-transform infrared spectrum of the NCN antisymmetric stretch band in the gas phase. Brown and coworkers[13-16] used laser-induced fluorescence and laser magnetic resonance to refine the spectroscopic constants of the $\tilde{X}$ and $\tilde{A}$ states and obtain estimates of the bend frequencies in the two states.

The photoelectron spectrum of NCN^- measured by Clifford *et al.*[17] showed the photodetachment process to be vertical, giving rise to no vibrational excitation of the neutral radical upon photodetachment. Higher energy photoelectron spectroscopy studies

performed by Taylor *et al.*[18] located the $\tilde{a}^1\Delta_g$ and $\tilde{b}^1\Sigma_g^+$ states relative to the $\tilde{X}^3\Sigma_g^-$ ground state, thereby determining the singlet-triplet splitting, $E(\tilde{a}^1\Delta_g - \tilde{X}^3\Sigma_g^-) = 1.010 \pm 0.010$ eV.

Theoretical studies of the geometry and bonding of the NCN radical showed the ground state to be linear with the central carbon doubly bonded to both nitrogen atoms.[17,19-23] Martin *et al.* have performed ab initio studies on both the NCN and CNN radicals for linear, cyclic and bent geometries[24] finding the barrier to isomerization to lie approximately 3 eV above the NCN ground state. This is consistent with the experimental observation of both isomers as distinct species.[25-30]

The NCN radical provides a rich system for photodissociation studies. It has several low-lying singlet and triplet excited states above the dissociation limit as well as multiple energetically accessible product states, as shown in Figure 1. Furthermore, the photodecomposition of NCN to products $N_2 + C(^3P)$ from the linear $\tilde{B}\ ^3\Sigma_u^- \leftarrow \tilde{X}\ ^3\Sigma_g^-$ transition observed by Milligan and coworkers[10] implies that the dissociation mechanism is complex, possibly involving bent or cyclic electronic states.

In this study, a mass selected beam of NCN radicals is generated from the photodetachment of NCN^- ions and subsequently photodissociated. We recently demonstrated the ability to probe transitions not only from the ground electronic state but also from low-lying excited states of different spin multiplicity.[31] A photodetachment energy slightly above the electron affinity produces the NCN radical in the ground $\tilde{X}^3\Sigma_g^-$ state exclusively, allowing us to examine the spectroscopy and dynamics of triplet

dissociative electronic states. A higher photodetachment energy can then be used to populate both the $\tilde{X}\,^3\Sigma_g^-$ and $\tilde{a}^1\Delta_g$ states, the latter providing access to the dissociative states in the singlet manifold. Overall, we have examined the photodissociation

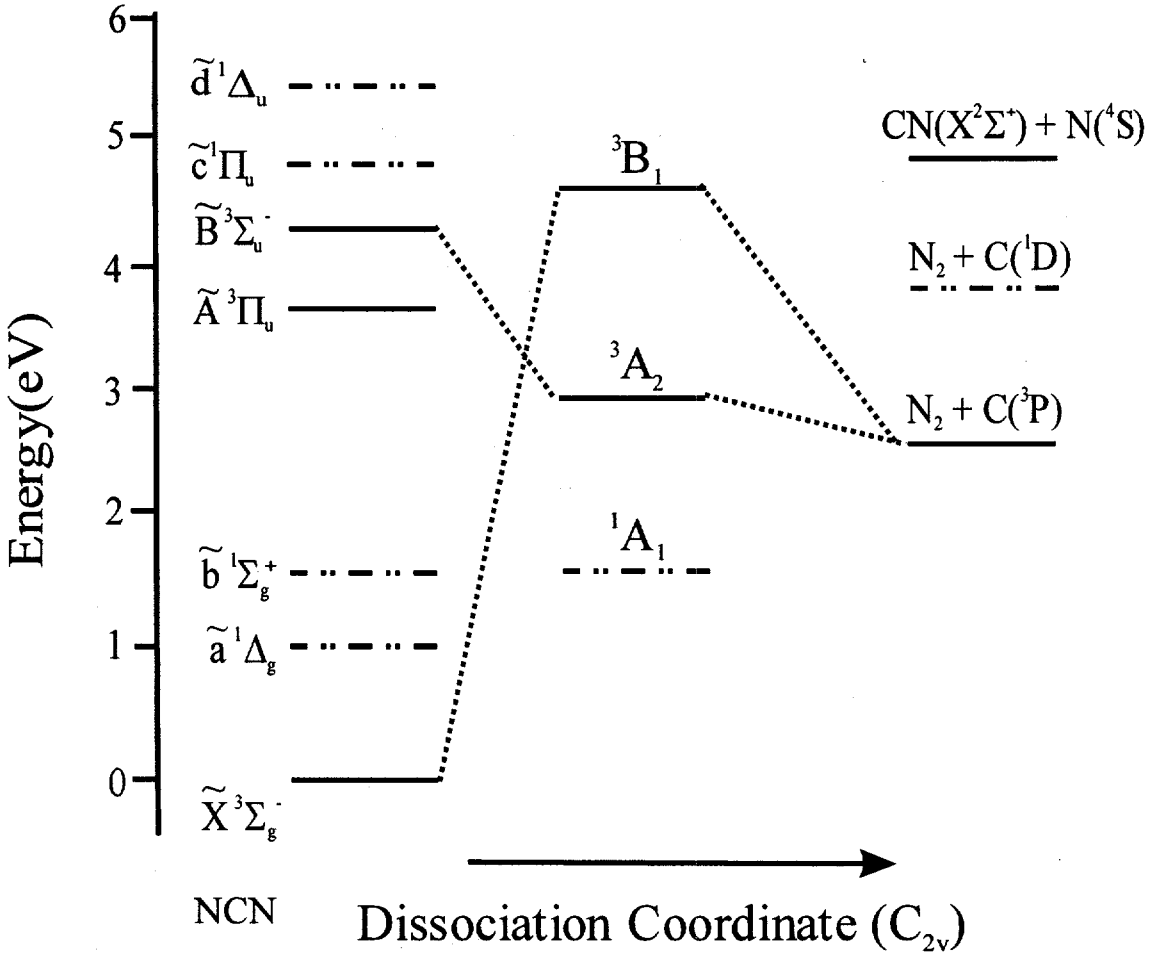

Figure 1. Energy level and correlation diagram for the NCN radical along a C_{2v} dissociation coordinate. The energies of the $\tilde{a}^1\Delta_g$, $\tilde{b}^1\Sigma_g^+$, $\tilde{A}^3\Pi_u$, $\tilde{B}^3\Sigma_u^-$, $\tilde{c}^1\Pi_u$, and $\tilde{d}^1\Delta_u$ states are based upon experimental work discussed in the text. The $^1A_1$, $^3A_2$, and $^3B_2$ states are from *ab inito* calculations (Ref. 24) and the product state energies are from JANAF thermochemical tables (Ref. 42)

dynamics of the $\tilde{B}\ ^3\Sigma_u^- \leftarrow \tilde{X}\ ^3\Sigma_g^-$, $\tilde{c}^1\Pi_u \leftarrow \tilde{a}^1\Delta_g$, and $\tilde{d}^1\Delta_u \leftarrow \tilde{a}^1\Delta_g$ electronic bands obtaining structured photodissociation cross-sections, product branching ratios, and detailed internal energy distributions of the photofragments.

II. Experiment

The fast beam photofragment translational spectrometer, Figure 2, has been described in detail elsewhere;[32-34] only a brief description will follow. In this experiment, we generate a clean source of neutral radicals by mass-selectively photodetaching a beam of stable negative ions. The neutral radicals are then photodissociated by a second laser.

To generate a sufficient number density of NCN^- ions, we made a slight modification to our pulsed electric discharge source[35] by inserting a reservoir containing cyanamide (H_2NCN) between the pulsed molecular beam valve and the pulsed electric discharge. Our adaptation of this source has been described in detail previously.[18] Neat O_2 at a stagnation pressure of ~3 atm is expanded through a pulsed molecular beam valve

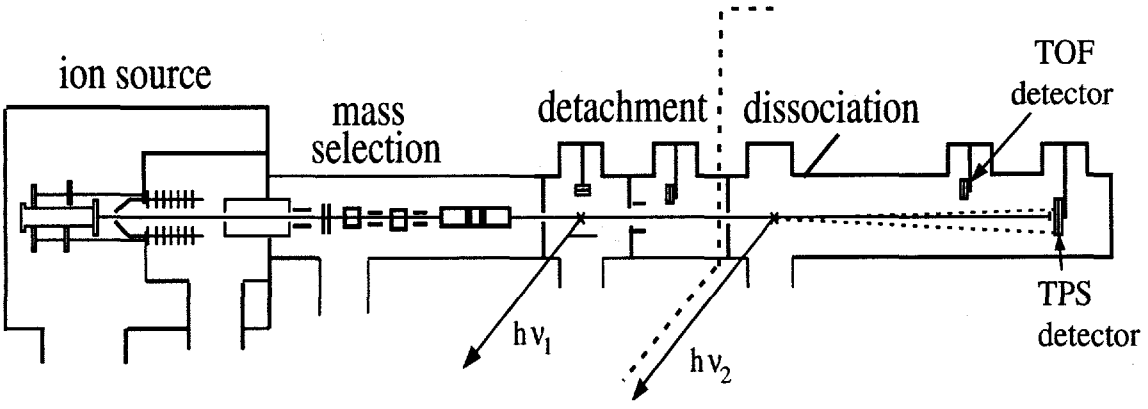

Figure 2. Fast radical beam translational spectrometer. The dotted line separates the radical production section on the left from the photodissociation experiment on the right.

into the reservoir containing the cyanamide and finally through the discharge, generating CN^-, NCN^-, $HNCN^-$ and NCO^- ions. Analysis of photofragment yield spectra obtained in this study indicates that this source produces anions with rotational and vibrational temperatures of 50 K and 200 K respectively.

The negative ions generated in the source region are accelerated to 8 keV and separated temporally by a Bakker time-of-flight (TOF) mass spectrometer, which induces very little kinetic energy spread of the ions.[36,37] The ion of interest is selectively photodetached by a pulsed laser. Based upon the photoelectron spectrum of Taylor *et al.*,[18] an excimer-pumped dye laser operating at 2.82 eV was used to photodetach NCN^- to produce the neutral $\tilde{X}\,^3\Sigma_g^-$ state exclusively, while 4.03 eV light (308 nm) from a XeCl excimer laser was used to populate both the $\tilde{a}\,^1\Delta_g$ and $\tilde{X}\,^3\Sigma_g^-$ states of the neutral. Any undetached ions are deflected out of the beam path.

In the dissociation region, the neutrals are intersected by the frequency-doubled output of an excimer-pumped dye laser with a bandwidth of 0.3 cm^{-1}. A fraction of the neutrals absorb and dissociate yielding photofragments detected directly by either the TOF or TPS (time and position sensing) microchannel plate detector assemblies in Figure 2. An aluminum strip is positioned at the center of each detector to prohibit any undissociated radicals from impacting the detector, so that any observed signal is entirely from the recoiling photofragments.

Two types of experiments are performed. First, the spectroscopy of the dissociative electronic states is examined by measuring the total flux of photofragments arriving at the retractable TOF detector, located at 0.68 m from the dissociation laser, as a function of photon energy. The resulting photofragment yield (PFY) spectra is

complementary to absorption and fluorescence measurements. The current study examined the photolysis of NCN between 30,000 to 43,500 cm^{-1}.

Once the spectroscopy of the dissociative states has been examined, a second type of experiment, which probes the dissociation dynamics, can be performed. In this detection scheme, both photofragments from a single parent radical are detected in coincidence using a time-and-position sensitive (TPS) detector of the type developed by de Bruijn and Los.[38] Our implementation of this detection scheme has been described in detail elsewhere.[32,33] The TPS detector records the positions and difference in arrival time of the two photofragments from a single dissociation event. This information is then used to determine the masses of the fragments, their relative translational energy E_T and the scattering angle θ between the relative velocity vector and the electric vector of the polarized dissociation laser (parallel to the ion beam axis). The photofragment mass resolution is $m/\Delta m \approx 10$ while the translational energy resolution for these experiments is $\Delta E_T/E_T = 3.0$ %.

Due to the geometry of the TPS detector, which is 40 mm in diameter with an 8 mm beam block located at the center, the detection efficiency of photofragments depends upon their values of θ and E_T. The beam block, in addition to blocking undissociated radicals, prevents fragments of low translational energy or with values of θ close to 0° to 180° from reaching the detector, while high-energy recoil fragments with values of θ close to 90° miss the detector. The raw translation energy distributions are therefore normalized by the calculated detector acceptance function, $D(E_T, \theta)$, which has been described in detail by Continetti *et al.*[39]

III. Results

A. Photofragment Yield Spectra $\tilde{B}\,^3\Sigma_u^- \leftarrow \tilde{X}\,^3\Sigma_g^-$ transitions

The PFY signal for the $\tilde{B}\,^3\Sigma_u^- \leftarrow \tilde{X}\,^3\Sigma_g^-$ band is shown in Figure 3, covering 33,000 to 43,000 cm^{-1}. The spectrum shows a progression of predissociative resonances spaced by approximately 1050 cm^{-1}. The positions, assignments and widths of these transitions are listed in Table I. This progression was observed previously in the ultraviolet absorption studies of Kroto[9] in the gas phase and by Milligan, Jacox, and Bass[10] in matrix isolation studies and was assigned to the symmetric stretch (1_0^n) progression. The extended progression and change in frequency from 1259 cm^{-1} in the ground state[40] to 1050 cm^{-1} for the excited state is consistent with promotion of an electron from the $1\pi_u$ to the $1\pi_g$ orbital.

A weaker 1050 cm^{-1} progression is observed ≈ 100 cm^{-1} to the blue of the 1_0^n progression. Travis and Herzberg[6] have shown for second row triatomics that the bending frequency increases with the number of electrons in the π_g orbital. The bending frequency of the $\tilde{A}^3\Pi_u$ state, which also has three electrons in the outermost π_g orbital, was found to be 96 cm^{-1} larger than the ground state bend frequency, estimated to be 437.7 cm^{-1}. [14] On this basis, we assign this progression to the $1_0^n 2_1^1$ sequence band and estimate the bend frequency of the $\tilde{B}^3\Sigma_u^-$ state to be 540 ± 20 cm^{-1}.

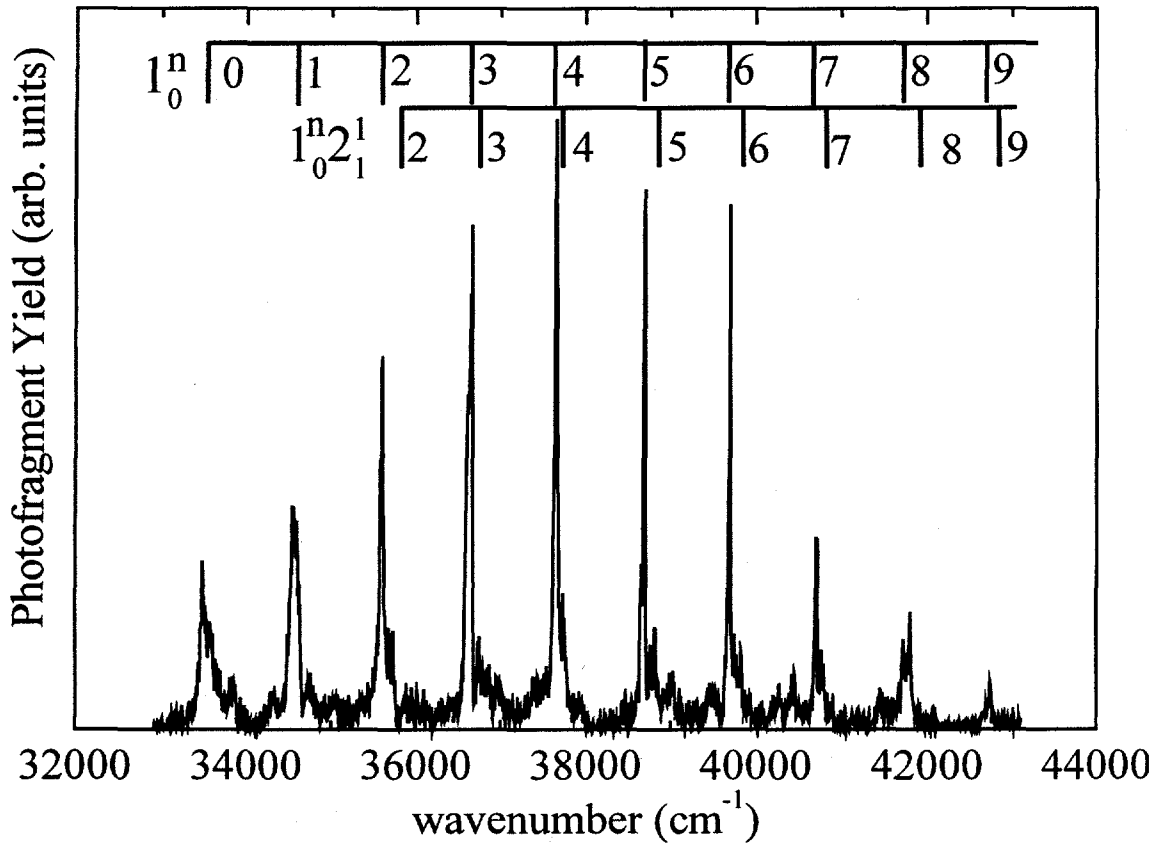

Figure 3. Photofragment yield spectrum of the $\widetilde{B}^3\Sigma_u^- \leftarrow \widetilde{X}^3\Sigma_g^-$ band obtained at a photodetachment energy of 2.82 eV. The vibrational combs denote symmetric stretch 1_0^n and sequence band $1_0^n 2_1^1$ progressions

Neither our photodissociation studies nor the previously mentioned absorption studies have been able to locate any transitions of the $\widetilde{B}\ ^3\Sigma_u^- \leftarrow \widetilde{X}\ ^3\Sigma_g^-$ band below the apparent origin at 33,488 cm^{-1}. In agreement with the observations of Kroto[9], the two lowest energy peaks were found to be remarkably broad, ~ 168 and 116 cm^{-1} in width. The peak widths gradually narrow as the photon energy is increased. The 1_0^3 transition is anomalously broad showing essentially three peaks with the most intense feature located to the blue.

Table I. Peak energies, assignments, progression spacings, and widths for the observed transitions in the $\widetilde{B}^3\Sigma_u^- \leftarrow \widetilde{X}^3\Sigma_g^-$ PFY spectrum.

Transition energy (cm^{-1})		Assignment	V(n) – v(n-1) (cm^{-1})		FWHM (cm^{-1})
33488		0_0^0			168
34555		1_0^1	1067		116
35597		1_0^2	1042		48
	35714	$2_1^1 1_0^2$			
36634		1_0^3	1037		86
	36738	$2_1^1 1_0^3$		1024	
37657		1_0^4	1023		40
	37740	$2_1^1 1_0^4$		1002	
38654		1_0^5	997		30
	38759	$2_1^1 1_0^5$		1019	
39698		1_0^6	1044		21
	39774	$2_1^1 1_0^6$		1015	
40707		1_0^7	1009		20
	40793	$2_1^1 1_0^7$		1019	
41762		1_0^8	1055		----
	41801	$2_1^1 1_0^8$		1008	
42736		1_0^9	974		20

Although we performed scans with a laser bandwidth of 0.2 cm^{-1} and a step size of 0.1 cm^{-1}, we were unable to resolve any rotational structure for the $\tilde{B} \leftarrow \tilde{X}$ band and therefore cannot determine the excited state lifetime from linewidth measurements. The relative intensities of the vibrational features in the PFY spectra are similar to those for the matrix absorption experiments of Milligan *et al.*,[10] suggesting that the quantum yield for photodissociation is ≈ 1.

Despite extensive efforts to observe the $\tilde{A}^3\Pi_u \leftarrow \tilde{X}\ ^3\Sigma_g$ transitions, we were unable to detect photodissociation signal from the origin or higher energy vibronic transitions associated with this band.

B. Photofragment Yield Spectra, $\tilde{c}^1\Pi_u \leftarrow \tilde{a}^1\Delta_g$ and $\tilde{d}^1\Delta_u \leftarrow \tilde{a}^1\Delta_g$ transitions

Figure 4 shows the PFY spectrum from 30,000 cm^{-1} to 30,150 cm^{-1} when the photodetachment energy is 4.03 eV. The recent photoelectron spectrum taken by Taylor *et al.*[18] showed that a photodetachment energy of 4.03 eV will populate both the $\tilde{X}\ ^3\Sigma_g^-$ and $\tilde{a}^1\Delta_g$ electronic states with an intensity ratio of approximately 2:1. Since the anion and neutral have essentially the same geometry, photodetachment of NCN^- yields minimal vibrational excitation of the neutral radical, allowing the anion to be photodetached well above threshold while maintaining a cold neutral vibrational distribution. Any new features in the PFY spectrum are therefore a result of transitions from the $\tilde{a}^1\Delta_g$ electronic state.

The intense transition centered around 30,045 cm^{-1} agrees well with the rotationally resolved spectrum obtained by Kroto, [7] which he assigns to the (000-000) transition of the $\tilde{c}^1\Pi_u \leftarrow \tilde{a}^1\Delta_g$ band. Additional weaker features seen at 30025, 30045,

and 30130 cm^{-1} are consistent with bandheads observed by Kroto and are assigned to the (100-100) $^1\Pi_u \leftarrow {}^1\Delta_g$, (010-010) $^1\Sigma_g^+ \leftarrow {}^1\Pi_u$, and (010-010) $^1\Delta_g \leftarrow {}^1\Phi_u$ vibronic transitions respectively. The rotational contour of the (000-000) band is characteristic of a perpendicular transition moment with an intense Q-branch and weaker P and R branches. The Q-branches of the (100-100) $^1\Pi_u \leftarrow {}^1\Delta_g$ and (010-010) $^1\Sigma_g^+ \leftarrow {}^1\Pi_u$ bands are heavily overlapped by the P and R-branches of the (000-000) transition, respectively. Using the previously determined rotational constants, the best fit to this rotational contour is achieved with a rotational temperature of 50 K.

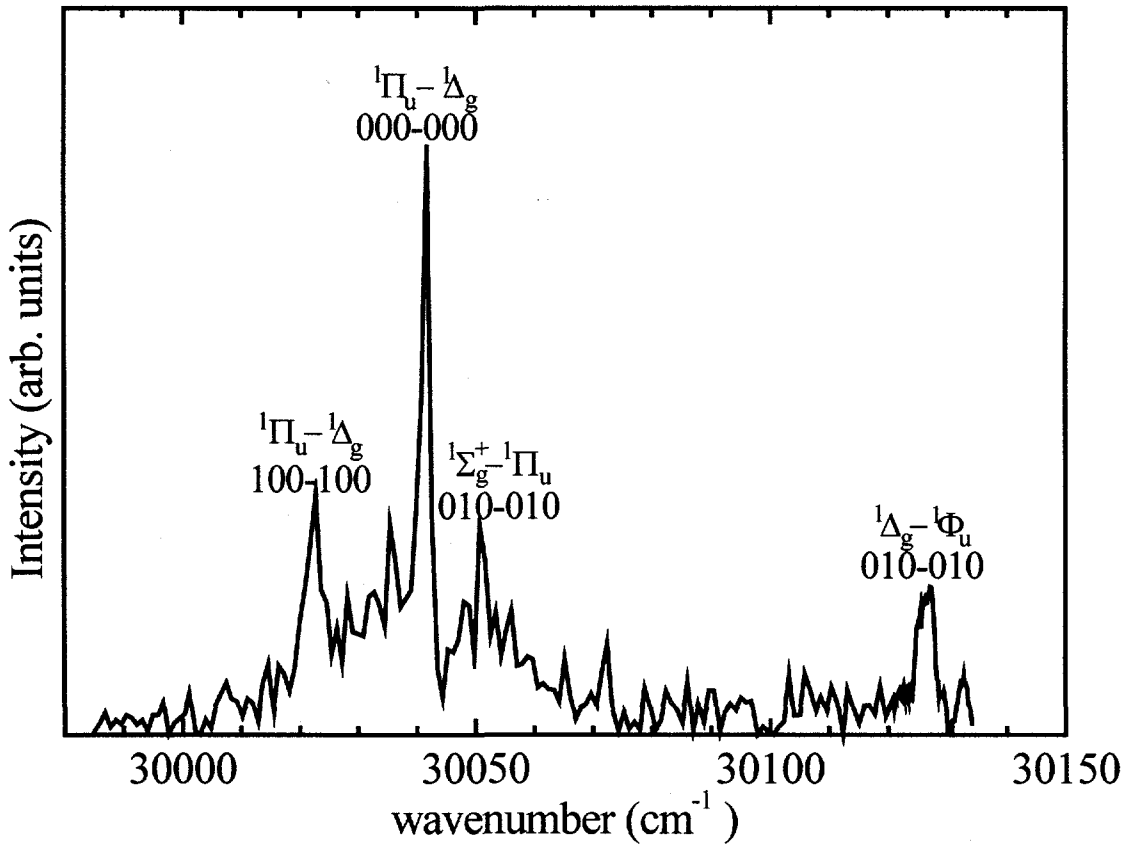

Figure 4. Photofragment yield (PFY) spectrum of the $\tilde{c}^1\Pi_u \leftarrow \tilde{a}^1\Delta_g$ origin band.

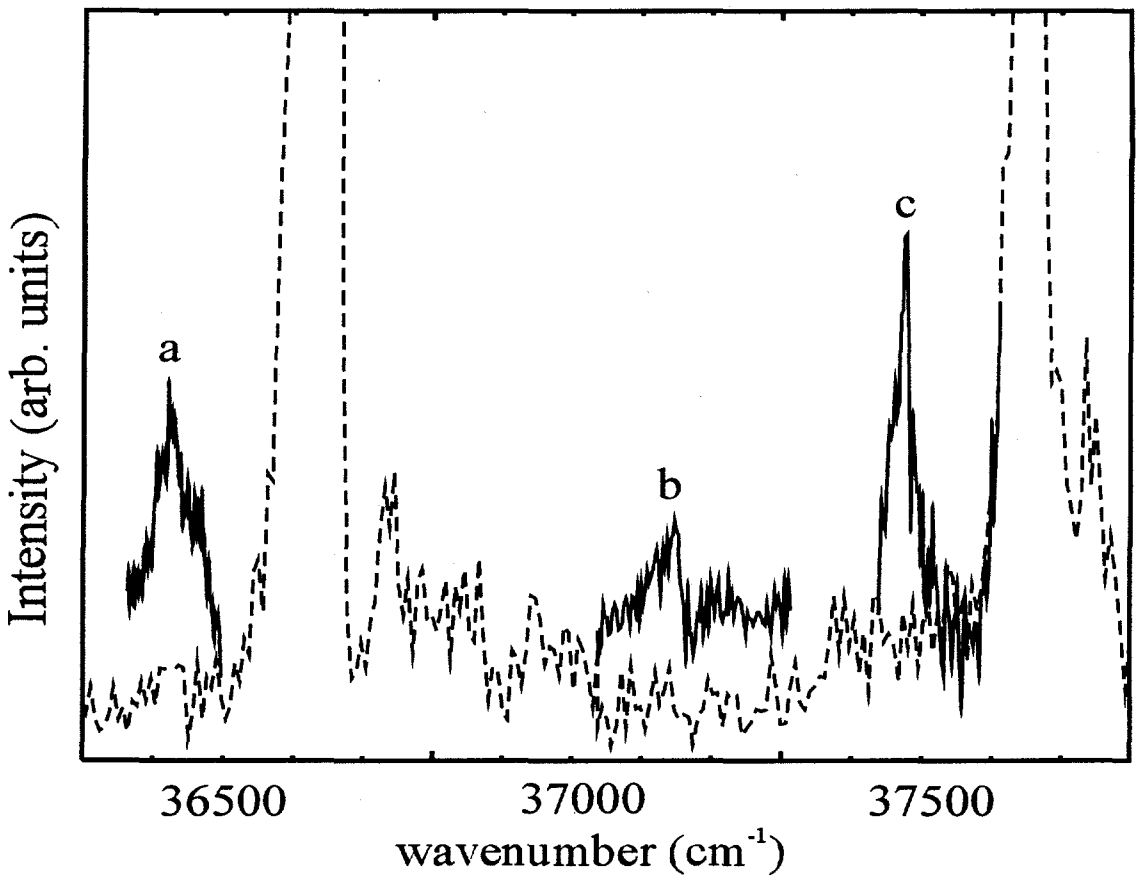

Figure 5. PFY spectrum from 36,300 to 37,800 cm^{-1}. The dashed line indicates features observed at a photodetachment energy of 2.82 eV. The solid line denotes additional features seen at a photodetachment energy of 4.03 eV. These features **a**, **b** and **c** are assigned to the $\tilde{d}^1\Delta_u \leftarrow \tilde{a}^1\Delta_g$ band.

Figure 5 shows the PFY spectrum for the wavelength region between 36,200 to 37,800 cm^{-1} obtained with a 4.03 eV photodetachment energy. In addition to the $\tilde{B}\ ^3\Sigma_u^- \leftarrow \tilde{X}\ ^3\Sigma_g^-$ transitions seen in Figure 3, a number of new transitions appear labeled **a**, **b**, and **c**. These transitions have been observed previously in the gas phase absorption studies of Kroto and coworkers[9] and were assigned to the $\tilde{d}^1\Delta_u \leftarrow \tilde{a}^1\Delta_g$ band based on

kinetic information and complicated vibrational structure. The most intense features, **a** and **c**, belong to a progression of ≈1020 cm^{-1} which is attributed to the symmetric stretch. The weaker feature **b** most likely involves bend excitation. Our photodetachment technique confirms that these transitions originate from the $\tilde{a}^1\Delta_g$ state.

C. Translational Energy Distributions

At the photon energies explored in this study, three possible dissociation channels are accessible:

$$NCN\,(\tilde{X}\ ^3\Sigma_g^-) \xrightarrow{h\upsilon}$$

$$N_2\,(X\ ^1\Sigma_g^+) + C\,(^3P) \qquad \Delta_{rxn}H_0 = 2.541 \pm 0.030\ eV \qquad (I)$$

$$N_2\,(X\ ^1\Sigma_g^+) + C(^1D) \qquad \Delta_{rxn}H_0 = 3.801 \pm 0.030\ eV \qquad (II)$$

$$CN(X\ ^2\Sigma^+) + N(^4S) \qquad \Delta_{rxn}H_0 = 4.563 \pm 0.050\ eV \qquad (III)$$

The above heats of reaction (at 0 K) represent a refinement of previous values and were determined directly from this work (see below).

All three channels are accessible following excitation of the $1_0^n, n \geq 4$ transitions in Fig. 3. For each dissociation event, the photofragment mass ratios are calculated from the relative recoil distance of the coincident photofragments from the center of the neutral beam. This enables us to largely but not completely distinguish C + N_2 from N + CN products, since our product mass resolution is only ~ 10. For data collected at a 1 m flight length, the $\tilde{B} \leftarrow \tilde{X}$ transitions with photon energies less than 5.1 eV produce a mass ratio of 12:28, indicating C + N_2 products. The observed mass distribution is significantly broadened at translational energies less than 0.7 eV for the 1_0^9 transition

implying that the N + CN channel contributes at low E_T. Increasing the flight length to 2 m improves the detection efficiency of low translational energy fragments. At this flight length, the 1_0^6 and 1_0^7 transitions exhibit a photofragment mass ratio of 14:26 (N + CN) at translational energies < 0.3 and <0.45 eV respectively and a mass ratio of 12:28 at higher translational energies, as shown in Figure 6. The photofragment mass ratio is 12:28 for the $\tilde{c}^1\Pi_u \leftarrow \tilde{a}^1\Delta_g$ and $\tilde{d}^1\Delta_u \leftarrow \tilde{a}^1\Delta_g$ transitions at all E_T.

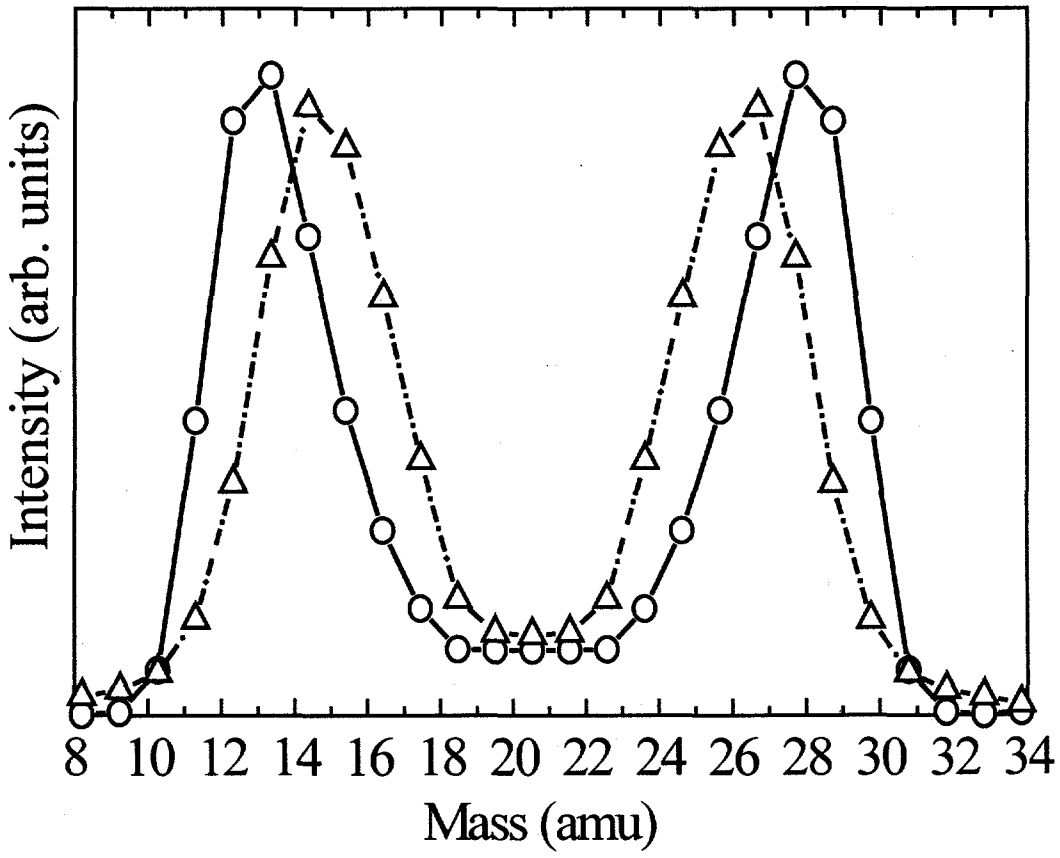

Figure 6. Fragment mass distribution for $E_T < 0.35$ eV for the 1_0^7 transition (open circles) and $E_T > 0.5$ for the 1_0^6 transition (open triangles). The data was collected with a 2m flight length.

$P(E_T)$ distributions for the C + N_2 channel from several $\tilde{B} \leftarrow \tilde{X}$ transitions are shown in Figure 7; these distributions were taken at a flight length of 1 m. The distributions display a sharp onset at high translational energy and well-resolved structure with peaks separated by approximately 290 meV, corresponding to excitation of the N_2 product vibration. The FWHM of each peak is approximately 150 meV with an asymmetric tail extending toward low translational energy. The assignment of the structure of the $P(E_T)$ distributions is presented in section IV with the resulting N_2 vibrational distributions listed in Table II. While the $P(E_T)$ distributions show highly structured features at high translational energy, the low kinetic energy regions ($E_T < 0.8$ eV) of these spectra are relatively broad and unresolved.

From our product mass analysis, of which Fig. 6 is an example, we expect significant N + CN contributions at low E_T for the $1_0^n, n \geq 6$ $\tilde{B} \leftarrow \tilde{X}$ transitions. The N + CN $P(E_T)$ distributions for the low E_T regions of the $1_0^6, 1_0^7$, and 1_0^9 transitions (the first two are from data at a flight length of 2 m) are shown in Figure 8. The $1_0^6, 1_0^7$, and 1_0^9 transitions yield $P(E_T)$ distributions with sharp narrow peaks (FWHM $\approx$ 100 meV) with maxima located at 0.19, 0.31, and 0.56 eV respectively. The peak positions shift with increased excitation energy; consistent with opening of the N(^{4}S) + CN($X\,^2\Sigma^+$) channel. The $P(E_T)$ distributions for the 1_0^7 and 1_0^9 transitions display additional peaks at $\approx$ 250 meV lower E_T; these are attributed to vibrational excitation of the CN fragment. There is signal extending to higher translational energies than energetically accessible for N + CN products. This is caused by our limited photofragment mass resolution that cannot completely exclude N_2 + C events from the N + CN distribution.

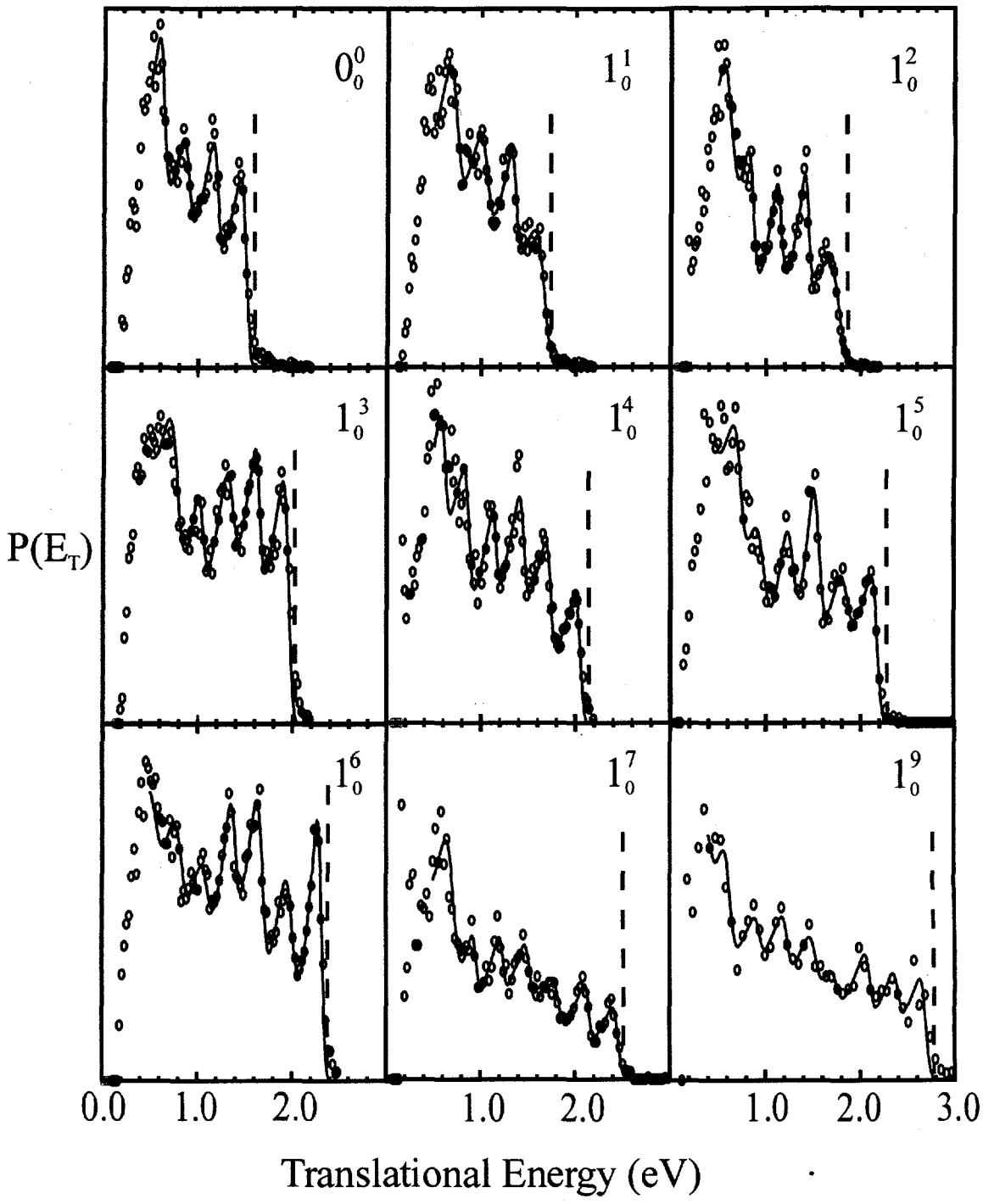

Figure 7. P(E$_T$) distributions for the N$_2$ + C(^{3}P) channel resulting from $\tilde{B}^3\Sigma_u^- \leftarrow \tilde{X}^3\Sigma_g^-$ transitions. The dashed vertical lines denote E_T^{max} for products. Data are shown with open circles, while the results of a fit to the product internal energy distribution are shown with a solid line.

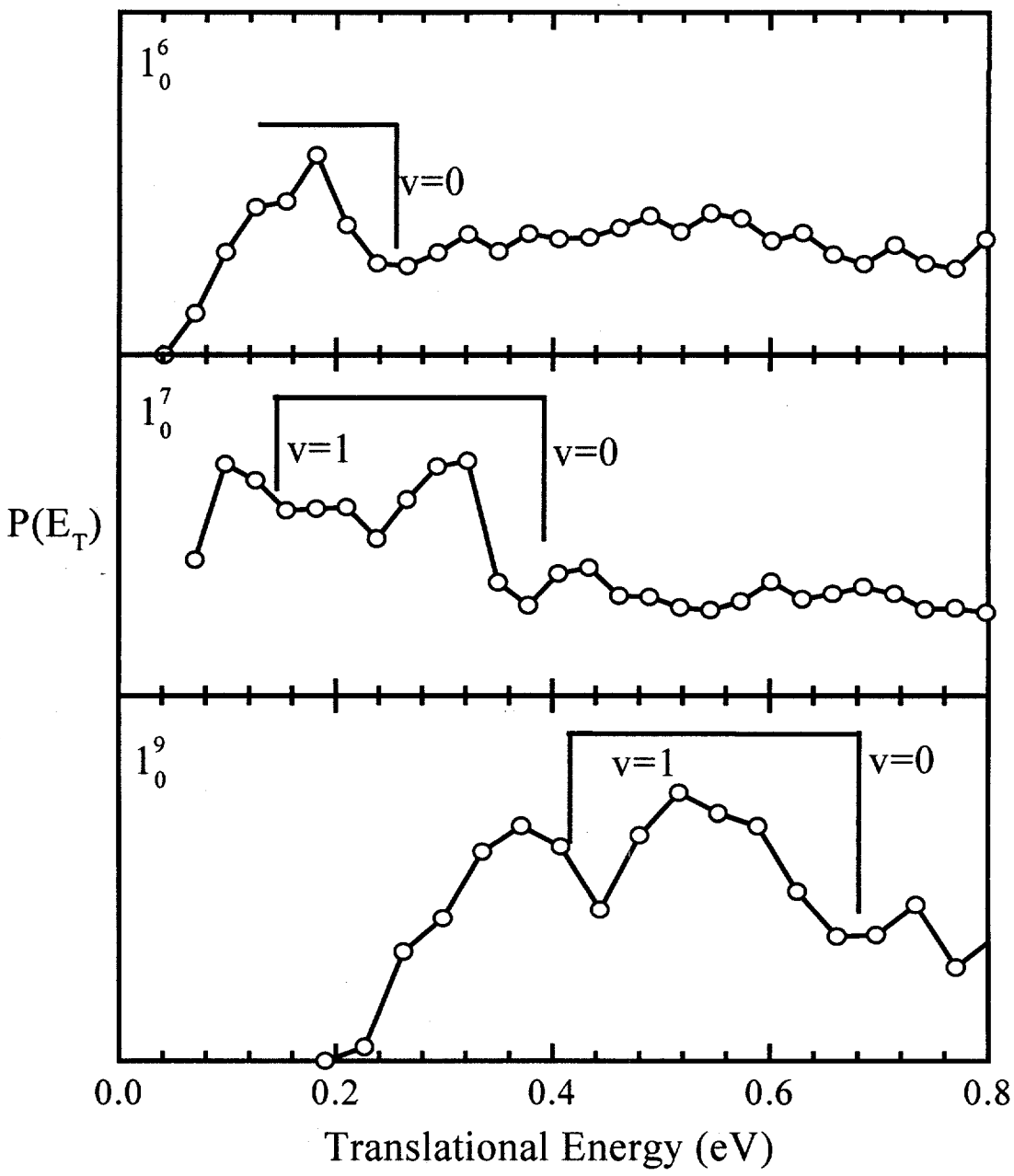

Figure 8. P(E_T) distributions analyzed with a 14:26 mass ratio for the 1_0^6, 1_0^7 and 1_0^9 transitions of the $\tilde{B}^3\Sigma_u^- \leftarrow \tilde{X}^3\Sigma_g^-$ band. The distributions for the 1_0^6 and 1_0^7 transitions were collected using a 2m flight distance between the dissociation laser and the detector while a 1m flight length was used for the 1_0^9 transition. The comb indicates the energetic onset for the CN(v=0) and CN(v=1) product states.

The N + CN photofragments have relatively low recoil energies (< 0.6 eV) and are therefore are preferentially detected over the more energetic N_2 + C products when a 2 m flight distance is used, preventing a precise determination of the branching ratio. By including the relative detector acceptances for the two product channels at both 1 m and 2 m flight lengths, we estimate the relative yield of the CN + N channel for the 1_0^6, 1_0^7 and 1_0^9 transitions to be $\approx 25 \pm 10\%$.

We have also obtained $P(E_T)$ distributions for $\tilde{c}^1\Pi_u \leftarrow \tilde{a}^1\Delta_g$ and $\tilde{d}^1\Delta_u \leftarrow \tilde{a}^1\Delta_g$ transitions. The $P(E_T)$ distribution resulting from the $\tilde{c}^1\Pi_u \leftarrow \tilde{a}^1\Delta_g$ (000-000) transition at a photon energy of 3.725 eV is shown in Figure 9. At this photon energy, the maximum translational energy (E_T^{max}) is 2.19 and 0.93 eV for C(^{3}P) and C(^{1}D) products, respectively. These values are indicated by the dashed vertical lines. The onset for dissociation clearly occurs near 2.19 eV indicating that spin-forbidden triplet products are the primary photodissociation products. The $P(E_T)$ distribution is remarkably similar to the $\tilde{B} \leftarrow \tilde{X}$ transitions, showing resolved structure at high E_T with peak spacing of $\approx$ 290 meV and a FWHM of $\approx$150 meV while the distribution is significantly less structured for $E_T < 0.8$ eV. It is not obvious from the distribution if C(^{1}D) products are present. However, the relative intensities of features with $E_T > 0.9$ eV are similar to those for $E_T <$ 0.9 eV, indicating that the C(^{1}D) products are at best a minor channel; this point is revisited in Section IV.

Excitation of the (010-010) $^1\Delta_g \leftarrow {}^1\Phi_u$ transition yields a $P(E_T)$ distribution (not shown) which is very similar to that observed for the (000-000) transition, in that there is a structured progression of $\approx$ 290 meV for $E_T > 0.8$ eV which becomes less structured for

$E_T < 0.8$ eV. The FWHM of the structured features are ≈ 180 meV, somewhat broader than those for the (000-000) transition. There does not appear to be any significant difference in the $C(^1D):C(^3P)$ product branching ratios for the two transitions.

The $P(E_T)$ distribution for the $\tilde{d}^1\Delta_u \leftarrow \tilde{a}^1\Delta_g$ transition at an excitation energy of 4.646 eV is shown in Figure 10. The singlet-triplet splitting, $E(\tilde{a}^1\Delta_g - \tilde{X}^3\Sigma_g^-)$, is 1.010 ± 0.010 eV. [18] Thus, the total energy of the radical above the ground electronic state after

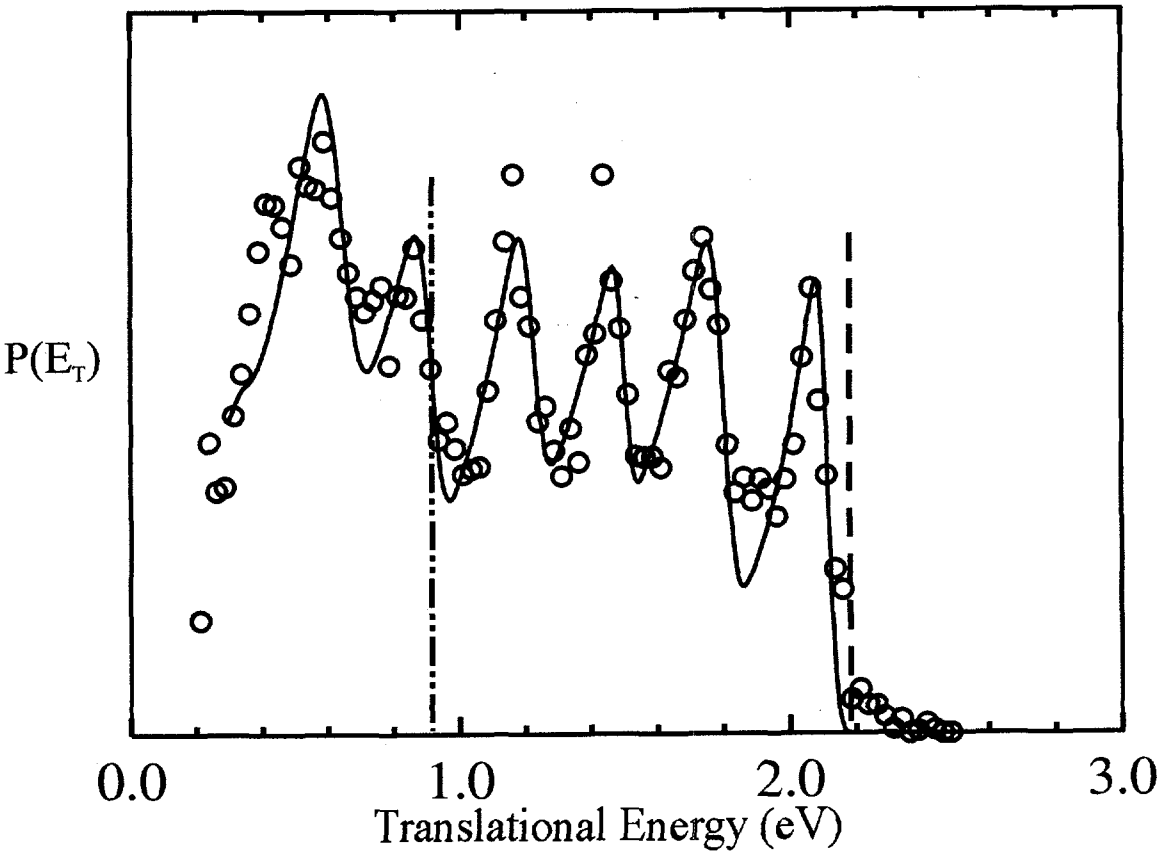

Figure 9. $P(E_T)$ distribution for N_2 + C products from the $\tilde{c}^1\Pi_u \leftarrow \tilde{a}^1\Delta_g$ 000-000 band. The two dashed vertical lines (- - -) and (-- - --) denote E_T^{max} for $C(^3P)$ and $C(^1D)$ products, respectively. Data are shown with open circles, while the results of a fit to the product internal energy distribution are shown with a solid line.

excitation is 5.656 eV with expected E_T^{max} values of 3.12 and 1.86 for $C(^3P)$ and $C(^1D)$ products, respectively. The onset for dissociation occurs near 1.8 eV indicating that the $C(^1D) + N_2$ products are the dominant channel. A small fraction (< 5%) of the total signal appears at translational energies greater than 1.8 eV. This feature is attributed to a hot band absorption from the $\tilde{X}$ state which dissociates to $C(^3P) + N_2$. The general features of the $P(E_T)$ distribution are similar to those for the $\tilde{B} \leftarrow \tilde{X}$ band. The distribution is highly structured with a peak spacing of approximately 290 meV and a

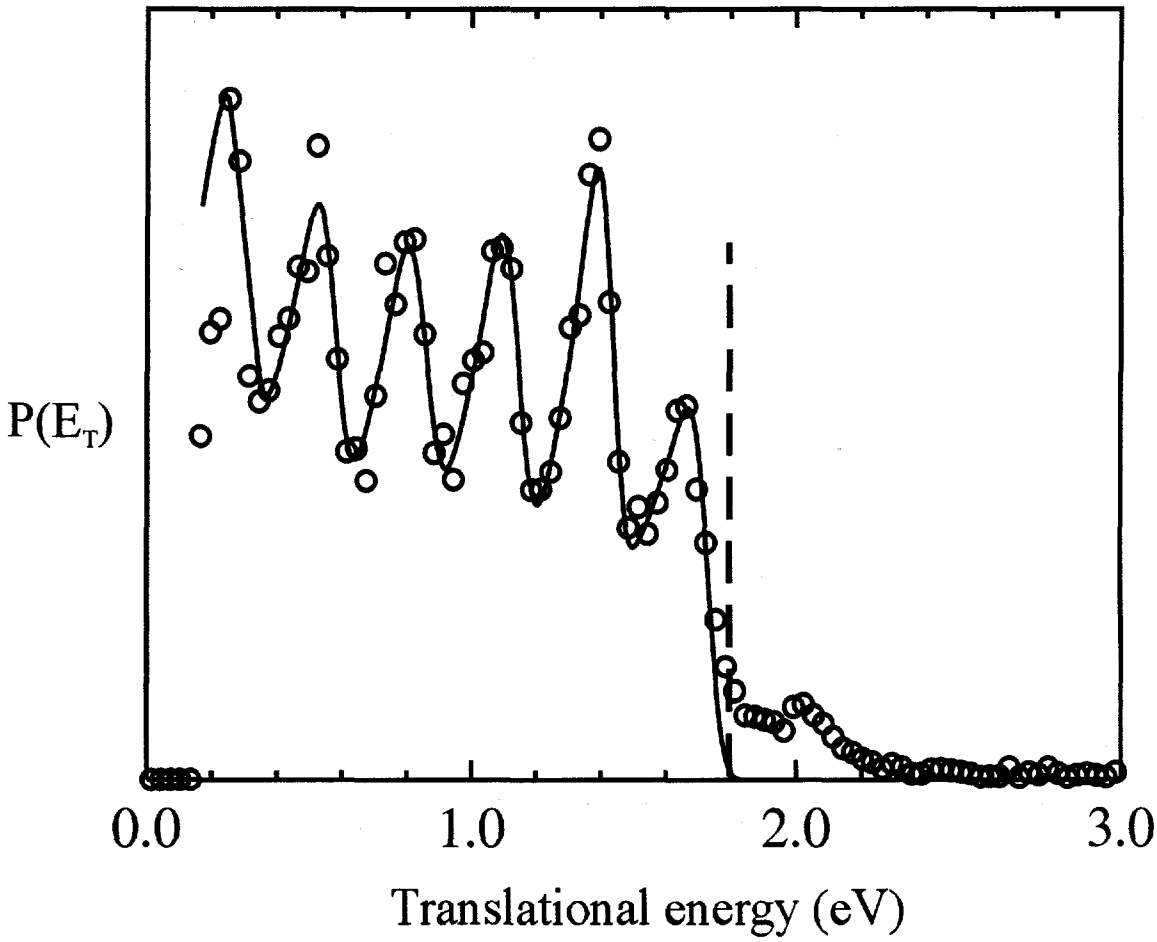

Figure 10. $P(E_T)$ distribution for N_2 + C products from a $\tilde{d}^1\Delta_u \leftarrow \tilde{a}^1\Delta_g$ transition at 37,476 cm^{-1}. Data are shown with open circles, while the results of a fit to the product internal energy distribution are shown with a solid line. The dashed vertical line represents E_T^{max} for $C(^1D)$ products.

FHWM of about 150 meV. However, in contrast to the $P(E_T)$ distributions for the $\tilde{B} \leftarrow \tilde{X}$ and $\tilde{c} \leftarrow \tilde{a}$ transitions, the $P(E_T)$ distribution for the $\tilde{d} \leftarrow \tilde{a}$ transition exhibits resolved structure at translational energies as low as 0.2 eV. It is worth emphasizing here that although the $N(^4S)+CN(X^2\Sigma^+)$ channel is energetically accessible by more than 1 eV, only a 12:28 mass ratio was observed for the photofragments.

The photofragment angular distributions are described by Eq. 1.[41]

$$I(\theta) = 1/(4\pi)[1 + P_2(\cos\theta)] \qquad (1.)$$

The anisotropy parameter, β, can range from +2 to –1, corresponding to $\cos^2\theta$ and $\sin^2\theta$ distributions, respectively. The angular distributions for the N_2 + C product channel for all three electronic transitions were found to be nearly isotropic with $\beta \approx 0$, while the N + CN channel was found to have an anisotropic angular distribution with by $\beta = 0.9$. The positive β parameter is consistent with the expected parallel transition dipole moment for the $\tilde{B}\,^3\Sigma_u^- \leftarrow \tilde{X}\,^3\Sigma_g^-$ band.

IV. Analysis

The $P(E_T)$ distributions in Figures 7-10 demonstrate how the excess energy above the dissociation threshold is distributed between the photofragments. The energy balance for NCN photodissociation to N_2 + C is described by Eq. 2,

$$h\nu + E_{int}(NCN) + E_{elec}(NCN) = D_0(NCN) + E_T + E_v(N_2) + E_R(N_2) + E_{elec}(C) \qquad (2.)$$

where $h\nu$ is the photon energy, $E_{int}(NCN)$ is the average rotational energy of the parent radical, $E_{elec}(NCN)$ is the initial electronic state of the radical, D_0 is the dissociation energy, E_T is the measured translational energy, $E_V(N_2)$ and $E_R(N_2)$ are the N_2 vibrational and rotational energies respectively and $E_{elec}(C)$ is the atomic state of carbon. An

analogous equation can be written for the CN +N channel. The parent rotational temperature of 50 K yields $E_{int}(NCN) \approx 33$ cm^{-1}. $D_0(NCN)$ for the N_2 loss channel can be extracted from these distributions by determining E_T^{max}, the translational energy corresponding to photofragments with zero internal energy.

Although E_T^{max} is not always obvious from a $P(E_T)$ distribution, it can be readily determined from the distributions in Figure 7 from the steep falloff in intensity toward the high energy side marked by the vertical dashed lines for each photon energy. Each $P(E_T)$ distribution then provides an independent measurement of D_0, all of which agree within our experimental resolution of 30 meV. An average of all of these values yields $D_0 = 2.54 \pm 0.03$ eV and $\Delta_f H_0(NCN) = 4.83 \pm 0.03$ eV. The latter agrees with the values of 4.89 ± 0.22 eV and 4.69 ± 0.13 eV from JANAF themochemical tables[42] and recent *ab initio* calculations,[17] respectively, but our error bar is smaller. Contamination of the $P(E_T)$ distributions for the CN+N channel by N_2+C products prevents an exact measurement of E_T^{max} for the CN+N channel directly from the $P(E_T)$ distribution. From our experimentally determined $\Delta H_{f,0\,K}(NCN)$ and literature values for $\Delta_f H_0(CN) = 4.51 \pm 0.02$ eV [43] and $\Delta_f H_0(N(^4S)) = 4.8796 \pm 0.0010$ eV,[42] we calculate $D_0(N\text{-}CN) = 4.56 \pm 0.04$ eV.

The $P(E_T)$ distributions for C + N_2 products and the N + CN products exhibit resolved structure corresponding to the vibrational excitation of the molecular fragment. In an attempt to determine the vibrational distribution of the diatomic fragment, we have fit each $P(E_T)$ distribution to a series of distribution functions f_n separated by the vibronic

energy levels of the diatomic fragment (N_2 or CN)[44] with the total distribution given by Eq. 3:

$$F(E_T) = \sum_{n=0}^{n'} \alpha_n f_n[E_T - (h\upsilon - n\omega_2 - D_0 - \Delta), T, \delta] \qquad (3.)$$

The individual distribution functions, f_n, are gaussians convoluted with a Boltzmann distribution. The offset Δ and rotational temperature T were adjusted to fit the peak and width of each vibrational feature. Attempts to model the $P(E_T)$ distributions with a single rotational temperature for each vibrational product state proved less successful. The $P(E_T)$ distributions for the C + N_2 mass channel of the $\tilde{B}^3\Sigma_u^- \leftarrow \tilde{X}^3\Sigma_g^-$ transition was fit with the $C(^3P)$ products while the $\tilde{c}^1\Pi_u \leftarrow \tilde{a}^1\Delta_g$ transitions were fit with both $C(^3P)$ and $C(^1D)$ products. No substantial improvement to the fit was obtained by including the $C(^1D)$ products. We estimate that the $C(^1D)$ products comprise ≤10% of the total photodissociation signal. The $\tilde{d}^1\Delta_u \leftarrow \tilde{a}^1\Delta_g$ transition was fit using $C(^1D)$ products exclusively.

The vibrational distributions for the $\tilde{B} \leftarrow \tilde{X}$ transitions, Table II., do not reveal any clear trends regarding the extent of vibrational excitation for the N_2 fragment as a function of excitation energy. There also does not appear to be any significant difference in the vibrational distributions resulting from the different NCN excited electronic states. The $P(E_T)$ distributions for the 1_0^7 and 1_0^9 transitions show population of both the v=0 and v=1 states of the CN fragment with an intensity ratio v=0:v=1 of ≈ 3:2.

We have also extracted the rotational distribution of the molecular fragment for each product vibrational state. The offset Δ and rotational temperature T in Eq. 3 are used

Table II. Vibrational distributions of the N_2 and CN photofragments obtained from a fit of the $P(E_T)$ distributions, Figures 7-10, resulting from excitation of $\tilde{B}^3\Sigma_u^- \leftarrow \tilde{X}^3\Sigma_g^-$, $\tilde{d}^1\Delta_u \leftarrow \tilde{a}^1\Delta_g$, and $\tilde{c}^1\Pi_u \leftarrow \tilde{a}^1\Delta_g$ transitions of NCN.

		N_2 vibrational distributions							CN vibrational distributions	
Transition	Photon Energy (eV)	v=0 (%)	v=1 (%)	v=2 (%)	v=3 (%)	v=4 (%)	v=5 (%)	v=6 (%)	v=0 (%)	v=1 (%)
$\tilde{B}^3\Sigma_u^- \leftarrow \tilde{X}^3\Sigma_g^-$										
0_0^0	4.153	22	22	26	30					
1_0^1	4.283	22	19	31	28					
1_0^2	4.414	22	13	13	30	12				
1_0^3	4.542	26	20	12	12	24	6			
1_0^4	4.670	11	17	12	12	33	15			
1_0^5	4.790	15	9	9	9	24	32			
1_0^6	4.927	15	11	16	10	17	18	12	100	---
1_0^7	5.049	9	10	14	12	12	13	30	60	40
1_0^9	5.299	14	12	14	9	19	17	15	60	40
$\tilde{d}^1\Delta_u \leftarrow \tilde{a}^1\Delta_g$										
?	4.646	18	16	17	14	21	14			
$\tilde{c}^1\Pi_u \leftarrow \tilde{a}^1\Delta_g$										
0_0^0	3.725	17	19	17	10	22	15			
2_1^1	3.735	13	12	19	17	19	20			

to determine N_{peak}, the rotational quantum number corresponding to the peak of each distribution, f_n. A unique N_{peak} value for each N_2 product vibrational state is then obtained for every $P(E_T)$ distribution. The $P(E_T)$ distributions for the $1_0^n\ \widetilde{B} \leftarrow \widetilde{X}$ transitions yield very similar N_{peak} values (± 3 quanta) for the same N_2 product vibrational state (i.e. N_{peak} is independent of n). However, the N_{peak} values exhibit a pronounced dependence on the vibrational quantum number of the N_2 fragment.

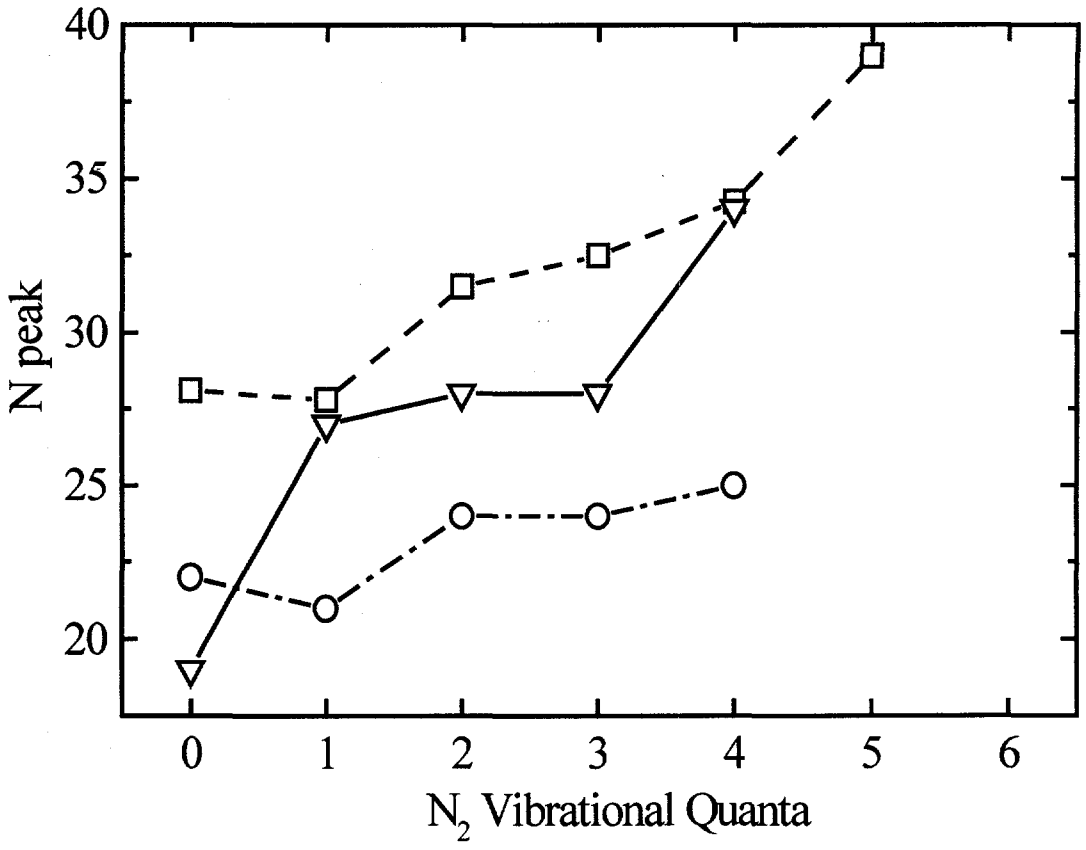

Figure 11. The average N_{peak} values for all the $1_0^n\ \widetilde{B} \leftarrow \widetilde{X}$ transitions in Fig. 7 (squares), as well as the N_{peak} values for the $\widetilde{c}^1\Pi_u \leftarrow \widetilde{a}^1\Delta_g$ origin (triangles) and $\widetilde{d}^1\Delta_u \leftarrow \widetilde{a}^1\Delta_g$ origin (circles) transitions are plotted versus the N_2 vibrational quantum number.

In Figure 11, the average N_{peak} values for the 1_0^n $\tilde{B} \leftarrow \tilde{X}$ transitions each N_2 product state are plotted versus the N_2 vibrational quantum number; the N_{peak} values for the $\tilde{c}^1\Pi_u \leftarrow \tilde{a}^1\Delta_g$ (000-000) and $\tilde{d}^1\Delta_u \leftarrow \tilde{a}^1\Delta_g$ transitions are also shown. For all three transitions, the N_2 fragment displays substantial rotational excitation with distributions peaking between 20-40 quanta of rotation depending on the vibrational quantum number of the fragment and the initial electronic transition. The N_{peak} values for the $\tilde{B}^3\Sigma_u^-$ and $\tilde{c}^1\Pi_u$ states increase substantially for higher vibrational states of the N_2 fragment, while the N_{peak} values for the $\tilde{d}^1\Delta_u$ state are generally lower than for the other two states and vary much less with N_2 vibrational state. The CN photofragment was found to have a rotational distribution described by a Boltzmann temperature of 700 K, with $N_{peak} \approx 10$.

V. Discussion

The product state energy distributions for the fragmentation of NCN reveal that complicated dynamics are involved in the dissociation of this triatomic radical. The $\tilde{B}\ ^3\Sigma_u^-$ state yields $N_2 + C(^3P)$ products at all photon energies explored. At photon energies greater than 4.9 eV, the $\tilde{B}\ ^3\Sigma_u^-$ state also produces $CN(X\ ^2\Sigma^+) + N(^4S)$ products as a minor channel $\approx 25 \pm 10$ %. $C(^3P)$ products are the dominant dissociation channel ($\geq 90\%$) for the $\tilde{c}^1\Pi_u$ state even though $C(^1D)$ products are energetically available by more than 0.9 eV, while the $\tilde{d}^1\Delta_u$ state dissociates to $C(^1D)$ products exclusively. The $\tilde{B}\ ^3\Sigma_u^-$ and $\tilde{c}^1\Pi_u$ states possess very similar $P(E_T)$ distributions with well resolved vibrational features for $E_T > 0.8$ eV and broad unresolved structure at lower translational

energies. The $\tilde{d}^1\Delta_u$ state in comparison exhibits resolved vibrational structure for translational energies as low as 0.2 eV. Finally, the CN fragment is produced with substantially less rotational excitation (N_{peak} = 10) than the N_2 photofragment (N_{peak} = 20-40), implying that the mechanisms for these two dissociation channel are distinct.

The ground and all excited electronic states accessed in this study are linear, but the dominance of C + N_2 photoproducts indicates that the photodissociation mechanism must involve cyclic and/or bent states. The extensive vibrational and rotational excitation of the N_2 product are also consistent with dissociation through a bent or cyclic state with the N-N bond forming and C-N bonds breaking at large N-N distances leading to an extended vibrational progression in the N_2 photoproduct. Rotational excitation of the N_2 fragment is generated from parent molecular rotation and from the torque applied at the transition state. The trend of increasing rotational excitation with N_2 vibrational quantum number for the $\tilde{B}\ ^3\Sigma_u^-$ and $\tilde{c}\ ^1\Pi_u$ states is similar to that seen by Continetti *et al.*[32] for the photodissociation of N_3 and by Zare and coworkers[45] for the photodissociation of ICN.

Formation of product from the two end atoms of a triatomic, particularly a linear one, is relatively uncommon as it requires a low energy cyclic (or at least strongly bent) transition state. Such a transition state has been proposed in the photodecomposition of OClO which yields the lowest energy products, O_2 + Cl, as a minor channel (≤ 4%).[46-48] The largest relative yields of this channel result from excitation of the bend and symmetric stretch modes, implying a concerted dissociation involving a transition state of approximately C_{2v} symmetry. *Ab initio* calculations[49-53] for O_3 have located minima for ring structures of D_{3h} symmetry, however, the poor Franck-Condon overlap with the ground state and a large barrier to dissociation via C_{2v} symmetry suggests that this

pathway does not contribute. The dissociative ionization of CS_2 yields S_2^+ as minor channel (< 9 %) from the decay of the linear excited states of CS_2^+.[54,55] The translational energy distributions of the S_2^+ ion[56] are structureless single peaks with only 10-26% of the available energy projected into translation indicating extensive vibrational and rotational excitation of the S_2^+ fragment, consistent with a dissociation pathway involving a cyclic intermediate.

Martin *et al.*[24] have performed ab initio calculations for linear, bent and cyclic structures for NCN and CNN. Their calculations within the C_{2v} point group have located a local minimum with $^3A_2$ symmetry and a transition state with $^3B_1$ symmetry at 3.01 and 4.76 eV, respectively, above the linear ground state of NCN. As shown in Figure 1, the $\tilde{X}\ ^3\Sigma_g^-$ state adiabatically correlates to the $^3B_1$ state while the $\tilde{B}\ ^3\Sigma_u^-$ state correlates to the lower lying $^3A_2$ state. Both the $^3A_2$ and $^3B_1$ states correlate to ground state products in C_{2v} symmetry. The $\tilde{A}\ ^3\Pi_u$ state correlates with higher energy states of either $^3A_1$ or $^3B_1$ symmetry. If we assume that the dissociation proceeds via C_{2v} symmetry, then the $\tilde{A}\ ^3\Pi_u$ state cannot dissociate since it does not correlate to the lower energy $^3A_2$ state and does not have enough energy to access the $^3B_1$ state. On the other hand, the $\tilde{B}\ ^3\Sigma_u^-$ state has a relatively low energy pathway through a cyclic transition state to $C(^3P) + N_2$ products. This simple picture therefore explains why only the $\tilde{B}\ ^3\Sigma_u^-$ state dissociates, even though both states lie above the $C + N_2$ asymptote.

Martin *et al.* also found a less symmetric $^3A''$ (C_s) transition state through uphill following of the bending mode of CNN. This state lies slightly lower in energy than the

$\tilde{A}\,^3\Pi_u$ state, but the absence of $\tilde{A}\,^3\Pi_u$ state dissociation suggests that this transition state does not play a role in the dissociation dynamics.

We next consider the dissociation mechanism of the $\tilde{c}\,^1\Pi_u$ state. Martin *et al.* report only one singlet minimum energy structure with symmetry $^1A_1$ located 1.57 eV above the ground state, which correlates adiabatically with the $\tilde{c}\,^1\Pi_u$ state. However, since spin-forbidden C(^{3}P) products are clearly the dominant dissociation channel from the $\tilde{c}\,^1\Pi_u$ state, it is unlikely that this structure is involved in the dissociation mechanism . The C(^{3}P):C(^{1}D) branching ratio does not appear to change significantly for the (010-010) $^1\Delta_g \leftarrow {}^1\Phi_u$ transition suggesting that this upper state is also not strongly coupled to the $^1A_1$ state.

The formation of C(^{3}P) products from the $\tilde{c}\,^1\Pi_u$ state clearly indicates that the dissociation mechanism involves intersystem crossing to a triplet surface. The P(E_T) distributions for the $\tilde{B}\,^3\Sigma_u^-$ and $\tilde{c}\,^1\Pi_u$ states are noticeably similar with both displaying an increase in rotational excitation with increased vibrational excitation. The $\tilde{c}\,^1\Pi_u$ state has been rotationally resolved by Kroto[7] with an instrument resolution of 0.1 cm^{-1} and appears to be instrument limited, indicating that the lifetime of the $\tilde{c}\,^1\Pi_u$ state is > 50 ps. The long lifetime, spin-forbidden products, and P(E_T) distribution suggest that the $\tilde{c}\,^1\Pi_u$ state first intersystem crosses to the $\tilde{B}\,^3\Sigma_u^-$ state prior to dissociation.

The $\tilde{d}\,^1\Delta_u$ state, in contrast to the $\tilde{c}\,^1\Pi_u$ state, leads to spin-allowed C(^{1}D) dissociation products. Although the N(^{4}S) + CN($X\,^2\Sigma^+$) products are energetically accessible by 1.18 eV, these spin-forbidden products are not observed. The P(E_T)

distribution which results from excitation to the $\tilde{d}\,^1\Delta_u$ state, Figure 8, exhibits an extended vibrational progression of the N_2 photofragment. However, Figure 11 shows that the degree of N_2 rotational excitation is lower for $\tilde{d}\,^1\Delta_u$ dissociation than for $\tilde{B}\,^3\Sigma_u^-$ or $\tilde{c}\,^1\Pi_u$ state dissociation. In addition, the rotational excitation of the N_2 fragment is approximately the same for all N_2 vibrational states, in contrast to the $\tilde{B}\,^3\Sigma_u^-$ and $\tilde{c}\,^1\Pi_u$ states. It therefore appears that the triplet and singlet surfaces have different topologies.

In NCN predissociation, the N_2 rotational distribution is determined largely by the energy and geometry of the transition state, and by the torque exerted on the N_2 in the exit channel. The lower rotational excitation for $C(^1D) + N_2$ products can therefore be attributed to a number of factors. The experiments of Milligan and Jacox[11] indicate that that $C(^1D)$ atoms react readily in a nitrogen matrix to form NCN while $C(^3P)$ atoms do not, implying that the $C(^1D)$ dissociation products do not have a barrier to recombination, while a substantial barrier exists for the triplet channel. This is consistent with the extensive work on reactions of atomic oxygen, in which $O(^1D)$ but not $O(^3P)$ is known to undergo a variety of insertion reactions with no barrier.[57] However, one must be careful in applying these considerations to our experiment, because recombination presumably occurs on the lowest energy singlet or triplet surface of NCN whereas the dissociation dynamics in our experiment are launched from an electronically excited state.

While the dominant photodissociation products observed in this study are $N_2 + C$, the CN + N channel is observed from the $\tilde{B}\,^3\Sigma_u^-$ state at photon energies > 4.9 eV. Both the CN(v=0) and vibrationally excited CN(v=1) products are observed, consistent with an expected large change in CN bond distance from the $\tilde{B}\,^3\Sigma_u^-$ state of the NCN radical to

the CN($X\,^2\Sigma^+$) fragment. The rotational distribution peaks at N=10, a value less than half that observed for the N_2 loss channels. The limited rotational excitation and positive photofragment anisotropy, β=0.9, are consistent with a linear dissociation pathway. Freysinger et al.[58] have examined the diabatic and adiabatic electronic correlations for the linear states of isoelectronic N_3^+ ion into products $N^+ + N_2$ and $N_2^+ + N$,[58] which are isoelectronic with the $C + N_2$ and N + CN products observed in this study. The $\tilde{B}\,^3\Sigma_u^-$ state correlates adiabatically to $N(^4S)$ + CN($X\,^2\Sigma^+$) and correlates diabatically to the higher energy products $N(^2D)$ + CN($A\,^2\Pi$), while the $N(^4S)$ + CN($X\,^2\Sigma^+$) products correlate diabatically to a higher-lying $^3\Sigma_u^-$ state. The crossing of these two diabatic surfaces will likely produce a conical intersection leading to a barrier to dissociation along the adiabatic surface. The CN + N channel is first observed at photon energies which exceed D_0(N-CN) by more than 0.39 eV, providing an upper limit for the barrier height.

It is surprising that the CN+N channel, which appears to dissociate via a linear pathway, does not become the dominant channel once it is energetically accessible, comprising only 25 ± 10% of the total dissociation signal. The dominance of the N_2 + $C(^3P)$ channel is further proof that the coupling of the $\tilde{B}\,^3\Sigma_u^-$ state to bent or cyclic states is highly efficient.

VI. Conclusions

The photodissociation dynamics of the $\tilde{B}\,^3\Sigma_u^-$, $\tilde{c}\,^1\Pi_u$, and $\tilde{d}\,^1\Delta_u$ states of NCN radical have been investigated by fast beam photofragment spectroscopy. Both the

$\widetilde{B}\ ^3\Sigma_u^-$ and $\widetilde{c}\ ^1\Pi_u$ states photodissociate to ground state products N_2 + C(^{3}P) while the $\widetilde{d}\ ^1\Delta_u$ state dissociates to N_2 + C(^{1}D). Based on the identity of the products, one expects dissociation to occur through a cyclic or strongly bent transition state; this is consistent with the extensive vibrational and rotational excitation of the N_2 photoproduct from all three states. For the $\widetilde{B}\ ^3\Sigma_u^-$ and $\widetilde{c}\ ^1\Pi_u$ states, the rotational excitation appears to increase with vibrational excitation. The similarity in the $P(E_T)$ distributions and the production of the same photoproducts for the $\widetilde{B}\ ^3\Sigma_u^-$ and $\widetilde{c}\ ^1\Pi_u$ states suggest that the two states dissociate along the same surface, requiring that the $\widetilde{c}\ ^1\Pi_u$ state undergoes intersystem crossing to the $\widetilde{B}\ ^3\Sigma_u^-$ state prior to dissociation.

Finally, the CN+N product channel was observed from the $\widetilde{B}\ ^3\Sigma_u^-$ state for photon energies greater than 4.9 eV comprising $\approx 25 \pm 10\%$ of the total dissociation signal. The rotational distribution and anisotropic angular distribution, β=0.9, suggests that these photoproducts are formed via a linear dissociation pathway.

Acknowledgements

This research is supported by the Director, Office of Energy and Research, Office of Basic Energy Sciences, Chemical Sciences Division, of the U.S. Department of Energy under Contract No. DE-AC03-76F00098. We would like to thank Alexandra Hoops for assistance in data collection.

References

[1] L. J. Butler and D. M. Neumark, J. Phys. Chem. **100,** 12801 (1996).

[2] K. R. Jennings and J. W. Linnett, Trans. Faraday Soc. **56,** 1737 (1960).

[3] G. P. Smith, R. A. Copeland, and D. R. Crosley, J. Chem. Phys. **91,** 1987 (1989).

[4] C. R. O'Dell, C. O. Miller, A. L. Cochran, W. D. Cochran, C. B. Opal, and E. S. Barker, Astrophys. J..**368,** 616 (1991).

[5] A. D. Walsh, J. Chem. Soc. , 2266 (1953).

[6] G. Herzberg and D. N. Travis, Can. J. Phys. **42,** 1658 (1964).

[7] H. W. Kroto, Can. J. Phys. **45,** 1439 (1967).

[8] H. W. Kroto, J. Chem. Phys. **44,** 831 (1966).

[9] H. W. Kroto, T. F. Morgan, and H. H. Sheena, Trans. Faraday Soc. **66,** 2237 (1970).

[10] D. E. Milligan, M. E. Jacox, and A. M. Bass, J. Chem. Phys. **43,** 3149 (1965).

[11] D. E. Milligan and M. E. Jacox, J. Chem. Phys. **45,** 1387 (1966).

[12] D. McNaughton, G. F. Metha, and R. Tay, Chem. Phys. **198,** 107 (1995).

[13] S. A. Beaton, Y. Ito, and J. M. Brown, J. Mol. Spec. **178,** 99 (1996).

[14] S. A. Beaton and J. M. Brown, J. Mol. Spec. **183,** 347 (1997).

[15] K. D. Hensel and J. M. Brown, J. Mol. Spec. **180,** 170 (1996).

[16] M. Wienkoop, W. Urban, and J. M. Brown, J. Mol. Spec. **185,** 185 (1997).

[17] E. P. Clifford, P. G. Wenthold, W. C. Lineberger, G. A. Petersson, and G. B. Ellison, J. Phys. Chem. A **101,** 4338 (1997).

[18] T. R. Taylor, R. T. Bise, K. R. Asmis, and D. M. Neumark, Chem. Phys. Lett. **301,** 413 (1999).

[19] Z. L. Cai, G. H. Sha, C. H. Zhang, and M. B. Huang, Theochem **85,** 303 (1992).

[20] G. Berthier and L. Kurdi, C.R. Acad. Sci., Paris, Ser. II (Mec., Phys., Chim., Sci. Univers, Sci. Terre) **299,** 1171 (1984).

[21] H. U. Suter, M. B. Huang, and B. Engels, J. Chem. Phys. **101,** 7686 (1994).

[22] C. Thomson, J. Chem. Phys. **58,** 841.

[23] G. R. Williams, Chem. Phys. Lett. **25,** 602 (1974).

[24] J. M. L. Martin, P. R. Taylor, J. P. Francois, and R. Gijbels, Chem. Phys. Lett. **226,** 475 (1994).

[25] V. E. Bondybey and J. H. English, J. Chem. Phys. **67,** 664 (1977).

[26] M. E. Jacox, J. Mol. Spec. **72,** 26 (1978).

[27] T. D. Goldfarb and G. C. Pimentel, J. Am. Chem. Soc. **82,** 1865 (1959).

[28] M. C. Curtis, A. P. Levick, and P. J. Sarre, Laser Chem. **9,** 359 (1988).

[29] G. W. Robinson and M. McCarty Jr., J. Am. Chem. Soc. **82,** 1859 (1960).

[30] E. Wasserman, L. Barash, and W. A. Yager, J. Am. Chem. Soc. **87,** 2075 (1965).

[31] H. Choi, D. H. Mordaunt, R. T. Bise, T. R. Taylor, and D. M. Neumark , J. Chem. Phys. **108,** 4070 (1998).

[32] R. E. Continetti, D. R. Cyr, D. L. Osborn, D. J. Leahy, and D. M. Neumark, J. Chem. Phys. **99,** 2616 (1993).

[33] D. J. Leahy, D. L. Osborn, D. R. Cyr, and D. M. Neumark, J. Chem. Phys. **103,** 2495 (1995).

[34] D. L. Osborn, H. Choi, D. H. Mordaunt, R. T. Bise, D. M. Neumark, and C. M. Rohlfing, J. Chem. Phys. **106,** 3049 (1997).

[35] D. L. Osborn, D. J. Leahy, D. R. Cyr, and D. M. Neumark, J. Chem. Phys. **104,** 5026 (1996).

[36] J. M. B. Bakker, J. Phys. E **6,** 785 (1973).

[37] J. M. B. Bakker, J. Phys. E **7,** 364 (1974).

[38] D. P. de Bruijn and J. Los, Rev. Sci. Instrum. **53,** 1020 (1982).

[39] R. E. Continetti, D. R. Cyr, D. L. Osborn, D. J. Leahy, and D. M. Neumark, J. Chem. Phys **99,** 2616 (1993).

[40] This gas phase value for ν'' is determined from $\nu' = 1254\ cm^{-1}$ (Ref. 3.) and $\nu'-\nu'' = -5\ cm^{-1}$ (Ref. 6).

[41] R. N. Zare, Mol. Photochem. **4,** 1 (1972).

[42] M. W. Chase, Jr., C. A. Davies, J. R. Downey, Jr., D. J. Frurip, R. A. McDonald, and A. N. Syverud, J. Phys. Chem. Ref. Data Suppl. 1, **14** (1985).

[43] Y. Huang, S. A. Barts, and J. B. Halpern, J. Phys. Chem. **96,** 425 (1992).

[44] K. P. Huber and G. Herzberg, *Constants of Diatomic Molecules* (Van Nostrand Reinhold, New York, 1979).

[45] M. A. O' Halloran, H. Joswig, and R. N. Zare, J. Chem. Phys. **87,** 303 (1987).

[46] H. F. Davis and Y. T. Lee, J. Phys. Chem. **96,** 5681 (1992).

[47] E. Bishenden and D. J. Donaldson, J. Chem. Phys **99,** 3129 (1993).

[48] E. Bishenden and D. J. Donaldson, J. Chem. Phys **101,** 9565 (1994).

[49] S. Xantheas, G. J. Atchity, S. T. Elbert, and K. Ruedenberg, J. Chem. Phys **94,** 8054 (1991).

[50] S. Xantheas, S. T. Elbert, and K. Ruedenberg, J. Chem. Phys **93,** 7519 (1990).

[51] T. Muller, S. S. Xantheas, H. Daschel, R. J. Harrison, N. Jaroslaw, R. Shepard, G. S. Kedziora, and H. Lischa, Chem. Phys. Lett. **293,** 72 (1998).

[52] A. Banichevich and S. D. Peyerimhoff, Chem. Phys. , 93 (1993).

[53] M. Braunstein, P. J. Hay, R. L. Martin, and R. T. Pack, J. Chem. Phys **95,** 8239 (1991).

[54] B. Brehm, J. H. D. Eland, R. Frey, and A. Kustler, Int. J. Mass Spectrom. Ion Phys. **12,** 212 (1973).

[55] J. H. D. Eland and J. Berkowitz, J. Chem. Phys **70,** 5151 (1979).

[56] M. Hamdan, F. M. Harris, and J. H. Beynon, Int. J. Mass Spectrom. Ion. Processes **74,** 303 (1986).

[57] M. Alagia, N. Balucani, P. Casavecchia, D. Stranges, and G. G. Volpi, J. Chem. Soc., Faraday Trans. **91,** 575 (1995).

[58] W. Freysinger, F. A. Khan, P. B. Armentrout, P. Tosi, O. Dmitriev, and D. Bassi, J. Chem. Phys. **101,** 3688 (1994).

Chapter 4. Photodissociation dynamics of the CNN free radical[†]

The spectroscopy and photodissociation dynamics of the $\tilde{A}^3\Pi$ and $\tilde{B}^3\Sigma^-$ states of the CNN radical have been investigated by fast beam photofragment translational spectroscopy. Vibronic transitions located more than 1000 cm^{-1} above the $\tilde{A}^3\Pi \leftarrow \tilde{X}^3\Sigma^-$ origin were found to predissociate. Photofragment yield spectra for the $\tilde{B}^3\Sigma^- \leftarrow \tilde{X}^3\Sigma^-$ band between 40800 and 45460 cm^{-1} display resolved vibrational progressions with peak spacing of $\approx$ 1000 cm^{-1} corresponding to symmetric stretch 1_0^n and combination band $1_0^n 3_0^1$ progressions. Ground state products $C(^3P) + N_2$ were found to be the major photodissociation channel for both the $\tilde{A}^3\Pi$ and $\tilde{B}^3\Sigma^-$ states. The translational energy distributions for the $\tilde{A}^3\Pi$ state are bimodal with high and low translational energy components. The distributions for the $\tilde{B}^3\Sigma^-$ state reveal partially resolved vibrational structure for the N_2 photofragment and indicate extensive vibrational and rotational excitation of this fragment. These results suggest that bent geometries are involved in the dissociation mechanism and provide more accurate values: $\Delta_f H_0(CNN) = 6.16 \pm 0.05$ eV and $\Delta_f H_{298}(CNN) = 6.15 \pm 0.05$ eV. These values, coupled with recent $D_0(RH)$ and $D_{298}(RH)$ values from Clifford et al.[J. Phys. Chem. **102**. 7100 (1998)], yield: $\Delta_f H_0(HCNN) = 5.02 \pm 0.18$ eV, $\Delta_f H_{298}(HCNN) = 4.98 \pm 0.18$ eV, $\Delta_f H_0(H_2CNN) = 3.09 \pm 0.21$ eV and $\Delta_f H_{298}(H_2CNN) = 3.03 \pm 0.21$ eV.

[†] In press, J. Chem. Phys. (2000).

I. Introduction

The CNN free radical is a potentially important combustion intermediate. It has been proposed as an intermediate in the mechanism for the formation of transient NO in the primary reaction zone of premixed flames of hydrocarbons with N_2-O_2 mixtures,[1] because it can provide a low energy pathway for the cleavage of N_2 to produce N atoms through the reaction $C+N_2 \rightarrow N+CN$. The resulting N atoms are rapidly oxidized to nitric oxide. To assess the importance of the CNN radical in combustion processes, accurate values for the dissociation energy, heat of formation and a better understanding of the $C + N_2$ potential energy surface is required. In order to address these issues, we have investigated the photodissociation spectroscopy and dynamics of CNN.

The CNN radical, like other 14 valence electron systems, has attracted interest from both experimentalists and theorists regarding its bonding and geometry. The majority of the spectroscopic studies of this radical have been performed in rare gas matrices. Electron spin resonance experiments[2,3] determined that the ground state symmetry is $^3\Sigma^-$. The first infrared absorption measurements on CNN revealed transitions at 1241, 393 and 2847 cm^{-1} which were assigned to fundamentals ν_1(symmetric stretch), ν_2(bend), and ν_3(asymmetric stretch) respectively.[4,5] More recent Fourier transform/laser induced fluorescence (FT-LIF) emission studies in an Ar matrix[6] found the ground state asymmetric stretch (ν_3) to be 1419 cm^{-1}, suggesting that the intensity of the infrared fundamental transition is "accidentally" zero and that the transition observed at 2847 cm^{-1} in previous work is the ν_3 overtone. This new value for

the "asymmetric stretch" led to similar force constants for the C-N and N-N bonds, indicating that both are double bonds.

A number of excited electronic states of CNN have also been observed in matrix ultraviolet absorption and emission studies. UV absorption bands near 23,870 and 25,250 cm^{-1} in a number of different rare gas matrices have been reported and have been subsequently assigned to the CNN radical.[4,7-10] Bondybey and English[11] have observed analogous bands in their LIF studies in an Ar matrix, assigning the transitions to the $\tilde{A}^3\Pi \leftarrow \tilde{X}^3\Sigma^-$ band. These authors reported values for the spin-orbit splitting, Renner-Teller parameter, and vibrational frequencies for the $\tilde{A}^3\Pi$ state. Higher energy absorption bands were observed by Jacox.[12] One band between 40000-47000 cm^{-1}, assigned to the $\tilde{B}^3\Sigma^- \leftarrow \tilde{X}^3\Sigma^-$ transition, displayed two main progressions with peak spacing of $\approx$ 1000 cm^{-1} while absorptions at 49116 and 48543 cm^{-1} in N_2 and Ar matrices, respectively, were associated with a different electronic transition. Gas-phase optical spectroscopic data for CNN is limited to low resolution UV absorption studies by Braun *et al.*,[13] who observed transitions at 23870 and 25190 cm^{-1}, and a rotationally resolved LIF spectrum of the $\tilde{A}^3\Pi \leftarrow \tilde{X}^3\Sigma^-$ origin by Curtis *et al.*,[14] yielding a gas-phase spin-orbit splitting, A = -26.5 cm^{-1}. Additionally, these authors reported a sequence band $\approx$ 145 cm^{-1} above the origin.

Recently, the gas-phase photoelectron spectrum of the CNN^- anion was measured by Clifford *et al.*[15] providing the electron affinity of CNN, 1.771 $\pm$ 0.010 eV, as well as the ground state neutral frequencies. Their experimental values for proton affinities and

electron affinities for CNN^- and $HCNN^-$ yield $\Delta_f H_0(CNN) = 5.9 \pm 0.2$ eV, which is well within the error bars for the previously reported value of 6.6 ± 1.0 eV by Gurvich.[16]

The electronic structure of CNN has been investigated in numerous theoretical studies. According to Walsh's rules,[17] all of the relevant electronic states for this 14 valence electron system, shown in Figure 1, are predicted to be linear with the dominant molecular orbital configurations shown below.

$...(6\sigma)^2(1\pi)^4(7\sigma)^2(2\pi)^2$ $\quad\quad$ $\tilde{X}^3\Sigma^-, \tilde{a}^1\Delta, \tilde{b}^1\Sigma^+$

$...(6\sigma)^2(1\pi)^4(7\sigma)^1(2\pi)^3$ $\quad\quad$ $\tilde{A}^3\Pi, {}^1\Pi$

$...(6\sigma)^2(1\pi)^3(7\sigma)^2(2\pi)^3$ $\quad\quad$ $\tilde{B}^3\Sigma^-$

$...(6\sigma)^1(1\pi)^4(7\sigma)^2(2\pi)^3$ $\quad\quad$ $^3\Pi$

DeKock *et al.*[5] examined the infrared frequencies, finding the geometry and force constants to be highly dependent on the theoretical method employed and were not able to produce the experimental values observed by Milligan and Jacox. More recent *ab initio* calculations by Suter *et al.*[18] yielded ground state vibrational frequencies in good agreement with the newer experimental values.[6] Configuration interaction methods were used to examine the $\tilde{X}^3\Sigma^-$, $\tilde{a}^1\Delta$, $\tilde{A}^3\Pi$, and $^1\Pi$ states,[19] yielding a calculated fluorescence lifetime value for the $\tilde{A}^3\Pi$ state of 216 ns in good agreement with the reported experimental lifetimes of 220 and 280 ns from matrix LIF emission studies.[11,19] Clifford *et al.*[15] have used *ab initio* methods to calculate the electron affinity, excited state term energies and ground state vibrational frequencies for the CNN radical. Their results compare favorably with their experimental photoelectron spectroscopy measurements. Martin *et al.*[20] have performed *ab initio* calculations on the linear, bent

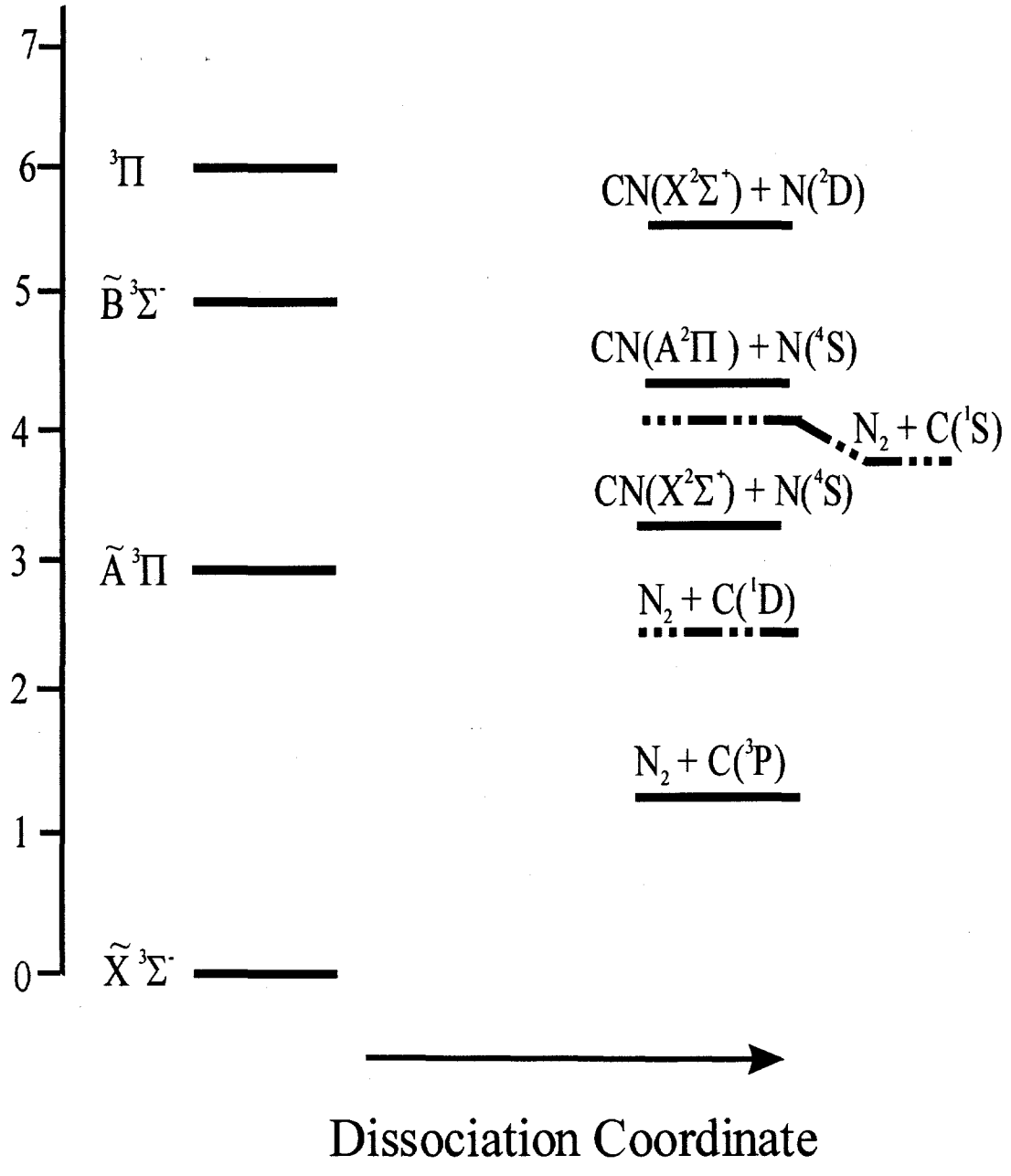

Figure 1. Energy level diagram of the excited triplet states of CNN and dissociation product states. The relative energetic position of the $\tilde{A}^3\Pi$ state is based on the work of Curtis *et al.*[14] and the $\tilde{B}^3\Sigma^-$ and $\tilde{C}^3\Pi$ states are from the studies by Jacox.[12] The dissociation energies have been determined from this work.

and cyclic states of NCN and CNN examining possible intermediates and pathways towards isomerization.

Our interest in the CNN radical has been further motivated by our recent study of the dissociation dynamics of the structural isomer NCN,[21] which dissociates to products $N_2 + C(^3P)$ via a cyclic transition state. The work presented here on the photodissociation dynamics of the CNN radical further characterizes the global potential energy surface for CN_2 species. Using the technique of fast beam photofragment translational spectroscopy, we have examined the photodissociation spectroscopy and dynamics of the $\tilde{A}^3\Pi \leftarrow \tilde{X}^3\Sigma^-$ and $\tilde{B}^3\Sigma^- \leftarrow \tilde{X}^3\Sigma^-$ bands of CNN. Vibrational levels of the $\tilde{A}^3\Pi$ state lying > 1000 cm^{-1} above the origin predissociate to photoproducts $C(^3P) + N_2$. Extended progressions of the $\tilde{B}^3\Sigma^- \leftarrow \tilde{X}^3\Sigma^-$ band are observed between 40820-45450 cm^{-1}. Translational energy ($P(E_T)$) distributions show $C + N_2$ as the dominant dissociation channel with extensive rotational excitation the N_2 photofragment, indicating that intermediate bent states are involved along the dissociation pathway.

II. Experiment

The fast beam photofragment translational spectrometer[22-24] used in these studies is shown in Figure 2. In this experiment, we generate a clean source of neutral radicals by mass-selectively photodetaching a beam of stable negative ions. The neutral radicals are photodissociated by a second laser and the photofragments detected with high efficiency.

CNN^- ions were generated in our pulsed discharge source described previously. A mixture of 5:1 $Ar:N_2O$ with a stagnation pressure of 2 atm was passed through a bubbler containing diazomethane (–78 °C). The resulting mixture was supersonically

expanded through a pulsed valve into a pulsed electric discharge,[25] generating vibrationally and rotationally cold negative ions. Diazomethane was prepared from N-nitroso-N-methyl urea and 50% wt KOH.[26] Analysis of the photofragment yield spectra indicates that the rotational temperature of the anions is ≈50 K. The negative ions generated in the source region are accelerated to 8 keV, separated temporally by a Bakker time-of-flight (TOF) mass spectrometer,[27,28] and selectively photodetached by an excimer-pumped dye laser operating at 2.48 eV. This photodetachment energy, based on the photoelectron spectrum of Clifford *et al.*,[15] predominantly populates the v=0 level (≈ 90%) of the CNN $\tilde{X}^3\Sigma_g^-$ state. Undetached ions are deflected out of the beam path.

In the dissociation region a second excimer-pumped dye laser intersects the CNN radical. A fraction of the neutrals absorb and dissociate yielding photofragments detected directly by either the TOF or TPS (time and position sensing) microchannel plate detector assemblies shown in Figure 2. An aluminum strip is positioned at the center of each detector to prohibit undissociated radicals from impacting the detector, so that the

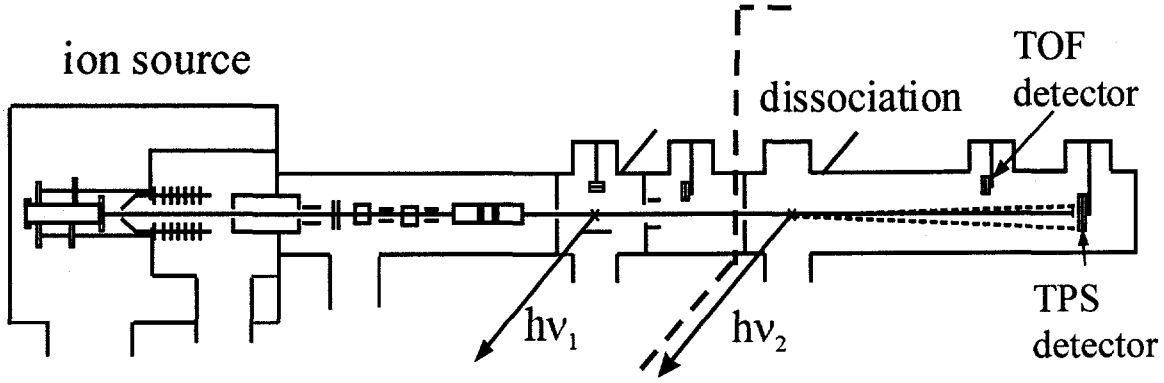

Figure 2. Fast beam photofragment translational spectrometer. The dotted line separates the radical production section on the left from the photodissociation experiment on the right.

observed signal is entirely from recoiling photofragments.

Two types of experiments are performed. First, the spectroscopy of the dissociative electronic states is examined by scanning the dissociation laser and monitoring the total flux of photofragments arriving at the retractable TOF detector, located at 0.68 m from the dissociation laser. The resulting photofragment yield (PFY) spectra is complementary to absorption and fluorescence measurements. We examined the photolysis of CNN between 23700-26000 cm^{-1} and 40800-48300 cm^{-1}. The fundamental output of the dye laser with a band-width of 0.3 cm^{-1} was used between 23700-26000 cm^{-1}. The dye laser was frequency-doubled to produce photon energies between 40800-48300 cm^{-1} with a bandwidth of 0.5 cm^{-1}.

Once the spectroscopy of the dissociative states has been examined, the dissociation dynamics at selected photolysis energies are investigated. In this experiment, both photofragments from a single parent radical are detected in coincidence using a time-and-position sensing (TPS) detector based on the concept developed by de Bruijn and Los.[29] Our implementation of this detection scheme has been described previously.[22,23] The TPS detector records the positions and difference in arrival time of the two photofragments from a single dissociation event. This information is then used to determine the masses of the fragments, their relative translational energy E_T, and the scattering angle θ between the relative velocity vector and the electric vector of the polarized dissociation laser. The photofragment mass resolution is $m/\Delta m \approx 10$ while the translational energy resolution for these experiments is $\Delta E_T/E_T = 2.0$ %. As discussed in previous papers,[21] the relatively poor mass resolution for the photofragments is due to the size of the radical beam at the TPS detector.

III. Results

A. Photofragment Yield Spectra, $\tilde{A}^3\Pi \leftarrow \tilde{X}^3\Sigma^-$ transitions

The photofragment cross-section for the $\tilde{A}^3\Pi \leftarrow \tilde{X}^3\Sigma^-$ band of CNN is shown in Figure 3a with peak positions and assignments listed in Table I. Our photofragment yield spectra are a convolution of both absorption and dissociation cross-sections. The laser fluences were typically 200 mJ/cm^2 for photon energies between 23500-24200 (i.e. peaks A-C) and 80 mJ/cm^2 from 24700-26000 cm^{-1} (remainder of spectrum). A broad feature with a width of $\approx$ 100 cm^{-1} is observed near 23850 cm^{-1} (A) in good agreement with the rotationally resolved origin band observed by Curtis *et al.*[14] Weaker features, B and C, are observed 200 and 300 cm^{-1} to the blue of the origin are most likely due to sequence bands involving vibrationally excited levels of the ground state. As discussed below, peak A results from two-photon dissociation, which is why such high laser fluences were needed.

A weak feature D is observed at 24810 cm^{-1} while prominent features E and F occur at 25044 and 25236 cm^{-1}, respectively; for the latter two and other features with multiplet structure, the wavenumber values refer to the most intense peak. Feature F shows a linear relationship between fragment intensity and laser fluence was observed for laser fluences < 30 mJ/cm^2, while saturation was seen at higher laser fluence. Expanded views of transitions E and F (scanned with laser fluences < 30 mJ/cm^2) are shown in Figure 3b, displaying significantly different rotational contours. Feature F displays three prominent sub-bands with a spacing of $\approx$ 27 cm^{-1} and a broader peak between the first

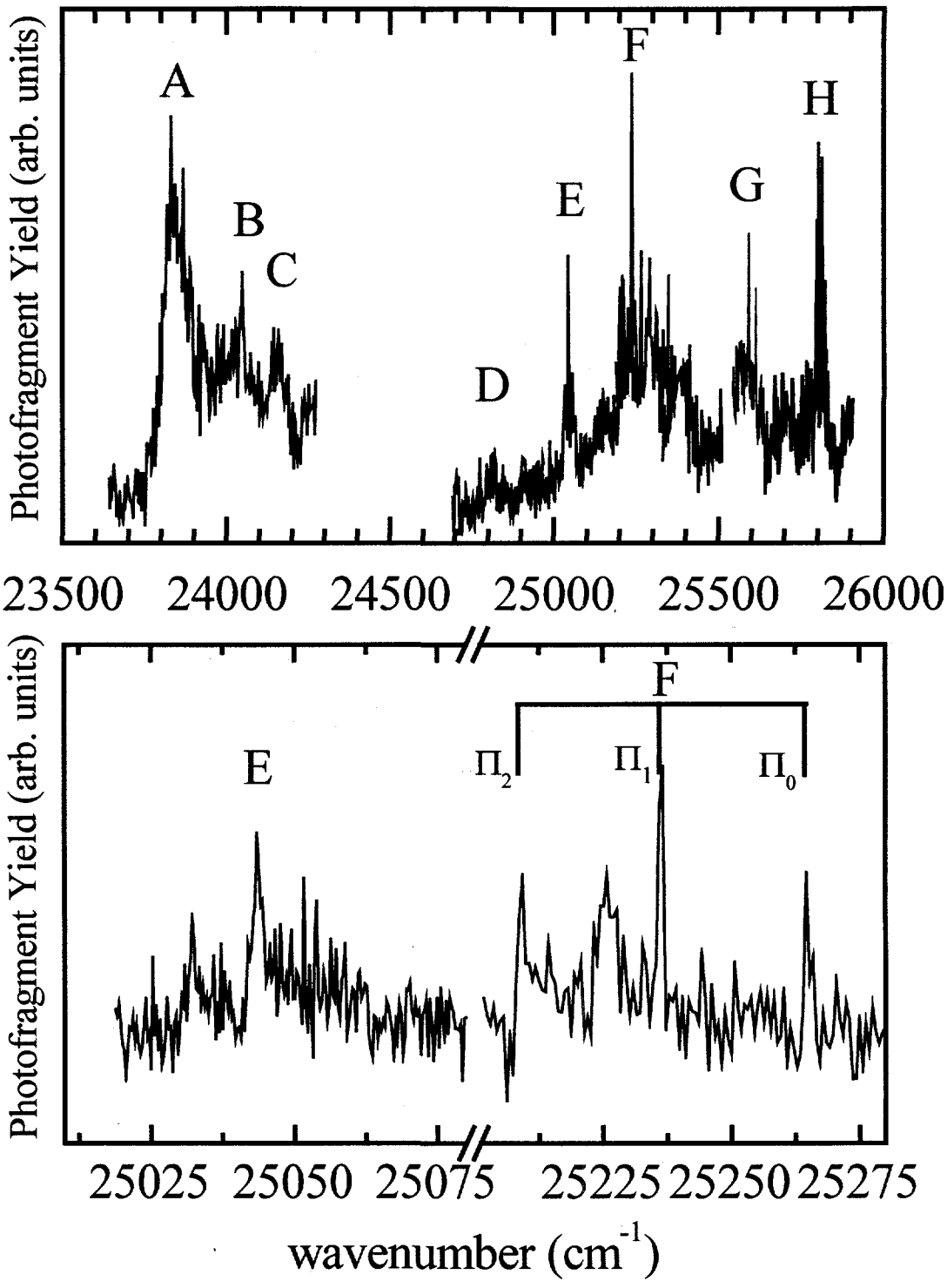

Figure 3. (**a**) Photofragment yield spectrum of the $\tilde{A}^3\Pi \leftarrow \tilde{X}^3\Sigma^-$ band of CNN. (**b**). Expanded views of features E and F. The spin orbit splitting for band F is illustrated with the comb denoting the Q-type transitions of the $^3\Pi_{2,1,0}$ states.

Table I. Peak positions, transition energies (cm^{-1}), and assignments of the $\tilde{A}^3\Pi \leftarrow \tilde{X}^3\Sigma^-$ PFY spectrum. Assignments and frequencies from previous LIF studies are shown for comparison.

		Frequency (cm^{-1})		
Peak	Transition Energy (cm^{-1})	This work	LIF[a]	Assignment
A	23850	----	---	000-000
			92	010-010 (Σ^+–Π)
			145[b]	010-010 (Δ–Π)
B	24047	197		----
			196	02^-0-020 (Π–Σ^-, Δ)
C	24157	307		020-020 (Φ–Δ)
D	24810	960	982	02^-0-000 (Π–Σ^-)
E	25044	1194	1098	02^+0-000 (Π–Σ^-)
F	25236	1386	1322	100-000
G	25592	1742		----
			1807	001-000
H	25805	1955		----

[a]Unless otherwise denoted, all LIF frequencies are from Bondybey *et al.*[11]

[b]Based on a reported sequence band from the gas-phase LIF study of Curtis *et al.*[14]

two of these. The sub-band spacing of 27 cm^{-1} is close to the spin-orbit spittling, A = -26.5 cm^{-1} reported for the 000-000 band observed at lower energy in the experiments of Curtis *et al.*[14] The most intense sub-band possesses a width of about 1.5 cm^{-1}. Feature E, in contrast, does not possess any obvious sub-band structure; it consists of a peak at 25044 cm^{-1} that is 3 cm^{-1} wide and a smaller feature ≈ 11 cm^{-1} to the red. Features G and

H located above 25300 cm^{-1} exhibit broader features. Feature H displays doublet structure with a splitting of $\approx$ 12 cm^{-1} and widths of 7 cm^{-1}.

B. Photofragment Yield Spectra, $\tilde{B}^3\Sigma^- \leftarrow \tilde{X}^3\Sigma^-$ transitions

Higher energy dissociative transitions are observed from 40000-46000 cm^{-1}, Figure 4; laser fluences of $\approx$ 15 mJ/cm^2 were used in these measurements. The PFY spectrum shows strong, broad transitions with widths of $\approx$ 300 cm^{-1}. Two major progressions with spacings of $\approx$ 1000 cm^{-1} are observed, in agreement with the absorption bands previously observed in the matrix studies of Jacox[12] and assigned to the $\tilde{B}^3\Sigma^- \leftarrow \tilde{X}^3\Sigma^-$ band. Our gas-phase transitions are shifted by ~ 85 cm^{-1} to the blue of the Ar matrix work. The most prominent progression in our spectrum originates at 40985 cm^{-1}, and, following the work of Jacox, is assigned to the symmetric stretch 1_0^n mode. Despite extensive scanning we were not able to detect a weak transition near 40000 cm^{-1} reported by Jacox. A second progression begins at 43450 cm^{-1} and also displays a peak spacing of ~ 1000 cm^{-1}. The separation between this progression and the 1_0^n progression is 447 cm^{-1}. Since the ground state is linear and the excited state is predicted to be linear by Walsh's rules, the bend mode is not expected to be active. This second progression is most easily assigned to a combination band involving the symmetric (ν_1) and one quanta of asymmetric (ν_3) stretch with ω_3'=1455 cm^{-1}, in good agreement with the value of 1450 cm^{-1} reported by Jacox.[12]

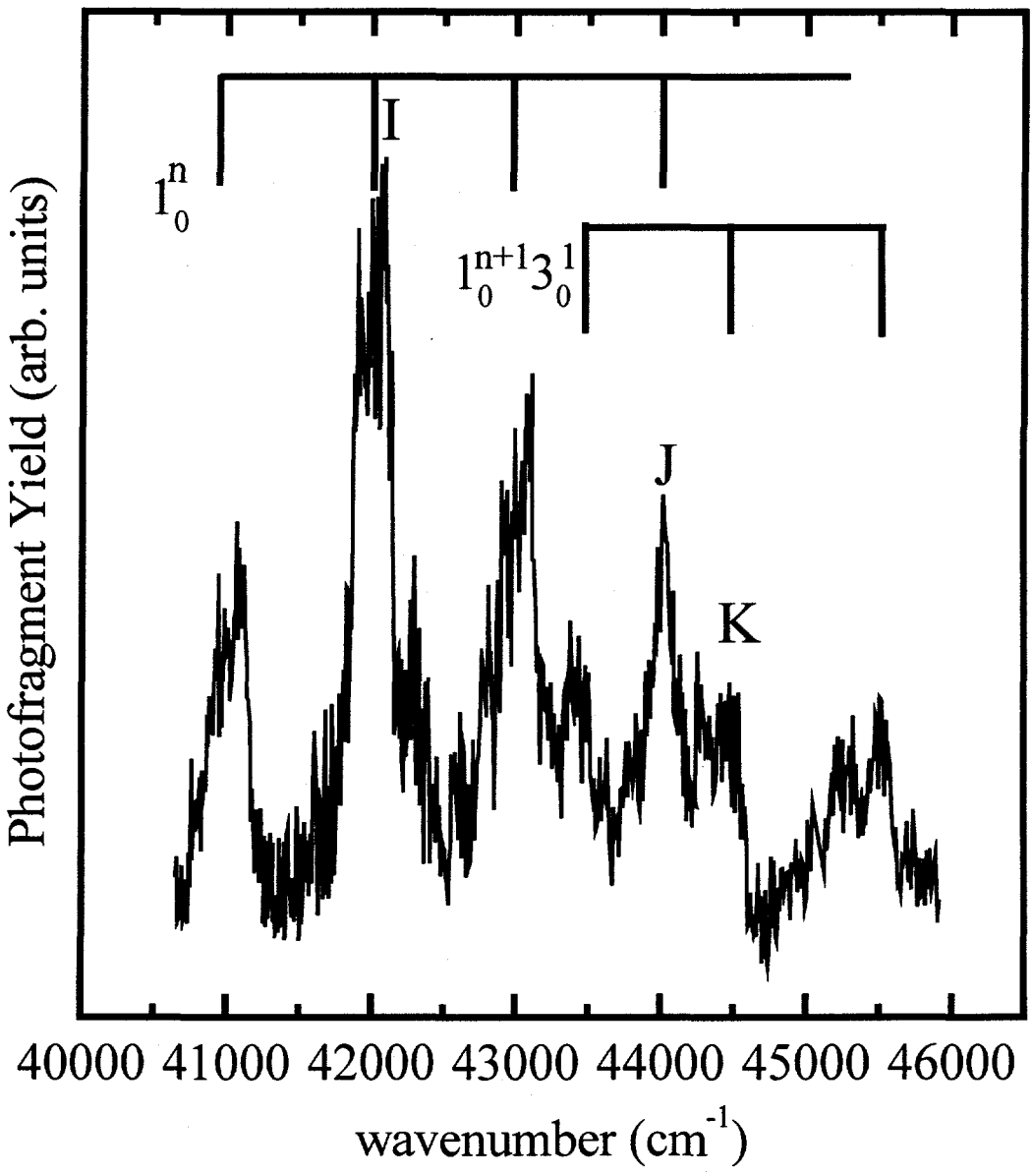

Figure 4. Photofragment yield spectrum of the $\tilde{B}^3\Sigma^- \leftarrow \tilde{X}^3\Sigma^-$ spectrum. The 1_0^n and $1_0^{n+1}3_0^1$ progressions are indicated by the vibrational combs. Features I, J and K denote the transitions for which translational energy distributions have been obtained.

C. Mass Distributions

At the photon energies employed in this study, multiple photodissociation product channels are available. The heats of reaction (at 0 K) for energetically available product channels derived from the current study are shown below. $\Delta_r H_0$ for channel I (equivalent to the bond dissociation energy D_0) is determined directly in this work. The higher energy reaction channels are based upon our experimental value for D_0, JANAF thermochemical tables[30] for the heats of formation of C, N and N_2 and the heat of formation for CN determined by Huang *et al.*[31]

$$CNN\,(\tilde{X}^3\Sigma^-) \xrightarrow{h\nu}$$

$$N_2\,(X^3\Sigma^-) + C\,(^3P) \qquad \Delta_r H_0 = 1.219 \pm 0.050 \text{ eV} \qquad \text{(I)}$$

$$N_2\,(X^1\Sigma_g^+) + C(^1D) \qquad \Delta_r H_0 = 2.479 \pm 0.050 \text{ eV} \qquad \text{(II)}$$

$$CN(X^2\Sigma^+) + N(^4S) \qquad \Delta_r H_0 = 3.233 \pm 0.050 \text{ eV} \qquad \text{(III)}$$

$$N_2\,(X^1\Sigma_g^+) + C(^1S) \qquad \Delta_r H_0 = 3.903 \pm 0.050 \text{ eV} \qquad \text{(IV)}$$

$$CN(A^2\Pi) + N(^4S) \qquad \Delta_r H_0 = 4.379 \pm 0.050 \text{ eV} \qquad \text{(V)}$$

$$CN(X^2\Sigma^+) + N(^2D) \qquad \Delta_r H_0 = 5.616 \pm 0.050 \text{ eV} \qquad \text{(VI)}$$

The upper states accessed in the $\tilde{A}^3\Pi \leftarrow \tilde{X}^3\Sigma^-$ transitions in Fig. 3 can only dissociate to channels I and II and the expected 12:28 photofragment mass ratio is observed. The higher energy $\tilde{B}^3\Sigma^- \leftarrow \tilde{X}^3\Sigma^-$ transitions between 5.1–6.0 eV have multiple dissociation pathways available. We have examined the mass distributions as a function of translational energy both above and below the thermodynamic limits for the CN + N channels III and V; examples are shown in Fig. 5 for transition K. At translational energies > 2.5 eV, only channels I and II are accessible and the expected 12:28 mass ratio

is observed. At translational energies > 1 eV the mass ratio continues to be 12:28 for all transitions in the $\tilde{B}^3\Sigma^- \leftarrow \tilde{X}^3\Sigma^-$ band. For transitions J and K in Fig. 4, the mass distributions broaden considerably at translational energies < 0.8 eV (circles in Fig. 5) and a slight shift to higher (lower) mass is observed for the light (heavy) photofragment, indicating that the N + CN mass channel contributes

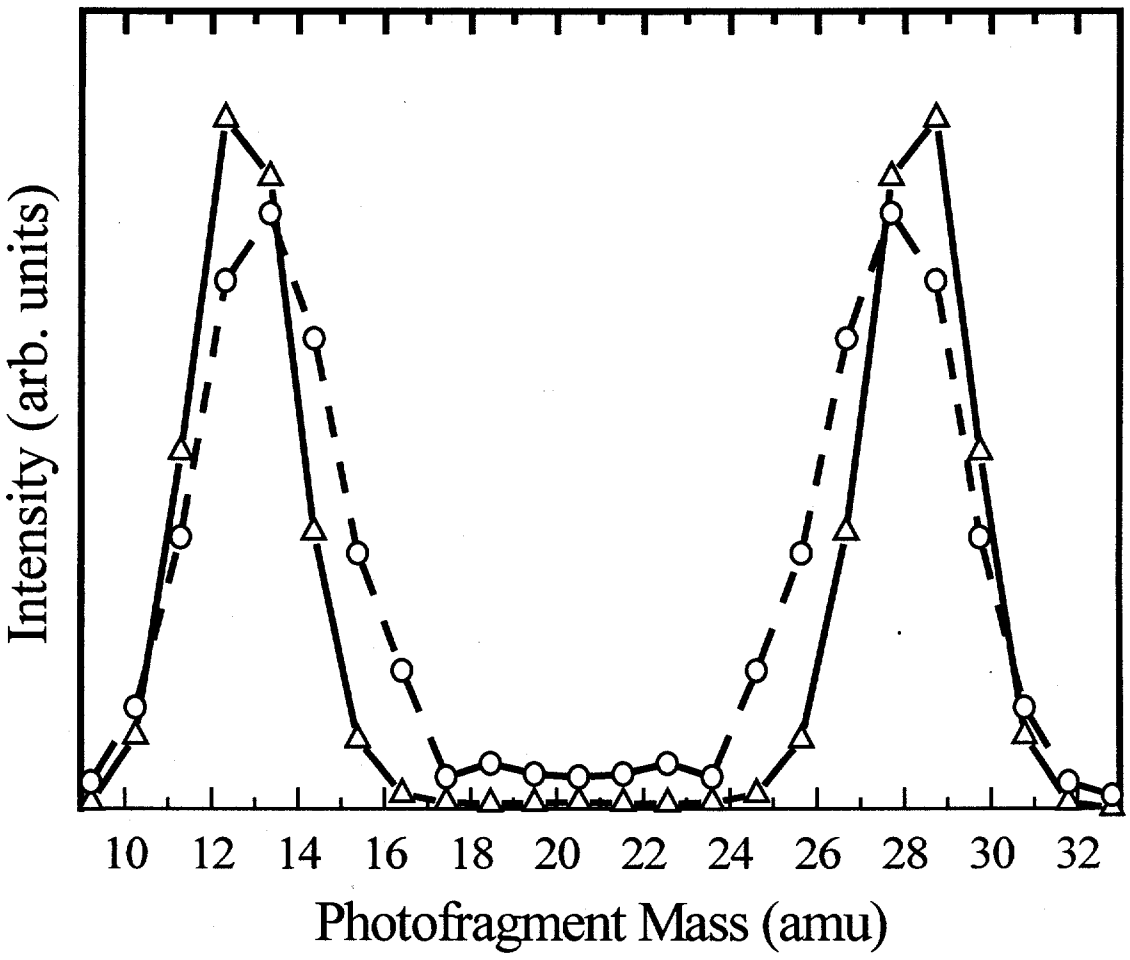

Figure 5. Photofragment mass distributions for transitions J and K of the $\tilde{B}^3\Sigma^- \leftarrow \tilde{X}^3\Sigma^-$ band for translational energies > 1 eV (triangles) and < 0.8 eV (circles). For low translational energies, the mass of the light (heavy) fragment shows a shift to higher (lower) masses.

D. Translational Energy Distributions

1. $\tilde{A}^3\Pi \leftarrow \tilde{X}^3\Sigma^-$ $P(E_T)$ distributions

The $P(E_T)$ distributions for peaks E, F, G, and H of the $\tilde{A}^3\Pi \leftarrow \tilde{X}^3\Sigma^-$ band are shown in Figure 6. We will comment on the origin band $P(E_T)$ distribution (peak A) in section III.D.3. The $P(E_T)$ distributions display bimodal distributions with a high energy component which extends toward ≈ 2 eV and a low energy feature peaked at 0.6 eV. The relative intensity of the higher energy component increases with larger photon energies. The $P(E_T)$ distribution for the 100-000 transition shows a sharp onset in signal at 1.91 eV, defining the maximum translational energy, E_T^{max}. The other $\tilde{A}^3\Pi \leftarrow \tilde{X}^3\Sigma^-$ transitions do not display such sharp onsets and instead show a gradual decrease in signal towards higher translational energies.

2. $\tilde{B}^3\Sigma^- \leftarrow \tilde{X}^3\Sigma^-$ $P(E_T)$ distributions

$P(E_T)$ distributions for three $\tilde{B}^3\Sigma^- \leftarrow \tilde{X}^3\Sigma^-$ transitions are shown in Figure 7. Figures 7a-c (peaks I, J, and K) correspond to $P(E_T)$ distributions for events analyzed as producing $C + N_2$ photofragments while Figure 7d (peak J) corresponds to N + CN events. As discussed in Section IIIC. and shown in Fig. 5, these two mass channels are incompletely resolved in our experiment. As a consequence, Figs. 7b and 7d obtained at the same photon energy are similar, the main difference being that the broad peak at $E_T \approx$ 0.5 eV, which only appears when transitions J or K are excited, is considerably enhanced relative to the signal above 1 eV in Fig. 7d. The signal above 1 eV in Figure 7 is entirely from $C + N_2$ since the mass spectrum of the fragments is identical to that obtained at lower photon energies where this is the only channel available (Fig. 5), whereas the peak

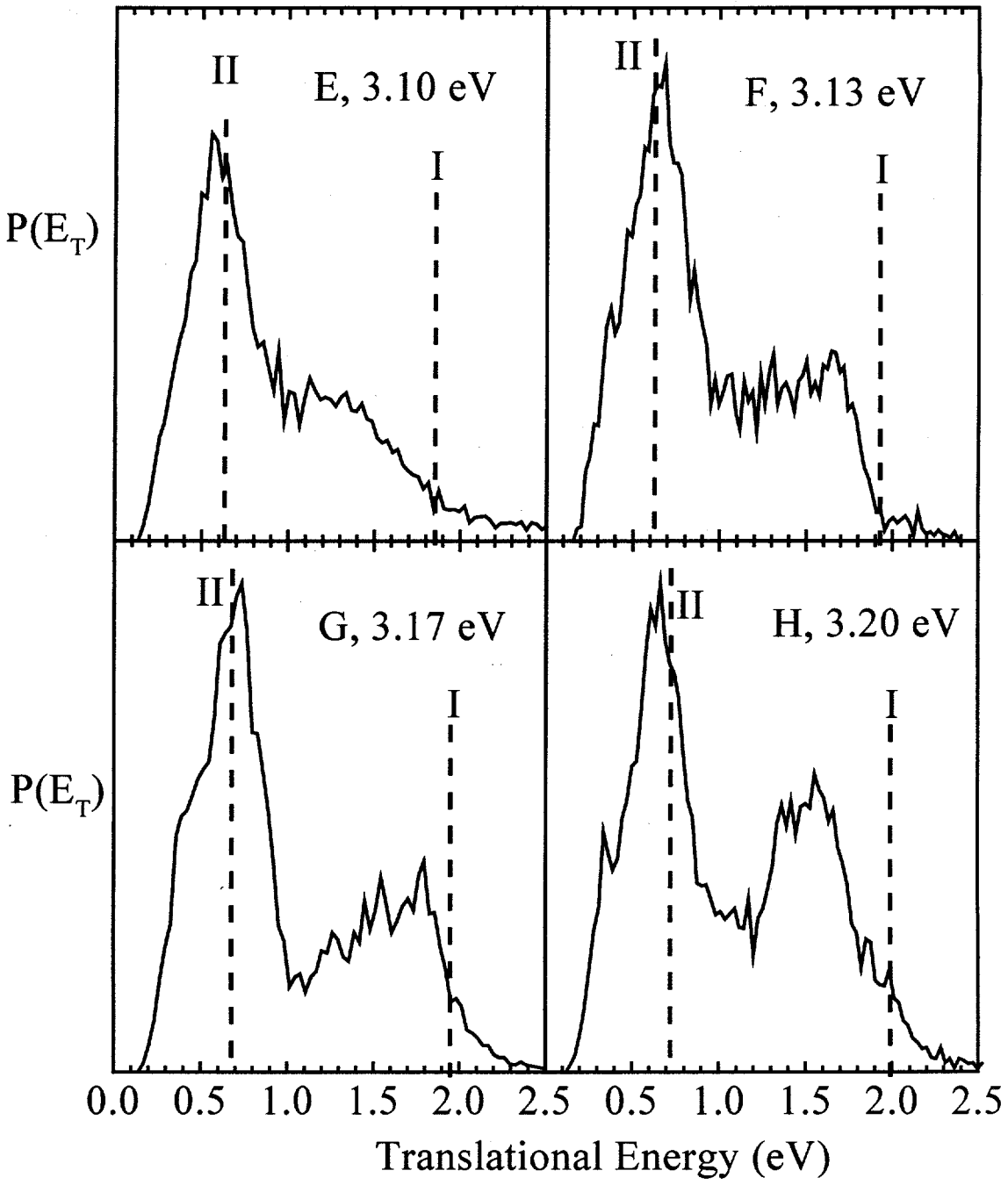

Figure 6. Translational energy distributions for $\tilde{A}^3\Pi \leftarrow \tilde{X}^3\Sigma^-$ band transitions E-G. The photon energies for each transition is given and the maximum translational energy for channels I and II are indicated with the dashed vertical lines.

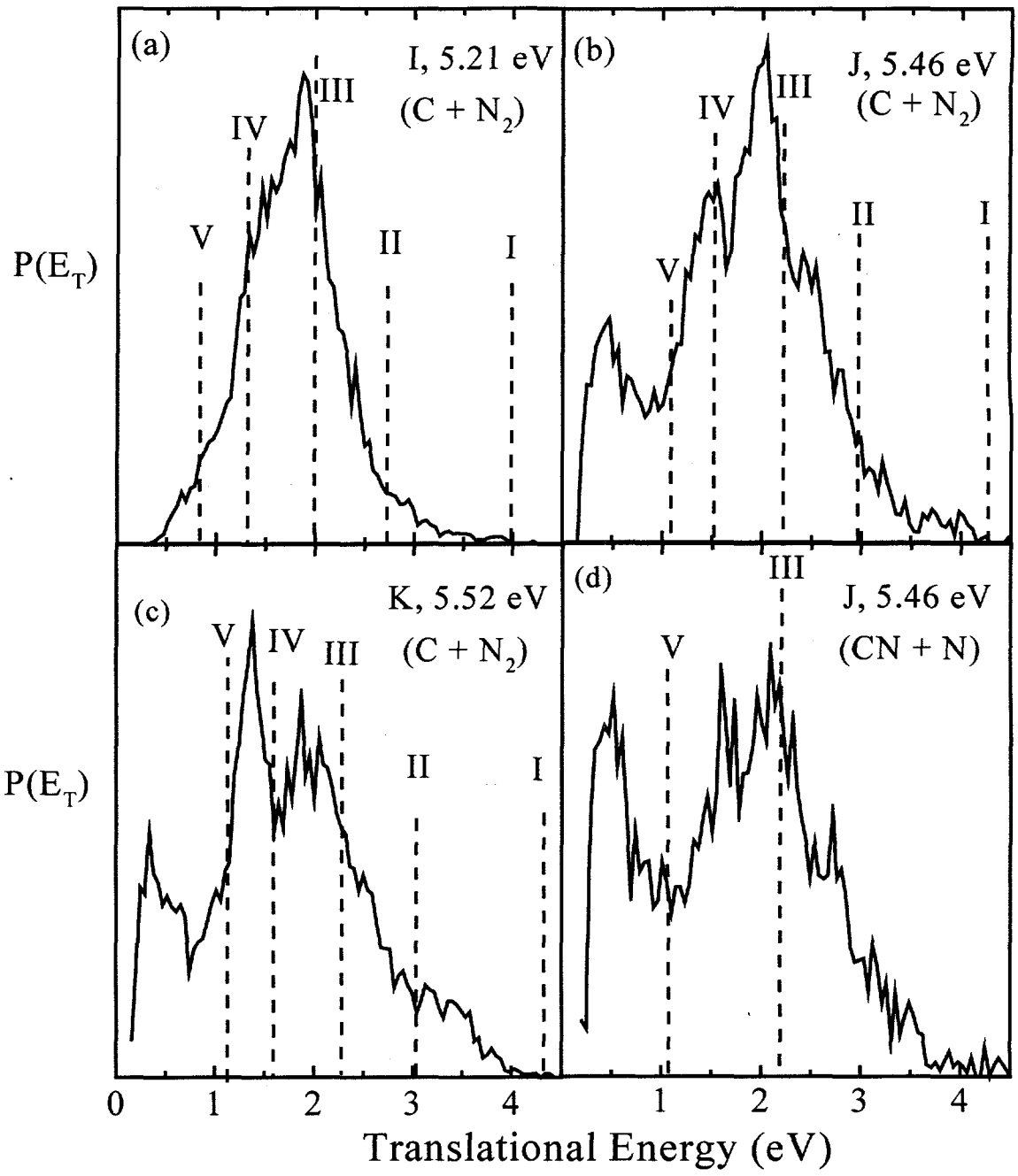

Figure 7. Translational energy distributions for the $\tilde{B}^3\Sigma^- \leftarrow \tilde{X}^3\Sigma^-$ transitions. The distributions for C + N_2 products for transitions I, J and K are shown in a, b and c respectively. The transition photon energies are indicated and the maximum translational energy (E_T^{max}) for product channel I-V are denoted by vertical dashed lines. The distribution for N + CN products for transition J is shown in d.

around 0.5 eV is attributed to N + CN because of its enhancement in Fig. 7d. The latter assignment is again consistent with the photofragment mass spectra in Fig. 5.

The observed structure for the C + N_2 mass channel, with features between 0.5 to 1.0 eV in width, is much too broad to attribute to individual vibrational states of the N_2 products. Furthermore, the sharp rises do not exactly coincide with the thermodynamic thresholds for various product states and do not shift with excitation energy, making the assignment of the product channel ambiguous. The internal energy distribution appears to depend both upon excitation energy as well as the vibronic character of the transition. The $P(E_T)$ distributions for transitions J and K show more signal above 3 eV than transition I and a peak near 1.5 eV not seen from transition I (the feature at 0.5 eV is from N + CN products, as discussed above). Although only 60 meV higher in energy than $J(1_0^n)$, the $P(E_T)$ distribution for $K(1_0^n 3_0^1)$ peaks sharply near 1.4 eV as opposed to 2.0 eV for J, suggesting that excitation of the asymmetric stretch leads to increased internal excitation of the photofragments.

3. $P(E_T)$ distributions from the origin and higher energy transitions

The $P(E_T)$ distribution for the origin transition at 2.955 eV, Figure 8, reveals a broad distribution peaked near 1.3 eV extending to 4.7 eV, which is 1.75 eV higher in energy than the initial photon energy. Gas phase kinetic data[13] and *ab initio* calculations[15,20,32] indicate that the CNN radical is thermodynamically stable with respect to the lowest energy dissociation asymptote. The high translational energy fragments must therefore be produced via a multi-photon process. The $P(E_T)$ distribution resulting from excitation with a single photon at 5.91 eV (i.e. 2x2.955 eV) is also shown

in Figure 9. Due to the low laser fluence ($\approx 3 mJ/cm^2$) and small absorption cross-section at the higher photon energy, this data set consists of approximately 1/10 the number of data points as the $P(E_T)$ distribution at 2.955 eV. Even with these poor statistics, similarities between the two data sets are readily apparent, both showing broad distributions peaking near 1.3 eV and extending towards higher translational energies. The similarity in $P(E_T)$ distributions suggests the distribution at lower photon energy

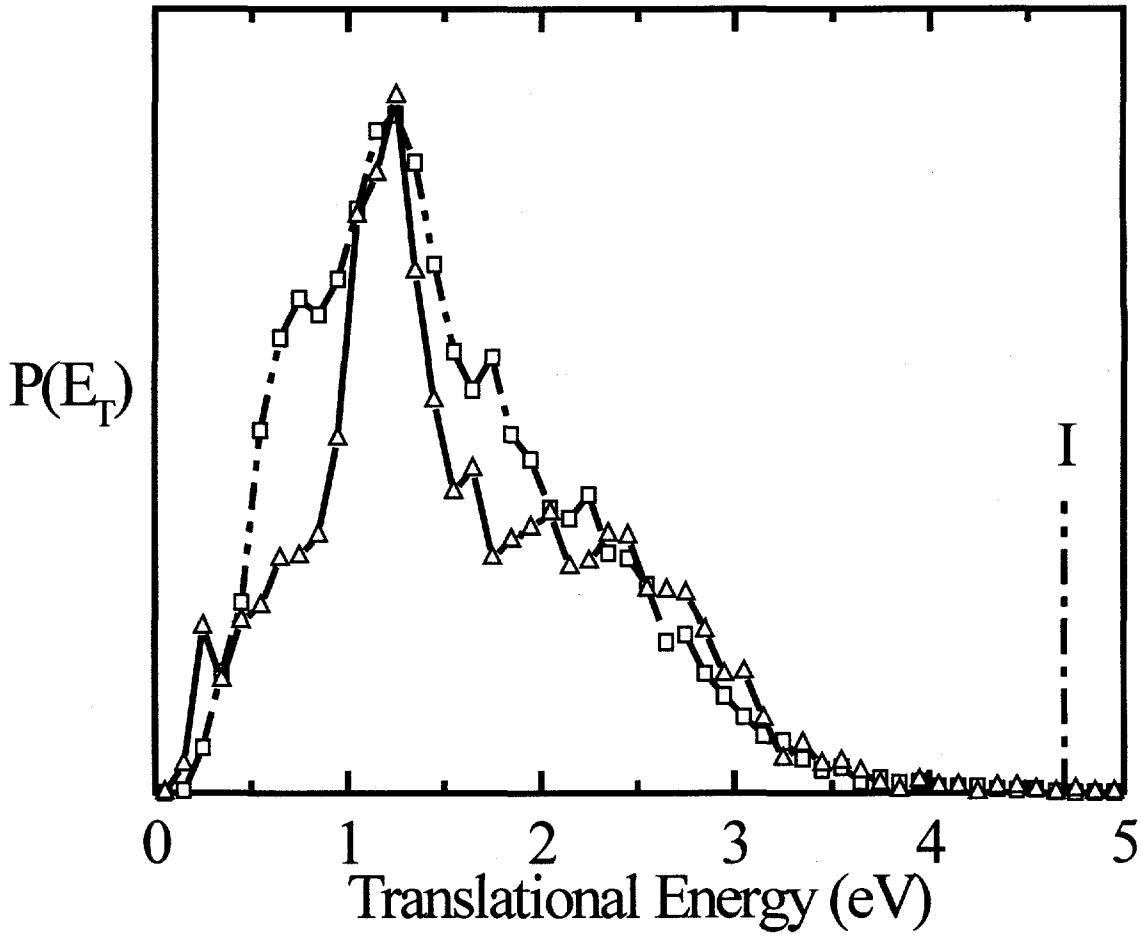

Figure 8. $P(E_T)$ distributions for photon energies of 2.955 eV (-□-), corresponding to the $\tilde{A}^3\Pi \leftarrow \tilde{X}^3\Sigma^-$ origin, and 5.91 eV (-Δ-).

results from two-photon absorption, and that the one- and two- photon processes access the same final excited state prior to dissociation.

E. Angular Distributions

The coincident detection scheme measures both the energy and angular distributions of the photofragments. The two-dimensional coupled translational energy distribution, $P(E_T, \theta)$ can be separated into the angle-independent translational energy distribution $P(E_T)$ and the energy-dependent anisotropy parameter $\beta(E_T)$ which describes the angular distribution of the fragments

$$P(E_T, \theta) = P(E_T)[1+ \beta(E_T)P_2(\cos\theta)]. \qquad (1)$$

The anisotropy parameter β ranges from +2 to −1, corresponding to $\cos^2\theta$ and $\sin^2\theta$ angular distributions respectively. Photofragment angular distributions for representative $\tilde{A}^3\Pi \leftarrow \tilde{X}^3\Sigma^-$ and $\tilde{B}^3\Sigma^- \leftarrow \tilde{X}^3\Sigma^-$ transitions as well as one-photon and two-photon transitions with total excitation energy of 5.91 eV are shown in Figure 9. The photofragment anisotropies for the $\tilde{A}^3\Pi \leftarrow \tilde{X}^3\Sigma^-$ band are essentially isotropic with $\beta \approx 0$ at translational energies less than 1 eV and become increasingly anisotropic at higher translational energies with $\beta = -0.2$ at 1.5 eV. The photofragment anisotropies for the $\tilde{B}^3\Sigma^- \leftarrow \tilde{X}^3\Sigma^-$ transitions are significantly more anisotropic showing positive β parameters which peak near 2. Although the $P(E_T)$ distributions in Fig. 8 at photon energies of 2.955 and 5.91 eV are similar, the photofragment angular distributions are quite different. Excitation at 5.91 eV results in a positive β parameter at all translational

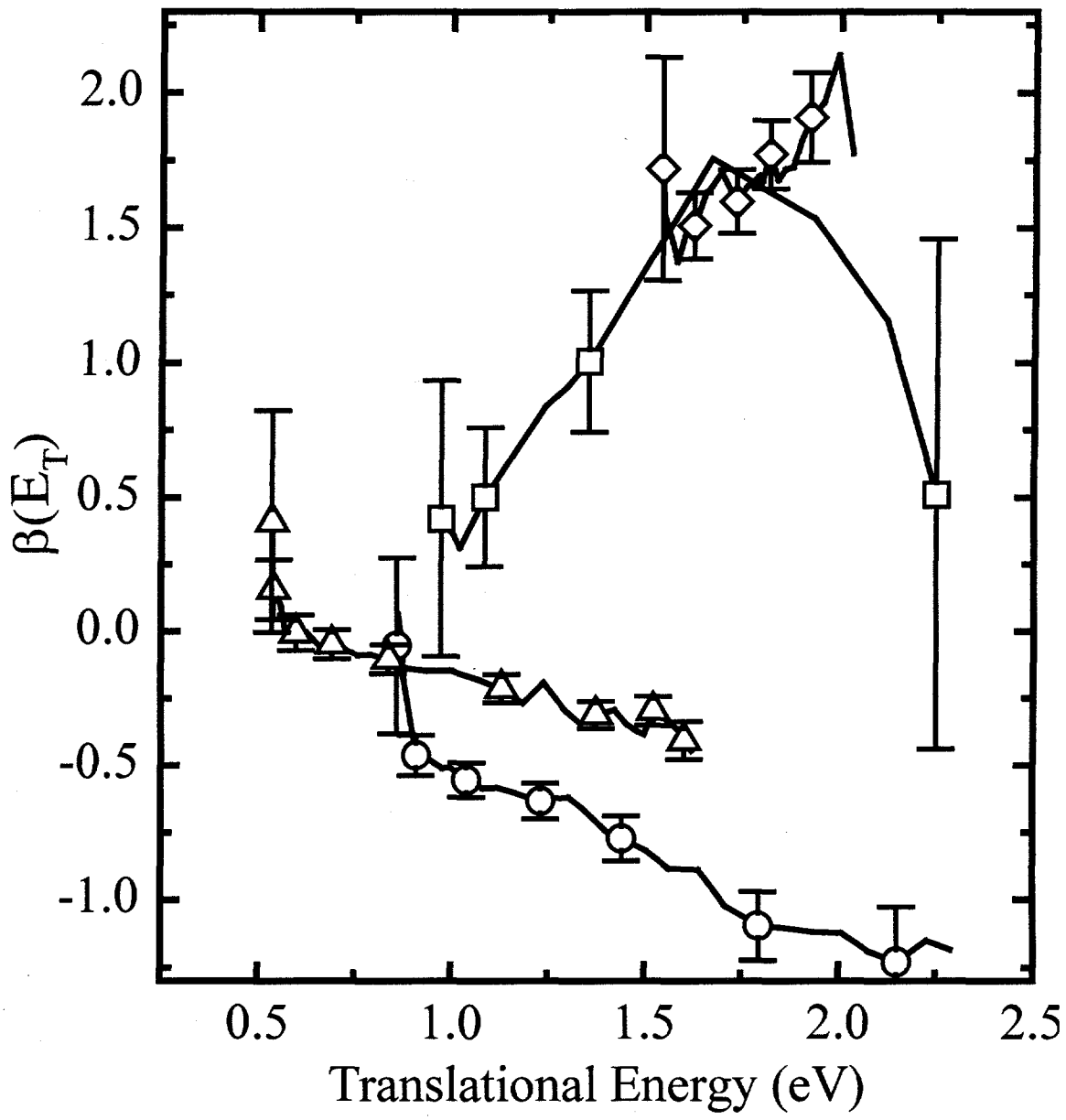

Figure 9. Photofragment anisotropy parameter, β, as a function of translational energy for the $\tilde{A}^3\Pi \leftarrow \tilde{X}^3\Sigma^-$ 3.173 eV transition -Δ-, the $\tilde{B}^3\Sigma^- \leftarrow \tilde{X}^3\Sigma^-$ (400-000) transition -◊-, the 5.91 eV transition -□-, and the 2.955 eV two-photon transition -O

energies, whereas excitation at 2.955 eV yields a negative β parameter reaching its limit of −1 for $E_T > 1.7$ eV.

IV. Analysis

A. Photofragment Yield Spectra

Although the CNN radical is a linear triatomic radical, the assignment of the vibronic features in the $\tilde{A}^3\Pi \leftarrow \tilde{X}^3\Sigma^-$ PFY spectra is not at all straightforward. The $\tilde{X}^3\Sigma^-$ and $\tilde{A}^3\Pi$ states have very similar geometries as evidenced by the dominance of the origin transition in both absorption and emission experiments as well as the similar rotational constants ($B' = 0.4250$ cm^{-1} and $B'' = 0.4136$ cm^{-1}). Therefore, there are only a limited number of transitions above the origin with any appreciable intensity. Further, the PFY spectra are a convolution of both absorption and dissociation and are therefore inherently different than LIF spectra. Short-lived dissociative states will appear as intense features in PFY spectra, but may go entirely undetected via LIF techniques. Despite the numerous complications, we have been able to assign several vibronic features.

Feature A, centered near 23,840 cm^{-1}, agrees well with the gas phase LIF excitation spectrum of the $\tilde{A}^3\Pi \leftarrow \tilde{X}^3\Sigma^-$ origin by Curtis *et al.*[14] with a reported term energy of 23850 cm^{-1}. The band contour of this feature in our PFY spectrum does not reveal the sharp fine-structure observed in the gas phase LIF spectrum. This PFY spectrum was recorded at high laser intensities, ≈ 200 mJ/cm^2, where saturation effects and power broadening of individual lines is likely. Furthermore, as discussed above, the $P(E_T)$ distribution for this transition shows that the photofragments are produced via a

two-photon process, indicating that the origin transition is a resonant state in the dissociation. Hence the observed PFY spectrum is a convolution of the initial $\tilde{A}^3\Pi \leftarrow \tilde{X}^3\Sigma^-$ transition and subsequent excitation to a higher energy dissociative state.

Since feature A in the PFY spectrum does not display resolved structure, a determination of the term energy for the $\tilde{A}^3\Pi \leftarrow \tilde{X}^3\Sigma^-$ band is not obvious and we therefore adopt the value of 23,850 cm^{-1} from Curtis *et al.* The excitation energies within the $\tilde{A}$ manifold are shown in Table I along with matrix LIF results. Curtis *et al.* have reported a weak band 145 cm^{-1} to the blue of the origin with analogous subband structure and has been tentatively assigned to the (010-010) $\Delta \leftarrow \Pi$ sequence band yielding a gas-phase bend frequency of 540 cm^{-1} for the $\tilde{A}^3\Pi$ state.[33] Our PFY spectrum exhibits broad dissociation signal 145 cm^{-1} above the origin along with more intense features B and C located $\approx$ 200 and 300 cm^{-1} above the origin. Feature C can be reasonably assigned to the (020-020) $\Phi \leftarrow \Delta$ transition, while the assignment of feature B is less certain.

We next consider the higher lying features. Transition F shows prominent features with sub-band spacing of about 27 cm^{-1} and a broader peak between the first two of these. It should be pointed out here, that the relative intensities of the sub-band structure observed by Curtis *et al.*[14] is quite different from that displayed in our PFY spectrum. However, their experiment reports a rotational temperature of 500 K as opposed to 50 K in our experiment. Using the same structural parameters used previously by Curtis *et al.* to simulate their spectrum and a rotational temperature of 50 K, the sharp features with sub-band spacing of $\approx$ 27 cm^{-1} are most easily assigned to the $^3\Pi_2$, $^3\Pi_1$, and $^3\Pi_0$ Q-type bandheads. The vibrational frequency of 1387 cm^{-1} and rotational contour are consistent with an assignment to the 100-000 transition, but the

gas-phase transition occurs 64 cm^{-1} to the blue of the corresponding matrix LIF transition (see Table I). The matrix LIF spectrum[11] shows two features with energies similar to D and E in the PFY spectrum that were assigned to transitions to the lower (02^-0) and upper (02^+0) Renner-Teller states, and these assignments appear reasonable for peaks D and E as well. The Renner-Teller interaction commonly reduces the spin-orbit splitting as has been observed previously in CCO.[34] The lack of subband structure associated with the $^3\Pi_{2,1,0}$ states for feature E supports its assignment to a Renner-Teller state.

Peak D lies 20 cm^{-1} below the corresponding matrix transition, while E is 100 cm^{-1} higher, indicating a strong matrix effect. In their matrix studies, Bondybey and English determined the Renner parameter $\varepsilon\omega_2$ to be -36.75 cm^{-1}, significantly less than the gas-phase values of –104.4 cm^{-1} and –91.1 cm^{-1} for the isoelectronic species CCO[34,35] and NCN.[36] Assigning transitions D and E to the 02^-0 and 02^+0 states respectively, we derive $\omega_2' = 539$ cm^{-1}, in good agreement with the value estimated from the work of Curtis *et al.*,[14] and a Renner value $\varepsilon = -0.154$ yielding $\varepsilon\omega_2 = -83$ cm^{-1}, in much better agreement with the other isoelectronic species. The large discrepancy between the gas-phase and matrix values is surprising. However, the spin orbit parameter, A was found to be - 9 and - 26.5 cm^{-1} respectively for matrix[11] and gas-phase[14] measurements on CNN, indicating that the matrix substantially perturbs the electronic coupling to the internuclear axis.

The relative intensities of the Renner-Teller features D and E are reversed in the matrix LIF and PFY spectra. In the absence of other perturbations, we expect the intensity for the two 020 Π states to be approximately equal. The intensity of the lower Renner-Teller state in LIF matrix measurements[11] is more than four times that of the upper Renner-Teller state, whereas our PFY measurements show the 02^+0 transition to be

at least 5 times more intense than the $02^{-}0$ band. These observations suggest that the lower Renner-Teller state decays primarily via emission, whereas the upper Renner-Teller component has a significantly higher quantum yield for dissociation, thereby depleting the LIF signal associated with this peak.

Higher energy features G and H are observed 1742 cm^{-1} and 1967 cm^{-1} above the origin. These features do not display clear sub-band structure nor do they agree well with reported LIF matrix transitions making their assignment tentative. Feature G could be the transition to the 001 level, although this implies a gas phase frequency shift of -65 cm^{-1} from the matrix value of 1807 cm^{-1}. Transition H is tentatively assigned to the $04^{-}0$-000 transition, as its excitation energy is about twice that of peak D. Other possible assignments include combination band transitions originating from vibrationally excited levels of the ground state.

All of the vibronic transitions of the $\tilde{A}^3\Pi \leftarrow \tilde{X}^3\Sigma^-$ band deviate to some extent from the LIF matrix studies, suggesting substantial host-guest interactions exist for CNN. Analogous shifts between matrix and gas-phase frequencies were observed previously by Bondybey and English[37] for the $\tilde{A}^2\Delta$ state of the CCN radical in solid Ar.

The agreement between the gas-phase measurements and matrix values for the $\tilde{B}^3\Sigma^- \leftarrow \tilde{X}^3\Sigma^-$ transitions appear to be much closer than for the $\tilde{A}^3\Pi \leftarrow \tilde{X}^3\Sigma^-$ band. The 1_0^n and $1_0^n 3_0^1$ progressions yield values of $\nu_1 \approx 1000$ cm^{-1} and $\nu_3 \approx 1455$ cm^{-1}, in good agreement with the matrix studies of Jacox.[12] The extended progressions are indicative of a large change in geometry between the $\tilde{X}^3\Sigma^-$ and $\tilde{B}^3\Sigma^-$ states; consistent with the promotion of an electron from a bonding π orbital to a non/antibonding π^* orbital. The broad resonances indicate lifetime broadening due to rapid predissociation.

B. Translational Energy Distributions

1. $\tilde{A}^3\Pi \leftarrow \tilde{X}^3\Sigma^-$ transitions

The $P(E_T)$ distributions in Figures 6 and 7 demonstrate how available energy is distributed between the photofragments. Energy balance for CNN photodissociation to N_2 + C is described by Eq. 2:

$$h\nu + E_{int}(CNN) + E_{elec}(CNN) = D_0(CNN) + E_T + E_v(N_2) + E_R(N_2) + E_{elec}(C) \quad (2)$$

where $h\nu$ is the photon energy, $E_{int}(CNN)$ is the average rotational energy of the parent radical, $E_{elec}(CNN)$ is the initial electronic state of the radical, D_0 is the dissociation energy, E_T is the measured translational energy, $E_V(N_2)$ and $E_R(N_2)$ are the N_2 vibrational and rotational energies respectively and $E_{elec}(C)$ is the atomic state of carbon. An analogous equation can be written for the CN +N channel. The parent rotational temperature of 50 K yields $E_{int}(CNN) \approx 33$ cm^{-1}. $D_0(CNN)$ for the N_2 loss channel can be extracted from these distributions by determining E_T^{max}, the translational energy corresponding to photofragments with zero internal energy. In the $\tilde{A}^3\Pi \leftarrow \tilde{X}^3\Sigma^-$ band, a sharp threshold for dissociation signal is observed for the 100-000 transition, yielding a dissociation energy, $D_0 = 1.22 \pm 0.05$ eV. The translational energy distributions for the other transition energies were measured at laser fluences ~ 80 mJ/cm^2 compared with 30 mJ/cm^2 for 100-000 transition. Multiphoton effects may give rise to the higher translational energy signal which tails off beyond the single-photon value for D_0. Furthermore, the assignments of transitions G and H are uncertain and involve vibrationally excited levels of the ground state giving rise to higher translational energy

signal than would be expected from transitions originating from the (000) level of the $\tilde{X}^3\Sigma^-$ state.

Using Eq. 3, we determine $\Delta_f H_0(CNN) = 6.16 \pm 0.05$ eV from our experimental value for D_0 and JANAF thermochemical tables for the heats of formation of C and N_2.[30]

$$\Delta_f H_0(CNN) = \Delta_f H_0(C(^3P)) + \Delta_f H_0(N_2(X^1\Sigma_g^+)) - D_0 \qquad (3)$$

This value is more precise than previous values of 6.6 ± 1.0 eV and 5.9 ± 0.2 eV reported by Gurvich[16] and Clifford *et al.*[15] respectively. The uncertainty in our value for the heat of formation for CNN is considerably less since the thermochemical cycle employed in this study is linked to the photofragments $C(^3P)$ and $N_2(X^1\Sigma_g^+)$ whose heats of formation are extremely well known. Our heat of formation is just outside the error bars of the value derived from recent photoelectron and proton affinity measurements of Clifford *et al.* However, the value obtained by Clifford *et al.* involves a thermochemical cycle referenced to $\Delta_f H_0(H_2CNN)$ for which the authors adopt a value of 2.85 eV based upon *ab initio* calculations, and this may be the cause of the discrepancy. Experimental[13,38-42] and theoretical[15,43-47] determinations for the heat of formation of diazomethane (H_2CNN) vary from 2.2-3.3 eV.

Using our $\Delta_f H_0(CNN)$, ground state frequencies from IR matrix studies,[6] and tabulated values for N_2 and C,[30] we determine $\Delta_f H_{298}(CNN) = 6.15 \pm 0.05$ eV. Our experimental results coupled with D_0(RH) and D_{298}(RH) values from Clifford *et al.* yield the heat of formation values: $\Delta_f H_0(HCNN) = 5.02 \pm 0.18$ eV, $\Delta_f H_{298}(HCNN) = 4.98 \pm 0.18$ eV, $\Delta_f H_0(H_2CNN) = 3.09 \pm 0.21$ eV, and $\Delta_f H_{298}(H_2CNN) = 3.03 \pm 0.21$ eV.

These values for the heat of formation of diazomethane are in excellent agreement with the experimental value, $\Delta_f H_{298}(H_2CNN) = 3.07 \pm 0.21$ eV, reported by Hassler and Setser[41] and theoretical values, $\Delta_f H_0(H_2CNN) = 3.09$ eV[44] and 3.06 eV,[47] based upon *ab initio* calculations of $D_0(CH_2\text{-}N_2)$.

In addition to obtaining an accurate heat of formation, the $P(E_T)$ distributions provide detailed information regarding the nature and extent of photofragment excitation and hence provide considerable insight into the dissociation mechanism. The distributions do not exhibit well-resolved vibrational structure of the N_2 fragment. The N_2 vibrational frequency is considerably larger than our energy resolution, and we would easily observe N_2 vibrational structure in the $P(E_T)$ distributions if the N_2 were rotationally cold, as was the case for NCN photodissociation.[21] The absence of such structure thus indicates that the N_2 is formed with a broad rotational energy distribution, the width of which is at least at large as the N_2 vibrational frequency (ω_e =2358 cm^{-1}) corresponding to $J \approx 35$. Assuming a single boltzmann rotational distribution for each vibrational feature and an instrument resolution of 30 meV, resolved vibrational structure of the N_2 fragment should be observed for rotational distributions which peak at J values less than 50 quanta. ($T_{rot} \approx 15{,}000$ K)

The bimodal $P(E_T)$ distributions suggest that two distinct dissociation pathways are present yielding different product state distributions. One explanation for two different distributions would be the presence of two different product channels (e.g. $C(^3P)$ and $C(^1D)$ products). However, this does not appear to be the case. E_T^{max} for the $C(^1D)$ + N_2 channel is indicated by the dot-dashed line in Figure 6. In all four $P(E_T)$ distributions

the lower energy component begins at translational energies ≥ 200 meV than this value of E_T^{max}, suggesting it is not due to $C(^1D) + N_2$. The low energy feature thus appears to be $C(^3P)$ plus highly internally excited N_2.

2. $\tilde{B}^3\Pi \leftarrow \tilde{X}^3\Sigma^-$ transitions

The $P(E_T)$ distributions for the $\tilde{B}^3\Sigma^- \leftarrow \tilde{X}^3\Sigma^-$ transitions in Figure 7 all peak at translational energies well below the maximum for ground state $C(^3P)$ products. While multiple product channels are energetically accessible, our product mass distributions suggest that the $C + N_2$ products are the dominant photolysis products. Transition K, a member of the $1_0^n 3_0^1$ progression, produces significantly more internal energy into the products than the nearby transition J of the 1_0^n progression suggesting that a mode-specific mechanism may be involved with excitation of the asymmetric stretch leading to additional excitation of the N_2 photofragment. The energy separation of the structured features in the $P(E_T)$ distributions for transitions J and K is much too large to attribute to vibrational structure of the N_2 photofragment.

The calculated maximum translational energies for channel I-V, based upon our experimentally determined value for D_0, are indicated in Figure 7 with vertically dashed lines. It is tempting to assign the various structured features to new dissociation channels. The features at 1.87 and 2.05 eV for transitions I and J appear to correspond to the opening of channel III. However, our mass ratio of 12:28 indicates that CN + N products are not formed at this translational energy and that these features must be due to internally excited $C + N_2$ products. A new feature appears to grow in for transition K peaking at 1.4 eV and the onset of this feature corresponds energetically with the opening of the spin-forbidden $C(^1S)$ channel. However, the broad resonances in the PFY spectra

suggest that the $\tilde{B}^3\Sigma^-$ state decays on an ~100 fs timescale, making an intersystem crossing mechanism less likely. We therefore propose that this feature at 1.4 eV for transition K does not correspond to C(^{1}S) products, but to vibrationally and rotationally excited C(^{3}P) products. Finally, low energy features near 0.5 eV are observed for transitions J and K. Our photofragment mass distributions, Figure 5, and N + CN $P(E_T)$ distribution for transition J, Figure 7d, indicate that this low energy feature is due to CN + N products. Due to its appearance at low translational energy (< 1 eV), we attribute this feature to CN($A^2\Pi$) + N(^{4}S) products. Our results do not show any evidence for the ground state CN($X^2\Sigma^+$) + N(^{4}S) channel, but we cannot rule it out as a minor channel contributing to the $P(E_T)$ distributions at higher E_T.

The photofragment anisotropy resulting from the $\tilde{B}^3\Sigma^- \leftarrow \tilde{X}^3\Sigma^-$ transitions are significantly more anisotropic than the $\tilde{A}^3\Pi \leftarrow \tilde{X}^3\Sigma^-$ transitions with β values close to the limiting value of +2 for a parallel transition dipole moment. This suggests rapid dissociation, a result consistent with the broad peaks seen in the PFY spectrum.

3. Origin and Higher Energy Transitions

As discussed earlier, the high translational energy signal observed for the $P(E_T)$ distribution at 2.955 eV (Fig. 8) is indicative of two-photon dissociation. The PFY spectrum at this photon energy shows a resonance corresponding to the $\tilde{A}^3\Pi \leftarrow \tilde{X}^3\Sigma^-$ (000-000) transition, indicating that the origin is an intermediate resonant state in the two-photon dissociation. It is of interest to determine the final state from which the radical dissociates. Matrix work by Jacox[4] has shown that the $\tilde{B}^3\Sigma^- \leftarrow \tilde{X}^3\Sigma^-$ band progression in an Ar matrix extends to 47619 cm^{-1}(5.90 eV) and a band assigned to a different electronic state with proposed $^3\Pi$ symmetry is observed at 48543 cm^{-1}(6.02 eV)

and 49116 cm^{-1}(6.08 eV) in Ar and N_2 matrices respectively. The electronic configurations for these states (Section I) show that both the $\tilde{B}^3\Sigma^- \leftarrow \tilde{A}^3\Pi$ and $^3\Pi \leftarrow A^3\Pi$ transitions are allowed. The $P(E_T)$ distribution obtained at an energy of 5.91 eV displays very similar structure to the 2.955 eV two-photon $P(E_T)$ distribution suggesting that the same excited state is accessed. The photofragment signal at 5.91eV was found to be particularly weak, < 1/8 of the signal of transition I, suggesting that at this energy, we do not access the strong absorption associated with the $^3\Pi$ state, but rather the blue edge of the $\tilde{B}^3\Sigma^-$ state.

Further insight is obtained from the photofragment angular distributions (Fig. 9). The anisotropy parameter for the single photon process at 5.91 eV approaches $\beta = +2$, indicating rapid dissociation via a final state of $^3\Sigma^-$ symmetry, presumably the $\tilde{B}^3\Sigma^-$ state. In contrast, the two-photon process yields negative β parameters at all E_T. Initial excitation of the $\tilde{A}^3\Pi \leftarrow \tilde{X}^3\Sigma^-$ band should in principle form aligned CNN radicals which are then dissociated by the absorption of a second photon, possibly leading to higher order terms in the angular distribution.[48,49] Nevertheless, the angular distribution is reasonably described by Eq. 1, with β approaching its limiting value of -1 at translational energies > 1.7 eV. We interpret this to mean that the lifetime of the $\tilde{A}^3\Pi$ state origin (>200 ns) is sufficiently long so that alignment is significantly reduced prior to absorption of the second photon, and that the negative anisotropy parameter reflects a perpendicular transition from the intermediate $\tilde{A}^3\Pi$ state to a rapidly dissociating upper state. This is consistent with assigning the second photon absorption to excitation of the $\tilde{B}^3\Sigma^- \leftarrow \tilde{A}^3\Pi$ band.

V. Discussion

The photofragment yield spectra, translational energy and angular distributions reveal that the CNN radical undergoes complicated dissociation dynamics. Vibronic states of the $\tilde{A}^3\Pi \leftarrow \tilde{X}^3\Sigma^-$ band $> 1000\ cm^{-1}$ above the origin dissociate readily to photoproducts $C(^3P) + N_2$ and display a bimodal internal energy distribution. At higher photon energies broad resonances attributed to the 1_0^n and $1_0^n 3_0^1$ progressions of the $\tilde{B}^3\Sigma^- \leftarrow \tilde{X}^3\Sigma^-$ band are observed. While multiple product states are available, the mass distributions indicate that N_2 loss channels dominate. A minor CN + N channel is observed for translational energies less than 0.8 eV. Finally the translational energy distributions for excitation at 2.955 eV indicate that the $\tilde{A}^3\Pi \leftarrow \tilde{X}^3\Sigma^-$ (000-000) transition is an intermediate resonant state for two-photon dissociation. For all the transitions examined, the $P(E_T)$ distributions do not exhibit well resolved vibrational structure, indicating that extensive rotational excitation of the nascent diatomic photofragments.

Previous LIF spectra[11] and our PFY spectra provide complementary information on the excited state dynamics of the CNN radical. The measured fluorescence lifetime of 220 ns for the $\tilde{A}^3\Pi$ state agrees well with the calculated value of 216 ns,[32] suggesting that this state does not undergo any radiationless processes. Since the $\tilde{A}^3\Pi$ state lies more than 1.73 eV above the lowest dissociation asymptote, these results imply a barrier to dissociation for the $\tilde{A}^3\Pi$ state. Our results concur, demonstrating that photofragments generated at the excitation energy of the $\tilde{A}^3\Pi \leftarrow \tilde{X}^3\Sigma^-$ origin are produced from a resonant two-photon process. Peak E, assigned to the 02^+0-000 transition and located

≈1200 cm^{-1} above the origin, does undergo rapid one-photon dissociation, whereas comparison of the LIF and PFY spectra indicates that fluorescence competes effectively with dissociation from the lower-lying 02^-0 state. A simple explanation of these results is the presence of a barrier located 960-1200 cm^{-1} above the origin, inhibiting dissociation from the 02^-0 state but not the 02^+0 state.

The $P(E_T)$ distributions for the $\tilde{A}^3\Pi \leftarrow \tilde{X}^3\Sigma^-$ band are bimodal with both fast and slow components attributed to $C(^3P) + N_2$ products, suggesting that there are two independent dissociation mechanisms involved. As can be seen in Figure 6, the high translational energy component is very sensitive to excitation energy, increasing in relative intensity by 250% over an energy range of only 100 meV. As mentioned above, peak E lies just above the exit barrier for dissociation from the $\tilde{A}^3\Pi$ state, so this pattern suggests that the high E_T component of the products distribution is affected by the exit barrier more than the low E_T component. As the photon energy is increased the fraction of higher translational energy products increases because passage over this barrier becomes more facile.

The absence of vibrational structure in the $P(E_T)$ distributions from the $\tilde{A}^3\Pi \leftarrow \tilde{X}^3\Sigma^-$ and $\tilde{B}^3\Sigma^- \leftarrow \tilde{X}^3\Sigma^-$ transitions and the implied high level of N_2 rotational excitation is surprising given that the ground and excited states are linear. It appears that that dissociation proceeds through bent transition states that exert substantial torque on the N_2 fragment. Extensive rotational excitation of the molecular fragment has been observed by Continetti *et al.*[22] in the photodissociation of N_3 from the linear $\tilde{B}^2\Sigma_u^+$ state; leading these authors to conclude that the dissociation mechanism involves bent geometries. In our recent photodissociation studies of the structural isomer NCN,[21]

molecular nitrogen was also found to be the dominant product channel. However, unlike the CNN radical, the translational energy distributions from NCN revealed well-resolved vibrational structure of the N_2 photofragment with fragment rotational distributions that peak between J=20-35. This relatively low level rotational excitation supports a symmetric, cyclic transition state for NCN photodissociation which can fall apart to C + N_2 without applying much torque to the molecular fragment.

The isoelectronic species, N_3^+ provides a useful system with which to compare the CNN radical. Friedman *et al.*[50] have been observed the predissociation cross-section of the $\tilde{A}^3\Pi_u \leftarrow \tilde{X}^3\Sigma_g^-$ band. No fragmentation was observed for the origin, located 0.87 eV above the $N^+(^3P) + N_2(X^1\Sigma_g^+)$ dissociation assymptote and the first assigned predissociative transition is the 020-000 band. No assignment of the upper and lower Renner components was made. Individual rotational lines for the 100-000 transition were resolved and all were found to be instrumentally narrow placing a lower limit on the excited state lifetime of > 50 ps. The authors propose that the inability of the origin to dissociate and the long lifetime of the 100-000 state is due to a barrier along the dissociation coordinate. This hypothesis is borne out by recent *ab initio* calculations by Bennett *et al.*[51] on the collinear adiabatic potential energy surfaces of N_3^+; these show a substantial barrier (~1 eV) for dissociation of the $\tilde{A}^3\Pi$ state to products $N^+(^3P) + N_2(X^1\Sigma_g^+)$ resulting from an avoided crossing between the $\tilde{A}^3\Pi$ state, which diabatically correlates with $N + N_2^+$ products (isoelectronic with N + CN), and a repulsive $^3\Pi$ state that correlates diabatically with lower-lying $N^+(^3P) + N_2(X^1\Sigma_g^+)$ products (isoelectronic with $C + N_2$). The absence of predissociation of the $\tilde{A}^3\Pi$ state

000 level due to a barrier along the dissociation coordinate thus occurs in both N_3^+ and CNN, and it is reasonable to assume a similar origin for this barrier in CNN.

The calculations by Bennett *et al.*[51] indicate that excited state dissociation of N_3^+ is strongly affected by non-adiabatic effects, including avoided crossings and conical intersections. For example, in addition to the avoided crossing involving the $\tilde{A}^3\Pi$ state in collinear geometries, this state also undergoes a conical intersection with an excited $^3\Sigma^-$ state. As a consequence, the effective barrier to dissociation is reduced if the molecule becomes non-linear. If a similar picture can be applied to CNN dissociation, dissociation through a bent geometry may provide the lowest energy pathway to C + N_2 products, providing a possible explanation for the extensive rotational excitation seen in the N_2 product in our experiment. We hope that future theoretical work on both linear and nonlinear potential energy surfaces of CNN will allow for a detailed picture of the nonadiabatic processes involved in its dissociation.

VI. Conclusions

The photodissociation spectroscopy and dynamics of the $\tilde{A}^3\Pi$ and $\tilde{B}^3\Sigma^-$ have been investigated by fast beam photofragment spectroscopy. Gas-phase predissociative resonances have been observed for the $\tilde{A}^3\Pi \leftarrow \tilde{X}^3\Sigma^-$ band. The origin transition of this band does not dissociate, but is an intermediate state in a resonant two-photon excitation promoting the CNN radical to a high vibronic states of the $\tilde{B}^3\Sigma^-$ state which subsequently dissociates. Our results suggest that the $\tilde{A}^3\Pi$ state possess a barrier to dissociation approximately 1000 cm^{-1} above the origin. PFY spectra show broad resonances for the $\tilde{B}^3\Sigma^- \leftarrow \tilde{X}^3\Sigma^-$ band providing the first gas-phase observation of this band.

Photodissociation of the CNN radical in the $\tilde{A}^3\Pi$ and $\tilde{B}^3\Sigma^-$ states induces large rotational excitation of the N_2 product obscuring any underlying vibrational structure of the N_2 fragment, implying that nonlinear geometries are involved in fragmentation. Further, our results show that the NCN and CNN radicals access different regions of the global $C + N_2$ potential energy surface. The former dissociates via a C_{2v} type mechanism yielding low rotational excitation, while the latter dissociates via bent transition states imparting much more torque on the recoiling N_2 fragment. Additionally, we have obtained an accurate heat of formation for the CNN radical from which we derive the heats of formation of HCNN and H_2CNN.

Acknowledgements

This research is supported by the Director, Office of Energy and Research, Office of Basic Energy Sciences, Chemical Sciences Division, of the U.S. Department of Energy under Contract No. DE-AC03-76F00098. RTB would like to thank Prof. G.B. Ellison and Dr. E.P Clifford for useful discussions regarding the synthesis of diazomethane and the preparation of CNN^-, A. J. Souers for synthetic equipment, and Prof. P.J. Sarre for useful comments regarding the $\tilde{A}^3\Pi \leftarrow \tilde{X}^3\Sigma^-$ spectrum.

References

1 C. P. Fenimore, in *Procedings of the Thirteenth Symposium (International) on Combustion* (The Combustion Institute, Pittsburgh, Pa, 1971), pp. 373.

2 E. Wasserman, L. Barash, and W. A. Yager, J. Am. Chem. Soc. **87,** 2075 (1965).

[3] G. R. Smith and W. Weltner, Jr., J. Chem. Phys. **62,** 4592 (1975).

[4] D. E. Milligan and M. E. Jacox, J. Chem. Phys. **44,** 2850 (1966).

[5] R. L. DeKock and W. Weltner, Jr., J. Am. Chem. Soc. **93,** 7106 (1971).

[6] B. E. Wurfel, A. Thoma, R. Schlachta, and V. E. Bondybey, Chem. Phys. Lett. **190,** 119 (1992).

[7] T. D. Goldfarb and G. C. Pimentel, J. Am. Chem. Soc. **82,** 1865 (1959).

[8] G. W. Robinson and M. McCarty Jr., J. Am. Chem. Soc. **82,** 1859 (1960).

[9] W. Weltner Jr. and D. McLeod Jr., J. Chem. Phys. **45,** 3096 (1966).

[10] M. Tulej, J. Fulara, A. Sobolewski, M. Jungen, and J. P. Maier, J. Chem. Phys. **112,** 3747 (2000).

[11] V. E. Bondybey and J. H. English, J. Chem. Phys. **67,** 664 (1977).

[12] M. E. Jacox, J. Mol. Spec. **72,** 26 (1978).

[13] W. Braun, A. M. Bass, D. D. Davis, and J. D. Simmons, Proc. Roy. Soc. Lond. **A312,** 417 (1969).

[14] M. C. Curtis, A. P. Levick, and P. J. Sarre, Laser Chem. **9,** 359 (1988).

[15] E. P. Clifford, P. G. Wenthold, W. C. Lineberger, G. A. Petersson, K. M. Broadus, S. R. Kass, S. Kato, C. H. DePuy, V. M. Bierbaum, and G. B. Ellison, J. Phys. Chem. A **102,** 7100 (1998).

[16] L. V. Gurvich, I. V. Veyts, C. B. Alcock, and V. S. Iorish, *Thermodynamic Properties of Individual Substances*, 4th ed. (Hemishpere, New York, 1991).

[17] A. D. Walsh, J. Chem. Soc. , 2266 (1953).

[18] H. U. Suter, M. B. Huang, and B. Engels, J. Chem. Phys. **101,** 7686 (1994).

[19] J. L. Wilkerson and W. A. Guillory, J. Mol. Spec. **66,** 188 (1977).

[20] J. M. L. Martin, P. R. Taylor, J. P. Francois, and R. Gijbels, Chem. Phys. Lett. **226,** 475 (1994).

[21] R. T. Bise, H. Choi, and D. M. Neumark, J. Chem. Phys. **111,** 4923 (1999).

[22] R. E. Continetti, D. R. Cyr, D. L. Osborn, D. J. Leahy, and D. M. Neumark, J. Chem. Phys. **99,** 2616 (1993).

[23] D. J. Leahy, D. L. Osborn, D. R. Cyr, and D. M. Neumark, J. Chem. Phys. **103,** 2495 (1995).

[24] D. L. Osborn, H. Choi, D. H. Mordaunt, R. T. Bise, D. M. Neumark, and C. M. Rohlfing, J. Chem. Phys. **106,** 3049 (1997).

[25] D. L. Osborn, D. J. Leahy, D. R. Cyr, and D. M. Neumark, J. Chem. Phys. **104,** 5026 (1996).

[26] F. Arndt., in *Organic Synthesis Collective*, Vol. vol II (John Wiley & Sons, 1943), pp. 165.

[27] J. M. B. Bakker, J. Phys. E **6,** 785 (1973).

[28] J. M. B. Bakker, J. Phys. E **7,** 364 (1974).

[29] D. P. de Bruijn and J. Los, Rev. Sci. Instrum. **53,** 1020 (1982).

[30] M. W. Chase Jr., J. Phys. Chem. Ref. Data **Monograph 9,** 1 (1998).

[31] Y. Huang, S. A. Barts, and J. B. Halpern, J. Phys. Chem. **96,** 425 (1992).

[32] Z. L. Cai, G. H. Sha, C. H. Zhang, and M. B. Huang, J. Mol. Struct. (THEOCHEM) **85,** 303 (1992).

[33] M. C. Curtis, Ph.D. Thesis, University of Nottingham .

[34] C. Devillers and D. A. Ramsay, Can. J. Phys. **49,** 2839 (1971).

[35] M. Fujitake, R. Kiryu, and N. Ohashi, J. Mol. Spec. **154,** 169 (1992).

[36] G. Herzberg and D. N. Travis, Can. J. Phys. **42,** 1658 (1964).

[37] V. E. Bondybey and J. H. English, J. Mol. Spec. **70,** 236 (1978).

[38] A. H. Laufer and H. Okabe, J. Am. Chem. Soc. **93,** 4137 (1971).

[39] A. Langer, J. A. Hipple, and D. P. Stevenson, J. Chem. Phys. **22,** 1836 (1954).

[40] G. S. Paulett and P. E. Ettinger, J. Chem. Phys. **39,** 825 (1963).

[41] J. C. Hassler and D. W. Setser, J. Am. Chem. Soc. **87,** 3793 (1965).

[42] W. Braun, A. M. Bass, and M. Pilling, J. Chem. Phys. **52,** 5131 (1970).

[43] G. Leroy and M. Sana, Theor. Chim. Acta (Berl.) **32,** 329 (1974).

[44] J. Lievin and G. Verhaegen, Theor. Chim. Acta (Berl.) **42,** 47 (1976).

[45] M. S. Gordon and S. R. Kass, J. Phys. Chem. **99,** 6548 (1995).

[46] S. P. Walch, J. Chem. Phys. **103,** 4930 (1995).

[47] A. Papakondylis and A. Mavridis, J. Phys. Chem. A **103,** 1255 (1999).

[48] R. N. Zare, Molecular Photochemistry **4,** 1 (1972).

[49] S. J. Singer, K. F. Freed, and Y. B. Band, J. Chem. Phys. **81,** 3064 (1984).

[50] A. Friedman, A. M. Soliva, S. A. Nizkorodov, E. J. Bieske, and J. P. Maier, J. Phys. Chem. **98,** 8896 (1994).

[51] F. R. Bennett, J. P. Maier, G. Chambaud, and P. Rosmus, Chem. Phys. **209,** 275 (1996).

Chapter 5. Photoisomerization and photodissociation pathways of the HNCN free radical.

The photodissociation spectroscopy and dynamics of the HNCN free radical have been investigated by fast beam photofragment translational spectroscopy. Predissociative transitions for both the $\tilde{B}^2A' \leftarrow \tilde{X}^2A''$ band and a higher energy band system assigned to the $\tilde{C}^2A'' \leftarrow \tilde{X}^2A''$ band were observed. Photofragment mass distributions indicate that the molecular elimination of N_2 is the primary dissociation pathway. Translational energy distributions reveal resolved vibrational structure of the N_2 fragment, suggesting that the HNCN radical first isomerizes to a cyclic-HCN_2 intermediate. The results of a modified impulsive model support a dissociation mechanism which involves a tight three-center transition state. The bond dissociation energy, D_0 and enthalpy of formation, $\Delta_f H_0(HNCN)$ were determined to be 2.80 ± 0.03 eV and 3.35 ± 0.03 eV respectively.

I. Introduction

The structural isomers of HCN_2 have been proposed as important intermediates in the formation of "prompt" NO,[1-5] providing low-energy pathways for the splitting of molecular nitrogen via the $CH(^2\Pi) + N_2 \rightarrow HCN + N(^4S)$ reaction, the initiating step of the Fenimore mechanism. Both N and HCN are subsequently oxidized rapidly by O atoms and OH radicals respectively to form nitric oxide. Although the initial reaction, is only slightly endothermic (< 0.1 eV) it is spin-forbidden and is expected to have a low cross-section.

The $CH + N_2$ reaction has been studied in detail both experimentally[1,3,5,6] and theoretically[2,3,7-16] Early experimental work on this reaction has been reviewed by Miller and Bowman.[2] Recent shock tube studies by Dean *et al.*[5] and Lindackers *et al.*[6] have directly detected the $N(^4S)$ atom and show that the $N(^4S)$ atom appearance is correlated with the removal of CH. Numerous theoretical studies[7-10,13] indicate that the reaction pathway with the highest probability proceeds through an intermediate doublet cyclic HCN_2 species which then intersystem crosses to a quartet surface and finally couples out to quartet products $N(^4S) + HCN$. However, recent *ab initio* calculations by Cui *et al.*[10] determine the thermal rate constant *k(T)* to be two orders of magnitude lower than experimental results.

The most stable HCN_2 isomer is HNCN, the subject of this study. With the exception of recent *ab initio* calculations by Moskoleva and Lin,[11] the HNCN isomer has been ignored as a possible intermediate in the $CH + N_2$ reaction. Previous studies by Clifford *et al.*[17] indicate that the structural isomer HNCN lies more than 2.8 eV below the $CH + N_2$ channel, compared to 1.13 eV for lin-HCNN(Ref. 18) and 1.02 eV for c-HCNN (Refs. 9 and 10) and may therefore be an important intermediate in the overall $CH + N_2$ reaction. Moskaleva and Lin[11] have calculated a low-lying transition state for the isomerization of HNCN to c-HCNN, at 0.51 eV above the $CH + N_2$ dissociation asymptote. Based upon their *ab initio* calculation and RRKM rate constants, these authors propose that at high temperatures the $CH + N_2$ does not yield the low-energy spin $N(^4S) + HCN$, but instead through the HNCN radical favors the more endoergic spin-allowed $H(^2S) + NCN(\tilde{X}\,^3\Sigma_g^-)$ products. Prompt NO is then formed by rapid oxidation

of the NCN radical. In an effort to further characterize the global CH + N_2 potential energy surface and assess the importance of the HNCN radical as a possible intermediate in the CH + N_2 reaction, we have investigated the photodissociation spectroscopy and dynamics of the HNCN radical.

The HNCN radical was first spectroscopically identified by Herzberg and Warsop,[19] who reported a rotationally resolved $^2A' \leftarrow ^2 A''$ electronic absorption (T_0 = 28994 cm^{-1}), determining the molecular structure for both the ground and excited state and tentatively assigning this absorption to the $\tilde{B}^2A' \leftarrow \tilde{X}^2A''$ band. The HNC bond angle for the ground state was found to be 116.5° with a nearly linear NCN backbone. Wu *et al.*[20] measured laser-induced fluorescence of the $\tilde{B}^2A' \leftarrow \tilde{X}^2A''$ origin determining the excited state lifetime to be 20 ± 5 ns. Upon dispersing the fluorescence, the symmetric stretch (ν_2 =1140 cm^{-1}) and the δ(HN-C-N) a″ mode ($\nu_6 \approx$ 440 cm^{-1}) were found to be vibronically active; the ν_6 mode was attributed to vibronic coupling via a Renner-Teller type interaction. Travis and Herzberg[21] have also reported higher energy absorption bands at 30475 cm^{-1} and 31550 cm^{-1} from the flash photolysis of diazomethane showing complicated sub-band structure which shifts upon deuteration. These higher energy absorption bands have been observed by Basco and Yee,[22] Kroto and coworkers,[23] and more recently by Mathews *et al.*[24] from a variety of photolysis sources.

In recent microwave absorption studies, Yamamoto and Saito[25] determined that the unpaired electron occupies an orbital perpendicular to the molecular plane of symmetry and estimate the energy difference between the Renner-Teller pairs, $\tilde{X}^2A''$ and $\tilde{A}^2A'$, to be approximately 1.5 eV. Photoelectron studies by Clifford *et al.*[17] of the

$HNCN^-$ anion yielded the electron affinity of HNCN (EA = 2.622 ± 0.005 eV) and vibrational frequencies of 1049 ± 162 cm^{-1} and 1879 ± 106 cm^{-1} for the ν_2 and ν_3 modes respectively, in reasonable agreement with the matrix IR[26] and dispersed fluorescence studies.[20] Additionally, their studies place the $\tilde{A}^2A'$ state at least 0.7 eV above the $\tilde{X}^2A''$ state. Higher energy photoelectron studies performed in our lab[27] have located the $\tilde{A}^2A'$ state, finding the $\tilde{X}^2A''$ - $\tilde{A}^2A'$ splitting to be 0.7 eV. Unlike the $\tilde{X}^2A''$ state, which displays a nearly vertical photodetachment spectrum showing little vibrational excitation, the $\tilde{A}^2A'$ state yields a broad band (~ 1 eV in width). No regular vibrational structure was observed for this state.

Ab initio calculations of the molecular geometry and vibrational frequencies of the ground state have been performed recently by Clifford *et al.*[17] Their calculations are in reasonable agreement with the experimental vibrational frequencies determined in their photoelectron studies, the LIF results of Wu *et al.*[20] and previous *ab initio* results of Tao *et al.*[28] Both sets of calculations support an acetylenic structure showing a shorter HNC ≡ N and longer HN-CN bond with HNC bond angles between 110.8° to 113.6° and a nearly linear NCN bond angle of 175°, in good agreement with the spectroscopic results of Herzberg and Travis[19]

The HNCN radical provides an intriguing system for photodissociation studies. The enthalpies of reaction (at 0 K), $\Delta_{rxn}H_0$, for the energetically available product channels derived from this work and accepted literature values are shown below.

$HNCN(\tilde{X}^2A'') \xrightarrow{h\upsilon}$

$N_2(\tilde{X}^1\Sigma_g^+) + CH(\tilde{X}^2\Pi)$	2.80 ± 0.03 eV	(I)
$HCN(\tilde{X}^1\Sigma^+) + N(^4S)$	2.87 ± 0.05 eV	(II)
$HNC(\tilde{X}^1\Sigma^+) + N(^4S)$	3.45 ± 0.05 eV	(III)
$N_2(\tilde{X}^1\Sigma_g^+) + CH(\tilde{a}^4\Sigma)$	3.54 ± 0.03 eV	(IV)
$H(^2S) + NCN(\tilde{X}^3\Sigma_g^-)$	3.72 ± 0.04 eV	(V)

Dissociation to the lowest energy channels (I-IV) requires substantial bond rearrangement and/or intersystem crossing (ISC) to quartet surfaces.

The photofragmentation studies performed here show that vibronic levels of both the $\tilde{B}^2A'$ state and a higher energy band system (31200 to 34700 cm^{-1}) assigned to the $\tilde{C}^2A''$ state are predissociatve. Photofragment mass distributions found N_2 + CH to be the primary dissociation channel. Translational energy distributions display resolved structure corresponding to vibrational excitation of the N_2 photofragment. The formation of N_2 in the photolysis of HNCN suggests that this raical is a likely intermediate in the reverse reaction of CH + N_2.

II. Experiment

The fast beam photofragment translational spectrometer[29-31] used in these studies is shown in Figure 1. Vibrationally and rotationally cold neutral radicals are produced by mass-selectively photodetaching a beam of stable negative ions. The neutral radicals are then photodissocated by a second laser and the photofragments are detected directly with high efficiency

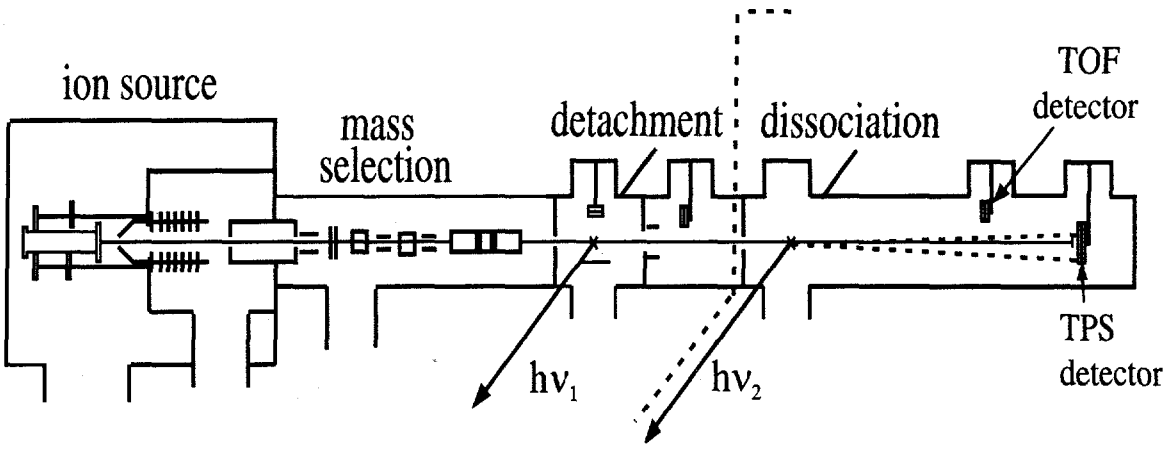

Figure 1. Fast beam photofragment translational spectrometer. The dotted line separates the radical production section on the left from the photodissociation experiment on the right.

. To generate sufficient number density of $HNCN^-$ ions, we made a slight modification to our pulsed electric discharge source[32] by inserting a reservoir of cyanamide (H_2NCN) between the pulsed molecular beam valve and the pulsed electric discharge. Our adaption of this source has been described previously.[33] Argon at a stagnation pressure of ~ 2 atm is expanded through a pulsed molecular beam valve into the reservoir containing cyanamide and finally through the discharge, generating CN^-, NCN^-, and $HNCN^-$ ions. Analysis of the photofragment yield spectrum obtained in this study and in previous studies[34] indicates that this source typically produces anions with rotational and vibrational temperatures of 60 and 200 K, respectively. D_2NCN was produced by repeated washing of the cyanamide crystals with a methanol-d_4/acetic acid-d_4 solution (20:1 by volume) followed by evaporation of the solvent. From our ion mass distributions, we estimate the extent of deuteration to be $\leq 40\%$.

The negative ions generated in the source region are accelerated to 8 keV and separated temporally by a Bakker time-of-flight (TOF) mass spectrometer[35,36] with a mass resolution ($m/\Delta m$) $\approx$ 100. The ion of interest is selectively photodetached by a pulsed dye laser. To generate vibrationally cold radicals, an excimer pumped dye laser is tuned to 2.74 eV, which is 118 meV above the detachment threshold based upon the photoelectron studies of Clifford *et al.*[17] Undetached ions are deflected out of the beam path.

In the dissociation region, the fast beam of neutrals are intersected by a second excimer-pumped dye laser. A fraction of the neutrals absorb and dissociate yielding photofragments detected directly by either the TOF or TPS (time and position sensing) microchannel plate detector assemblies shown in Figure 1. An aluminum strip is positioned at the center of each detector to prohibit undissociated radicals from impacting the detector, so that the observed signal is entirely from recoiling photofragments.

Two types of experiments are preformed. First, the spectroscopy of the dissociative electronic states is examined by scanning the dissociation laser and monitoring the total flux of photofragments arriving at the retractable TOF detector, located 0.68 m from the dissociation laser. The resulting photofragment yield (PFY) spectra is complementary to absorption and fluorescence measurements. We examined the photolysis of the HNCN radical from 28800 to 34850 cm^{-1}. The fundamental output of the dye laser with a bandwidth of 0.2 cm^{-1} was used to cover the $\tilde{B}^2A' \leftarrow \tilde{X}^2A''$ band from 28800 cm^{-1} to 29850 cm^{-1} while the dye laser output was frequency-doubled using KDP-R6G and BBO-B crystals to cover frequencies from 29850 to 34850 cm^{-1} with a laser bandwidth of 0.3 cm^{-1}. Saturation and power-broadening effects were observed for

the $\tilde{B}^2A' \leftarrow \tilde{X}^2A''$ band at laser fluences > 30 mJ/cm^2 and it was therefore scanned at fluences < 20 mJ/cm^2. No noticeable saturation effects were seen for the higher energy transitions.

Once the spectroscopy of the dissociative states has been examined, the dissociation dynamics at selected photolysis energies are investigated. In this experiment, both photofragments from a single parent radical are detected in coincidence using a time-and-position sensing (TPS) detector based upon the concept developed by de Bruijn and Los.[37] This detection scheme has been described in detail elsewhere.[29,30] The TPS detector records the positions and difference in arrival time of the two photofragments from a single dissociation event. This information is then used to determine the masses of the fragments, their relative translational energy, E_T, and the scattering angle θ between the relative velocity vector of the polarized dissociation laser. This coincident detection scheme requires that photofragment mass ratio be less than 4. The photofragment mass resolution, $m/\Delta m$, is $\approx$10 and the translational energy resolution is $\Delta E_T/E_T = 2.0\%$. As discussed in a previous paper,[34] the relatively poor mass resolution for the photofragments is due to the size of the radical beam of ~1mm diameter at the TPS detector.

III. Results

A. Photofragment Yield Spectra

1. $\tilde{B}^2A' \leftarrow \tilde{X}^2A''$ transitions

The photofragment yield spectra for the $\tilde{B}^2A' \leftarrow \tilde{X}^2A''$ band are displayed in Figures 2a and 2b. Figure 2a shows the photofragment yield spectra between 28850 to

29170 cm^{-1} and displays sharp intense features separated by ≈ 40 cm^{-1}, consistent with the $\tilde{B}^2A' \leftarrow \tilde{X}^2A''$ origin transition first observed in higher resolution absorption experiments by Herzberg and Warsop[19] and later via LIF by Wu *et al.*[20] The band displays features characteristic of a perpendicular transition for a nearly prolate symmetric top, with sharp Q-branches and weaker P and R branches. The K_a selection rules for this transition, where K_a is the projection of rotational angular momentum along the *a*-inertial axis, are $\Delta K_a = \pm 1,3 \ldots$ The excited and ground state K_a quantum numbers, K_a' and K_a'' respectively, are indicated for each sub-band in Figure 2a. using the notation K_a'-K_a''. A fit to the rotational contour of the $K_a' = 2 \leftarrow K_a'' = 1$ sub-band yields a temperature of ≈ 60 K for rotation about the *b* and *c*-axes. The K_a-structure reveals a hotter distribution with a characteristic temperature of ~200K. $K_a \neq 0$ levels are two-fold degenerate and hence the $K_a' = 2 \leftarrow K_a'' = 1$ subb-band is nearly twice as intense as the $K_a' = 0 \leftarrow K_a'' = 1$ sub-band.

In addition to the origin band, we observe a new weak band located ≈ 560 cm^{-1} to the blue, see Figure 2b. The most intense features are spaced by approximately 80 cm^{-1}, twice that observed for the origin band, and display broader rotational contours than the origin band. The band is attributed to a parallel vibronic transition (see section IV.A) with K_a selection rules $\Delta K_a = 0, \pm 2, 4 \ldots$ The sub-band K_a values are labeled using the same notation described above for the $\tilde{B}^2A' \leftarrow \tilde{X}^2A''$ origin transition.

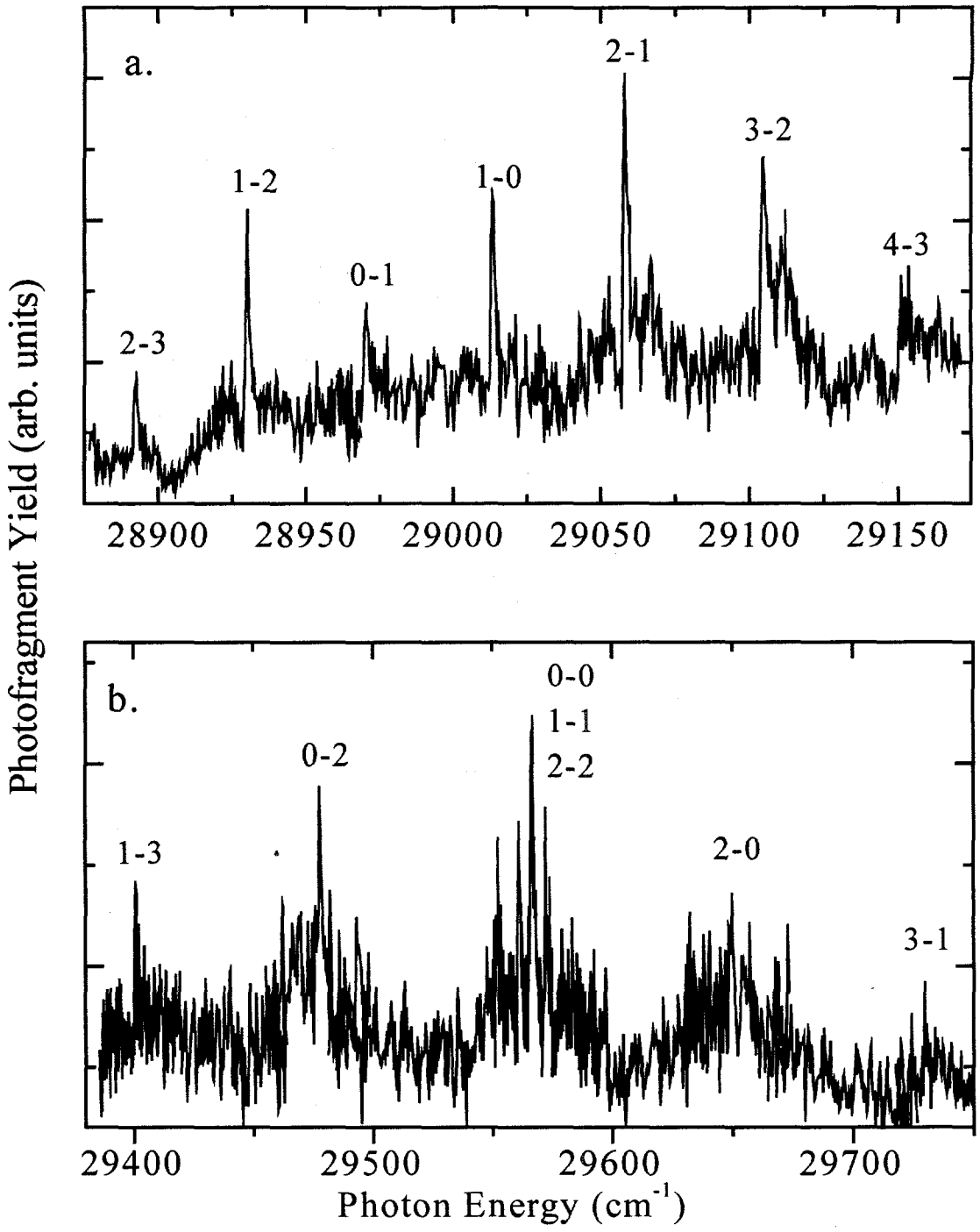

Figure 2. (a) Photofragment Yield (PFY) spectra of the $\tilde{B}^2A' \leftarrow \tilde{X}^2A''$ origin, showing $\Delta K_a = \pm 1$ transitions. The K_a stacks are labeled as $K_a' - K_a''$. **(b)** PFY spectra of a parallel vibronic band of the $\tilde{B}^2A' \leftarrow \tilde{X}^2A''$ band showing $\Delta K_a = 0, \pm 2$. This band is assigned to the $\delta(HN-C-N)$ a'' ν_6 bend mode.

2. Higher energy transitions

Higher energy transitions originate near 31500 cm^{-1} and show a progression of features spaced by ~1000 cm^{-1}, see Figure 3a, with the most intense feature located near 32500 cm^{-1}. A detailed list of the transition energies and relative intensities for the HNCN and DNCN photofragment yield spectra is given in Table I with the vibrational spacing defined as the energy difference between the intensity maxima of each vibronic transition. The observed PFY transitions are consistent a number of previously reported absorption bands.[21-24] Despite extensive scanning, we were unable to observe the lowest reported member of this progression near 30475 cm^{-1}.[21,24]

Expanded views of 31550 cm^{-1} and 32550 cm^{-1} transitions are shown in Figure 3b. As can be seen in Figures 3a and 3b, the sub-band structure of the 31500 cm^{-1} transition is remarkably different from the higher energy transitions. The 31550 cm^{-1} transition displays three main sub-bands of nearly equal intensity and a spacing of $\approx$ 24 cm^{-1} which are denoted X,Y and Z following the labeling scheme of Mathews and coworkers.[24] Feature X is split into three main peaks split by nearly 5 and 7 cm^{-1}, while Y shows smaller splittings of 2 and 3 cm^{-1}. Feature Z is split into a doublet with a peak separation of 6 cm^{-1}. The observed sub-band structure for this transition is excellent agreement with that observed by Kroto and coworkers[23] (see Figure 4, Ref. 23) and by Mathews *et al.*[24]

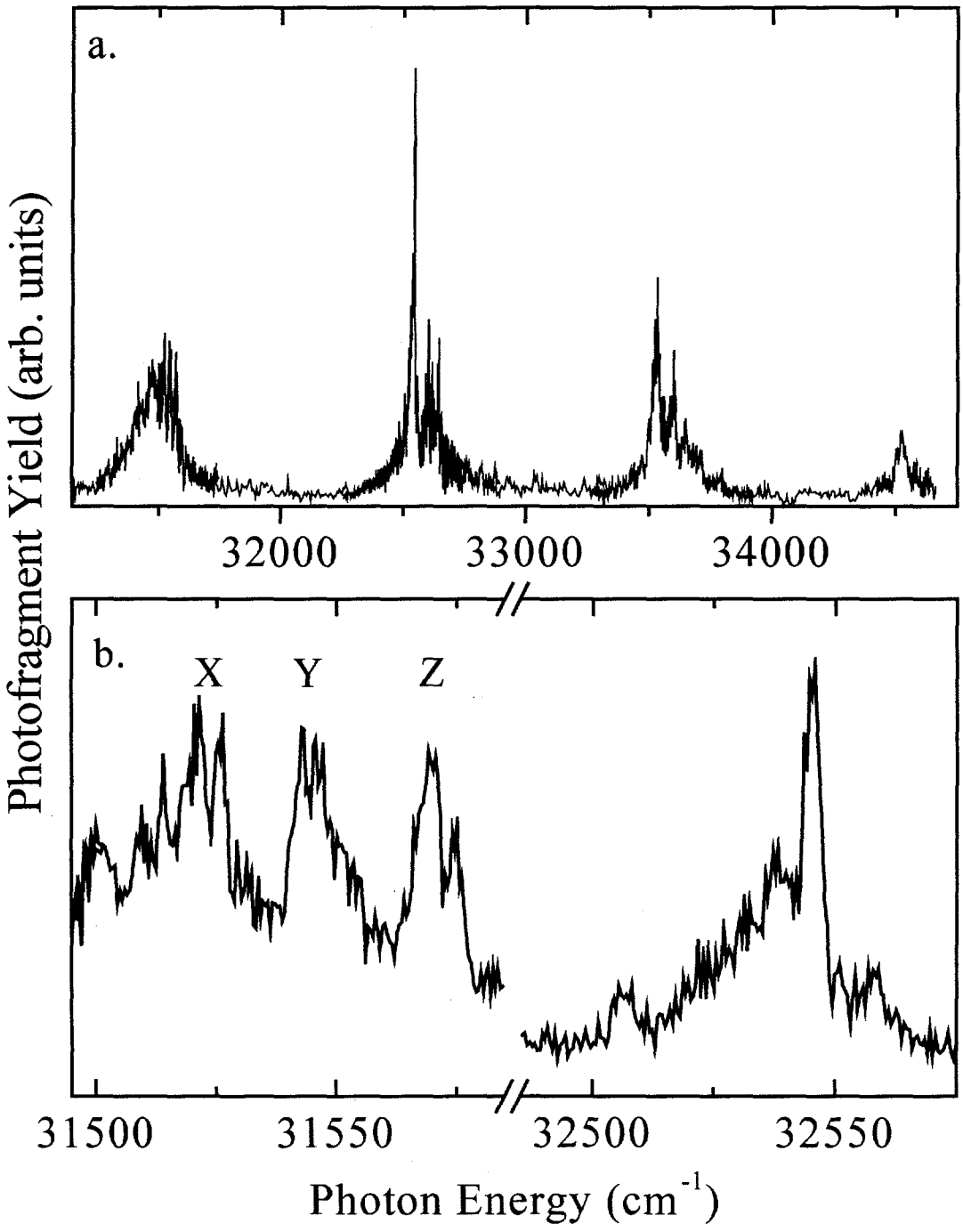

Figure 3(a) PFY spectra of the HNCN radical from 31000-35000 cm^{-1}. This band has been assigned to the $\tilde{C}^2A'' \leftarrow \tilde{X}^2A''$ band. (b) Expanded views of the 31550 cm^{-1} and 32550 cm^{-1} vibrionic transitions. For the 31550 cm^{-1} band, three major sub-bands are labeled X, Y, and Z are labeled with a spacing of $\approx$ 24 cm^{-1}

Table I. Photofragment Yield Transition Energies for HNCN and DNCN

HNCN			DNCN		
Transition (cm^{-1})	Relative Intensity	Vibrational Spacing (cm^{-1})	Transition (cm^{-1})	Relative Intensity	Vibrational Spacing (cm^{-1})
31521	5		31506	10	
31526	5		31522	8	
31543	5		31531	6	
31545	5				
31547	5				1036
31568	5		32542	8	
31574	4				
		1024			
32505	2				
32538	6				
32545	10				
32603	4				
32620	3				
32640	3				
32645	3				
		989			
33521	4				
33534	5				
33601	3				
33644	2				
		991			
34525	1.3				

Higher energy transitions, of which the 32550 cm^{-1} band in Figure 3b is an example, are dominated by an intense peak to the red which is strongly red degraded. Less intense sub-bands (not shown in the Figure 3b.) are located to the blue and do not display any regular sub-band spacing. The FWHM of the most intense sub-bands of each vibronic transition increase with photon energies with values of 5, 10 and 50 cm^{-1} respectively for the features at 32545, 33524, and 34525 cm^{-1}.

For DNCN, transitions were observed near 31530 and 32547 cm^{-1} and are strongly red degraded. The peak positions are similar to those observed for HNCN showing no real isotope effect. A significant isotope effect is observe for the sub-band structure of the 31531 cm^{-1} band with peak spacings of 9 and 16 cm^{-1} compared to 24 cm^{-1} for HNCN indicating that the sub-band structure is due to rotational K_a structure. Unlike, HNCN the intensity of the sub-bands increase to the blue with the most intense sub-band peaking at 31531 cm^{-1}. This may be due to more effective rotational cooling of K_a structure for DNCN. Only a single red degraded peak for the 32547 cm^{-1} transition. These observations are again in excellent agreement with the absorption studies of Kroto and coworkers[23] and Mathews *et al.*[24]

B. Photofragment Mass Distributions

At the photon energies employed in this study between 3.603 and 4.157 eV, multiple dissociation channels are energetically accessible. Prior to this study, the best available value for $\Delta_f H_0(\mathrm{HNCN}) = 3.34 \pm 0.17$ eV was provided by the work of Clifford *et al.*[17] The energy separation of products I and II and products III and IV is less than this uncertainty. We therefore cannot rely on the energetics alone to identify the major product channel and use experimental photofragment mass distributions to

distinguish between products. As mentioned in our earlier work,[34] our photofragment mass resolution, $m/\Delta m \approx 10$ is limited by the finite diameter of our molecular beam. With this limited mass resolution, it is difficult to distinguish between CH + N_2 products from HCN + N products with mass ratios of 13:28 and 14:27 respectively. An unambiguous assignment of the product channels required photolysis of the deuterated species, DNCN. For DNCN, both the CD + N_2 and DCN + N have the same photo-

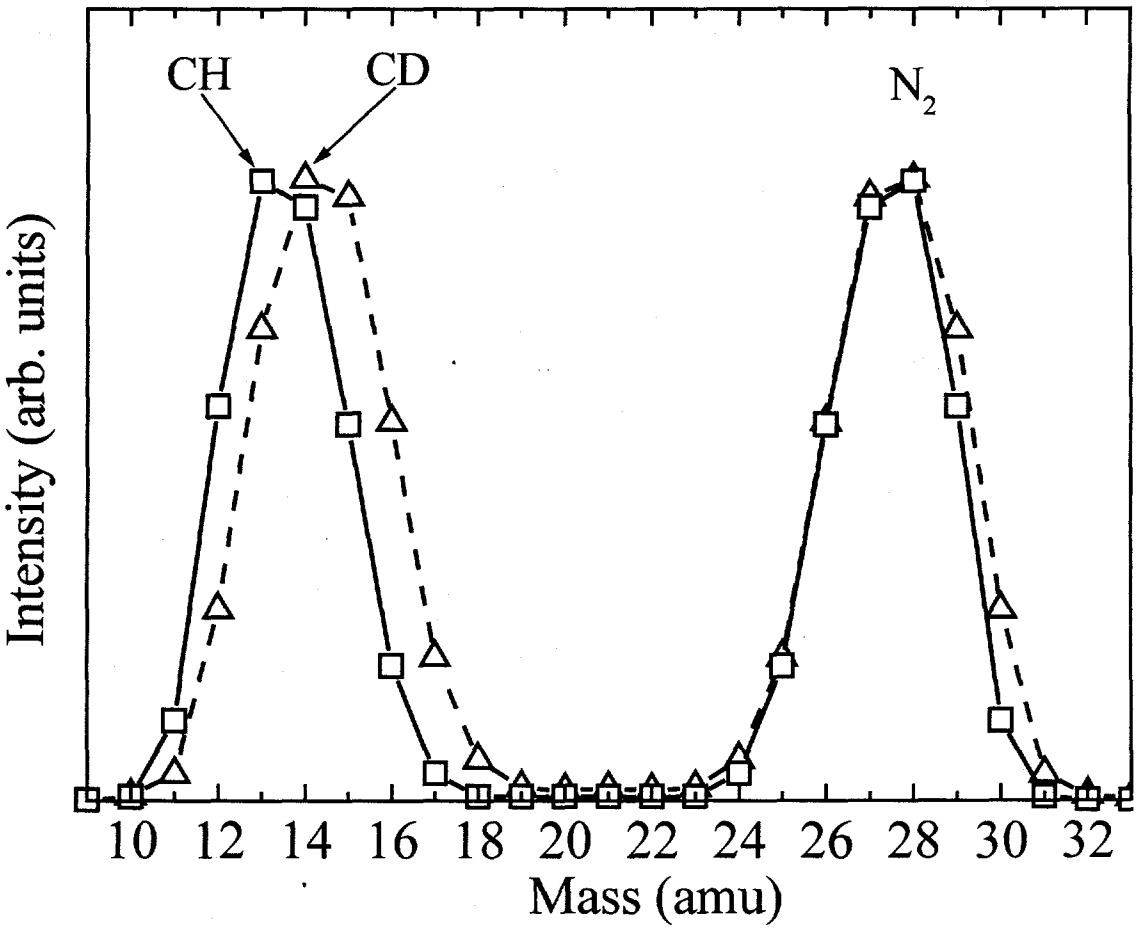

Figure 4. Photofragment mass distributions for the fragmentation of HNCN (squares) and DNCN(triangles) showing the photoproducts to be CH(CD) + N_2.

fragment mass ratio of 2:1. Figure 4 shows the photofragment mass distributions for HNCN and DNCN. The width of the mass distributions for HNCN is identical to that for DNCN indicating that only one mass channel contributes. The mass of the light photofragment from HNCN is shifted one mass unit lower than DNCN, establishing CH + N_2 as the product channel. Although the H-loss channel is energetically available for transitions greater than 3.72 eV, our coincident detection scheme requires a photofragment mass ratio < 4 and we are therefore insensitive to the H-loss channel.

C. Photofragment Translational Energy Distributions

The translational energy distributions for the $\tilde{B}^2A' \leftarrow \tilde{X}^2A''$ origin band and the higher energy transitions are shown for HNCN and DNCN in Figures 5 and 6 . All the distributions display sharp onsets at high translational energy and reveal structured features with peak separations ranging from 220 to 260 meV. For HNCN, the $P(E_T)$ distribution from excitation at 3.603 eV displays a particularly sharp onset at 0.795 eV, defining the maximum translational energy, E_T^{max}. Using this value of E_T^{max} we determine the bond dissociation energy (see section IV.B.) from which we calculate the expected E_T^{max} values for higher photon energy transitions, which are displayed as dashed vertical lines in Figures 5 and 6. The signal for these $P(E_T)$ distributions rise sharply near the calculated values of E_T^{max}. Very weak signal is observed above E_T^{max} and is attributed to photoexcitation from vibrationally excited levels of the ground state.

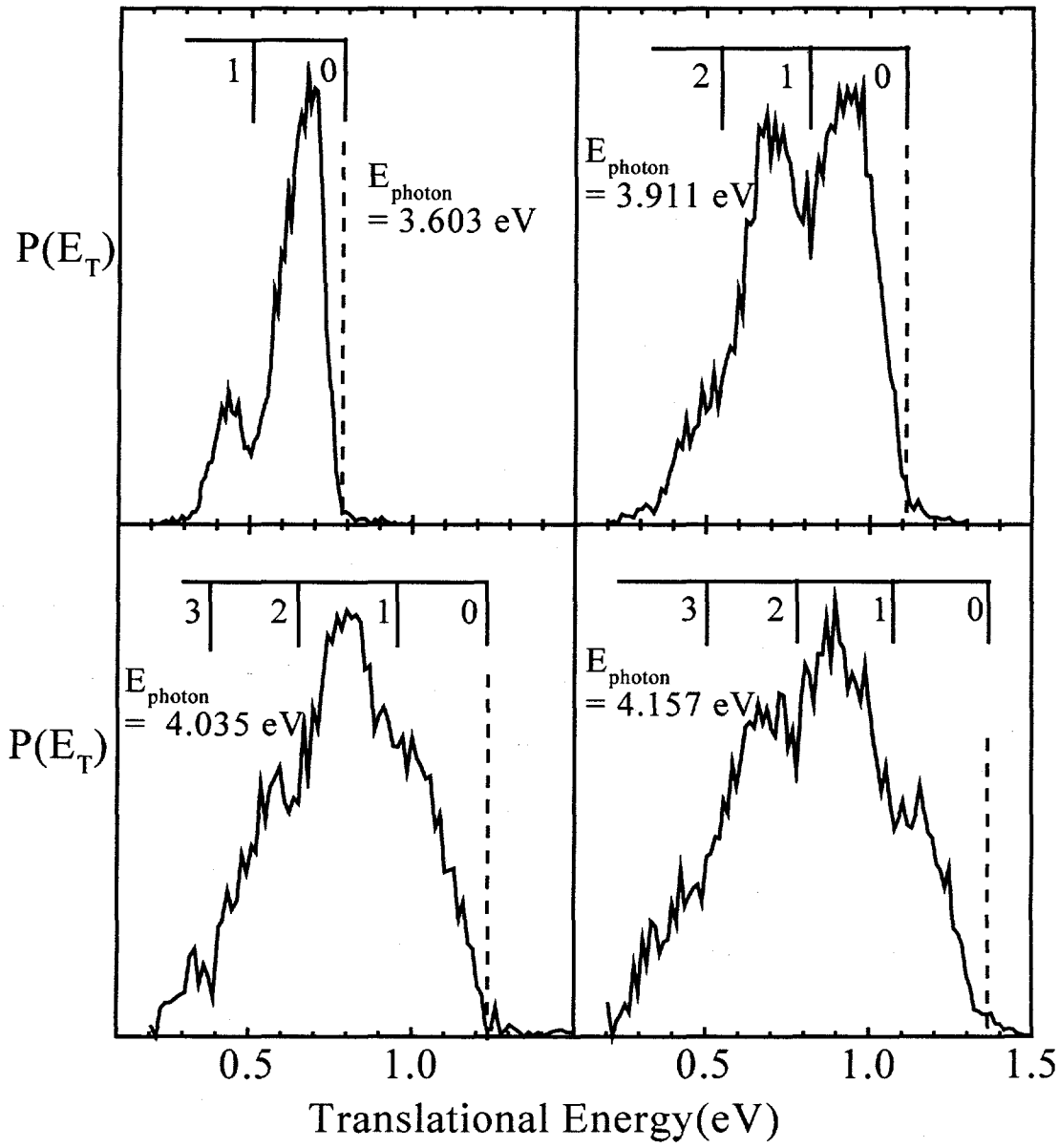

Figure 5. $P(E_T)$ distributions for the molecular elimination of N_2 from HNCN. The photon energies are given and the maximum translational energies, E_T^{max} are indicated with dashed vertical lines. The energetic onsets for the vibrational states of the N_2 fragment are denoted with a comb.

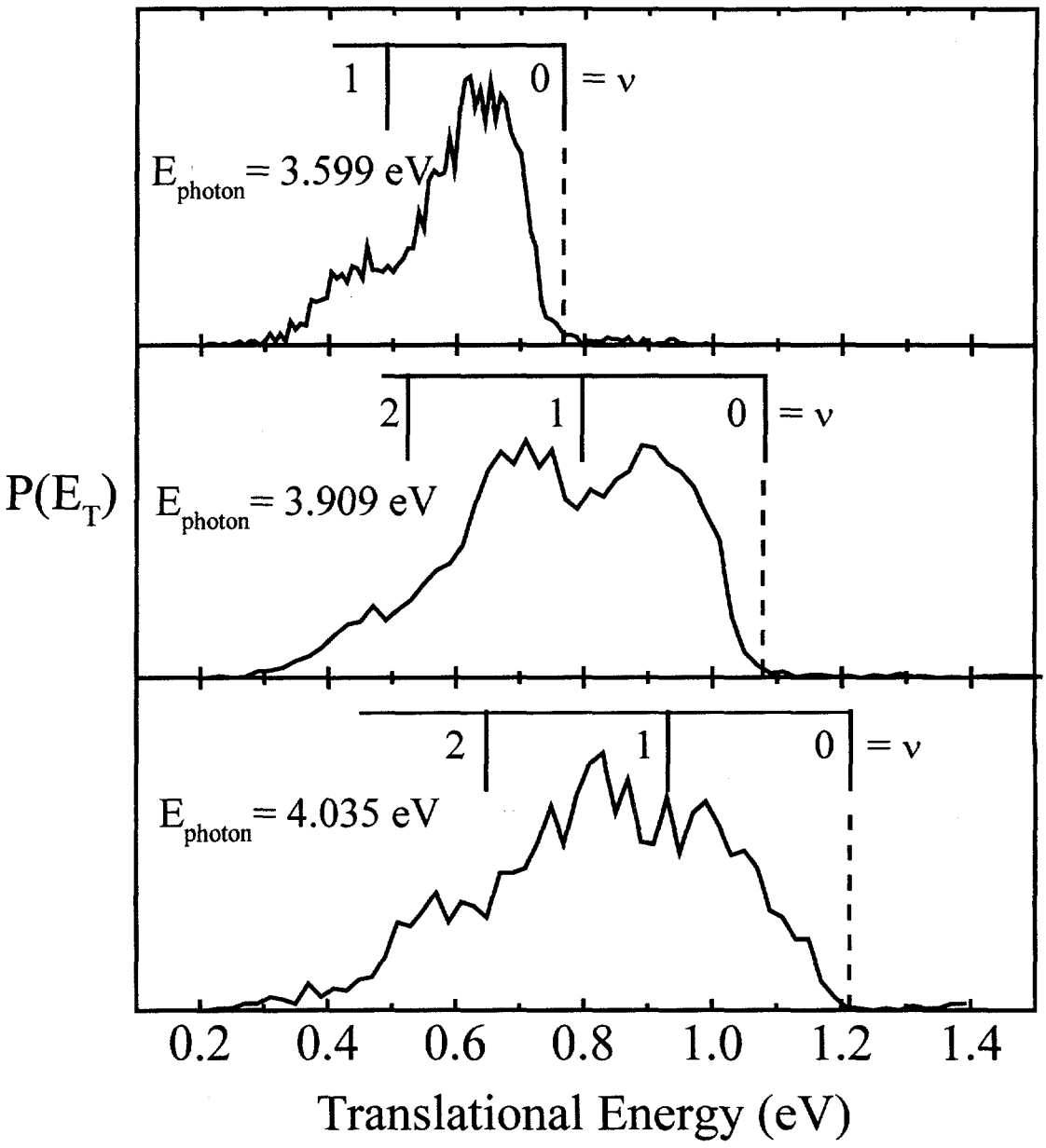

Figure 6. $P(E_T)$ distributions for the molecular elimination of N_2 from DNCN. The photon energies are given and the maximum translational energies, E_T^{max} are indicated with dashed vertical lines. The energetic onsets for the vibrational states of the N_2 fragment are denoted with a comb

Analogous structure is observed for both DNCN and HNCN. The distributions change dramatically with increased photon energy. For HNCN, the lowest energy transition displays two major features peaked at 0.67 and 0.44 eV respectively with the former comprising ≈ 85% of the total distribution and a full-width-half-maximum (FWHM) = 150 meV and a slight asymmetry to lower translational energy. The width of the corresponding feature for DNCN, peaked at 0.73 eV is slightly broader, FWHM = 170 meV. At higher excitation energies the overall widths of the $P(E_T)$ distributions increase and the structured features are considerably broadened. The higher energy distributions are not as sharply peaked towards high translational energy, e.g. excitation at 4.035 and 4.157 eV for HNCN yields $P(E_T)$ distributions peaked 0.44 and 0.46 eV below the maximum translational energy. The structure of the $P(E_T)$ distributions reflect the internal energy distribution of the nascent N_2 + CH (CD) photofragments. The observed structure with an energy separation of ≈ 250 meV can be reasonably assigned to the vibrational excitation of the N_2 photofragment. Further comment on the internal energy distribution of the photofragments will be made in section IV.B. For all photon energies, the angular distributions were found to be nearly isotropic.

IV. Analysis

A. Photofragment Yield Spectra

1. $\tilde{B}^2A' \leftarrow \tilde{X}^2A''$ transitions

The $\tilde{B}^2A' \leftarrow \tilde{X}^2A''$ origin, observed in this work via photofragment yield spectroscopy, Figure 2a, has been characterized previously in higher resolution absorption[19] and emission studies.[20] In this section, we will therefore focus our attention towards the new band observed in our PFY spectra centered ≈ 560 cm^{-1} to the blue of the

origin (Figure 2b). Wu *et al.*[20] determined the *a*-axis rotational constants for the $\tilde{X}^2A''$ and $\tilde{B}^2A'$ state to be 21.298 cm^{-1} and 22.300 cm^{-1} respectively. The rotational sub-band spacing in Fig 2a is nearly 80 cm^{-1}, approximately $4A'$, consistent with $\Delta K_a = \pm 2$ transitions, suggesting a parallel-type transition with K_a selection rules $\Delta K_a = 0, \pm 2, 4 \ldots$ The sub-band spacing is larger towards the blue, in agreement with the upper state *a*-axis rotational constant being slightly larger than that for the ground state. Based upon the K_a sub-band spacing and intensity, we assign the largest feature near 29570 cm^{-1} to the $\Delta K_a = 0$ bands, which is expected to contain $K_a = 0$, 1, 2 and 3 branches. The exact positions of the individual $\Delta K_a = 0$ bands cannot be clearly ascertained from our spectrum. The rotational contours of each sub-band are broad, lacking the sharp intense Q-branch features observed for the origin band. The broader rotational contours are consistent with a parallel vibronic transition. While the $\Delta K_a = 0$ bandhead is most intense, the $\Delta K_a = \pm 2$ sub-bands show considerable intensity. The energy spacing of 560 cm^{-1} from the origin suggests that this band involves an HN-C-N bend mode and the parallel band structure indicates that the overall vibronic symmetry of this band is the same as the ground state, A''.

An analogous parallel band, centered $\approx$ 440 cm^{-1} to the red of the $\tilde{B}^2A' \rightarrow \tilde{X}^2A''$ has been observed in dispersed fluorescence measurements by Wu *et al.*[20]. As in our spectra, the $\Delta K_a = \pm 2$ sub-bands show significant intensity. The authors assign this band to the out of plane bend mode, δ(HN-C-N) a'', of the ground state and suggest that this band becomes active via a Renner-Teller type mechanism in which the $\tilde{X}^2A''$ and $\tilde{A}^2A'$ bands are contaminated by the $\tilde{B}^2A'$ state, giving the $\tilde{X}^2A''$ states some A' character.

These authors argue that the mechanism is similar to the Renner-Teller interaction described by Bolman and Brown[38] to account for the 'forbidden' parallel bands in the analogous $\tilde{A}^2\Sigma^+ - \tilde{X}^2\Pi$ band system of NCO. We propose that a similar Renner-Teller interaction is responsible for the parallel vibronic band centered about 560 cm^{-1} to the blue of the $\tilde{B}$ state origin in which the zero point vibrational level of the $\tilde{X}^2A''$ state is mixed with vibrational states of the $\tilde{B}^2A'$ state with a'' character. The parallel band is accordingly assigned to the out of plane bend, δ(HN-C-N), a'' mode of the $\tilde{B}^2A'$ with an estimated frequency of 560 ± 10 cm^{-1}. An alternative mechanism for this parallel vibronic transition involves vibronic coupling between the vibrational levels of the $\tilde{B}^2A'$ state with the nearby $\tilde{C}^2A''$ state to which the higher energy bands between 31500-34500 cm^{-1} are assigned below.

2. Higher Energy Bands, $\tilde{C}^2A'' \leftarrow \tilde{X}^2A''$

The PFY spectra in Figure 3 reveals transitions at higher photon energies starting at 31500 cm^{-1}. The observed transitions are in excellent agreement with earlier reported absorptions.[21-24] All of the authors indicate that these reported bands appear simultaneously with the rotationally resolved $\tilde{B}^2A' \leftarrow \tilde{X}^2A''$ band of HNCN, leading Kroto and coworkers[23] and Basco and Yee[22] to associate these bands with another excited electronic state of HNCN. However, based upon isotopic substitution data and partial rotational analysis of the 31500 cm^{-1} band, Mathews *et al.*[24] have assigned the carrier of these bands near 30500, 31500 and 32500 cm^{-1} to the HCNN species, an assignment we believe is incorrect. We confidently assign this transition and the higher energy transitions to the HNCN radical based upon two observations. First, a photoelectron spectrum taken on a separate apparatus in our laboratory using the same

source conditions shows that only the HNCN isomer is produced upon photodetachment.[27] Secondly, the experimental thresholds for $P(E_T)$ distributions for the bands between 31500-34500 cm^{-1} match the expected E_T^{max} values determined from the $P(E_T)$ distribution of the well-known $\tilde{B}^2A' \leftarrow \tilde{X}^2A''$ band of HNCN. These higher energy bands must therefore also correspond to the HNCN isomer. For comparison, based upon the heats of formation listed in Table II, the predicted E_T^{max} value the HCNN isomer at a photon energy of 4.035 eV is 2.91 ± 0.18 eV.[18]

The HNCN radical is isoelectronic with the linear NCO radical, which has electron configuration $...(6\sigma)^2(1\pi)^4(7\sigma)^2(2\pi)^3$. The HNCN radical is bent, splitting the π orbitals into a' and a'' orbital yielding $...(6a')^2(7a')^2(1a'')^2(8a')^2(9a')^2(2a'')^1$. The perpendicular $\tilde{B}^2A' \leftarrow \tilde{X}^2A''$ transition corresponds to promotion of an electron from a non-bonding $8a'$ to the $2a''$ lone pair on the hydrogen-bonded N atom. The next electronic absorption should correspond to the promotion of an electron from a strongly bonding π-type orbital, $1a''$ or $7a'$, to the out of plane lone pair orbital $2a''$, analogous to the $\tilde{B}^2\Pi \leftarrow \tilde{X}^2\Pi$ transition of the NCO radical.[39,40] An electronic transition of this type is expected to give rise to an extended progression of the HN-C-N symmetric stretch. Excitation of an electron from the $1a''$ or $7a'$ orbital yields a parallel *a*-type or perpendicular *c*-type transition respectively.

The vibrational progression of ≈ 1000 cm^{-1} is similar to that of 1050 cm^{-1} observed for the symmetric stretch progression of the $\tilde{B}^3\Sigma_u^- \leftarrow \tilde{X}^3\Sigma_g^-$ band of the NCN radical.[23,34] and is in reasonable agreement with experimental values of 1140 cm^{-1}(Ref. 20) and 1146 cm^{-1}(Ref. 26) for the HN-C-N ground state symmetric stretch. The

observed PFY transitions are red-degraded indicating an increase in the overall HN-C-N bond distance. The reduced excited state frequency and increased bond length is consistent with the excitation of a strongly bonding electron. The vibronic transitions near 32500, 33500 and 34500 cm^{-1} clearly do not exhibit the sharp, well-separated K_a structure associated with the perpendicular *c*-type $\tilde{B}^2A' \leftarrow \tilde{X}^2A''$ transition and are instead dominated by an intense sub-band to the red with less intense sub-bands located to the blue with irregular spacing. The most intense sub-bands can be reasonably described by a parallel electronic transition in which the *a*-axis rotational constants are similar and hence the K_a-stacks are superimposed on each other. The parallel nature of these vibronic features suggests that the transition involves electronic excitation from the $1a''$ orbital to the $2a''$ orbital and is assigned to the $\tilde{C}^2A'' \leftarrow \tilde{X}^2A''$ band. Assignment of the weaker sub-bands to the blue of these vibronic transitions is unclear and may be due to either *b*-type components of the transition or vibrational hot-bands.

The band structure associated with the 31550 cm^{-1} band is particularly complex, as demonstrated by the previous misassignment of this band to the HCNN isomer.[24] Based upon the vibrational spacing, this transition appears to be a lower vibronic transition of the $\tilde{C}^2A'' \leftarrow \tilde{X}^2A''$ band. However, the regular sub-band spacing of ≈ 24 cm^{-1} is dramatically different from the band structure of the higher energy transitions and is not consistent with either parallel or perpendicular electronic transitions. Complicated sub-band structure which shifts upon deuteration has also been observed for a lower member of this progression at 30450 cm^{-1}.[21,24] The deceptive band structure of the lower members of the $\tilde{C}^2A'' \leftarrow \tilde{X}^2A''$ band near 30450 and 31550 cm^{-1} may be due to perturbations by the nearby $\tilde{B}^2A'$ state. Strong perturbations have been observed for the

analogous $\tilde{B}^2\Pi$ and $\tilde{A}^2\Sigma^+$ states of NCO.[39-41] Mathews *et al.*[24] indicates that the band at 31550 cm^{-1} is more strongly predissociated than the band at 30450 cm^{-1}. Our inability to observe this lower member of the $\tilde{C}^2A'' \leftarrow \tilde{X}^2A''$ band may be due to a lower photodissociation quantum yield.

B. Translational Energy Distributions

The $P(E_T)$ distributions reveal how the available energy is distributed among the photofragments. The energy balance for dissociation of HNCN to CH + N_2 is described by Eq 1.

$$h\nu + E_{INT}(HNCN) = D_0(HNCN) + E_T + E_{VR}(N_2) + E_{VR}(CH) \qquad (1.)$$

where hν is the photon energy, $E_{INT}(HNCN)$ is the average rotational energy of the parent radical about the *b* and *c* axes (≈ 60 K) plus the rotational energy associated with a particular K_a level. For the $\tilde{C}^2A'' \leftarrow \tilde{X}^2A''$ transitions, we excite the largest feature of the R bandhead and assume that the $K_a = 0$ levels dominate this feature. D_0 is the dissociation energy, E_T is the measured translational energy, $E_{VR}(N_2)$ and $E_{VR}(CH)$ represent the internal vibrational and rotational energies of the N_2 and CH photofragments. D_0(HNCN) for the N_2 loss channel can be extracted from these distributions by determining E_T^{max}, the thermodynamic limit in which all of the available energy goes towards relative translational motion, corresponding to photofragments with zero internal energy. Sharp thresholds towards high translational energy, defining this thermodynamic limit, are observed for all four $P(E_T)$ distributions, with a particularly sharp threshold at 0.795 eV seen for the $P(E_T)$ distribution obtained at 3.603 eV, yielding $D_0 = 2.805 \pm 0.020$ eV. An average of all of the onsets from all of the $P(E_T)$ distributions

yields $D_0 = 2.80 \pm 0.03$ eV. From our experimental value for D_0, literature values for the photofragment heats of formation, (see Table II.) and heat capacities[42] we calculate $\Delta_f H_{0\,K}\,(HNCN) = 3.35 \pm 0.03$ eV and $\Delta_f H_{298}\,(HNCN) = 3.31 \pm 0.03$ eV in reasonable agreement with $\Delta_f H_{298}\,(HNCN) = 3.34 \pm 0.13$ eV derived by Clifford *et al*,[17] but smaller error bars are associated with our value.

In addition to providing accurate values for bond dissociation energies, the $P(E_T)$ distributions describe the internal energy distributions of the nascent N_2 and CH photofragments. The $P(E_T)$ distributions show resolved structure reflecting the photofragment vibrational distributions. The nearly identical structure of the $P(E_T)$ distributions for HNCN and DNCN at similar photon energies indicates that the observed structure is not associated with H-atom motion and is most likely due to vibration of the N_2 photofragment. The peak spacing is between 220-260 meV, in reasonable agreement with the N_2 vibrational frequency, 292 meV, compared to 354 meV for CH. The combs shown above the $P(E_T)$ distributions indicate the calculated onsets for vibrationally excited levels of the N_2 fragment. The N_2 vibrational distribution for each of the HNCN and DNCN $P(E_T)$ distributions are estimated by fitting the vibrational features of the $P(E_T)$ distributions with nearly gaussian functions with a slightly asymmetric tail to lower translational energies. The resulting vibrational distributions and average vibrational energy, $\langle E_{vib} \rangle$ are listed in Table III. Table III and Figures 5 and 6 show that the N_2 vibrational excitation increases as a function of the overall photon energy. Increasing the photon energy from the $\tilde{B}$ state origin at 3.603 eV to the $\tilde{C}$ state at 3.911 eV shifts the .

Table II. Heats of formation of relevant $H_xC_yN_z$ species

Species	$\Delta_f H_0(eV)$	$\Delta_f H_{298}(eV)$	Reference
C	7.3708 ± 0.005	7.428 ± 0.005	42
H	2.239 ± 0.00006	2.2594 ± 0.00006	42
N	4.8797 ± 0.001	4.8989 ± 0.001	42
CH	6.149 ± 0.013	6.1846 ± 0.013	43
NH	3.90 ± 0.17	3.90 ± 0.17	42
N_2	0	0	Ref. State
CN	4.513 ± 0.021	4.498 ± 0.021	44
CNN	6.16 ± 0.03	6.15 ± 0.03	18
NCN	4.83 ± 0.03	4.82 ± 0.03	34
HCN	1.34 ± 0.03	1.336 ± 0.03	45
HNC	1.92 ± 0.04	1.95 ± 0.04	46
HCNN	5.02 ± 0.18	4.98 ± 0.18	18
HNCN	3.35 ± 0.03	3.31 ± 0.03	This work
H_2CNN	3.09 ± 0.20	3.03 ± 0.20	18
H_2NCN	1.46 ± 0.11	1.38 ± 0.11	This work with 17
		1.39 ± 0.05	47,48 with 49

Table III. N_2 photofragment vibrational distributions and average vibrational energy for the HNCN and DNCN $P(E_T)$ distributions.

Parent Molecule	*Photon Energy (eV)*	E_T^{max} *(eV)*	*(v=0)*	*(v=1)*	*(v=2)*	*(v=3)*	$\langle E_{vib} \rangle$ *(eV)*
HNCN							
	3.6027	0.795	85	15	---	---	0.043
	3.911	1.115	43	39	18		0.216
	4.035	1.235	31	41	25	3	0.288
	4.157	1.36	18	39	30	13	0.396
DNCN							
	3.599	0.764	83	17	---	---	0.049
	3.909	1.074	44	41	15	---	0.203
	4.035	1.200	33	42	24	2	0.276
Franck-Condon mapping of TS2			17.5	33.8	31.0	17.7	0.427

relative vibrational population, v=0:v=1, from 6:1 to nearly 1:1 where v is the vibrational state of the N_2 photofragment. For more energetic vibronic transitions of the $\tilde{C}$ state, the v=1 state of N_2 dominates the vibrational distribution and the population in the v=2 and 3 states increase as well.

The peak widths and shape of the vibrational features of the $P(E_T)$ distributions are determined by the experimental energy resolution (≈ 20 meV) and the rotational distribution of the N_2 and CH photofragments. An approximate measure of the extent of photofragment rotational excitation is provided by the energetic difference of the peak maxima for each N_2 vibrational state from its energetic onset or photofragments in their lowest rotational levels. This value, denoted E_{rot}, is determined for each N_2 vibrational state for all of the $P(E_T)$ distributions and is given by equation 3.

$$E_{rot} = E_T^{max}(\nu) - E_{peak}(\nu) \qquad (3),$$

where $E_{peak}(\nu)$ is the translational energy of the peak maximum of a particular N_2 vibrational state and $E_T^{max}(\nu)$ represents the maximum translational energy for a specific N_2 vibrational state, corresponding to photofragments with zero rotational excitation and is given by equation 4

$$E_T^{max}(\nu) = h\nu - D_0 - E_{N_2}^{vib}(\nu) \qquad (4),$$

where hv is the photon energy, D_0 is the dissociation energy and $E_{N_2}^{vib}(\nu)$ is the energy for the vth vibrational state of N_2. The values of E_{rot} are listed in Table IV for both HNCN and DNCN. The vibrational structure is increasingly broadened for higher photon energies making a precise determination of the peak positions less certain as reflected by the reported error bars. The values of E_{rot} exhibit a strong dependence on the N_2

Table IV. Rotational energy maxima as a function of N_2 vibrational quantum number and the effective barrier height, $E'_{barrier}$, based on impulsive model calculations.

Photon Energy (eV)	E_T^{max} *(eV)*	E_{rot} *(v=0) (eV)*	E_{rot}*(v=1) (eV)*	E_{rot} *(v=2) (eV)*	$E'_{barrier}$ *(eV)*
HNCN					
3.603	0.795	0.125 ± .010	0.064 ± .010	----	0.66 ± 0.05
3.911	1.115	0.178 ± .020	0.131 ± .020	0.049 ± .025	0.90 ± 0.05
4.035	1.235	---	0.147 ± .015	0.064 ± .020	0.97± 0.05
4.157	1.360	0.21 ± .020	0.173 ± .025	0.096 ± .025	1.22± 0.05
DNCN					
3.599	0.764	0.13 ± .015	0.045 ± .020	----	0.44± 0.05
3.909	1.074	0.174 ± .020	0.075 ± .020	0.031 ± .020	0.67± 0.05
4.035	1.200	0.210 ± .030	0.081 ± .030	0.056 ± .030	0.78± 0.05

vibrational quantum number with higher N_2 vibrational states yielding smaller values of E_{rot}. E_{rot} also increases for higher photon energy transitions. The increased width of the vibrational quantum number with higher N_2 vibrational states yielding smaller values of vibrational features at higher photon energies is associated with a broader fragment rotational distribution.

Finally, we can place limits on the rate of dissociation for the $\tilde{B}^2A' \leftarrow \tilde{X}^2A''$ origin transition. The LIF experiments of Wu *et al.*[20] measured the radiative lifetime of

the $\tilde{B}^2A' \leftarrow \tilde{X}^2A''$ to be 20 ± 5 ns, hence rate of non-radiative decay must at least be this long. The dissociation lifetime, τ_d, reduces the effective flight length between the photolysis laser and the detector (1 m) resulting in a 1/e broadening. For a typical beam velocity of ≈ 200 000 m/s, the flight time, t, is ≈ 5 μs. The FWHM for the 3.603 $P(E_T)$ distribution is 150 meV indicating that 20 ± 5 ns < τ_d < 250 ± 50 ns.

V. Discussion

The formation of CH + N_2 photofragments from the HNCN radical is an interesting and surprising result, requiring both an H-atom shift to the central carbon and bending of the NCN backbone to allow N-N bond formation, suggesting linear or cyclic isomers of HCNN as possible intermediate structures. Such a complicated rearrangement process is expected to give rise to substantial potential energy barriers. The goal of this section is to use the experimental product state internal energy distributions to gain insight into the essential features of the overall dissociation mechanism such as the barrier heights and transition state geometries associated with isomerization and dissociation and which electronic states are involved in the overall mechanism to determine how the HNCN radical is coupled to the CH + N_2 surface.

The experimental $P(E_T)$ distributions are all extend towards E_T^{max} and display resolved vibrational structure of the N_2 photofragment. Considering the density of states for the CH and N_2 products, with 2 linear rotors and vibrators, resolved vibrational structure is quite unanticipated, indicating that the forces involved in dissociation yield photofragments with a narrow distribution of available vibrational and rotational states. Preferential partitioning of the available energy into translation is frequently associated

with dissociation via a tight transition state in which the repulsive exit valley does not allow for coupling and randomization of all degrees of freedom. Additionally, the experimental N_2 vibrational distributions are narrow, peaking at v=0 or 1 with a maximum range between 0-3 quanta, in contrast to the broad N_2 vibrational distributions from the photodissociation of the NCN radical for which nearly equal populations of all energetically available N_2 vibrational states are observed.[34] The narrow N_2 product vibrational distributions for HNCN suggests that the N_2 bond length at the transition state is similar to that of the free diatomic.

Ab initio calculations by Cui *et al.*[9,10], Moskoleva and Lin,[11] and Walch[13] on the potential energy surfaces of CH + N_2 have identified a number of bound intermediates and transition states structures which may be relevant to the dissociation mechanism of HNCN. Of particular interest are the linear (lin-) HCNN isomer, and the cyclic (c-) HCNN transition state (labeled as TS2 in Figure 7), which have been calculated to lie 1.2 eV below and 0.5 eV above the CH + N_2 dissociation asymptote respectively. The linear isomer does not have a barrier to dissociation and so product state distributions from this intermediate should be reasonably described by statistical models such as a prior distribution[50] which predicts between 25-42% of the available energy is partitioned into translation. This statistical distribution is in sharp contrast to the experimental $P(E_T)$ distributions with 61-75% of the available energy partitioned into translation. Furthermore, the barrier to interconversion between the lin-HCNN and c-HCNN isomers was calculated to be 1.34 eV above the dissociation asymptote or 4.14 eV above the HNCN ground state and therefore, at the photon energies employed in this study (3.603 – 4.157 eV), the lin-HCNN isomer is not expected to play an important role in the

dissociation mechanism. The TS2 structure appears to be a much more likely candidate structure in the dissociation of HNCN. The tight three-center transition state is expected to give rise to a nonstatistical products state distribution and the low barrier height implies that this structure is energetically accessible. To assess the viability of the TS2 transition state in the dissociation of HNCN, we have compared our experimental product state distributions with those expected from simple dissociation models involving rapid dissociation via the TS2 transition state. The product vibrational and rotational distributions are treated separately. The structural parameters for TS2 calculated by Cui *et al.*[9,10] at the UCCSD(T)/6-311G(d,p) level of theory are reproduced in Table V.

Table V. Transition state (TS2) bond angles and distances from the *ab intio* calculations of Cui *et al.*[9,10] The bond distances for the free diatomic fragments[51] are shown for comparison.

	Cyclic Transition state (TS2)	Diatomic fragments
R_{CH}	1.103 Å	1.1199 Å
R_{NN}	1.189 Å	1.0976 Å
R_{CN1}	1.522 Å	
R_{CN2}	1.883 Å	
θ_{CH}	81.6°	
θ_{CN2}	53.8°	
Dih H-C-N_2-N_1	-158.4°	

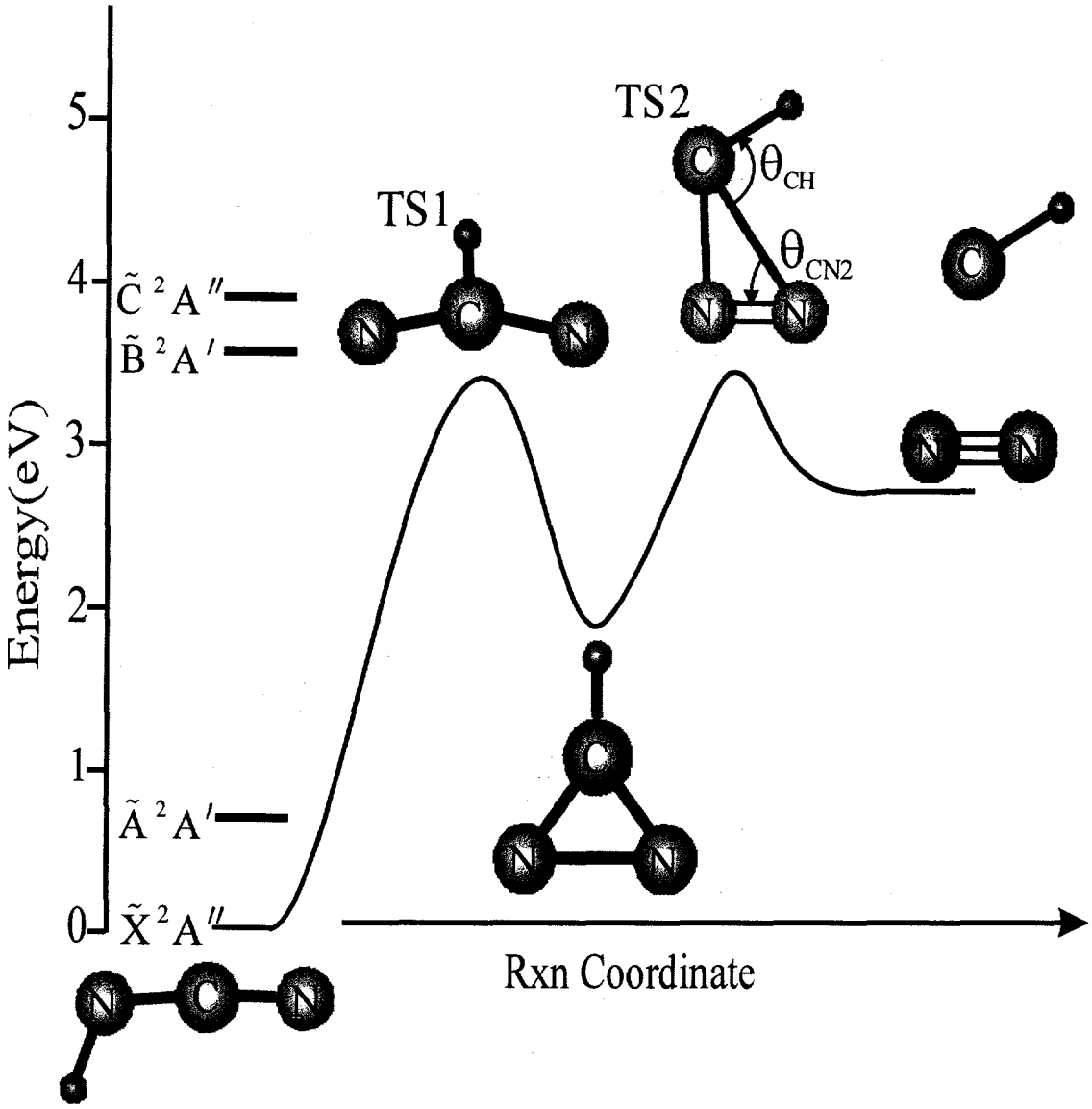

Figure 7. Energetics of the excited states of HNCN and shematic of the overall dissociation reaction mechanism. The energetic positions of the $\tilde{X}^2A''$ state is based upon this work, the term values for the $\tilde{A}^2A'', \tilde{B}^2A'$ and $\tilde{C}^2A''$ states are based upon the respective spectroscopic studies, Refs. 27, 21 and 23. The structure for HNCN is based upon spectroscopic results 21, the structure and energies for TS1 are from Ref. 11 while the TS2 and INT1 are from Ref. 10.

A. Vibrational Distributions

The N_2 vibrational distribution for the 3.603 eV transition shows nearly 85% of the total population is in v=0. This distribution changes rapidly with photon energy, peaking at v=1 for the highest energy transitions. One qualitative explanation for these results is that the lowest photon energy (3.603 eV) is energetically close to the exit barrier and the resulting photofragment vibrational distribution is generated from the zero point of the transition state. As the photon energy is increased, higher vibrational levels of the transition state are populated leading to an increased degree of photofragment vibrational excitation.

In the limit of rapid dissociation over a barrier the steep repulsive exit valley does not allow for coupling between vibrational and translational modes. A simple model for describing the resulting photofragment vibrational distribution is provided by a Franck-Condon mapping of the transition state equilibrium geometry onto the photofragment equilibrium bond distances.[52] As is seen in Table V, the CH bond length changes only 0.017 Å from TS2 to the free diatomic. Franck-Condon mapping of the transition state produces > 99% of the vibrational population in v=0. The N_2 bond distance shows a more substantial change, decreasing by ~ 0.09 Å from TS2, leading to an N_2 vibrational distribution which peaks at v=1 with nearly equal populations in v=1 and v=2. Table IV shows that a Franck-Condon mapping of the transition greatly overestimates the extent of N_2 vibrational excitation compared to the $P(E_T)$ distribution resulting from excitation at 3.603 eV, yet agrees quite well with the 4.157 eV $P(E_T)$ distributions.

An alternative description of the product vibrational distribution is the statistically adiabatic channel model (SACM).[53,54] In this model it is assumed that the vibrational levels of the transition state are statistically populated and that the vibrational quantum numbers are preserved through dissociation to product degrees of freedom. The CH and N_2 product vibrational populations are then a reflection of the populations of the CH and N_2 stretch modes at the transition state. Using the vibrational frequencies of Cui *et al.*,[9,10] and assuming that the vibrational modes are harmonic, the relative population of the vibrational levels of the transitions state were calculated as a function of energy above the barrier using the Beyer-Swinehart algorithm.[54] These calculations indicate that a statistical distribution of transition state vibrational states and a barrier height of 0.5 eV above the dissociation asymptote is required to produce the N_2 vibrational distribution of the 3.603 eV $P(E_T)$ distribution. However, using this same barrier height underestimates the N_2 vibrational distribution for higher energy transitions suggesting that the vibrational populations of the transition state modes are not statistically distributed. The Fanck-Condon and SACM model respectively overestimate and underestimate the experimental product state vibrational distributions. However, both models give rise to a reasonably narrow product vibrational distribution, supporting the TS2 structure as a possible transition state in the dissociation of HNCN.

B. Rotational Distributions - Modified Impulsive model

As is visible from Table IV, the rotational distributions, described by E_{rot} are strongly dependent on the N_2 vibrational quantum number showing a decrease in E_{rot} for higher N_2 vibrational states. A simple model for fragment rotational excitation which displays this inverse relationship between vibrational and rotational excitation is the

modified impulsive model,[55-57] which assumes that dissociation is mediated by an instantaneous repulsive force between the departing atoms and that the vibrations of the recoiling fragments are infinitely stiff. The impulsive fragment rotational energy, E_{rot}^{imp}, described by Eq. 6, is dependent upon the parent molecular geometry and the energy available for translation, E_{avail},

$$E_{rot}^{imp} = \alpha \cdot (E_{avail}) \qquad (6),$$

where α describes the geometric factors as described by Buttenhoff et al.[58]

For simple bond cleavage, the impulsive force is naturally applied along the breaking bond, however, for three-center type dissociations, such as c-HCN_2, the impulse need not occur along an individual bond.[58] An approximate direction of the impulse can be obtained from the motion along reaction coordinate at the transition state, the ν_6 eigenvector, which is primarily associated with stretching of the long C-N bond (C-N2). In the subsequent calculations we have assumed that the impulse lies along this bond. As pointed out by Buttenhoff *et al.*,[58] the impulsive force occurs in the exit valley past the transition state geometry since at the transition state itself, there is no force on the photofragments. Here, we have made the further approximation that the geometry at which the impulse is applied is that of the transition state. The results of the modified rotationally impulsive model for both HNCN and DNCN are shown in Figure 7 in which the rotational energy of the impulsive model, E_{rot}^{imp}, is plotted versus E_{avail}. The impulsive force primarily excites the N_2 photofragment, e.g. a value of E_{avail} = 0.6 eV gives rise to a rotational quantum numbers of 19 and 3 for j_{N_2} and j_{CH} respectively. The

steeper slope for the DNCN system is due to the larger impact parameter associated with the CD fragment.

For dissociation via a barrier, the impulsive force is defined by the barrier height, $E_{barrier}$. In the modified impulsive model, the impulse does not generate fragment vibrational excitation. The fragment vibrational distribution is formed prior to the impulse and hence this vibrational energy, E_{vib}, is not available to translation or rotation and is subtracted from the impulsive energy, yielding relation 7.,

$$E_{rot}^{imp} = \alpha \cdot (E_{barrier} - E_{vib}) \qquad (7).$$

The experimental values of E_{rot} determined from the $P(E_T)$ distributions increase nearly linearly with $-E_{vib}^{N_2}$ with slopes similar to that of α from the impulsive model calculations. The experimental values of E_{rot} are displayed as points in Figure 8. The effective barrier height, $E'_{barrier}$, for each excitation energy is then determined from the x-axis offset value required to place the experimental values of E_{rot} for HNCN and DNCN along the lines from the impulsive model calculations. The values of $E'_{barrier}$ are fixed for each photon energy and are listed in Table IV. The values of $E'_{barrier}$ vary between 0.6-1.12 eV for HNCN and 0.44-0.78 eV for DNCN with larger values of $E'_{barrier}$ observed for higher photon energies. Cui *et al.*[9,10] calculate the barrier height for TS2 to be 0.51 eV above the dissociation asymptote, while Walch[13] calculates the barrier height of a similar transition to be 0.78 eV. The experimental observation of photofragment signal at 3.59 eV places an upper limit on the barrier height at 0.79 eV.

It is particularly surprising that the values of $E'_{barrier}$ increase with photon energy. One possible explanation for this effect is that at higher excitation energies, vibrationally

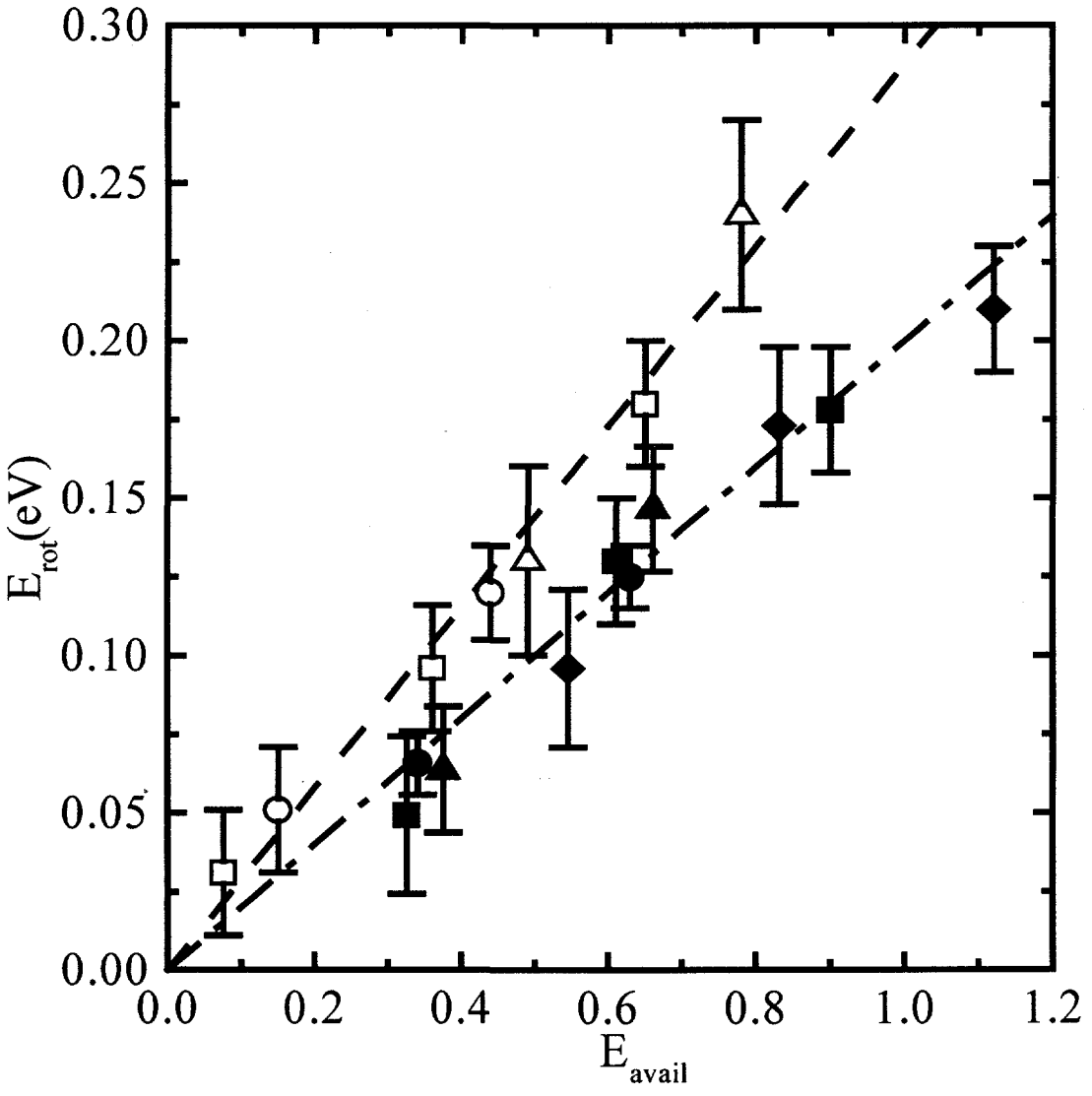

Figure 8. Plot of the photofragment rotational energy, E_{rot} as a function of the energy available to translation, E_{avail}. The results of the impulsive model calculation for HNCN and DNCN are indicated by a dot-dash and dashed line respectively. The experimental values for E_{rot} from the experimental $P(E_T)$ distributions are shown as closed symbols for HNCN and open symbols for DNCN with photon energies of 3.6 eV (○), 3.9 eV (□), 4.03 eV (△) and 4.16 eV (◊). The effective barrier heights for each transition, $E'_{barrier}$ are estimated by determining the intercept value required to place the experimental data on the line of the impulsive model calculations, see text.

excited states of the transition state are accessed. The dissociation from these higher vibrational levels may then give rise to a larger effective barrier heights for the transition state. The agreement in slope of both the HNCN and DNCN data with the calculated modified impulsive model suggests that the approximation of the impulsive force along the longer C-N bond (C-N2) is reasonable.

The modified impulsive model provides only a single rotational energy and therefore does not describe the width of the rotational distributions. A rotational distribution can be obtained by including the effect of parent vibrational and rotational motion.[56] Using the eigenvectors and frequencies for the transition state normal modes,[59] see Figure 9, and following the work of Buttenhoff *et al.*,[58] we have determined the contribution of the zero-point motion of each transition state eigenvector towards the fragment rotational distributions. Vibrational motion in CNN plane will have the largest effect upon the rotational distribution since this momentum will add or subtract from the impulsive momentum. The asymmetric stretching of the C-N bonds, ν_4, leads to largest spread in the N_2 vibrational distribution with a FWHM of 4 rotational quanta while the in-plane H-atom bending mode , ν_3, leads to a FWHM of 2 quanta for the CH fragment. Converting the rotational distribution into an energy distribution and then convoluting with our experimental energy resolution yields the dashed line in Figure 10 for the 3.603 eV $P(E_T)$ distribution. As can be seen in Figure 10, the vibrational motion does not completely account for the total width of the experimental translational energy distribution. Parent rotational excitation is also expected to contribute to the fragment rotational distribution and should broaden the overall spectrum. While the initial ground state rotational distribution of HNCN is characterized by a temperature of approximately

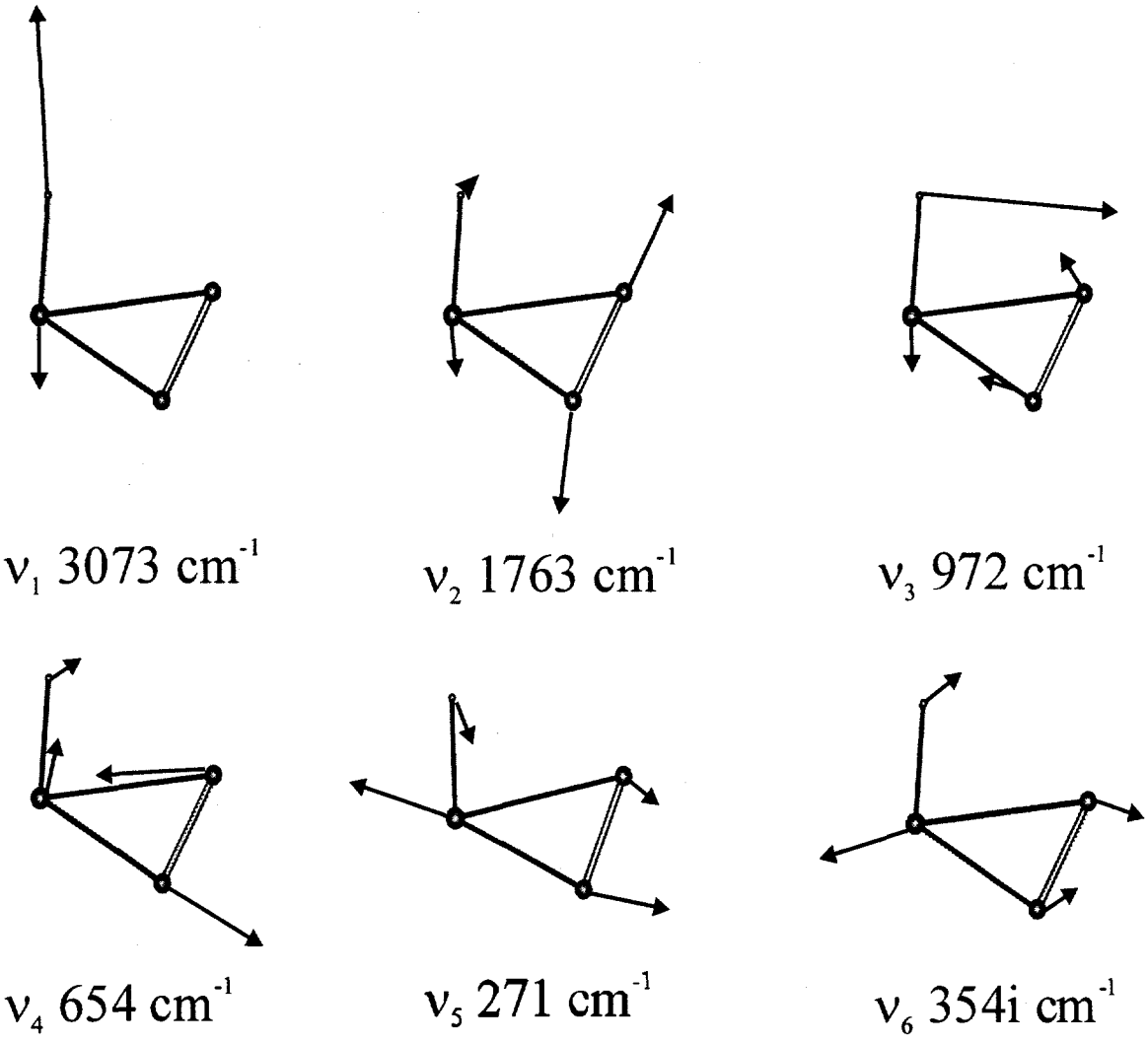

Figure 9. Eigenvectors and eigenvalues of the normal modes for TS2 from the *ab initio* calculations of Cui *et al.*[59]. Only the motion in the C-N1-N2 plane is shown here; ν_5 and ν_6 possess "out-of-plane" H-atom motion.

60 K, it is unclear how the rotational angular momentum distribution of the HNCN radical maps onto the cyclic transition state. Despite this uncertainty, a temperature of 100 K for the rotational distribution of the transition state provides a reasonable fit to the experimental data, shown with a solid line in Figure 10.

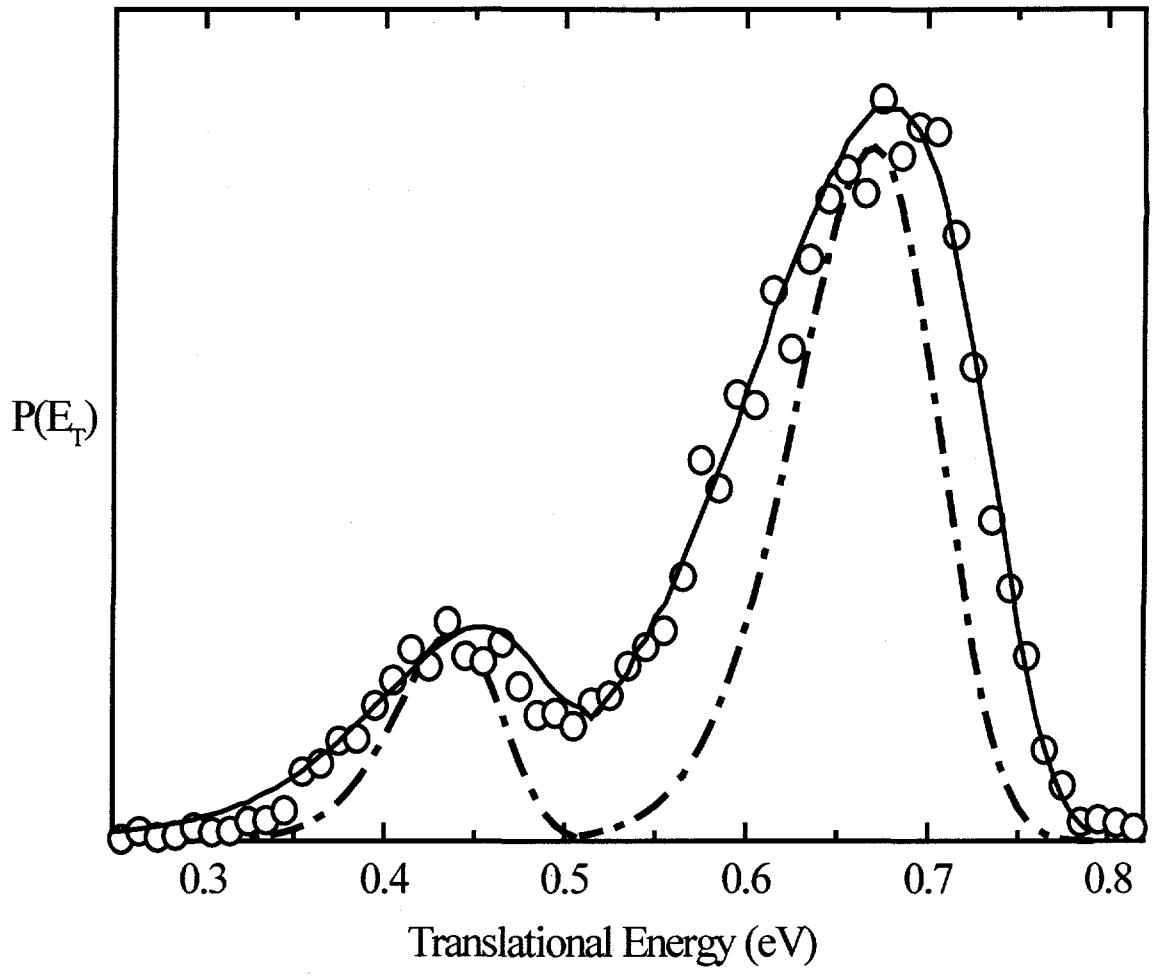

Figure 10. Comparison of the experimental $P(E_T)$ distribution for excitation at 3.6027 eV (○) with the impulsive model calculation. The dashed-dot line is the results of the impulsive model including the zero-point vibrational motion of the transition state. The solid line includes the zero-point motion and an estimated parent rotational distribution of 100 K.

Using the same procedure described above for higher energy $P(E_T)$ distributions was unable to account for the total width of the experimentally observed vibrational features. Both the fragment vibrational distributions and the impulsive model calculations suggest that the higher energy transitions dissociate via excited vibrational levels of the transition state. The larger momentum associated higher vibrational

transition states will lead a broader fragment rotational distribution. For example, the first harmonic of ν_4 yields a FWHM $\approx$ 7 rotational quanta for the N_2 fragment, yields a width of 170 meV for the $N_2(v=0)$ feature of the 3.911 eV $P(E_T)$ distribution, accounting for most of the observed FWHM of 210 meV.

C. Dissociation Mechanism

The simple dissociation models employing the tight three-center transition state, TS2, of Cui *et al.*[9,10] qualitatively and quantitatively describe many of the essential features associated with the experimental product state distributions. The narrow product vibrational energy distributions and a rotational distribution which shifts to lower quanta with increased N_2 vibrational excitation suggest that HNCN radical dissociates thru a cyclic transition state similar in nature to the TS2 structure. One remaining question is then how does the electronically excited HNCN radical couple to this dissociation surface. Clearly the initial step towards the formation of c-HCNN from HNCN is an H-atom transfer reaction. The calculations by Moskoleva and Lin[11] predict a transition state (TS1) for this isomerization near 0.5 eV, see Figure 10. This isomerization then occurs directly via optically prepared excited states or internal conversion (IC) to vibrationally excited levels of the ground state prior to isomerization. Both the excited $\tilde{B}^2A'$ and $\tilde{C}^2A''$ states yield ground state CH + N_2 products. Furthermore, the N_2 vibrational distribution and width of the rotational distributions appear to increase smoothly with excitation energy and do not display any obvious dependence on either the electronic or vibrational character of the optically prepared excited state. The formation of the same product channel and the gradual increase in product exictation with excitation energy suggests that both the excited $\tilde{B}^2A'$ and $\tilde{C}^2A''$ states access the same final dissociative

surface. The dissociation lifetime, τ_d, of the $\tilde{B}^2A'$ state has been estimated, 20 ± 5 ns $\leq \tau_d \leq 250 \pm 50$ ns. The slow rate of dissociation suggests that the dissociation does not occur directly on an excited state surface and more likely undergoes internal conversion (IC) to vibrationally excited levels of the $\tilde{X}^2A''$ state prior to isomerization or dissociation. The overall proposed reaction mechanism is outlined below,

$$HNCN(\tilde{B} \text{ or } \tilde{C}) \xrightarrow{IC} HNCN(\tilde{X}) \xrightarrow{isomerization} c\text{-}HCNN \xrightarrow{dissociation} CH+N_2$$

and shown schematically in Figure 7. The simple dissociation models employed above imply that the vibrational distribution at the transition state is not statistically distributed, which appears to be at odds with the above mechanism. Passage over the isomerization barrier may lead to a nonstatistical partitioning of vibrationals level in the final transition state.

The results of this study suggest that the CH + N_2 reaction does access the HNCN intermediate and therefore our results are relevant to combustion. Based upon their *ab initio* calculations, Moskoleva and Lin,[11] have proposed that reaction of CH + N_2, an initial step in the formation of prompt NO, does not yield the low-energy spin-forbidden $N(^4S)$ + HCN products, but instead accesses the higher energy spin-allowed $H(^2S)$ + $NCN(\tilde{X}^3\Sigma_g^-)$ products through the HNCN radical. Our experimental results support these calculations, confirming that the barriers to formation of HNCN from CH + N_2 are less than 0.79 eV and imply the presence a c-HCNN intermediate.

VI. Conclusion

The photodissociation dynamics and spectroscopy of the HNCN radical has been measured. This work conclusively shows that the carrier of the absorption bands between 31500-34500 cm^{-1} must indeed be HNCN and have assigned these transitions to the $\tilde{C}^2A'' \leftarrow \tilde{X}^2A''$ band. At all photon energies, CH + N_2 are found to be the primary dissociation channel. The product state distributions are highly nonstatistical and show an inverse relationship between rotational and vibrational excitation.

A modified impulsive model using the c-HCNN transition state geometry calculated by Cui and Morokuma[9] provides a reasonable fit to the experimental $P(E_T)$ distribution for the lowest energy transition, suggesting that the dissociation pathway for HNCN involves a c-HCNN intermediate which dissociates via a tight-three-center transition state. Based upon the variation of the product state distributions with photon energy, a dissociation mechanism is proposed in which the excited states undergo internal conversion to the ground state, followed by isomerization to c-HCNN which then dissociates to CH + N_2. The strong coupling of the HNCN radical to the CH + N_2 potential energy surface supports recent *ab initio* calculations[11] and implies the HNCN radical as an important intermediate in the formation of prompt NO. It is hoped that detailed measurements of the fragment rotational distribution and dynamical calculations using high level ab initio potential energy surfaces will allow this dissociation mechanism to be examined in more detail.

Acknowledgements

This research is supported by the Director, Office of Energy and Research, Office of Basic Energy Sciences, Chemical Sciences Division, of the U.S. Department of Energy

under Contract No. DE-AC03-76F00098. R.T.B. would like to thank Professor C.W. Mathews for stimulating discussions and for generously providing absorption data prior to publication, Dr. Qiang Cui and Professor Keiji Morokuma for providing the eigenvectors of the cyclic transition state normal modes, and Ms. Moskoleva and Professor Lin for providing a copy of their manuscript prior to publication.

References

1 J. A. Miller and C. T. Bowman, Progress in Energy and Combustion Science **15,** 287 (1989).

2 J. A. Miller and S. P. Walch, Int. J. Chem. Kinet. **29,** 253 (1997).

3 M. R. Berman and M. C. Lin, J. Phys. Chem. **87,** 3933 (1983).

4 L. J. Medhurst, N. L. Garland, and H. H. Nelson, J. Phys. Chem. **97,** 12275 (1993).

5 A. J. Dean, R. K. Hanson, and C. T. Bowman, in *Proceedings of the 23rd Symposium (International) on Combusiton* (The Combusiton Institute, Pittsburg, 1990), pp. 259.

6 D. Lindackers, M. Burmeister, and P. Roth, in *Proceedings of the 23rd Symposium (International) on Combustion*, Vol. 23 (The Combustion Institute, Pittsburgh, 1990), pp. 251.

7 M. R. Manaa and D. R. Yarkony, J. Chem. Phys. **95,** 1808 (1991).

8 M. R. Manaa and D. R. Yarkony, Chem. Phys. Lett. **188,** 352 (1992).

9 Q. Cui and K. Morokuma, Theor. Chem. Acc. **102,** 127 (1999).

10 Q. Cui, K. Morokuma, J. M. Bowman, and S. Klippenstein, J. Chem. Phys. **110,** 9469 (1999).

11 L. V. Moskaleva and M. C. Lin, Colloquium on NOx, SOx and Pollutant Emission Kinetics (2000).

12 J. M. L. Martin and P. R. Taylor, Chem. Phys. Lett. **209,** 143 (1993).

13 S. P. Walch, Chem. Phys. Lett. **208,** 214 (1993).

14 T. Seideman and S. P. Walch, J. Chem. Phys. **101,** 3656 (1994).

15 S. P. Walch, J. Chem. Phys. **103,** 4930 (1995).

16 T. Seideman, J. Chem. Phys. **101,** 3662 (1994).

17 E. P. Clifford, P. G. Wenthold, W. C. Lineberger, G. A. Petersson, and G. B. Ellison, J. Phys. Chem. A. **101,** 4338 (1997).

18 R. T. Bise, A. A. Hoops, and D. M. Neumark, J. Chem. Phys. **113,** 1 (2000).

19 G. Herzberg and P. A. Warsop, Can. J. Phys. **41,** 286 (1963).

20 W. Wu, G. Hall, and T. J. Sears, J. Chem. Soc., Faraday Trans. **89,** 615 (1993).

21 G. Herzberg and D. N. Travis, Can. J. Phys. **42,** 1658 (1964).

22 N. Basco and K. K. Yee, Chem. Commun. **3,** 150 (1968).

23 H. W. Kroto, T. F. Morgan, and H. H. Sheena, Trans. Faraday Soc. **66,** 2237 (1970).

24 C. W. Mathews, B. S. Pappas, and D. A. Ramsay, in *NRC Spectroscopy Conference in Memory of Gerhard Herzberg* (Ottawa, Canada, 1999).

25 S. Yamamoto and S. Saito, J. Chem. Phys. **101,** 10350 (1994).

26 G. Maier, J. Eckwert, A. Bothur, H. P. Reisenauer, and C. Schmidt, Leibigs Ann. , 1041 (1996).

27 Z. Liu, R. T. Bise, and D. M. Neumark, unpublished results (2000).

28 F.-M. Tao, W. Klemperer, M. C. McCarthyy, C. A. Gottlieb, and P. Thanddeus, J. Chem. Phys. **100,** 3691 (1994).

29 D. J. Leahy, D. L. Osborn, D. R. Cyr, and D. M. Neumark, J. Chem. Phys. **103,** 2495 (1995).

30 R. E. Continetti, D. R. Cyr, R. B. Metz, and D. M. Neumark, Chem. Phys. Lett. **182,** 406 (1991).

31 D. L. Osborn, H. Choi, D. H. Mordaunt, R. T. Bise, D. M. Neumark, and C. M. Rohlfing, J. Chem. Phys. **106,** 3049 (1997).

32 D. L. Osborn, D. J. Leahy, D. R. Cyr, and D. M. Neumark, J. Chem. Phys. **104,** 5026 (1996).

33 T. R. Taylor, R. T. Bise, K. R. Asmis, and D. M. Neumark, Chem. Phys. Lett. **301,** 413 (1999).

34 R. T. Bise, H. Choi, and D. M. Neumark, J. Chem. Phys. **111,** 4923 (1999).

35 J. M. B. Bakker, J. Phys. E **6,** 785 (1973).

36 J. M. B. Bakker, J. Phys. E **7,** 364 (1974).

37 D. P. de Bruijn and J. Los, Rev. Sci. Instrum. **53,** 1020 (1982).

38 P. S. H. Bolman and J. M. Brown, Chem. Phys. Lett. **21,** 213 (1973).

39 R. N. Dixon, Can. J. Phys. **38,** 10 (1960).

40 R. N. Dixon, M. J. Trenouth, and C. M. Western, Mol. Phys. **60,** 779 (1987).

41 S. A. Wright and P. J. Dagdigian, J. Chem. Phys. **104,** 8279 (1996).

42 M. W. Chase Jr., J. Chem. Phys. Ref. Data **Monograph 9,** 1 (1998).

43 M. Danielsson, P. Erman, A. Hishikawa, M. Larsson, R.-K. E., and G. Sundström, J. Chem. Phys. **98,** 9405 (1993).

44 Y. Huang, S. A. Barts, and J. B. Halpern, J. Phys. Chem. **96,** 425 (1992).

45 E. P. Clifford, P. G. Wenthold, W. C. Lineberger, G. A. Petersson, K. M. Broadus, S. R. Kass, S. Kato, C. H. DePuy, V. M. Bierbaum, and G. B. Ellison, J. Phys. Chem. A **102,** 7100 (1998).

46 A. Hansel, C. Scheiring, M. Glantschniq, and W. Lindinger, J. Chem. Phys. **109,** 1748 (1998).

47 D. J. Salley and J. B. Gray, J. Am. Chem. Soc. **70,** 2650 (1948).

48 D. J. Salley and J. B. Gray, J. Am. Chem. Soc. **73,** 5925 (1951).

49 H. G. M. De Wit, J. C. Van Miltenburg, and C. G. De Kruif, J. Chem. Thermodynamics **15,** 651 (1983).

50 R. D. Levene, in *Theory of Chemical Reaction Dynamics*, Vol. IV, edited by M. Baer (CRC Press, Inc., Boca Raton, Florida, 1985), p. 1.

51 K. P. Huber and G. Herzberg, *Constants of Diatomic Molecules* (Van Nostrand Reinhold, New York, 1979).

52 R. Schinke, *Photodissociation Dynamics* (Cambridge University Press, Cambridge, 1993).

53 M. Quack and J. Troe, in *Theoretical Chemistry*, Vol. 6b, edited by D. Henderson (Academic, New York, 1981).

54 T. Baer and W. L. Hase, *Unimolecular Reaction Dynamics* (Oxford University Press, New York, 1996).

55 G. E. Busch and K. R. Wilson, J. Chem. Phys. **56,** 3626 (1972).

56 H. B. Levene and J. J. Valentini, J. Chem. Phys. **87,** 2594 (1987).

57 A. F. Tuck, J. Chem. Soc., Faraday Trans. **73,** 689 (1977).

58 T. J. Buttenhoff, K. L. Carleton, and C. B. Moore, J. Chem. Phys. **92,** 378 (1990).

59 Q. Cui and K. Morokuma, private communication (2000).

Appendix 1. Publications list

D. H. Mordaunt, D. L. Osborn, H. Choi, R. T. Bise and D. M. Neumark, "Ultraviolet Photodissociation of the HCCO Radical Studied By Fast Radical Beam Photofragment Translational Spectroscopy." J. Chem. Phys. **105**, 6078 (1996).

D. L. Osborn, H. Choi, D.H. Mordaunt, R.T. Bise, D.M. Neumark, and C.M. Rohlfing, "Fast beam photodissociation spectroscopy and dynamics of the vinoxy radical." J. Chem. Phys. **106**, 3049 (1997).

L. R. Brock, B. Mischler, E. A. Rohlfing, R. T. Bise and D. M. Neumark, "Laser-induced fluorescence spectroscopy of the ketenyl radical." J. Chem. Phys. **107**, 665 (1997).

D. L. Osborn, D. H. Mordaunt, H. Choi, R.T. Bise, D.M. Neumark, and C.M. Rohlfing, "Photodissociation spectroscopy and dynamics of the HCCO free radical." J. Chem. Phys. **106**, 10087 (1997).

H. Choi, D. H. Mordaunt, R. T. Bise, T. R. Taylor and D. M. Neumark, "Photodissociation of triplet and singlet states of the CCO radical." J. Chem. Phys. **108**, 4070 (1998).

T. R. Taylor, R. T. Bise, K. R. Asmis and D. M. Neumark, "The singlet-triplet splittings of NCN." Chem. Phys. Lett. **301**, 413 (1999).

R. T. Bise, H. Choi, H. B. Pedersen, D. H. Mordaunt and D. M. Neumark, "Photodissociation spectroscopy and dynamics of the methylthio radical (CH_3S)." J. Chem. Phys. **110**, 805 (1999).

R. T. Bise, H. Choi and D. M. Neumark, "Photodissociation dynamics of the singlet and triplet states of the NCN radical." J. Chem. Phys. **111**, 4923 (1999).

R. T. Bise, A. A. Hoops, H. Choi and D. M. Neumark, "Photoisomerization and Photodissociation Dynamics of the NCN, CNN and HNCN free radicals" in *Imaging in Chemical Dynamics*. Eds., A.G. Suits and R. E. Continetti. Washington, D.C., American Chemical Society. **770,** Chapter 17, (1999).

H. Choi, R. T. Bise and D. M. Neumark, "Photodissociation Dynamics of the ethoxy radical (C_2H_5O)." J. Phys. Chem. A. **ASAP**, (2000).

H. Choi, R. T. Bise, A. A. Hoops and D. M. Neumark, "Photodissociation dynamics of the triiodide anion I_3^-." J. Chem. Phys. **113**, 2255 (2000).

H. Choi, R. T. Bise, A. A. Hoops, D. H. Mordaunt and D. M. Neumark, "Photodissociation of linear carbon clusters C_n (n=4-6)." J. Phys. Chem. A. **104**, 2025 (2000).

R. T. Bise, A. A. Hoops and D. M. Neumark, "Photodissociation dynamics of the CNN free radical." J. Chem. Phys. in press (2000).

H. Choi, T. R. Taylor, R. T. Bise, A. A. Hoops, and D. M. Neumark, "Photodissociation Dynamics of the Triiodide radical (I_3)." J. Chem. Phys. (2000).

R. T. Bise, A. A. Hoops and D. M. Neumark, "Photoisomerization and Photodissociation Pathways of the HNCN free radical." J. Chem. Phys. in preparation (2000).